

FACILITATING BAYESIAN IDENTIFICATION OF ELASTIC CONSTANTS THROUGH
DIMENSIONALITY REDUCTION AND RESPONSE SURFACE METHODOLOGY

By

CHRISTIAN GOGU

A DISSERTATION PRESENTED TO THE GRADUATE SCHOOL
OF THE UNIVERSITY OF FLORIDA IN PARTIAL FULFILLMENT
OF THE REQUIREMENTS FOR THE DEGREE OF
DOCTOR OF PHILOSOPHY

UNIVERSITY OF FLORIDA

2009

© 2009 Christian Gogu

To my parents, Ileana and Grigore

ACKNOWLEDGMENTS

First, I would like to thank Prof. Raphael Haftka and Dr. Jérôme Molimard, my main advisors during this period, for their time, availability and excellent guidance. I remain in awe of their never-ending enthusiasm and feel very fortunate to have been advised by them. I am also very grateful to my three other advisors Dr. Rodolphe Le Riche, Prof. Alain Vautrin and Prof. Bhavani Sankar for their advice, patience and very generous support.

I would like to especially thank Prof. Peter Ifju and his student Weiqi Yin for the collaboration on the experimental part of this work, collaboration thanks to which I was able to have a real test case in a relatively short amount of time.

I would also like to thank my PhD committee members, Dr. Nam-Ho Kim, Prof. Christian Bes and Dr. Lawrence Winner, for their willingness to serve on my committee, for evaluating my dissertation, and for offering constructive criticism to help me improve this work.

Financial support by the NASA Constellation University Institute Program (CUIP) and the Ecole Nationale Supérieure des Mines de Saint Etienne grant is gratefully acknowledged.

Many thanks go also to Dr. Satish Bapanapalli for the collaboration on the ITPS at the beginning of my PhD, to Dr. Tushar Goel for his assistance with surrogates and sensitivity analysis, and to Dr. Gustavo Silva for his support with the open hole plate model.

I duly thank all my labmates and colleagues both in Saint Etienne and in Gainesville for the interaction we had during all this period. Whether research or administration related, or just as good friends you were there for me and helped me out when needed, often putting a smile back on my face.

Last but not least I want to thank my parents who have always supported me in everything I have done. Your love and understanding has never stopped being there for me. To you I dedicate this work.

TABLE OF CONTENTS

	<u>page</u>
ACKNOWLEDGMENTS	4
LIST OF TABLES	9
LIST OF FIGURES	13
ABSTRACT.....	16
ABSTRACT (FRENCH)	18
EXTENDED SUMMARY (FRENCH)	20
CHAPTER	
1 INTRODUCTION – HOW DIMENSIONALITY REDUCTION AND RESPONSE SURFACE METHODOLOGY CAN BENEFIT BAYESIAN IDENTIFICATION	30
Motivation and Scope	30
Application Problems and Outline.....	34
2 DIMENSIONALITY REDUCTION FOR RESPONSE SURFACE APPROXIMATIONS APPLIED TO THERMAL DESIGN	37
Introduction.....	37
Methodology for Reducing the Number of Variables in an RSA	40
ITPS Atmospheric Reentry Application Problem	44
Finite Element Model of the Thermal Problem.....	46
Minimum Number of Parameters for the Temperature Response Surface.....	48
Simplifying Assumptions for the Thermal Problem	48
Nondimensionalizing the Thermal Problem.....	49
Maximum BFS Temperature RSA	55
RSA Construction Computational Cost.....	60
Applying the RSA for Comparison of Materials for the ITPS	61
Summary.....	63
3 LIMITS OF BASIC LEAST SQUARES IDENTIFICATION - AN INTRODUCTION TO THE BAYESIAN APPROACH APPLIED TO ELASTIC CONSTANTS IDENTIFICATION	64
Introduction.....	64
Least Squares and Bayesian Methodologies to Parameter Identification.....	66
Least Squares Formulations	66
Bayes' Theorem.....	67

The Bayesian Identification.....	68
Progressing from Least Squares to Bayesian Identification.....	71
A Three Bar Truss Didactic Example.....	73
Description of the Three Bar Truss Example.....	73
Sources of uncertainty.....	74
The Least Squares Method.....	74
The Bayesian Method.....	75
Illustrative Example.....	77
Least Squares and Bayesian Comparison for the Three Bar Truss Problem.....	82
The Comparison Method.....	82
Results for Different-Sensitivity Strains.....	83
Least Squares Implicit Weighting According to Response Sensitivity.....	85
Results for Different Uncertainty in the Strains.....	89
Results for Correlation among the Responses.....	92
Results for All Three Effects Together.....	93
Average Performance of the Least Squares and Bayesian Approach.....	96
Vibration Identification Problem.....	97
Description of the Problem.....	97
Sources of uncertainty.....	98
The Identification Methods.....	99
Results.....	102
Importance of Handling Multiple Uncertainty Sources.....	104
Summary.....	106
4 CHOOSING AN APPROPRIATE FIDELITY FOR THE APPROXIMATION OF NATURAL FREQUENCIES FOR ELASTIC CONSTANTS IDENTIFICATION.....	109
Introduction.....	109
Dickinson’s Analytical Approximation.....	110
Frequency Response Surface Approximation (RSA).....	112
Determining Nondimensional Variables for the Frequency RSA.....	112
RSA Construction Procedure.....	115
Frequency RSA Results.....	116
Identification Schemes.....	119
Sources of uncertainty affecting the identification.....	121
Identification Using the Response Surface Approximation.....	122
Least Squares Identification.....	122
Bayesian Identification.....	123
Identification Using Dickinson’s Analytical Approximate Solution.....	124
Least Squares Identification with Bounds.....	124
Least Squares Identification without Bounds.....	125
Bayesian Identification.....	126
Graphical Comparison of the Identification Approaches with the Low Fidelity Approximation.....	128
Summary.....	131

5	BAYESIAN IDENTIFICATION OF ORTHOTROPIC ELASTIC CONSTANTS ACCOUNTING FOR MEASUREMENT ERROR, MODELLING ERROR AND PARAMETER UNCERTAINTY	133
	Introduction.....	133
	Vibration Problem	135
	Bayesian Identification	136
	Bayesian Formulation.....	136
	Sources of Uncertainty	137
	Error and Uncertainty Models	138
	Bayesian Numerical Procedure	141
	Applicability and Benefits of Separable Monte Carlo Simulation to Bayesian Identification	143
	Bayesian Identification Results	144
	Uncertainty propagation through least squares identification	150
	Identification of the plate’s homogenized parameters	152
	Summary	153
6	REDUCING THE DIMENSIONALITY OF FULL FIELDS BY THE PROPER ORTHOGONAL DECOMPOSITION METHOD	155
	Introduction.....	155
	Proper Orthogonal Decomposition	156
	Simulated Experiment	159
	Experiment Description.....	159
	Numerical Model.....	159
	Dimensionality Reduction Problem.....	161
	Problem Statement.....	161
	POD Implementation.....	161
	POD Results.....	164
	POD Modes	164
	POD Truncation.....	165
	Cross Validation for Truncation Error	166
	Material Properties Sensitivities Truncation Error.....	168
	POD Noise Filtering.....	170
	Summary	171
7	BAYESIAN IDENTIFICATION OF ORTHOTROPIC ELASTIC CONSTANTS FROM FULL FIELD MEASUREMENTS ON A PLATE WITH A HOLE	181
	Introduction.....	181
	Open Hole Plate Tension Test.....	183
	Bayesian Identification Problem.....	184
	Formulation	184
	Sources of Uncertainty	185
	Error Model	186
	Bayesian Numerical Procedure	188

	Response Surface Approximations of the POD coefficients	188
	Bayesian Identification on a Simulated Experiment	191
	Bayesian Identification on a Moiré Full Field Experiment	193
	Full Field Experiment	193
	Bayesian Identification on Moiré Full Field Displacements	196
	Summary	200
8	SUMMARY AND FUTURE WORK	202
	Summary	202
	Future Work	204
APPENDIX		
A	POLYNOMIAL RESPONSE SURFACE APPROXIMATIONS	206
	Background	206
	Polynomial Response Surface Approximation Modeling	207
	General Surrogate Modeling Framework	207
	Design of Experiments (DoE)	208
	Numerical Simulation	208
	Polynomial Response Surface Construction	208
	Response Surface Verification	210
B	GLOBAL SENSITIVITY ANALYSIS	212
C	PHYSICAL INTERPRETATION OF THE BAYESIAN IDENTIFICATION RESULTS WITH EITHER MEASUREMENT OR INPUT PARAMETERS UNCERTAINTIES	215
D	MOIRE INTERFEROMETRY FULL FIELD MEASUREMENTS TECHNIQUE	218
E	COMPARISON OF THE MOIRE INTERFEROMETRY FIELDS AND THEIR PROPER ORTHOGONAL DECOMPOSITION PROJECTION	220
	LIST OF REFERENCES	223
	BIOGRAPHICAL SKETCH	233

LIST OF TABLES

<u>Table</u>	<u>page</u>
2-1 Dimensions of the ITPS (see also Figure 2-1) used among other to establish the simplifying assumptions.	49
2-2 Dimensional groups for the thermal problem.	51
2-3 Lower bounds (LB) and upper bounds (UB) used for sampling in the 15 variables space.....	56
2-4 Ranges of the nondimensional design variables	57
3-1 Numerical values for different-sensitivity strains.....	83
3-2 Extreme case identification results for different-sensitivity strain.	84
3-3 Numerical values for variable response uncertainty.....	90
3-4 Extreme case identification results for different response uncertainty.....	90
3-5 Numerical values for response correlation.	92
3-6 Extreme case identification results for response correlation.	92
3-7 Numerical values for the three combined effects.	93
3-8 Extreme case identification results for the three combined effects.	93
3-9. Average performance of the methods in the different cases.....	96
3-10 Assumed true values of the laminate elastic constants.....	97
3-11 Assumed uncertainties in the plate length, width, thickness and density (a , b , h and ρ).	98
3-12 Simulated experimental frequencies.....	103
3-13 Least squares and Bayesian results for a randomly simulated particular case.	103
3-14 Average performance for the plate vibration problem with 100 repetitions.....	103
4-1 Expression of the coefficients in Dickinson’s approximate formula (Eq. 4-1) for natural frequencies of free plate.....	111
4-2 Variables involved in the vibration problem and their units.....	113
4-3 Nondimensional parameters characterizing the vibration problem	113

4-4	Wide Bounds on the model input parameters (denoted WB)	117
4-5	Mean and maximum relative absolute error of the frequency RSA predictions (denoted RSA_{WB}) compared at 250 test points	117
4-6	Mean and maximum relative absolute error of the analytical formula frequency predictions compared at 250 test points.....	118
4-7	Narrow bounds on the model input parameters (denoted NB)	118
4-8	Mean and maximum relative absolute error of the frequency RSA predictions (denoted RSA_{NB}) compared at 250 test points.....	118
4-9	Experimental frequencies from Pedersen and Frederiksen (1992).....	120
4-10.	Plate properties: length (a), width (b), thickness(h) and density (ρ).....	120
4-11	Normal uncorrelated prior distribution of the material properties.....	121
4-12	Truncation bounds on the prior distribution of the material properties	121
4-13	Assumed uncertainties in the plate length, width, thickness and density (a, b, h and ρ).	122
4-14	LS identified properties using the frequency RSA_{WB}	122
4-15	Residuals for LS identification using the frequency RSAs.	123
4-16	Most likely point of the posterior pdf using the frequency RSA_{NB}	124
4-17	LS identified properties using the analytical approximate solution (bounded variables).....	125
4-18	Residuals for LS identification using the analytical approximate solution.	125
4-19	LS identified properties using the analytical approximate solution (unbounded variables).....	125
4-20	Residuals for LS identification using the analytical approximate solution.	126
4-21	Most likely point of the posterior pdf using the analytical approximate solution.	127
5-1	Experimental frequencies from Pedersen and Frederiksen (1992).	135
5-2	Plate properties: length (a), width (b), thickness(h) and density (ρ).....	135
5-3	Normal uncorrelated prior distribution for the glass/epoxy composite material.	137
5-4	Truncation bounds on the prior distribution of the material properties	137

5-5	Absolute difference between the frequencies obtained with thin plate theory and thick plate theory for the mean values of the a priori material properties	140
5-6	Assumed uncertainties in the plate length, width, thickness and density (a , b , h and ρ). Normal distributions are used.....	141
5-7	Least squares identified properties.....	145
5-8	Mean values and coefficient of variation of the identified posterior distribution.....	146
5-9.	Variance-covariance matrix (symmetric) of the identified posterior distribution.	146
5-10	Correlation matrix (symmetric) of the identified posterior distribution.	147
5-11	Mean values and coefficient of variation obtained by uncertainty propagation through the least squares identification.....	151
5-11	Least squares and Bayesian results for ply elastic constants identification with normally distributed measurement error.....	153
5-12	Least squares and Bayesian results for homogenized bending elastic constants identification with normally distributed measurement error.	153
5-13	Least squares and Bayesian results for bending rigidities identification with normally distributed measurement error.	153
6-1	Bounds on the input parameters of interest (for a graphite/epoxy composite material)..	162
6-2	Input parameters for snapshots 1 and 199.....	163
6-3	Error norm truncation criterion.....	165
6-4	Cross validation CV_{RMS} truncation error criterion.....	167
6-5	Input parameters to the finite element simulation for the sensitivity study and the simulated experiment.....	168
6-6	Truncation errors for the sensitivities to the elastic constants.....	169
6-7	Difference (in absolute value) between the finite element field and the projection of the noisy field onto the first 5 POD basis vectors.....	171
7-1	Normal uncorrelated prior distribution of the material properties for a graphite/epoxy composite material.....	185
7-2	Truncation bounds on the prior distribution of the material properties	185
7-3	Error measures for RSA of the U-field POD.....	190

7-4	Error measures for RSA of the V-field POD.	190
7-5	Material properties used for the simulated experiments.	191
7-6	Mean values and coefficient of variation of the identified posterior distribution for the simulated experiment.	191
7-7	Correlation matrix (symmetric) of the identified posterior distribution for the simulated experiment.	192
7-8	Manufacturer’s specifications and properties found by Noh (2004) based on a four points bending test.	193
7-9	Normal uncorrelated prior distribution of the material properties.	198
7-10	Truncation bounds on the prior distribution of the material properties	198
7-11	Mean values and coefficient of variation of the identified posterior distribution from the Moiré interferometry experiment.	198
7-12	Correlation matrix (symmetric) of the identified posterior distribution from the Moiré interferometry experiment.	198
7-12	Mean values and coefficient of variation of the identified posterior distribution from the Moiré interferometry experiment using a prior based on Noh’s (2004) values.	199
E-1	Average values of the experimental fields and of the components of the fields that were filtered out by POD projection.	222

LIST OF FIGURES

	<u>page</u>
2-1 Corrugated core sandwich panel depicting the thermal boundary conditions and the geometric parameters.	45
2-2 Incident heat flux (solid line) and convection (dash dot line) profile on the TFS surface as a function of reentry time.	45
2-3 1D heat transfer model representation using homogenization (not to scale).	46
2-4 Simplified thermal problem for dimensional analysis.	50
2-5 Summary of the dimensionality reduction procedure for the ITPS problem.	55
2-6 Maximum BFS temperature two-variable RSA.	58
2-7 Absolute error Δ of the response surface estimates compared to FE predictions.	59
2-8 Thermal comparison of materials suitable for the web using the contour plot of the maximum BFS temperature RSA.	62
3-1 Three bar truss problem.	73
3-2 Likelihood value using the distribution of ε_C if E were 5 GPa.	79
3-3 Likelihood function of E given $\varepsilon_C^{measure}$	81
3-4 Illustration of least squares solution $z^* = Ax^*$ and partial solutions z^{*i} for $m=2, n=1$	86
3-5 Illustration of least squares solution $z^* = Ax^*$ and virtual measurements z^{*i} for two different slopes A	87
3-6 Graphical representation of the least squares and Bayesian results for the three bar truss example for the different sensitivity case (i.e. different strain magnitude).	89
3-7 Graphical representation of the least squares and Bayesian results for the three bar truss example for the different uncertainty case.	91
3-8 Posterior distribution of $\{ E_x, G_{xy} \}$ found with the Bayesian approach.	104
3-9 Identified posterior pdf for: A) Only Gaussian measurement noise (case i.) B) Only model input parameters uncertainty (case ii.) C) Both Gaussian measurement noise and model input parameters uncertainty (case iii.).	105
4-1 Illustration of the procedure for sampling points in the nondimensional space.	116

4-2	Two dimensional representation in a three point plane of: A) The posterior pdf. B) The likelihood function.....	128
4-3	Two dimensional representation in a three point plane of the least squares objective function.....	129
5-1	Identified posterior joint distribution plots.....	146
5-2	Convergence of the: A) mean value. B) standard deviation. C) correlation coefficient of the identified distribution.....	148
6-1	Specimen geometry.....	159
6-2	Finite element mesh.....	160
6-3	Displacement and strain maps for snapshot 1.....	172
6-4	First six POD modes for U displacement fields.....	173
6-5	First six POD modes for V displacement fields.....	174
6-6.	First five strain equivalent POD modes for ε_x (first column), ε_y (second column) and ε_{xy} (third column)	175
6-7	Displacements truncation error in snapshot 1 using 3, 4 and 5 modes.....	176
6-8	Displacements truncation error in snapshot 199 using 3, 4 and 5 modes.....	177
6-9	Strain equivalent truncation error in snapshot 1 using 3, 4 and 5 modes for ε_x (first column), ε_y (second column) and ε_{xy} (third column).....	178
6-10	Strain equivalent truncation error in snapshot 199 using 3, 4 and 5 modes for ε_x (first column), ε_y (second column) and ε_{xy} (third column).....	179
6-11	Cross validation error (CV_{RMS}) as a function of truncation order.....	180
6-12	Noisy U and V fields of the simulated experiment.....	180
7-1	Specimen geometry.....	183
7-2	Flow chart of the cost (in green) and dimensionality reduction (in red) procedure used for the likelihood function calculation.....	191
7-3	Specimen with the Moiré diffraction grating (1200 lines/mm).....	194
7-4	Experimental setup for the open hole tension test.....	195
7-5	Fringe patterns in the: A) U direction. B) V direction for a force of 700N.....	195

7-6	Displacement fields obtained from the fringe patterns (no filtering was used at all) in: A) The U direction. B) The V direction.....	196
A-1	One dimensional polynomial response surface approximation	207
A-2	Steps in surrogate modelling.....	207
A-3	Latin hypercube sampling with sampling size $N_s=6$	208
C-1	Identified posterior pdf for: A) Only Gaussian measurement noise (case i.) B) Only model input parameters uncertainty (case ii.) C) Both Gaussian measurement noise and model input parameters uncertainty (case iii.)	215
D-1	Schematic of a Moiré interferometry setup.	218
E-1	Difference between the displacement fields obtained from the Moiré fringe patterns and their POD projection for the: A) U field. B) V field.....	220
E-2	Strain equivalent difference maps between the fields obtained from the Moiré fringe patterns and their POD projection for A) ε_x . B) ε_y . C) ε_{xy}	221

Abstract of Dissertation Presented to the Graduate School
of the University of Florida in Partial Fulfillment of the
Requirements for the Degree of Doctor of Philosophy

FACILITATING BAYESIAN IDENTIFICATION OF ELASTIC CONSTANTS THROUGH
DIMENSIONALITY REDUCTION AND RESPONSE SURFACE METHODOLOGY

By

Christian Gogu

December 2009

Chair: Raphael T. Haftka
Cochair: Jerome Molimard
Major: Aerospace Engineering

The Bayesian method is a powerful approach to identification since it allows to account for uncertainties that are present in the problem as well as to estimate the uncertainties in the identified properties. Due to computational cost, previous applications of the Bayesian approach to material properties identification required simplistic uncertainty models and/or made only partial use of the Bayesian capabilities.

Using response surface methodology can alleviate computational cost and allow full use of the Bayesian approach. This is a challenge however, because both response surface approximations (RSA) and the Bayesian approach become inefficient in high dimensions. Therefore we make extensive use of dimensionality reduction methods including nondimensionalization, global sensitivity analysis and proper orthogonal decomposition.

Dimensionality reduction of RSA is also important in optimization and this is demonstrated first on a problem of material selection for an integrated thermal protection system, where we reduced the number of variables required in an RSA from fifteen to only two (Chapter 2).

We then introduce the Bayesian identification approach, first on a simple three bar truss problem, then on a plate vibration problem. On these problems we find three general situations in which the Bayesian approach has a significant advantage over least squares identification: large differences in the response sensitivities to the material properties, large differences in the response uncertainties and their correlation (Chapter 3).

We then move to the identification problem of orthotropic elastic constants from the natural frequencies of free plates. To maintain reasonable computational cost, response surface approximations of the natural frequencies are constructed aided by nondimensionalization. We show that the fidelity of the approximations is essential for accurate identification (Chapter 4).

We then apply the Bayesian approach to identify the posterior probability distributions of the orthotropic elastic constants (Chapter 5) from the vibration test. Some of the properties could only be identified with high uncertainty, which partly illustrates the difficulties of accurately identifying the ply elastic constants from frequency measurements on a multi-ply multi-orientation structure.

The final two chapters look at identifying the four orthotropic elastic constants from full field displacement measurements taken on a tensile test on a plate with a hole. To make the Bayesian approach tractable the proper orthogonal decomposition method is used to reduce the dimensionality of the fields (Chapter 6).

Finally we present the results of the Bayesian identification for the open hole tension test, first on a simulated experiment, then on a Moiré interferometry experiment that we carried out (Chapter 7). As for the vibration based identification we find that the different properties are identified with different uncertainties, which we are able to quantify.

ABSTRACT (FRENCH)

FACILITER L'IDENTIFICATION BAYESIENNE DES PROPRIETES ELASTIQUES PAR REDUCTION DE DIMENSIONNALITE ET LA METHODE DES SURFACES DE REPONSE

La méthode d'identification bayésienne est une approche qui peut tenir compte des différentes sources d'incertitude présentes dans le problème et permet d'estimer l'incertitude avec laquelle les paramètres sont identifiés. Cependant, à cause du coût en temps de calcul, ces applications de l'approche bayésienne à l'identification des propriétés des matériaux nécessitaient soit des modèles d'incertitude simplistes ou n'utilisaient pas la méthode bayésienne à son potentiel entier.

L'utilisation de la méthode des surfaces de réponse permet de palier aux problèmes de temps de calcul et l'utilisation du potentiel entier de l'approche bayésienne. Cela continue par contre de poser le problème de l'inefficacité en haute dimension des surfaces de réponse ainsi que de la méthode bayésienne. Pour cela nous utilisons des méthodes de réduction de dimensionnalité telles que l'adimensionnalisation, l'analyse de sensibilité globale et la décomposition orthogonale propre.

Les approches de réduction de dimensionnalité appliquées aux surfaces de réponse sont également importantes en optimisation. C'est pourquoi le Chapitre 2 illustre cette utilisation sur un problème de sélection de matériaux pour un système de protection thermique intégré, où l'approche a permis de réduire le nombre de variables requises pour la surface de réponse de 15 à 2 seulement.

Nous introduisons ensuite l'approche d'identification bayésienne, d'abord sur un problème relativement simple d'un treillis à trois barres, puis sur un problème de vibration de plaques. Sur ces deux problèmes nous trouvons trois situations générales où l'approche bayésienne présente

un avantage par rapport à l'identification par moindres carrés classique: sensibilité variable, incertitude ou corrélation des réponses (Chapitre 3).

Nous passons ensuite à l'identification de propriétés élastiques orthotropes du matériau composite à partir de mesures de fréquences propres. Pour maintenir le temps de calcul raisonnable, des approximations par surface de réponse des fréquences propres sont construites en utilisant des paramètres adimensionnels. Nous montrons dans le Chapitre 4 que la fidélité des surfaces de réponse des fréquences propres est essentielle pour le problème d'identification que nous considérons.

Dans le Chapitre 5 nous appliquons l'approche bayésienne en vue d'identifier la densité de probabilité à posteriori des propriétés élastiques orthotropes. Une partie des propriétés a été identifiée avec une incertitude plus élevée, illustrant les difficultés pour identifier toutes les quatre propriétés en même temps à partir d'une structure laminée multi-ply et multi-orientations.

Enfin dans les deux derniers chapitres nous nous intéressons à l'identification des quatre propriétés élastiques orthotropes à partir de mesures des champs des déplacements sur une plaque trouée en traction. En vue de pouvoir appliquer l'approche bayésienne à ce problème nous réduisons la dimensionnalité des champs en appliquant la méthode de décomposition orthogonale propre (Chapitre 6).

Dans le Chapitre 7 nous présentons les résultats de l'identification bayésienne appliquée à la plaque trouée d'abord sur une expérience simulée puis sur une expérience de Moiré interférométrique que nous avons réalisé. Comme pour l'identification à partir de fréquences propres nous trouvons que les différentes propriétés sont identifiées avec une incertitude variable et nous quantifions cette incertitude.

EXTENDED SUMMARY (FRENCH)

Un grand nombre de techniques expérimentales sont disponibles en vue de déterminer les propriétés mécaniques des matériaux. En ce qui concerne les propriétés élastiques les techniques vont de simples essais uni-axiaux (ASTM D 3039) à des techniques basées sur des mesures de champs de déplacements sur des structures composites plus complexes (Molimard et al. 2005), chaque technique ayant ses avantages et inconvénients.

L'identification est le terme associé à la meilleure estimation possible des paramètres d'un modèle (les propriétés matériaux ici) à partir d'un jeu de mesures expérimentales donné. Les méthodes les plus fréquentes pour cela sont basées sur la détermination des paramètres d'un modèle numérique qui donnent le meilleur accord, usuellement en termes d'erreur moindres carrés, entre les mesures et les prédictions du modèle (Lawson et al. 1974, Bjorck 1996). D'autres méthodes ont également été proposées dans le domaine de l'identification des propriétés élastiques, tel que la méthode des champs virtuels (Grediac et al. 1989, 1998b), la méthode de l'écart en relation de comportement (Geymonat et al. 2002, 2003) ou la méthode de l'écart à l'équilibre (Amiot et al. 2007).

Indépendamment de la méthode d'identification utilisée deux défis majeurs continuent d'être :

- La gestion dans l'identification de sources d'incertitude inhérentes à l'expérience et à la modélisation de l'expérience
- L'estimation et la réduction de l'incertitude avec laquelle les propriétés sont identifiées

Les méthodes les plus couramment utilisées tiennent rarement compte de ces deux aspects de manière exhaustive, ne gérant pas de l'information statistique et fournissant uniquement une valeur numérique pour les paramètres sans autres information de nature statistique. Différentes sources d'incertitude peuvent cependant affecter les résultats, ne pas en tenir compte peut donc

biaisier l'identification. De plus, une valeur numérique seule est d'une utilité plus limitée car à partir d'un seul essai les différentes propriétés matériaux sont le plus souvent estimées avec un niveau de confiance différent. Typiquement pour des matériaux composites, le module de cisaillement et le coefficient de Poisson sont estimés beaucoup moins précisément à partir de la plupart des essais cherchant à déterminer toutes les quatre propriétés élastiques en même temps. Par conséquent, estimer l'incertitude avec laquelle les différentes propriétés matériaux sont déterminées peut être aussi important que de déterminer leur valeur la plus probable.

Plusieurs approches statistiques d'identification existent, qui peuvent gérer à divers niveaux, de l'information statistique. Ces méthodes incluent les moindres carrés pondérés (Bjorck 1996, Tarantola 2004) ou la méthode du maximum de vraisemblance (Norden 1972). Parmi les méthodes les plus générales qui peuvent tenir compte des incertitudes dans l'expérience et la modélisation et peuvent également fournir une estimation de l'incertitude dans les propriétés identifiées on peut aussi citer la méthode bayésienne. Cette approche est basée sur une formule très simple introduite il y a plus de deux siècles par Thomas Bayes (1793). Cependant, malgré la simplicité de la formule, elle peut poser aujourd'hui encore des problèmes de temps de calcul. En effet lorsque des distributions statistiques quelconques doivent être utilisées au sein de formules quelconques la simulation de Monte Carlo (Fishman 1996) est la plupart du temps requise.

L'objectif de cette thèse est de montrer comment en combinant des méthodes de réduction de dimensionnalité et d'approximation par surfaces de réponse, l'approche bayésienne peut être utilisée à son plein potentiel à un coût numérique raisonnable.

A cause de problèmes de temps de calcul, les applications précédentes de l'approche d'identification bayésienne utilisaient des modèles d'incertitudes simplistes (bruit additif gaussien uniquement) ou alors n'utilisaient pas la méthode bayésienne à son plein potentiel

(n'estimant pas les incertitudes avec lesquelles les propriétés étaient identifiées). Sol (1986) a été parmi les premiers à appliquer la méthode bayésienne dans le domaine de l'identification des propriétés élastiques des matériaux composites. Plusieurs auteurs ont suivi (Papazoglou et al. 1996, Lai et Ip 1996, Hua et al. 2000, Marwala et Sibisi 2005, Daghia et al. 2007). Cependant toutes ces études considéraient le bruit additif gaussien sur les mesures comme seule source d'incertitude dans le problème. Ceci permettait de traiter l'approche bayésienne d'une manière purement analytique, évitant ainsi des problèmes de temps de calcul. L'inconvénient est cependant qu'une telle hypothèse de bruit n'est souvent pas assez proche de la réalité. En effet, en plus de l'incertitude sur les mesures il y a souvent de l'incertitude sur le modèle et ses autres paramètres d'entrée. Ces incertitudes ne mènent pas nécessairement à un bruit additif gaussien sur la réponse mesurée. De plus, parmi les études mentionnées, seule celle de Lai et Ip (1996) donnait l'écart type avec lequel les propriétés étaient identifiées. Mais lorsqu'il y a des corrélations entre les propriétés identifiées une description complète de la densité de probabilité des propriétés identifiées est nécessaire.

L'utilisation de la simulation de Monte Carlo est nécessaire pour gérer des incertitudes non gaussiennes sur un modèle quelconque. Pour obtenir un ordre de grandeur du défi en termes de coût de calcul nous utilisons l'exemple d'une identification de la distribution de probabilité des quatre propriétés élastiques orthotropes d'un composite à partir de 10 fréquences propres de vibration de la plaque stratifiée. Appliquer à ce problème, l'approche bayésienne basée sur la simulation de Monte Carlo ferait typiquement intervenir 2 milliards d'évaluation de fréquences propres. Il est évident alors qu'utiliser des solutions numériques (tels que les éléments finis) au problème de vibration est beaucoup trop coûteux.

Le coût des calculs est encore exacerbé si au lieu de 10 mesures (les 10 fréquences propres) nous avons des centaines de milliers de mesures tel qu'est le cas pour des mesures de champ de déplacement pour lesquelles chaque pixel représente un point de mesure. En plus du problème précédent lié au nombre d'évaluations nécessaires, un nouveau problème se pose en termes de la dimension des distributions de probabilité intervenant dans la méthode bayésienne. Gérer des distributions de probabilité jointes en dimension de plusieurs centaines de milliers est hors de portée à l'heure actuelle.

Le but de ce travail est de développer une approche bayésienne pouvant tenir compte de distributions d'incertitudes non gaussiennes et d'utiliser la méthode bayésienne à son potentiel entier tout en maintenant un temps de calcul raisonnable. Les deux points décrits précédemment doivent être abordés pour cela :

1. Réduire considérablement le temps de calcul d'une évaluation de fonction
2. Réduire considérablement la dimensionnalité des densités de probabilité jointes intervenant dans le problème

Pour aborder le premier point nous avons choisi d'utiliser la méthode des surfaces de réponse (Myers et Montgomery 2002), en vue d'obtenir une approximation peu coûteuse en temps de calcul de la solution numérique par éléments finis. Un des défis réside alors dans le fait que les surfaces de réponse perdent en précision lorsque la dimension augmente. C'est pourquoi nous nous intéressons à plusieurs méthodes de réduction de dimensionnalité pouvant être appliquées à la méthode des surfaces de réponse : l'adimensionalisation et l'analyse de sensibilité globale (Sobol 1993).

Pour aborder le second point nous avons choisi d'utiliser la décomposition orthogonale propre (Berkooz et al. 1993). La décomposition orthogonale propre permet d'exprimer les champs de déplacement dans une base de très faible dimension (typiquement moins d'une

dizaine). Cependant cette réduction de dimensionnalité n'enlève en rien le requis du point 1 et nous devons toujours utiliser des surfaces de réponse pour approximer les résultats coûteux du code numérique par éléments finis.

L'application finale est l'identification bayésienne des propriétés élastiques orthotropes d'un composite à partir de mesures de champs de déplacements sur une plaque trouée en traction. Du point de vue mécanique cet essai présente plusieurs avantages. Les champs hétérogènes permettent en effet d'identifier toutes les quatre propriétés élastiques alors que seulement une ou deux propriétés sont typiquement déterminées à partir des essais normalisés. L'hétérogénéité du champ permet également d'avoir de l'information sur des variabilités spatiales de propriétés matériaux à l'intérieur de la plaque laminée. L'essai sur la plaque trouée a récemment été utilisé pour l'identification dans le cadre d'une approche moindres carrés (Silva 2009) et les résultats obtenus ont été très encourageants.

Du point de vue de la méthode bayésienne, l'identification à partir de l'essai sur plaque trouée est extrêmement difficile car il présente simultanément les deux défis mentionnés dans les points un et deux ci-dessus. L'identification fait, en effet, intervenir d'une part un code éléments finis coûteux en temps de calcul qui doit être remplacé par une approximation très fidèle mais peu coûteuse. D'autre part les mesures de champ contiennent des milliers de points de mesure nécessitant une réduction de dimensionnalité. Avant de relever les défis de cette application finale nous avons évalué les différentes techniques envisagées sur une série de problèmes moins complexes.

La réduction de dimensionnalité pour la construction des surfaces de réponse est un aspect également très important dans le contexte des problèmes d'optimisation. Dans le Chapitre 2 nous illustrons l'utilisation des surfaces de réponse ensemble avec des méthodes de réduction de

dimensionnalité sur un problème de sélection de matériaux optimaux pour un système de protection thermique intégré. Un système de protection thermique intégré pour véhicules spatiaux a pour but d'intégrer les fonctions de résistance mécanique structurales et de protection thermique lors de la rentrée atmosphérique. Nous nous intéressons dans ce chapitre essentiellement à la fonction de protection thermique qui nécessitait une approximation par surface de réponse pour la sélection de matériaux optimaux.

Nous montrons dans ce chapitre comment une réduction très significative dans le nombre de variables nécessaires pour la surface de réponse peut être obtenue en utilisant les techniques d'analyse de sensibilité globale (Sobol 1993) et d'adimensionalisation. Nous proposons d'abord une approche générale pour la réduction de dimensionnalité puis nous l'appliquons au problème du système de protection thermique intégré, pour lequel une surface de réponse de la température maximale atteinte par la face intérieure est requise. Le modèle éléments finis utilisé pour le calcul de cette température met en jeu 15 paramètres physiques d'intérêt pour la conception. L'adimensionalisation du problème en combinaison avec une analyse de sensibilité globale a néanmoins permis de montrer que la température ne dépend que de deux paramètres adimensionnels, représentant ainsi une réduction de dimensionnalité de 15 à 2 seulement. Ces deux paramètres ont été utilisés pour construire la surface de réponse et la vérifier avec des simulations éléments finis. Nous trouvons que la majeure partie de l'erreur dans la surface de réponse vient du fait que les paramètres adimensionnels manquent de rendre compte d'une petite partie de la dépendance de la température envers les 15 variables initiales. Cette différence a néanmoins été trouvée négligeable pour le but de la sélection de matériaux optimaux pour le système de protection thermique intégré, sélection qui est illustrée à la fin du chapitre.

Dans les chapitres suivants nous nous intéressons à l'identification bayésienne en considérant de problèmes de plus en plus complexes. Nous commençons dans le Chapitre 3 par un problème de treillis à trois barres avec deux objectifs en tête : d'une part le problème permet d'introduire l'approche bayésienne d'identification de manière didactique et d'autre part nous cherchons à identifier sur ce problème trois cas généraux où la méthode bayésienne présente systématiquement un avantage par rapport à l'identification classique par moindres carrés. Nous avons choisi d'analyser dans un premier temps le problème assez simple du treillis, car il permet d'isoler les différents effets qui affectent l'identification. Nous nous intéressons ainsi au cas où les différentes réponses mesurées ont des sensibilités différentes au paramètre à identifier, au cas où les réponses mesurées ont des incertitudes différentes et finalement au cas où les réponses mesurées sont corrélées entre-elles. Nous montrons alors que dans ces trois cas l'identification bayésienne est systématiquement plus précise que l'identification par moindres carrés classique. Dans le pire des cas, lorsque les trois effets s'additionnent nous trouvons que la méthode bayésienne peut mener à un paramètre identifié plus de dix fois plus proche de la vraie valeur que la méthode classique des moindres carrés.

Après le treillis à trois barres nous nous intéressons à un problème plus complexe, l'identification des propriétés élastiques orthotropes d'une plaque composite à partir de mesures de fréquences propre. Nous utilisons d'abord une expérience simulée sur une plaque simplement appuyée pour analyser sur ce cas l'influence des trois effets mis en évidence sur le problème du treillis. Nous trouvons à nouveau que l'identification bayésienne est systématiquement plus précise que l'identification moindres carrés classique, même si la différence entre les deux est moins importante que pour le treillis.

Dans les Chapitre 4 et 5 nous utilisons des mesures réelles de fréquences propres, effectuées par Pedersen et Frederiksen (1992) sur des plaques en fibre de verre/époxy aux conditions aux limites libres. Pour ce type de conditions aux limites il n'existe pas de solution analytique exacte pour les fréquences propres. Nous analysons donc dans le Chapitre 4 quel type d'approximation nous pouvons utiliser pour maintenir les couts des calculs raisonnables. Nous nous intéressons d'une part à une solution analytique approximative développée par Dickinson (1978) et d'autre part à des approximations par surface de réponse adimensionnelles d'un code éléments finis. Tandis que la solution analytique approximative a une erreur de l'ordre de 5%, nous montrons que nous pouvons obtenir des surfaces de réponse très précises en utilisant des variables adimensionnelles, avec une erreur inférieure à 0.1%. Nous comparons ensuite les résultats d'identifications effectuées avec ces deux types d'approximations. Ceci confirme que l'erreur dans la solution analytique approximative est trop grande pour qu'elle puisse être utilisée pour l'identification. Nous choisissons donc d'utiliser les approximations par surfaces de réponses adimensionnelles pour l'identification bayésienne qui est effectuée dans le Chapitre 5.

Les résultats de cette identification présentent plusieurs intérêts. D'une part nous avons pu tenir compte de plusieurs sources d'incertitude dans le problème : des incertitudes de mesure, des incertitudes de modélisation et des incertitudes sur divers paramètres d'entrée du modèle. D'autre part nous obtenons une distribution de probabilité pour les propriétés identifiées. Cette distribution permet une caractérisation complète des incertitudes avec lesquels les propriétés sont déterminées. Nous trouvons que les différentes propriétés sont identifiées avec un degré de confiance très différent puisque le module longitudinal est identifié le plus précisément avec un coefficient de variation (COV) de 3%, tandis que le coefficient de Poisson est identifié avec la plus grande incertitude avec un COV de 12%. Nous trouvons de plus qu'il y a une corrélation

significative entre plusieurs propriétés, corrélation qui est rarement identifiée par d'autres méthodes.

Dans les Chapitres 6 et 7 nous passons ensuite au problème final d'identification des propriétés élastiques orthotropes à partir de mesures de champs de déplacements. Par rapports au problème de vibration, la difficulté supplémentaire réside dans le grand nombre de points de mesures (à chaque pixel) résultant des mesures de champ. Nous détaillons dans le Chapitre 6 l'approche que nous utilisons pour réduire la dimensionnalité des champs. L'approche est basée sur la décomposition orthogonale propre (Berkooz et al. 1993). Cette technique est également connue sous le nom d'expansion de Karhunen Loeve ou d'analyse de composante principale selon son domaine d'utilisation. Elle permet d'exprimer dans une base modale de faible dimension (moins d'une dizaine ici) tout champ dans un certain domaine. Nous montrons que pour le domaine qui nous intéresse pour l'identification les champs peuvent être exprimés très précisément (erreur maximale de moins de 0.01% sur les déplacements) avec seulement 4 modes. L'approche présente également l'intérêt de filtrer les bruits de mesure dans les champs.

Dans le Chapitre 7 nous présentons l'identification bayésienne à partir d'un essai de traction sur plaque trouée. L'identification est réalisée d'abord sur une expérience simulée pour vérifier les résultats obtenus. Nous utilisons ensuite de véritables données expérimentales venant d'un essai de Moiré interférométrique que nous avons réalisé. La technique du Moiré interférométrique présente l'avantage d'offrir une excellent résolution spatiale et un bon rapport signal sur bruit. La distribution de probabilité identifiée montre, comme sur le problème de vibration, que les propriétés sont identifiées avec des incertitudes différentes et sont partiellement corrélées entre elles, l'avantage de l'approche bayésienne étant alors de pouvoir quantifier ces incertitudes et corrélations.

Enfin dans le Chapitre 8 nous concluons ce travail et présentons quelques pistes possibles pour de travaux futurs, notamment l'utilisation de l'indépendance statistique des sources d'incertitude pour réduire encore les temps de calcul, la combinaison de plusieurs expériences pour identifier un jeu de propriétés matériaux et comment utiliser au mieux toutes les informations statistiques dans un contexte de conception fiabiliste.

CHAPTER 1
INTRODUCTION – HOW DIMENSIONALITY REDUCTION AND RESPONSE SURFACE
METHODOLOGY CAN BENEFIT BAYESIAN IDENTIFICATION

Motivation and Scope

The best possible knowledge of material properties has always been a goal to strive for in the physics and engineering community. In mechanical design, more accurate knowledge of the material constants has direct implications on performance, efficiency and cost. In aerospace structures for example, more accurately known mechanical properties allow for reduced safety margins, which lead to lighter structures thus improving the vehicles efficiency and operational cost (Acar 2006).

To determine a given mechanical property, a multitude of experimental techniques can be used. For determining elastic constants for example, techniques range from simple tensile tests on standardized specimen (ASTM D 3039) to full field displacement measurements on more complex composite structures (Molimard et al. 2005), with each technique having its advantages and drawbacks.

Identification is the term associated with moving from a given experimental measurement to the best possible estimate of the model parameters (material properties here). The most common methods are based on finding the parameters of a numerical model that provide the best match, usually in terms of least squares error, between the measurements and the predictions of the model (Lawson et al. 1974, Bjorck 1996). When the numerical model is finite element based the method is often referred to as finite element model updating. In the domain of elastic constants identification from full field displacement measurements other methods have been introduced as well, such as the virtual fields method (Grediac et al. 1989, 1998b), the constitutive equation gap method (Geymonat et al. 2002, 2003) or the equilibrium gap method (Amiot et al. 2007).

Independently of the chosen method however, two major remaining challenges in identification are:

- handling inherent uncertainties in the experiment and modeling of the experiment
- estimating and reducing the uncertainty in the identified properties

The most commonly used methods rarely account for these two points however, since they do not handle statistical information and usually provide only a numerical estimate for the parameters. Uncertainties can however affect this estimate, so not accounting for them can bias the results. Furthermore, a numerical estimate alone for a material property is of questionable usefulness. Indeed it is often observed that from a single test, different material properties are not obtained with the same confidence. Typically for composite materials the shear modulus and the Poisson's ratio are known with significantly less accuracy from most tests that seek to determine all four elastic constants simultaneously. Accordingly, estimating the uncertainty with which a property is determined can be as important as estimating its mean or most likely value.

Multiple identification frameworks exist that can handle, to a variable degree, information of statistical nature. These include weighted least squares (Bjorck 1996, Tarantola, 2004) or maximum likelihood methods (Norden 1972). Among the most general methods that can both account for uncertainties in measurements and simulation and provide an estimate of the uncertainties in the identified properties is also the Bayesian updating method. This formulation is based on a very simple formula introduced almost two and a half centuries ago by Thomas Bayes (1763). Yet, in spite of the simplicity of the formula it can lead even today to major computational cost issues when applied to identification. Indeed, as many other statistical methods as well, it requires statistical sampling and Monte Carlo simulation (Fishman 1996) when applicability to any type of probability distribution as well as any formula is required.

The objective of the present dissertation is to demonstrate that by combining multiple dimensionality reduction techniques and response surface methodology, Bayesian identification can be performed to its full capabilities at reasonable computational cost.

Due to computational cost issues previous applications of the Bayesian approach to identification employed either simplistic uncertainty models (additive Gaussian noise only) and/or made only partial use of the Bayesian capabilities (did not estimate the uncertainty on the identified properties). In the domain of identification of elastic constants of composite materials Sol (1986) was probably the first to use a basic Bayesian approach. Others have followed since (Papazoglou et al. 1996, Lai and Ip 1996, Hua et al. 2000, Marwala and Sibisi 2005, Daghia et al. 2007), however all these studies considered exclusively additive Gaussian noise on the measurements. This assumption allowed handling probability density functions in a purely analytical way thus avoiding the need for expensive statistical sampling and Monte Carlo simulation. The downside is that such noise assumption is often not very realistic. Indeed, apart from measurement noise there are also uncertainties in the model and its input parameters. These uncertainties propagate to the measured quantity in different ways and additive Gaussian noise might not accurately account for this. Furthermore, even under the Gaussian noise assumption, only Lai and Ip (1996) estimated the standard deviation in the identified properties, which as discussed earlier can be of key interest to a designer. Moreover, if there is strong correlation in the properties, then providing only standard deviation estimates may not be sufficient, so a complete characterization of the probability density function would be more appropriate.

In order for the Bayesian approach to be able to handle not only Gaussian but any type of uncertainty both on measurements and model, Monte Carlo simulation needs to be used. To get an idea of the computational cost challenge involved let us consider a problem where we seek to

identify four material properties (the orthotropic elastic constants for example) and their uncertainties from ten simultaneously measured quantities (the ten natural frequencies of a plate for example). Applying the Bayesian method involving Monte Carlo simulation to this problem would typically imply 2 billion frequency evaluations (see Chapter 5 for the detailed count leading to this number). Numerical solutions (such as finite elements) that are usually used in identification are by far too expensive to be utilized for such a high number of evaluations.

The problem is exacerbated even further if instead of 10 measured quantities we have 100,000 as is typical for full field displacement techniques where each pixel of the image is a measurement on its own. Not only does the number of required evaluations increase, but even if the cost of these evaluations was decreased, it would still not be possible to directly apply the Bayesian approach. Indeed, applying the Bayesian method directly to 100,000 measured quantities would mean handling a 100,000-dimensional joint probability density function. This is by far outside the realm of what is computationally imaginable today.

The goal of the present work is then to make the Bayesian identification of elastic constants computationally tractable even in its most general form and even when used to its full capabilities.

The two previously mentioned issues need to be dealt with to achieve this objective:

1. Drastically reduce the computational cost required for each function evaluation.
2. Drastically reduce the dimensionality of the joint probability density functions involved.

To address the first point we chose to use response surface methodology (Myers and Montgomery 2002) to approximate the expensive response of numerical simulations. The difficulty here is that response surface approximations (RSA) can be relatively inaccurate in higher dimensions (more than 10). Indeed, they suffer from the “curse of dimensionality” meaning that for a given accuracy, the number of simulations required to construct the

approximation increases exponentially with the dimensionality of the variables space. To achieve our goal we investigate various dimensionality reduction methods that can be applied to response surface approximations, including nondimensionalization and global sensitivity analysis (Sobol 1993).

To address the second point we chose to use the proper orthogonal decomposition technique (Berkooz et al. 1993) also known as Karhunen Loeve expansion or principal component analysis depending on the application field. Proper orthogonal decomposition (POD) allows to express the full field pattern of the displacements in a reduced dimension basis (typically a few dozen dimensions). Note however that POD does not remove the requirement of point 1, since the finite element simulations used to obtain a strain field would still be expensive. This means that response surface methodology will be used in combination with POD by constructing RSA of the basis coefficients of the POD full field decomposition.

Application Problems and Outline

The ultimate application to which we want to apply the Bayesian approach is the identification of the orthotropic elastic constants of a composite material from full field displacement measurements from a tensile test on a plate with a hole. From a mechanical point of view this application has multiple advantages. The heterogeneous strain field allows indeed identifying all four constants from this single experiment, unlike traditional standard tests, which identify only one or two properties at a time. It can also provide information on the variability of the properties from point to point in the plate. The experiment on the plate with a hole has been recently used for identification within a classical least squares framework (Silva 2009) and led to very promising results as to the validity of the technique.

From a Bayesian identification point of view this final application is however extremely challenging. Both issues associated with Bayesian identification mentioned in points one and two

above are simultaneously present. First, the application involves an expensive finite element model for calculating the strain field. This requires cost reduction to be able to obtain the required number of function evaluations. Second, the full field technique produces tens of thousands of measurement points. This requires dimensionality reduction to achieve computationally tractable joint probability density functions.

Before taking up the challenge on this final application we investigate various dimensionality reduction methods on a series of less demanding problems. Dimensionality reduction in the context of response surface approximations is very relevant to many optimization problems as well. Indeed RSA are often used in optimization on complex problems and reducing their dimensionality can be beneficial at two levels, first for RSA construction cost reasons, and second because optimization algorithms are less efficient in high dimensions.

In Chapter 2 we demonstrate efficient use of response surface methodology and dimensionality reduction techniques first on a problem of optimal material selection for an integrated thermal protection system (ITPS). On this problem we investigate how physical reasoning, nondimensionalization and global sensitivity analysis can reduce the dimensionality of the problem.

We then move to Bayesian identification and gradually consider problems of increasing complexity. In Chapter 3 we look at a simple three bar truss problem, with two objectives in mind. First, the example allows to didactically introduce the Bayesian approach to identification, second, it aims, in combination with a simple vibration based identification problem, at identifying general situations in which the Bayesian method has a significant advantage in terms of accuracy over classical identification techniques such as least squares.

Next we move in Chapters 4 and 5 to the Bayesian identification of the four orthotropic elastic constants from natural frequencies of a free plate. This is a problem where we use actual experimental measurements and which provides the challenge of point 1 at full scale. Finite element simulations are indeed too expensive to be used here, so a drastic computational cost reduction is required. We first investigate in Chapter 4 the applicability of analytical approximate formulas for the natural frequencies and compare them with nondimensional response surface approximations constructed based on finite element simulations. Bayesian identification of the joint probability density function of the four orthotropic elastic constants is then carried out in Chapter 5.

In Chapters 6 and 7 we tackle the final problem of identification from full field measurements on a plate with a hole, offering the full scale challenges. We first investigate in Chapter 6 the dimensionality reduction of the full fields by the proper orthogonal decomposition method. Then in Chapter 7 we apply the Bayesian identification approach, first on a simulated experiment, then on a Moiré interferometry experiment that we carried out.

Finally in Chapter 8 we provide concluding remarks and possible future work items.

CHAPTER 2 DIMENSIONALITY REDUCTION FOR RESPONSE SURFACE APPROXIMATIONS APPLIED TO THERMAL DESIGN

Introduction

Dimensional analysis is a several hundred years old concept going as far back as Galilei (1638). This concept has its roots in a very simple idea: the solution to a physical problem has to be independent of the units used. This means that the equations modeling a problem can always be written in a nondimensional form. In the process, nondimensional parameters are constructed, which, when done appropriately, are the minimum number of variables required to formulate the problem.

These basic concepts turned out very powerful, and throughout the past century dimensional analysis has been extremely successful for solving scientific and engineering problems and for presenting results in a compact form. The first theoretical foundations of dimensional analysis were set by Vaschy (1892) and Buckingham (1914) at the end of the 19th century. Since then and up to the 1960s nondimensional solutions have been a major form of transmitting knowledge among scientists and engineers, often in the form of graphs in nondimensionalized variables. Then, the advent of widely available numerical simulation software and hardware made it easier to obtain solutions to physical problems without going through nondimensionalization. This led to reduced interest in dimensional analysis except for reduced scale modeling and in areas where nondimensional parameters have a strong physical interpretation and allow us to differentiate between regimes of different numerical solution techniques (Mach number, Reynolds number etc.).

With the increase in computational power, numerical simulation techniques such as finite element analysis (FEA) became not only feasible for single engineering design analyses but also

in design optimization, often in conjunction with the use of surrogate models, also known as response surface approximations (RSA).

Surrogate models seek to approximate the response of a process based on the knowledge of the response in a limited number of points (points called design of experiments). A typical surrogate model is polynomial response surface which fits a polynomial through a small number of simulations of the process such as to minimize the least squares error between the response surface prediction and the actual simulated values. For a more in depth description of polynomial response surface approximations the reader can refer to Appendix A. Other types of surrogate models include kriging (Matheron 1963, Sacks et al. 1989), radial basis neural networks (Orr 1996, 1999) and support vector regression (Vapnik 1998) among others.

Surrogate models, however, suffer from the “curse of dimensionality”, i.e., the number of experiments needed for a surrogate for a given accuracy increases exponentially with the number of dimensions of the problem.

This issue can be generally attacked in two ways: one is by reducing the cost of a single analysis thus allowing a large number of analyses to be run for the RSA construction; the other being to reduce the number of design variables thus reducing the dimensionality of the problem. Many techniques, often referred to as model reduction, have been developed to deal with these issues including static and dynamic condensation, modal coordinate reduction, Ritz vector method, component mode synthesis, proper orthogonal decomposition and balanced realization reduction. An excellent overview of these techniques can be found in the book by Qu (2004).

A simple, yet relatively little used way of reducing the dimensionality of the surrogates or response surface approximations is by applying dimensional analysis to the equations of the physical problem that the finite element (FE) model describes. Kaufman et al. (1996), Vignaux

and Scott (1999) and Lacey and Steele (2006) show that better accuracy of the RSA can be obtained by using nondimensional variables. This is mainly because for the same number of numerical simulations the generally much fewer nondimensional variables allow a fit with a higher order polynomial. Vignaux and Scott (1999) illustrated such a method using statistical data from a survey while Lacey and Steele (2006) applied the method to several engineering case studies including an FE based example.

Venter et al. (1998) illustrated how dimensional analysis can be used to reduce the number of variables of an RSA constructed from FE analyses modeling a mechanical problem of a plate with an abrupt change in thickness. The dimensional analysis was done directly on the governing equations and the boundary conditions that the FEA solved, reducing the number of variables from nine to seven.

Dimensional analysis can be used to reduce the number of variables in any FE based model. Indeed FEA models an underlying set of explicit equations (ordinary or partial differential equations, boundary conditions and initial conditions). These equations whether coming from mechanical, thermal, fluids or other problems, can be nondimensionalized in a systematic way using the Vaschy-Buckingham theorem, also known as Pi theorem (Vaschy 1892, Buckingham 1914). Systematic nondimensionalization techniques are also described in Rieutord (1985), Sonin (1997) and Szirtes (1997).

Although dimensional analysis is a natural tool to reduce the number of variables through which a problem has to be expressed, an even higher reduction can be obtained if it is combined with other analytical and numerical techniques. The aim of this chapter is to show that through a combination of physical reasoning, dimensional analysis and global sensitivity analysis, a drastic reduction in the number of variables needed for an RSA is possible.

The basic idea is the following: even after nondimensionalization, it is still possible to end up with nondimensional parameters that only have marginal influence on the quantity of interest for the design problem considered. Identifying and removing these parameters can further reduce the total number of variables. This can be done at two moments. Before nondimensionalization, physical reasoning can allow formulating a set of assumptions that simplify the equations of the problem. After nondimensionalization a global sensitivity analysis, e.g. Sobol (1993), can be used to fix any remaining parameters with negligible effects.

In the next section we present the general methodology for reducing the number of variables in a response surface approximation. In the rest of the chapter we apply the method to solve a transient thermal problem of spacecraft atmospheric reentry wherein the maximum temperature attained is critical. First we describe the thermal problem of atmospheric reentry and the corresponding FE model used in the analysis. Dimensional analysis on a simplified problem in conjunction with global sensitivity analysis is used next to reduce the number of variables. The RSA is constructed using the accurate FE model and the ability of the RSA to account for all the variables of interest to the problem tested. We then discuss advantages of the procedure in terms of computational cost. Finally we give a brief overview of how the RSA was used to carry out a material comparison and selection for the design and optimization of an integrated thermal protection system (ITPS). We close the chapter by presenting concluding remarks.

Methodology for Reducing the Number of Variables in an RSA

We consider the general problem in which we are interested in the response Y of a finite element (FE) problem denoted by S . The response Y potentially depends on s parameters of interest, denoted $\mathbf{w}^s = \{w_1, \dots, w_s\}$. We consider the case where a response surface approximation (RSA) of Y is needed. If s is high (>10), then it can be beneficial to seek to construct the RSA in a lower dimension space. Indeed an RSA in a lower dimension space reduces the computational

cost (number of simulations required) for a fixed accuracy or improves the accuracy for a fixed computational cost. A low dimension is also preferable especially if the RSA is later used for optimization.

In order to construct the RSA as a function of a small number of parameters we use the following procedure, involving three major steps.

(i.) Using preliminary physical reasoning we can often determine that only r out of the s initial parameters ($r \leq s$) significantly affect the response Y . Indeed in many engineering problems it is known based on empirical, theoretical or numerical evidence that some parameters have little effect on the response for the particular problem considered. Different choices for the numerical model or the use of homogenization can also allow to simplify the problem. The simplified problem involving only $\mathbf{w}^r = \{w_1, \dots, w_r\}$ is denoted by S^* .

Sometimes a designer might not have enough domain expertise to formulate all the simplifying assumptions through physical reasoning. If little or nothing is known in advance that can help simplify the problem, this step can then be aided by a global sensitivity analysis (GSA) as described by Sobol (1993). GSA is a variance based technique, quantifying the part of the variance of the response explained by each parameter, thus determining the parameters that have negligible effects. However, the GSA can only be carried out if the computational cost does not become prohibitive. If nothing works it is always possible to go directly to step (ii.).

The aim of step (i.), when successful, is to define the simplified problem S^* which will facilitate the next step, the nondimensionalization.

(ii.) In this step we further reduce the number of variables by determining the nondimensional parameters characterizing the problem. The dimensional problem S^* can indeed be transformed into the nondimensional problem Σ , using the Vaschy-Buckingham theorem

(Vaschy 1892, Buckingham 1914). Systematic nondimensionalization techniques are provided in Rieutord (1985) and Sonin (2001). We can then express the nondimensional response ψ of the problem Σ as a function of the nondimensional parameters $\omega^q = \{\omega_1, \dots, \omega_q\}$. According to the Vaschy-Buckingham theorem $q \leq r$.

Note that the problem Σ is equivalent to S^* , so no additional approximation is involved in this step. However, since ψ is a solution to Σ , which is equivalent to S^* , it will only provide an approximate solution to the initial problem S .

(iii.) Out of the ω^q nondimensional parameters that we have determined in step (ii.) not all will necessarily have a significant influence on the response ψ . To determine and fix parameters with negligible influence we carry out in this step a global sensitivity analysis (GSA) (cf. Sobol 1993). After such parameters have been fixed we can write ψ approximately as a function of $\omega^f = \{\omega_1, \dots, \omega_f\}$, with $f \leq q$.

At the conclusion of the process, we have $f \leq q \leq r \leq s$. The case with equality everywhere, while theoretically possible, is extremely unlikely for an actual engineering problem and hopefully we achieved after these three steps f significantly smaller than s .

At this point we have determined that the approximate nondimensional response ψ approximately depends only on the parameters ω^f . However our final aim is to construct a response surface approximation of Y , the actual response, and not of ψ , which is the response of the approximate problem Σ . Accordingly, we chose to construct an RSA Y' of Y but as a function of the reduced number of nondimensional parameters ω^f .

That is, even though we made simplifying assumptions and a GSA to determine ω^f , we will construct the RSA function of these ω^f parameters but using simulations of Y , coming from the initial nonsimplified FE model of S . This allows part of the error induced by constructing the

RSA function of ω^f instead of ω^s to be compensated by fitting to the actual nonsimplified FE simulations of Y .

The sampling for the RSA simulations is done in the ω^f space. The RSA $Y'=f(\omega^f)$ is then constructed and the quality of its fit can be analyzed using classical techniques (prediction sum of squares (PRESS) error for example Allen 1971, Myers and Montgomery 2002). Note however that these analyses provide mainly the quality of the fit in the reduced nondimensional variables ω^f but not in the initial variables ω^s . To remedy this, an additional validation step can be carried out. A number of additional points are sampled in the initial, high-dimensional ω^s space. The FE response Y is calculated at these points and compared to the prediction of the reduced nondimensional RSA Y' to make sure the accuracy of the RSA Y' is acceptable.

In the rest of the chapter we show how we applied this procedure to a transient thermal problem of spacecraft atmospheric reentry, for which a response surface approximation of the maximum temperature was required. Note that the application problem presented is a 1D heat transfer problem. However, the general method described can be applied as well to 2D or 3D finite element problems. Steps (i.) and (iii.) are not affected much by moving from 1D to 3D models other than maybe through increased computational cost. Nondimensionalizing the governing equations of the problem in step (ii.) may be slightly more complex. However, while for 1D problems nondimensionalization is simple enough to be often applied by hand, there are systematic nondimensionalization techniques (e.g. Rieutord 1985, Sonin 2001), that can be applied to any governing equations and boundary conditions.

A final note concerns the application of the nondimensional RSA in a design optimization framework. Since the RSA is in terms of nondimensional parameters, these could be chosen as variables for the optimization algorithm. This is however often a bad choice, since it is often

difficult to move from a point (the optimum for example) in the nondimensional variables space to the corresponding design point in the physical, dimensional variables space. A better choice in this case is to do the optimization in terms of the dimensional variables. A typical function evaluation step in the optimization routine would then look as follows: dimensional variables point at which the response is required → calculate the corresponding nondimensional variables for this point → calculate the response at this point using the nondimensional RSA. While this may leave a large number of design variables, that is usually affordable because surrogate-based function evaluations are inexpensive.

ITPS Atmospheric Reentry Application Problem

An Integrated Thermal Protection System (ITPS) is a proposed spacecraft system that differs from traditional TPS in that it provides not only thermal insulation to the vehicle during atmospheric reentry but at the same time it carries structural loads. Thus the thermal protection function is integrated with the structural function of the spacecraft. Our study involves an ITPS based on a corrugated core sandwich panel construction. The design of such an ITPS involves both thermal and structural constraints. In the present study we focus on the thermal constraint represented by the maximum temperature of the bottom face sheet (BFS) of the ITPS panel. The combined thermo-structural approach is presented in Bapanapalli et al. (2006) and Gogu et al. (2007a).

A response surface approximation (RSA) of the maximum BFS temperature was needed in order to reduce computational time. The RSA is used in order to carry out material selection for the ITPS panel.

In order to calculate the maximum BFS temperature we constructed a finite element (FE) model using the commercial FE software Abaqus[®]. The corrugated core sandwich panel design as well as the thermal problem of atmospheric reentry is shown in Figure 2-1. The ITPS panel is

subject to an incident heat flux assumed to vary as shown in Figure 2-2. This heat flux is typical of a reusable launch vehicle (RLV).

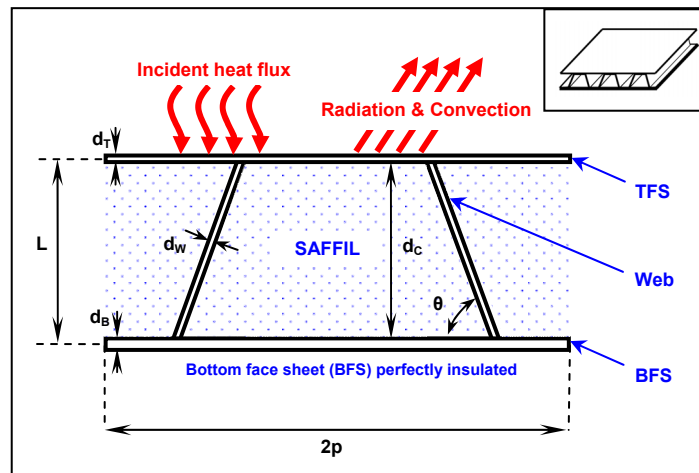


Figure 2-1. Corrugated core sandwich panel depicting the thermal boundary conditions and the geometric parameters.

Radiation is also modeled on the top face sheet (TFS), while the BFS is assumed perfectly insulated, which is a worst case assumption, since if heat could be removed from the BFS, the maximum temperature would decrease, becoming less critical. The core of the sandwich panel is assumed to be filled with Saffil foam insulation, while we explore different materials for the three main sections: top face sheet (TFS), bottom face sheet (BFS) and web (cf. Figure 2-1) in order to determine the combinations of materials that result in low BFS temperatures.

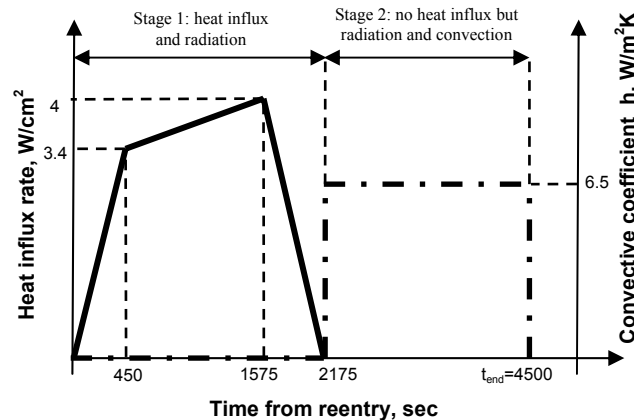


Figure 2-2. Incident heat flux (solid line) and convection (dash dot line) profile on the TFS surface as a function of reentry time.

Finite Element Model of the Thermal Problem

The FE thermal problem is modeled as a one dimensional heat transfer analysis as shown in Figure 2-3. The core of the sandwich panel has been homogenized using the rule of mixtures formulae given below.

$$\rho_c = \frac{\rho_w V_w + \rho_s V_s}{V_c} = \frac{\rho_w d_w + \rho_s (p \sin \theta - d_w)}{p \sin \theta} \quad (2-1)$$

$$C_c = \frac{C_w \rho_w V_w + C_s \rho_s V_s}{\rho_c V_c} = \frac{\rho_w C_w d_w + \rho_s C_s (p \sin \theta - d_w)}{\rho_w d_w + \rho_s (p \sin \theta - d_w)} \quad (2-2)$$

$$k_c = \frac{k_w A_w + k_s A_s}{A_c} = \frac{k_w d_w + k_s (p \sin \theta - d_w)}{p \sin \theta} \quad (2-3)$$

where ρ stands for density, C for specific heat, k for conductivity, d for thickness, θ for the corrugation angle and p for the length of a unit cell (cf. Figure 2-1). Symbol A stands for the area of the cross-section through which the heat flows and V for the volume of each section. The subscripts C , S and W stand for the homogenized core, the Saffil foam and the structural web sections respectively.

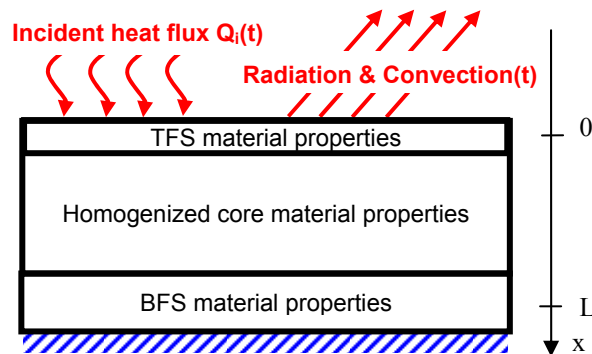


Figure 2-3. 1D heat transfer model representation using homogenization (not to scale).

It has been shown by Bapanapalli et al. (2006) that a one dimensional FE model can accurately predict the temperature at the bottom face sheet of the sandwich panel. The maximum difference in the BFS temperature prediction between the 1D model and a 2D model is typically

less than 8K. For this preliminary design phase of the ITPS, this difference is acceptable.

Radiation, convection and the incident heat flux (as shown in Figure 2-1 and 2-2) were modeled in the Abaqus[®] 1D model using four steps (three for stage one of Figure 2-2 and one for stage two). Fifty-four three node heat transfer link elements were used in the transient analyses.

For this one-dimensional thermal model the governing equations and boundary conditions are as follows:

$$\text{Heat conduction equation: } \frac{\partial}{\partial x} \left(k(x, T) \frac{\partial T(x, t)}{\partial x} \right) = \rho(x, T) C(x, T) \frac{\partial T(x, t)}{\partial t} \quad (2-4)$$

$$\text{Initial condition: } T(x, t = 0) = T_i \quad (2-5)$$

$$\text{Boundary conditions: } Q(x = 0, t) = -k_T \frac{\partial T(x, t)}{\partial x} \Big|_{x=0} = Q_i(t) - \varepsilon T(0, t)^4 - h(t)T(0, t) \quad (2-6)$$

$$Q(x = L, t) = 0 \quad (2-7)$$

where ρ is the density, k the thermal conductivity and C the specific heat of the ITPS panel. T_i is the initial temperature of the panel before atmospheric reentry, ε the emissivity of the TFS while $q_i(t)$ is the heat influx and $h(t)$ the convection coefficient at the TFS, which vary with time of reentry as shown in Figure 2-2. Most of the material properties are temperature dependent and due to the different materials in the different ITPS sections most material properties also depend on the position x . The temperature and spatial dependency make nondimensionalization of the previous equations cumbersome. Furthermore, these dependencies increase the number of nondimensional parameters needed, which is contrary to our goal. Accordingly, the thermal problem is studied in the next section under several assumptions that allow easier nondimensionalization of the equations as well as a reduction in the number of variables.

Minimum Number of Parameters for the Temperature Response Surface

Simplifying Assumptions for the Thermal Problem

Our goal for the ITPS study is to determine which materials are the best for use in the ITPS panel, based on the maximum BFS temperature. Considering that the expected range of this temperature when the materials are varied is about 250 K, an approximation of the temperature with an accuracy of the order of 12.5 K (5%) is considered acceptable for the purpose of material selection.

The thermal model presented in the previous section involves 13 material parameters (specific heat C_i , conductivities k_i and densities ρ_i of the TFS, BFS, web and Saffil as well as the emissivity ε of the TFS) of which most are temperature dependent. Some of these parameters are considered fixed, including ε as well as all the foam parameters (Saffil has been determined in previous studies by Blosser et al. (2004) and Poteet et al. (2004) to be the best suited foam for use in similar thermal protection systems). Note that the emissivity ε is defined as the relative emissivity times the Stefan-Boltzmann constant. The relative emissivity of the TFS depends more on surface treatments than on the nature of the TFS material (thus a typical value for this kind of application of 0.8 was used cf. Poteet et al. (2004) and Myers et al. (2000)). Fixing these parameters leaves 9 material variables. Describing temperature dependency of the material properties would increase this number further.

On top of the 9 material parameters, we also have 6 geometric design variables (cf. Figure 2-1) we use to find the optimal geometry for each material combination. In total we have 15 variables of interest for the maximum BFS temperature determination.

In order to reduce the number of design variables, the equations were studied under several simplifying assumptions that removed parameters that have a negligible role on the maximum BFS temperature. These assumptions have been established and checked on a Nextel(TFS) -

Zirconia(Web) - Aluminum(BFS) ITPS material combination having the dimensions given in

Table 2-1. The assumptions are:

1. The three thermal properties of the TFS (C_T , k_T and ρ_T) have negligible impact on the maximum BFS temperature, mainly due to the small thickness of the TFS (about 2.2mm compared to a total ITPS thickness of about 120mm). This assumption allowed removing C_T , k_T , ρ_T and d_T from the relevant parameters influencing the BFS temperature.
2. The temperature is approximately constant through the BFS, because the BFS thickness is small (typically 5mm thick compared to a total ITPS thickness of 120mm) and its conductivity is about one order of magnitude higher than that of the homogenized core. This assumption allowed removing k_B and simplifying the boundary condition at the BFS.
3. The temperature dependence of the material properties have been simplified as following. In the FE model temperature dependence has been included for all materials, but the largest dependence was for the Saffil foam. Hence in the simplified problem, TFS, web and BFS materials were assigned constant properties provided by the CES Selector (Granta Design 2005) material database. For Saffil the material properties were assigned values at a representative temperature chosen such as to minimize the difference between the maximum BFS temperature when using the constant values and the one when using temperature dependent values for an ITPS design with the dimensions given in Table 2-1 and a Nextel(TFS) - Zirconia(Web) - Aluminum(BFS) material combination. The effects of varying the materials were then found to be small enough to use this constant value for the range of materials we consider (detailed results of the numerical tests are provided in the following sections).

These assumptions reduced the number of relevant material parameters from 15 to 10 and also simplified the problem so that it can be easily nondimensionalized as will be shown next.

Table 2-1. Dimensions of the ITPS (see also Figure 2-1) used among other to establish the simplifying assumptions. These dimensions were optimal for an Inconel (TFS) - Ti6Al4V (Web) - Al (BFS) ITPS (cf. Bapanapalli et al. 2006).

Parameter	d_T (mm)	d_B (mm)	d_W (mm)	θ (deg)	L (mm)	p (mm)
Value	2.1	5.3	3.1	87	120	117

Nondimensionalizing the Thermal Problem

Under the previous simplifying assumptions the thermal problem is equivalent to the one shown in Figure 2-4 and its equations can be rewritten as follows.

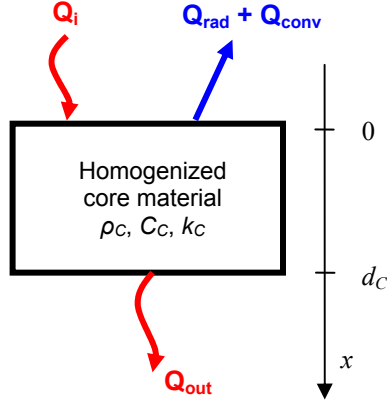


Figure 2-4. Simplified thermal problem for dimensional analysis.

$$\text{Heat conduction equation: } k_c \frac{\partial^2 T(x,t)}{\partial x^2} = \rho_c C_c \frac{\partial T(x,t)}{\partial t} \quad \text{for } 0 < t < t_{end} \quad (2-8)$$

$$\text{Initial condition: } T(x,t=0) = T_i \quad (2-9)$$

$$\text{Boundary conditions: } Q_{out} = -k_c \left. \frac{\partial T(x,t)}{\partial x} \right|_{x=d_c} = \rho_B C_B d_B \left. \frac{\partial T(x,t)}{\partial t} \right|_{x=d_c} \quad (2-10)$$

$$Q_{in} = -k_c \left. \frac{\partial T(x,t)}{\partial x} \right|_{x=0} = Q_i(t) - \varepsilon T(0,t)^4 - h(t)T(0,t) \quad (2-11)$$

where d_c and L_B are the thicknesses of the homogenized core and the BFS, respectively; t_{end} is the duration of the heat influx; ρ_c , C_c and k_c are the density, specific heat and conductivity of the homogenized core; ρ_B and C_B those of the BFS.

In order to nondimensionalize these equations, we use the Vaschy-Buckingham or Pi theorem (Vaschy 1892, Buckingham 1914), which also provides the minimum number of nondimensional variables. The theorem states that we have to count the total number of variables and the corresponding number of dimensional groups. The variables and the groups are listed in Table 2-2.

Table 2-2. Dimensional groups for the thermal problem.

Variable	T	T_i	x	d_C	t	t_{end}
Unit	K	K	m	m	s	s
Variable	k_C	$\rho_C C_C$	$\rho_B C_B d_B$	Q_i	ε	h
Unit	$\frac{W}{m \cdot K}$	$\frac{W \cdot s}{m^3 \cdot K}$	$\frac{W \cdot s}{m^2 \cdot K}$	$\frac{W}{m^2}$	$\frac{W}{m^2 \cdot K^4}$	$\frac{W}{m^2 \cdot K}$

We have a total of 12 variables in 4 independent dimensional groups, namely length, time, temperature and power (m, s, K, W). From the Vaschy-Buckingham theorem we know that we can have a minimum of $12 - 4 = 8$ nondimensional variables which are provided in Equations 2-12 to 2-19.

$$\frac{T}{T_i} = \Gamma \quad (2-12)$$

$$\frac{x}{d_C} = \xi \quad (2-13)$$

$$\frac{t}{t_{end}} = \tau \quad (2-14)$$

$$\frac{k_C t_{end}}{d_C^2 \rho_C C_C} = \beta \quad (2-15)$$

$$\frac{d_B \rho_B C_B}{d_C \rho_C C_C} = \gamma \quad (2-16)$$

$$\frac{d_C \varepsilon T_i^3}{k_C} = \kappa \quad (2-17)$$

$$\frac{d_C Q_i(t)}{k_C T_i} = \varphi(\tau) \quad (2-18)$$

$$\frac{h(t)d_C}{k_C} = Bi(\tau) \quad (2-19)$$

In terms of these nondimensional variables the simplified thermal problem can be written in the following nondimensional form:

$$\text{Heat conduction equation: } \beta \frac{\partial^2 \Gamma}{\partial \xi^2} = \frac{\partial \Gamma}{\partial \tau} \quad \text{for } 0 < \tau < 1 \quad (2-20)$$

$$\text{Initial condition: } \Gamma(\xi, \tau = 0) = 1 \quad (2-21)$$

$$\text{Boundary conditions: } -\beta \left. \frac{\partial \Gamma}{\partial \xi} \right|_{\xi=1} = \gamma \left. \frac{\partial \Gamma}{\partial \tau} \right|_{\xi=1} \quad (2-22)$$

$$-\left. \frac{\partial \Gamma}{\partial \xi} \right|_{\xi=0} = \varphi(\tau) - \kappa \cdot \Gamma(0, \tau)^4 - Bi(\tau) \cdot \Gamma(0, \tau) \quad (2-23)$$

The complete set of nondimensional variables needed for the problem is given in Equations 2-12 through 2-19. Note that the nondimensional formulation of the equations was carried out only to determine a reduced number of nondimensional parameters function of which the response surface approximation could be expressed. The nondimensional formulation is not used for solving the problem, neither do the finite element simulations use this formulation directly.

The nondimensional temperature Γ can be expressed function of the nondimensional distance ξ and the nondimensional time τ as well as function of five other nondimensional parameters. Since at the maximum BFS temperature we are at a fixed location and we are not interested in the time at which this maximum occurs, the nondimensional distance ξ and the nondimensional time τ are not needed for the maximum BFS temperature RSA.

The physical interpretation of the remaining five nondimensional parameters in Equations 2-15 to 2-19 is the following. β , the Fourier number or a nondimensional thermal diffusivity, is

the ratio of the rate of heat conduction and the rate of heat storage (thermal energy storage) of the homogenized core. γ is the ratio of the heat capacity of the BFS and heat capacity of the homogenized core, κ the ratio between the rate of radiation and the rate of heat conduction. φ is the ratio of the incident heat flux and the rate of heat conduction, or can be seen as a nondimensional heat flux. Finally Bi , the Biot number, is the ratio of the rate of convection and the rate of heat conduction.

We can note that the three nondimensional parameters κ , φ and Bi are all proportional to d_C/k while all the other parameters defining κ , φ and Bi are fixed in our study. Indeed we are only interested in varying the materials and the geometry but the initial temperature T_i , the emissivity ε , the incident heat flux profile $Q_i(t)$ and the convection film coefficient profile $h(t)$ are all fixed in the present study (cf. Figure 2-2 for the profiles of $Q_i(t)$ and $h(t)$ used). This means that for our purpose we can consider only one of these three nondimensional parameters: κ for example.

Summing up, simplifying assumptions together with dimensional analysis allowed us to determine that we can construct a response surface approximation of the maximum BFS temperature function of the three parameters β , γ and κ . An initial 3rd degree polynomial response surface in these three parameters was constructed from 40 finite element simulations using Latin hypercube sampling and used for a global sensitivity analysis, according to Sobol's approach (Sobol 1993). We found that variable β accounts for 35.7% of the model variance, variable γ accounts for 64.1% of the model variance while variable κ accounts for only 0.06% of the model variance. The 0.06% correspond to 9.3 K, which is within the 12.5 K accuracy requirement we set ourselves for the material selection. Note that the GSA was made on an approximation of the response. This is reasonable since in the next section we check and validate in more details the validity of the approach.

From a physical point of view the fact that κ has a negligible role can be explained as follows: κ is proportional to d_C/k_C which is also present in β . That means that if we want to change κ while keeping β constant we need to also modify t_{end} (which is the only other variable in β that does not appear neither in γ nor in κ). If we increase κ by decreasing k_C we need to also increase t_{end} by a certain amount to keep β constant. Decreasing k_C has the effect of lowering the BFS temperature while increasing t_{end} has the effect of making it higher. From the global sensitivity analysis it turns out that these two effects cancel out, which explains why κ has very little impact. Note that both d_C and k_C are relevant to the problem and none of them could be neglected. Parameter κ , which is proportional to d_C/k_C turns out however to have negligible impact based on the GSA results. This is because both d_C and k_C appear in the remaining two nondimensional parameters β and γ .

A summary of the procedure used to reduce the number of variables needed for constructing the RSA from 15 to 2 is given in Figure 2-5.

The reduction obtained is higher than what could have been obtained by applying any single technique. The use of only simplifying assumptions based on physical reasoning allows a reduction of 15 to 10 variables. Global sensitivity (GSA) analysis alone on the initial problem, which can be seen as an initial screening of the variables, would have allowed a reduction from 15 to 9 variables. Such a GSA showed that parameters d_T , k_T , ρ_T , C_T , k_B and θ have negligible effects. Applying the GSA on the original problem is indeed almost equivalent to the simplifying assumptions we had arrived to based on the physical understanding of the problem, which is not surprising. Depending on the complexity of temperature dependency of the materials properties,

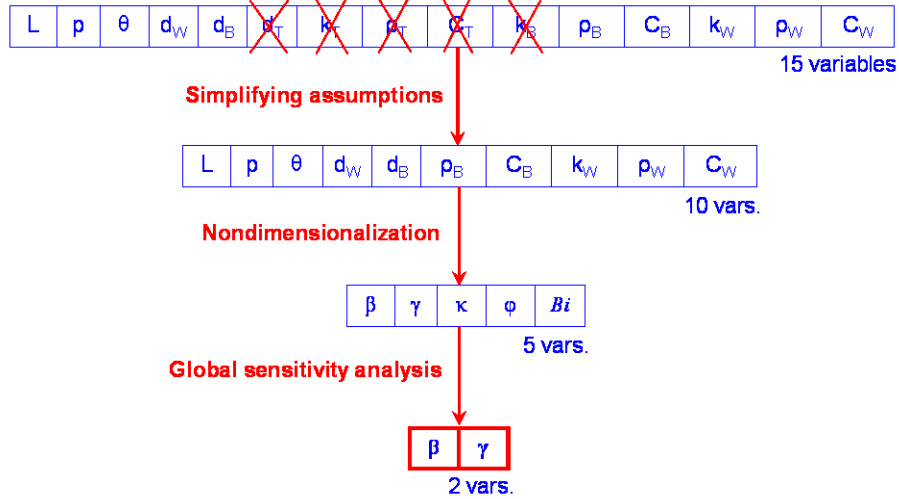


Figure 2-5. Summary of the dimensionality reduction procedure for the ITPS problem.

dimensional analysis alone could have achieved a maximum reduction of 15 to 8 (this reduction is in the case where no temperature dependency is considered). So we can see that neither of the three techniques alone (simplifying assumptions, nondimensionalization, GSA) could have achieved the reduction of 15 to 2 obtained by combining all three.

Maximum BFS Temperature RSA

A response surface approximation (RSA) in the two nondimensional parameters β and γ was now constructed. We chose to construct a 3rd degree polynomial response surface (PRS) in β and γ . For additional details on polynomial response surface modeling and construction the reader can refer to Appendix A. The two variables β and γ account for the thermal material properties (C_i, k_i, ρ_i) as well as for the geometric parameters of the ITPS panel (d_i, p, L, θ) as is shown in equations 2-24 and 2-25. These equations were obtained by substituting back the expressions of ρ_C, C_C and k_C from Equations 2-1 to 2-3 into the equations 2-15 and 2-16 of the nondimensional parameters β and γ .

$$\beta = \frac{[k_W d_W + k_S (p \sin \theta - d_W)] \cdot t_{end}}{(L - 0.5d_T - 0.5d_B)^2 \cdot [\rho_W C_W d_W + \rho_S C_S (p \sin \theta - d_W)]} \quad (2-24)$$

$$\gamma = \frac{d_B \rho_B C_B p \sin \theta}{(L - 0.5d_T - 0.5d_B) \cdot [\rho_W C_W d_W + \rho_S C_S (p \sin \theta - d_W)]} \quad (2-25)$$

Note that a given (β, γ) point can be obtained by a multitude of combinations of the 15 individual variables (9 materials properties and 6 geometric parameters discussed earlier). If the simplifying assumptions we made are exact, then all the different parameter combinations that lead to a same (β, γ) couple should have the same maximum BFS temperature. If on the other hand the effect of the simplifying assumptions is large, then the difference in the BFS temperature for different combinations of the same (β, γ) couple would be large as well. Indeed even if two points have the same (β, γ) values they might not have the same values of the other parameters that we ignored through simplifying assumptions or global sensitivity analysis.

The Design of Experiments (DoE) for constructing the RSA involved sampling 855 Latin Hypercube (LHS) points in the initial 15 dimensional space with the bounds provided in Table 2-3 (see also Appendix A for the basic response surface methodology).

Table 2-3. Lower bounds (LB) and upper bounds (UB) used for sampling in the 15 variables space. All units are SI.

	k_W	ρ_W	C_W	k_B	ρ_B	C_B	k_T	ρ_T	C_T	d_T	d_B	d_W	θ	L	p
LB	2	2,500	500	2	1,550	900	3	2,000	500	0.001	0.0046	0.00224	80	0.102	0.099
UB	7	6,000	950	50	3,000	1,820	50	5,000	1,700	0.0037	0.007	0.00416	90	0.150	0.150

Variables β and γ were calculated for each of these points and a subset of 20 out of the 855 points was selected according to the D-optimality criterion in the (β, γ) space within the bounds given in Table 2-4. Finite elements (FE) analyses, using the model described earlier and involving none of the simplifying assumptions done for nondimensionalization, were run at these 20 points and the 3rd degree PRS was constructed in (β, γ) . This RSA is represented in Figure 2-6. One of the advantages of having only two variables in the RSA is an easy graphical

representation of the results. This graphical representation possibility will be later used for the material selection.

The RMS error in the approximation was 1.09 K, the cross-validation PRESS error 1.96 K and the R^2 was 0.99989 (the range of the RSA is about 250 K). These are satisfactory error measures for our application, but they poorly account for the total error involved in using this RSA. Indeed part of the total error is due to the fact that the FE results, obtained without the simplifying assumptions, will not be the same for different combinations of the dimensional parameters corresponding to a same (β, γ) couple. This error is poorly accounted for with only 20 points. Instead, to check this error we randomly sampled 100 out of the 855 LHS points in the 15-dimensional space. We calculated the maximum BFS temperature at these 100 points using FE analyses that included temperature dependent core material material properties and compared to the two-dimensional variables RSA predictions. We obtained the following errors: the RMS error was 2.74 K, the mean of the absolute error was 2.1 K and the standard deviation of the absolute error 1.70 K. These errors are well within the 12.5 K accuracy requirement we set ourselves for the material selection.

Note that an alternative for the error estimation would have been to construct the RSA directly using the 20 + 100 points and look only at the corresponding PRESS error, which leads to similar results.

Table 2-4. Ranges of the nondimensional design variables

Variable	β	γ
Range	0.1-0.5	0.6-2.4

If we wanted to know how much of the error is due to each of the techniques used (simplifying assumptions, dimensional analysis, global sensitivity analysis (GSA)) we can note

the following. Dimensional analysis alone never involves any error since the nondimensional equations are strictly equivalent to the initial ones. GSA turned out in our case to give very good

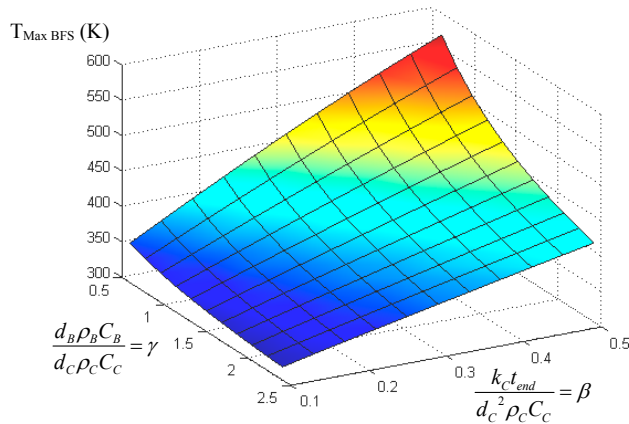


Figure 2-6. Maximum BFS temperature two-variable RSA.

results. Indeed we found that 99.94% of the variance of the response could be explained by two variables. Since we showed that three out of the five variables are equivalent to each other and account for this very small part of the variance, the error of going from five to two variables is likely to be very small in our case. This means that most of the error in the RSA is explained by the simplifying assumptions.

To gain more insight of where the maximum errors occur and which simplifying assumptions have the most impact, anti-optimization (Elishakoff 1991, Lee et al. 1994) of the error in the RSA was carried out. The anti-optimization process looks to find the places (i.e. materials and geometries) with the highest error in the RSA, and by looking at the designs corresponding to the anti-optimum we can understand what causes these errors. Anti-optimization was carried out in Gogu et al. (2007a). It showed that the RSA has poor accuracy when the geometry is far away from the one for which the representative temperature of assumption 3.) was established. For these unusual geometries the representative temperature shifts due to temperature dependence of the core; this shift is not accounted for by the RSA

which explains the poor accuracy for these geometries. To further improve the accuracy of the RSA for a large range of geometries we would have to add nondimensional parameters that account for the temperature dependence. However, for the geometry for which we will use the RSA in the next section, the maximum absolute error among eight test points corresponding to actual material combinations was 7.6 K with a mean of 1.87 K (see Figure 2-7). The figure shows the absolute error Δ of the response surface estimates compared to FE predictions for eight different material combinations (format for the material combination names: Web material – BFS material). The TFS material is alumino-silicate - Nextel 720 composite laminate except in the reference all-titanium design. The maximum BFS temperature from the RSA is superposed as a contour plot, with the bottom (330 K) and the top (540 K) contour lines being labeled.

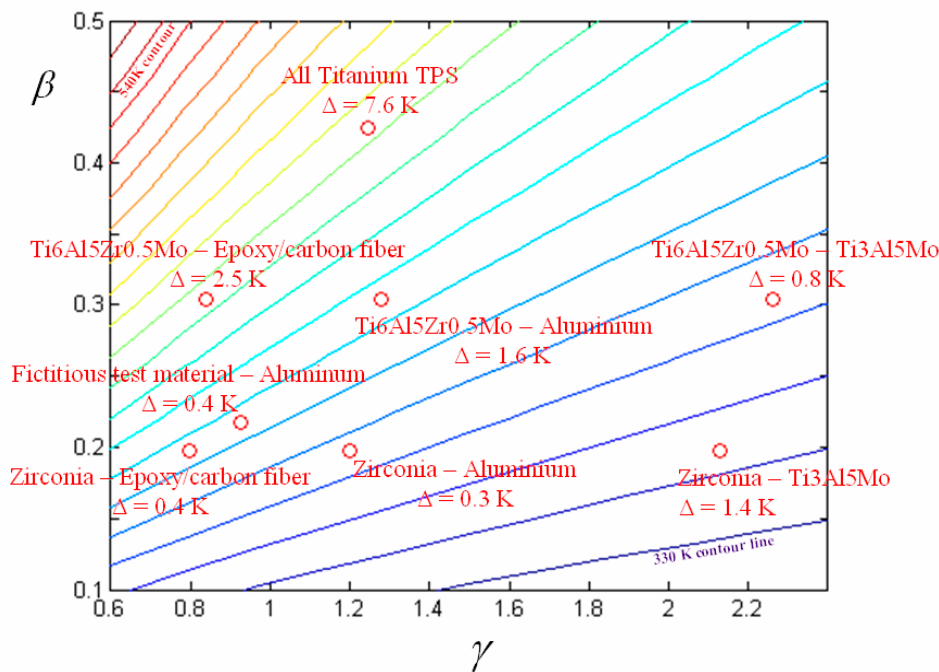


Figure 2-7. Absolute error Δ of the response surface estimates compared to FE predictions.

For varying geometries as well as varying materials the anti-optimization carried out by Gogu et al. (2007a) showed that the worst case error is 9.05 K. Note that we compare the RSA

predictions to FE results which also have limited accuracy. A convergence study on the finite element model showed that the discretization error for the BFS temperature is less than 0.007 K. Accordingly, considering that the errors in the RSA are of the order of 10 K we can assume the finite element simulations are exact, meaning that all the error is considered to come from the use of the dimension reduction method. These errors are within the 12.5 K requirement we set ourselves for the material selection.

RSA Construction Computational Cost

The possibility of graphical representation of the two nondimensional variables RSA is of great benefit in our case. Most of the problems however cannot be reduced to only two or three nondimensional variables. In these other cases, constructing the RSA in nondimensional variables can still benefit computational cost.

In our case we used 40 FE simulations for the global sensitivity analysis in 3 dimensional space, 20 simulations for constructing the 3rd degree PRS in (β, γ) and 108 simulations to verify the accuracy of the RSA. In total we used 168 simulations.

Constructing the maximum BFS temperature RSA in the 15 initial variables leads to following results. A linear PRS in the 15 variables required 32 FE simulations and led to an RSA with an RMS error of 9.16 K, a PRESS error of 12.9 K and an R^2 of 0.969 (for recall the range of the RSA is about 250 K). A 2nd degree PRS in the 15 variables required 272 FE simulations and led to an RSA with an RMS error of 1.23 K, a PRESS error of 1.78 K and an R^2 of 0.99989.

We can note that constructing the 3rd degree PRS in the two nondimensional variables had an overall computational cost about 40% lower than constructing a 2nd degree PRS in the initial 15 variables, while the error was maintained at an acceptable level for our application.

Note also that in most problems a 2nd degree PRS is the minimum usable, linear PRS being very rarely acceptable. Often 3rd degree PRS are even required to achieve acceptable error

measures. For 3rd degree PRS the computational cost difference between using all the variables or using the reduced number of nondimensional variables can become very significant. For the thermal problem for example, a 3rd degree PRS in the 15 dimensions would have required 1,632 experiments.

Applying the RSA for Comparison of Materials for the ITPS

The graphical representation possibility of the two-dimensional RSA was used next for comparison of alternate materials for the ITPS sections. For this part the dimensions of the ITPS are once again fixed to the values in Table 2-1.

We used the CES Selector (Granta Design 2005) material database software. Constraints on properties such as maximum service temperature, fracture toughness and Young's modulus were imposed during the search in the database in order to avoid unreasonable materials.

In order to compare the web materials, the BFS material was fixed to Aluminum alloy 2024 and the potential web materials were plotted in the (β, γ) plane with the RSA of the maximum BFS temperature superposed as a contour plot as shown in Figure 2-8. Note that in this figure numerous materials are grouped under generic names (denoted by an asterisk) such as stainless steels, nickel chromium alloys or cobalt superalloys.

Figure 2-8 shows that materials such as alumino-silicate/Nextel 720 composites or Zirconia ceramics provide a significant reduction in the maximum BFS temperature compared to metals such as Ti alloys or Nickel Chromium alloys, which were considered in previous designs (cf. Bapanapalli et al. 2006). Since we seek materials leading to a low maximum BFS temperature these materials were selected for further study as good potential candidates for the web of the ITPS panel.

The same material selection procedure was applied for BFS materials. The complete results are given in Gogu et al. (2007a). In summary, the material selection process based on the

RSA constructed here identified a small number of good potential material candidates for the different sections of the ITPS. These materials were used in an optimization routine developed

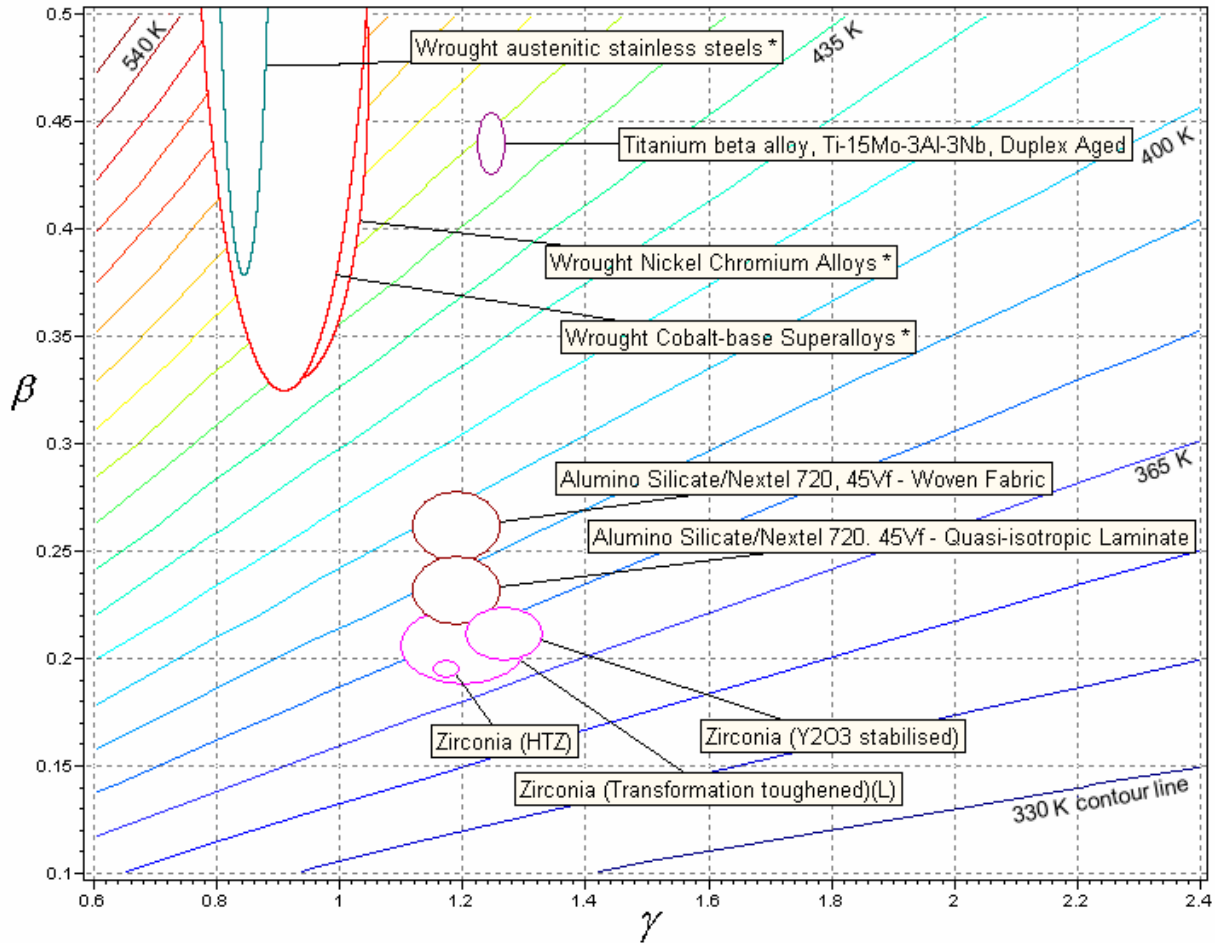


Figure 2-8. Thermal comparison of materials suitable for the web using the contour plot of the maximum BFS temperature RSA.

for the ITPS. The optimization procedure used is the one presented in Bapanapalli et al. (2006), which seeks to minimize the mass of an ITPS panel by finding the optimal geometry parameters for a given material combination. Applying it to the different material combinations found through this material selection process allowed us to obtain both the best suited material combination and the optimal corresponding geometry for the ITPS panel.

Summary

The present chapter illustrates the use of combined physical reasoning, dimensional analysis and global sensitivity analysis to significantly reduce the number of variables in response surface approximations (RSA) used for a material selection study for an integrated thermal protection system.

Nondimensionalizing the exact equations involved in the finite element analysis, while reducing the numbers of variables, can be relatively cumbersome and lead to a still relatively high number of nondimensional parameters. Some of these parameters might only have marginal influence on the quantity of interest. In this case the process can be aided by simplifying assumptions and a global sensitivity analysis that can help further reduce the number of nondimensional parameters by keeping only those that control most of the variation of the quantity of interest. It is important to note that removing variables that have small impact on the problem can have relatively small detrimental effects on the accuracy of the RSA, since the RSA is fitted to the finite element simulations obtained without simplifying assumptions thus allowing for error compensation.

The presented approach is general and can be applied to any finite element based response surface construction. It was used here with success on a transient thermal heat transfer problem for an integrated thermal protection system (ITPS). Dimensional analysis in combination with several simplifying assumptions and a global sensitivity analysis allowed reducing the number of parameters of the response surface approximation of the maximum temperature from 15 to only 2 while maintaining reasonable accuracy of the RSA.

The basic idea of constructing response surface approximations in terms of nondimensional variables to reduce computational cost or improve accuracy will be used again in the next chapters.

CHAPTER 3
LIMITS OF BASIC LEAST SQUARES IDENTIFICATION - AN INTRODUCTION TO THE
BAYESIAN APPROACH APPLIED TO ELASTIC CONSTANTS IDENTIFICATION

Introduction

Current design of aerospace structures tends to increasingly consider uncertainty in material properties. Variability in strength, for example, is now used to define the A-basis or B-basis design allowable (Rust et al. 1989) to comply with Federal Aviation Administration (FAA) regulations (FAR Part 25.613). Uncertainty in elastic constants due to measurement and modeling errors is also beginning to be considered.

In this context, elastic constants identification from standard tests can doubly benefit from statistical methods. These can not only improve the accuracy with which the materials properties are identified but also provide an estimate of the uncertainty with which the properties are known.

Currently, a very widespread method for elastic constants identification is based on minimizing the least squares error between the experimental data and the model predictions. In spite of the existence of advanced least squares formulations, that take into account statistical information, (e.g. books by Lawson and Hanson (1974), Bjorck (1996), Tarantola (2004)), the simplest formulations of the least squares method, based on minimizing the L_2 norm of the misfit (Bjorck 1996), are still extensively used today (e.g. in the domain of identification of mechanical constitutive laws Frederiksen (1997), Le Magorou et al. (2002), Lauwagie et al. (2003, 2004), Maletta and Pagnotta (2004), Molimard et al. (2005), Genovese et al. (2005)). The basic, non-statistical least squares formulations used in these studies have the advantage of great simplicity and most often work well leading to reasonably accurate results. In some cases however, using statistical identification frameworks may lead to further improvements in accuracy.

The objective of the present chapter is twofold. First, it seeks to introduce the Bayesian identification approach on a didactic three bar truss example problem. Second, it seeks to identify and illustrate such situations where the advanced, statistical identification methods lead to significantly better results compared to the basic least squares approach. As an advanced method we chose the Bayesian approach, which we find is among the most general statistical approaches while its formulation remains relatively simple. Isenberg (1979) detailed a Bayesian framework for parameter estimation, which later was applied by others in particular to frequency or modal identification, i.e. identifying material properties from vibration test data (Sol 1986, Alvin 1997, Beck and Katafygiotis 1998, Elseifi and Irvine 2002, Dascotte 2004, Marwala and Sibisi 2005, Daghia et al. 2007). The Bayesian method has also been proposed in the context of model validation and verification (Rebba et al. 2006a, 2006b), domain which, similarly to identification, is concerned with the agreement between model predictions and experimental data.

In the next section we provide a brief theoretical overview of the methods used. Then we introduce a three bar truss illustrative example for the Bayesian identification procedure. In the following section we compare the Bayesian and the least squares approach on the three bar truss, identifying situations differing significantly in the results. We then provide a comparison of the two methods for the more complex problem of identifying elastic constants from natural frequencies of a composite plate. We finally illustrate the advantage of a Bayesian procedure that can handle not only measurement error. Some concluding remarks close the chapter.

Least Squares and Bayesian Methodologies to Parameter Identification

Least Squares Formulations

The most common least squares approach to parameter identification is based on finding the parameters that minimize the squared error between experimental observations and model predictions.

Let \mathbf{x} be a vector of n material properties that we seek to identify and \mathbf{y}^0 a vector of m experimental observations. We assume we have a mathematical model relating \mathbf{x} to predictions of \mathbf{y} such that $\mathbf{y}(\mathbf{x})$ is the vector of m model predictions. Note that $\mathbf{y}(\mathbf{x})$ is usually a function of parameters other than material properties as well (geometry, loads, etc).

The simplest least squares formulation minimizes the objective function $J(\mathbf{x})$ defined in Equation 3-1 (Bjorck 1996, chapter 1). The material properties \mathbf{x} corresponding to the minimum are the identified properties.

$$J(\mathbf{x}) = \frac{1}{2} (\mathbf{y}(\mathbf{x}) - \mathbf{y}^0)^T (\mathbf{y}(\mathbf{x}) - \mathbf{y}^0) = \frac{1}{2} \sum_{i=1}^m (y_i(\mathbf{x}) - y_i^0)^2 \quad (3-1)$$

A variation of this basic formulation is to normalize each component of the residue vector by the corresponding experimental observation. This is a partly weighted least squares formulation which has its own limitations as will be shown in the next section.

A more general least squares formulation is based on minimizing the following objective function:

$$J(\mathbf{x}) = \frac{1}{2} (\mathbf{y}(\mathbf{x}) - \mathbf{y}^0)^T C(\mathbf{x})^{-1} (\mathbf{y}(\mathbf{x}) - \mathbf{y}^0) \quad (3-2)$$

where $C(\mathbf{x})$ is the variance-covariance matrix of $\mathbf{y}(\mathbf{x})$, thus taking statistical information into account. The variance-covariance structure for the response y needs to be assumed (based on

empirical evidence) or calculated using a model. If $C(\mathbf{x})$ is calculated from a model this can significantly increase the computational cost of the method.

Due to the challenge of constructing a realistic variance-covariance matrix $C(\mathbf{x})$, most least squares identification applications revert to the use of the formulation of Equation 3-1, which is equivalent to assuming that $C(\mathbf{x})$ is equal to the identity matrix, thus ignoring potential statistical information. The formulation of Equation 3-1 or its normalized version have been recently used for example in the domain of elastic constants identification from full field strain measurements (Mauvoisin et al. 1994, Lecompte et al. 2005 and 2007, Molimard et al. 2005, Silva 2009) or from vibration data (Sol 1986, Pedersen and Frederiksen 1992, Ayorinde and Yu 1999, Araujo et al. 2000, Rikards et al. 2001 and 2003, Cugnoni 2004, Shi et al. 2005). These approaches provided reasonable results in these studies, however more advanced statistical methods (whether advanced least squares or Bayesian) may sometimes lead to more accurate results. In the present work we seek situations where the advantage of using statistical methods would be the greatest.

Bayes' Theorem

The Bayesian identification approach is based on the application of Bayes' rule which gives the probability of an event A , knowing that an event B occurred as shown in Equation 3-3. Often $P(A)$ is called the prior probability of A , $P^{prior}(A)$, to mark the distinction to the probability of A knowing B , which is also called the posterior probability of A .

$$P(A / B) = \frac{P(B / A) \cdot P(A)}{P(B)} \quad (3-3)$$

Assuming now that A and B are random variables having continuous probability distributions (denoted by π), Bayes' rule can be extended to Equation 3-4.

$$\pi_{A/B=b}(a) = \frac{\pi_{B/A=a}(b) \cdot \pi_A(a)}{\pi_B(b)} \quad (3-4)$$

The function $\pi_{B/A=a}(b)$ is called the likelihood function, denoted $l(a)$, while $\pi_A(a)$ is usually called the prior distribution of A. The denominator can also be written in a different way using the law of total probabilities for continuous distributions, which leads to Equation 3-5.

$$\pi_{A/B=b}(a) = \frac{\pi_{B/A=a}(b) \cdot \pi_A(a)}{\int_{-\infty}^{\infty} \pi_{B/A=a}(b) \cdot \pi_A(a) \cdot da} \quad (3-5)$$

It is worth noting that the integral in the denominator represents just a normalizing constant, denoted by K from now on and which rarely needs to be calculated explicitly.

The Bayesian Identification

The Bayesian identification approach is a statistical approach. Unlike the least squares identification method it will not provide a single value for the identified parameter but a probability distribution.

The unknown material properties have a single value, but it is unknown, and their possible values are represented by the random variable X (with x being an instance of X). Its probability density function (pdf) is denoted $\pi_X(x)$. In the Bayesian identification we seek to identify the distribution of the material properties X given a vector of measurements \mathbf{y}^0 . The vector of measurements is assumed to be contaminated by a vector of unknown measurement errors \mathbf{e}^{meas} , stemming from the random variable Σ^{meas} . The true, but unknown response is then given by $\mathbf{y}_{true}^{meas} = \mathbf{y}^0 - \mathbf{e}^{meas}$. Letting Y_{true}^{meas} be the random variable of the true response value (it is a random variable because \mathbf{y}_{true}^{meas} is unknown), we can then write:

$$Y_{true}^{meas} = \mathbf{y}^0 - \Sigma^{meas} \quad (3-6)$$

For the identification we compare the measurements to a model's predictions (e.g. finite element model) $y_{p0}(\mathbf{x})$, that is a function of the material properties \mathbf{x} and other input parameters \mathbf{p} (e.g. geometry, loading) taken at their values \mathbf{p}_0 . Because of modeling error, and because the input parameters may not be accurately known, the random variable of the true response is given as:

$$\mathbf{Y}_{true}^{model}(\mathbf{x}) = y_{p0}(\mathbf{x}) - \Sigma^{model} \quad (3-7)$$

where Σ^{model} is the random variable of the error due to modeling uncertainty and uncertainty in the other input parameters.

Bayesian identification involves calculating for given material properties \mathbf{x}^{fixed} the probability that the true response is the same whether derived from the measurement or from the model, i.e. the probability that $\mathbf{Y}_{true}^{meas} = \mathbf{Y}_{true}^{model}$, which can also be written:

$$\mathbf{D} = \mathbf{Y}_{true}^{model} - \mathbf{Y}_{true}^{meas} = \mathbf{0} \quad (3-8)$$

This probability is called likelihood of \mathbf{x}^{fixed} given the measurements. For all possible \mathbf{x}^{fixed} the likelihood becomes a function of \mathbf{x} , denoted as $l(\mathbf{x})$, and defined as the pdf of \mathbf{D} given that $\mathbf{X}=\mathbf{x}$ (denoted $\mathbf{D}/\mathbf{X}=\mathbf{x}$) taken at zero:

$$l(\mathbf{x}) = \pi_{\mathbf{D}/\mathbf{X}=\mathbf{x}}(\mathbf{0}) \quad (3-9)$$

It is important to note that the pdf of \mathbf{D} given $\mathbf{X}=\mathbf{x}$ is a distribution in terms of the random variable \mathbf{D} and that \mathbf{x} can be seen as a parameter of this distribution. That is, for a certain material properties value \mathbf{x} , we need to determine what the distribution of \mathbf{D} is. The likelihood then, which is a function of \mathbf{x} , will be this pdf of \mathbf{D} for the given \mathbf{x} taken at $\mathbf{D}=\mathbf{0}$.

An alternative formulation of the likelihood function can be achieved by introducing the random variable \mathbf{Y} of the measurement prediction for a given \mathbf{x} :

$$\mathbf{Y}(\mathbf{x}) = y_{p0}(\mathbf{x}) - \Sigma^{model} + \Sigma^{meas} \quad (3-10)$$

Equation 3-8 can then be written as $Y = y^0$ and the likelihood function of \mathbf{x} given that the measurement prediction Y should be equal to the actual measurement y^0 is then:

$$l(\mathbf{x}) = \pi_{Y/X=\mathbf{x}}(y^0) \quad (3-11)$$

For each \mathbf{x} , the likelihood value is the pdf of the measurement prediction given the material properties, $Y/X=\mathbf{x}$, taken at the point of the actually measured response y^0 .

In the rest of the paper we will use this second formulation involving the random variable of the measurement prediction, which is the most common formulation used in Bayesian identification literature. Note though that traditionally most studies call Y simply the random variable of the measurements. We preferred calling it measurement prediction, since it is constructed for any \mathbf{x} (not just the true value of the properties) and because it can include modeling uncertainty Σ^{model} .

Briefly, note that the advantage of the first formulation is that it allows to take advantage of the independence of the random variables Y_{true}^{meas} and Y_{true}^{model} in order to reduce the computational cost of Monte Carlo simulations, which may be required to propagate uncertainties through the model. This aspect will be briefly discussed in Chapter 5.

A particular point of interest in the Bayesian approach is that it can not only account for the measurements through the likelihood function but it can also easily account for prior knowledge on the material properties using the prior distribution $\pi_X^{prior}(\mathbf{x})$, i.e. the pdf of \mathbf{X} prior to observing y^0 . Such prior knowledge can come from manufacturer's specifications or previous tests.

Based on the likelihood function and the prior distribution, Bayes' rule then gives $\pi_{X/Y=y^0}(\mathbf{x})$, the pdf of \mathbf{X} given that the measurement prediction Y should be equal to y^0 , by the product of the likelihood function by the prior distribution as shown in Equation 3-12.

$$\pi_{X/Y=y^0}(\mathbf{x}) = \frac{1}{K} \cdot l(\mathbf{x}) \cdot \pi_X^{prior}(\mathbf{x}) = \frac{1}{K} \cdot \pi_{Y/X=x}(\mathbf{y}^0) \cdot \pi_X^{prior}(\mathbf{x}) \quad (3-12)$$

where K denotes a normalizing constant, which is rarely required to be calculated in practice.

The identified pdf, $\pi_{X/Y=y^0}(\mathbf{x})$, can be characterized by mean and most likely values as well as variance-covariance matrix, thus providing uncertainty measures in the identified properties, which are usually not obtained in studies applying the basic least squares approach.

For additional details on the theory of Bayesian analysis and identification the reader can refer to Berger (1985) and Kaipio and Somersalo (2005).

Progressing from Least Squares to Bayesian Identification

Compared to other statistical approaches to identification, we chose the Bayesian approach because it has a simple formulation yet it can incorporate prior knowledge and provide statistical information about the identified parameters (it provides a distribution instead of a single value).

We provide here a quick overview of different identification formulations from the simplest to the most general and the progress made at each step.

a. Basic least squares:

$$\mathbf{x}^* = \arg \min_x J(\mathbf{x}) \text{ where } J(\mathbf{x}) = \frac{1}{2} (\mathbf{y}(\mathbf{x}) - \mathbf{y}^0)^T (\mathbf{y}(\mathbf{x}) - \mathbf{y}^0) \quad (3-13)$$

b. Generalized least squares:

$$\mathbf{x}^* = \arg \min_x J_c(\mathbf{x}) \text{ where } J_c(\mathbf{x}) = \frac{1}{2} (\mathbf{y}(\mathbf{x}) - \mathbf{y}^0)^T C(\mathbf{x})^{-1} (\mathbf{y}(\mathbf{x}) - \mathbf{y}^0) \quad (3-14)$$

c. Maximum likelihood:

$$\mathbf{x}^* = \arg \max_x L(\mathbf{x}) \text{ where } L(\mathbf{x}) = \pi_{Y/X=x}(\mathbf{y}^0) \quad (3-15)$$

d. Bayesian identification:

$$\pi_{X/Y=y^0}(\mathbf{x}) = \frac{1}{K} \cdot \pi_{Y/X=x}(\mathbf{y}^0) \cdot \pi_X^{prior}(\mathbf{x}) \quad (3-16)$$

Compared to the basic least squares formulation the generalized formulation appropriately handles normalization as well as statistical information present in the variance covariance matrix $C(\mathbf{x})$. These points will be illustrated in details in the rest of the chapter.

Moving from the generalized least squares formulation to maximum likelihood has the advantage of being able to handle distributions other than Gaussian. Also the likelihood function provides an easily obtainable estimate of the uncertainty in the identified parameters.

Finally moving from maximum likelihood to Bayesian identification we can now incorporate prior knowledge on the parameters to be identified in form of the prior distribution. Like the maximum likelihood, the Bayesian approach can handle non-Gaussian distributions. Moreover, because the Bayesian method identifies a probability density function it has the advantage over the previous identification formulations of immediately providing an estimate of the uncertainty (variance-covariance matrix) in the identified parameters.

In this chapter we compare the basic least squares identification (a) to the Bayesian identification (d) using simulated experiments. We made the choice of simulated experiments since these allow more flexibility in isolating different factors that affect the identification. In Chapter 5 we will provide least squares and Bayesian identification results using actual experimental measurements.

The identification comparison will illustrate how the two methods handle normalization of the measurements and statistical information about the measurements, such as coefficient of variation or correlation of the measurements. It also illustrates the advantage of obtaining the uncertainty in the identified parameters with the Bayesian approach. Note however that we do not investigate here the advantage of using prior information in the Bayesian approach.

Accordingly, we will choose wide prior distributions (i.e. we assume we have only vague prior information).

A Three Bar Truss Didactic Example

Description of the Three Bar Truss Example

The first example is a simple material property identification problem for which the application of both identification approaches is straight forward, avoiding complexity which could cloud the comparison. Our aim is to illustrate when and why the basic least squares and the Bayesian approaches lead to significantly different identified parameters.

The truss is subject to a horizontal force p and a vertical force r as shown in Figure 3-1. All three bars are assumed to have the same Young modulus E of 10 GPa, which is unknown and which we want to identify from strain measurements on two or three of the bars. The cross sectional areas of the bars are known exactly: A_A is the cross sectional area of bars A and C and A_B the cross sectional area of bar B .

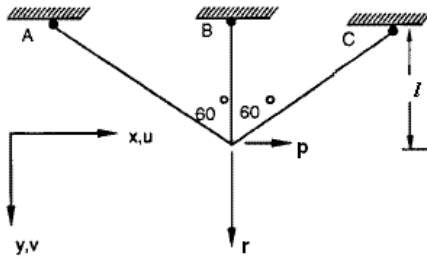


Figure 3-1. Three bar truss problem.

From static analysis we find the relationships for the strains in the bars given in Equations 3-17 to 3-19.

$$\varepsilon_A = \frac{1}{E} \left(\frac{r}{4A_B + A_A} + \frac{p}{\sqrt{3}A_A} \right) \quad (3-17)$$

$$\varepsilon_C = \frac{1}{E} \left(\frac{r}{4A_B + A_A} - \frac{p}{\sqrt{3}A_A} \right) \quad (3-18)$$

$$\varepsilon_B = \frac{1}{E} \frac{4r}{4A_B + A_A} \quad (3-19)$$

Sources of uncertainty

We consider that the magnitudes of the forces p and r are uncertain, meaning that due to measurement error the measured values of the forces might not be their true value. We assume the measured values of both forces are normally distributed with a mean value of $10^4 N$ for p and $10^5 N$ for r and a standard deviation of $500 N$ for both.

Note that we consider these to be the only sources of uncertainty in the problem. In reality there might also be uncertainties in the strain measurements and cross section measurements. We made this simplifying assumption however, so that the problem is not clouded by too many variables, which would make it difficult to draw the underlying processes affecting the results. This is in line with the objective of the chapter which is to identify general situations where the Bayesian and basic least squares identifications significantly differ in results. Assuming uncertainties only on the forces was a reasonable compromise between simplicity and flexibility for identifying such situations.

The Least Squares Method

The basic least squares formulation (see formulation a. in the previous section) finds the parameters that minimize the sum of the squares of the errors between experimental strain observations and model predictions. Assuming we measure the strains in bars A and B, the least squares objective function (of Equation 3-1) can be written as:

$$J(E) = \frac{1}{2} \left(\left(\varepsilon_A(E) - \varepsilon_A^{measure} \right)^2 + \left(\varepsilon_B(E) - \varepsilon_B^{measure} \right)^2 \right) \quad (3-20)$$

Note that even though the loads p and r are uncertain we have to provide a single nominal value for each. The most natural candidates are the means of the distributions of p and r . Note also that in this simple case it was possible to find the minimum analytically.

The Bayesian Method

Applying Equation 3-12 to the three bar truss problem we can write the distribution of the Young modulus of the bars given that we measured $\varepsilon_A^{measure}$ and $\varepsilon_B^{measure}$ in bars A and B respectively as shown in Equation 3-21.

$$\pi_{E/\{\varepsilon_A=\varepsilon_A^{measure}, \varepsilon_B=\varepsilon_B^{measure}\}}(E) = \frac{1}{K} \pi_{\{\varepsilon_A, \varepsilon_B\}/E}(\{\varepsilon_A^{measure}, \varepsilon_B^{measure}\}) \cdot \pi_E^{prior}(E) \quad (3-21)$$

The right hand side of this equation is composed, apart from the normalization constant K , of two quantities. The first is the likelihood function of E given the measurements and the other is the prior probability distribution of E . Here we assume that the prior knowledge is in the form of a truncated normal distribution with mean value 9.5 GPa and standard deviation 1.5 GPa. We truncate the distribution at 8 GPa and 11 GPa, meaning that we consider impossible for the properties to lie outside these bounds. As explained earlier, this is a wide prior, centered relatively far away from the true value of 10 GPa to avoid significantly biasing our comparison in favor of the Bayesian identification procedure. A few additional details on the impact of the prior will be given in the following sections.

The other right hand side term in Equation 3-21 is the likelihood function of E given the measurements $\varepsilon_A^{measure}$ and $\varepsilon_B^{measure}$. The likelihood function measures the probability of getting the test result for a given value of the modulus, and consequently, it provides an estimate of the likelihood of different modulus values given the test results. As we vary E successively from $-\infty$ to ∞ , we calculate the joint probability density function (pdf) of the strains for that E at the

measured strain point $\{ \varepsilon_A = \varepsilon_A^{measure}, \varepsilon_B = \varepsilon_B^{measure} \}$, that is $\pi_{\{\varepsilon_A, \varepsilon_B\}/E}(\{ \varepsilon_A^{measure}, \varepsilon_B^{measure} \})$. For a given E we have a probability distribution for the strains, due to the uncertainty in the loads p and r , which propagates to the strains (we use Monte Carlo simulation to generate 100,000 samples of the loads p and r and propagate these to strains using Equations 3-17 to 3-19). The strains obtained through the Monte Carlo simulation are fitted with a joint normal pdf using mean values and variance co-variance matrix. This pdf is then evaluated at the point

$$\{ \varepsilon_A = \varepsilon_A^{measure}, \varepsilon_B = \varepsilon_B^{measure} \}.$$

This procedure is repeated for a series of E values ranging from $-\infty$ to ∞ , thus constructing point by point the posterior pdf of the left hand side of Equation 3-21. In practice infinity is truncated by reasonable bounds for the property considered. In our case these are the truncation bounds of the prior distribution.

Note that the entire Bayesian identification for the three bar truss example took about 10s on a Pentium Core 2 Duo 2.00 GHz PC. This computational cost can increase significantly as m , the number of experimental values and n , the number of parameters to be identified, increase. The major part of the computational cost is the propagation of uncertainties through the model. Note that the three bar truss model involved only analytical expressions. If more complex models were used (e.g. finite elements) the computational cost would increase significantly or even become prohibitive without the use approximations (e.g. response surface approximations (Myers and Montgomery 2002)). To further reduce computational cost one can use advanced simulation techniques. A common advanced technique used in Bayesian methods is Markov Chain Monte Carlo simulation (Tarantola 2004). The combination of the aforementioned methods usually allows to bring the computational cost down to reasonable levels for many real-life problems, but still significantly higher than that of the basic least squares method. This is

however the price to pay for using statistical information in input and obtaining the statistics of the identified parameters with arbitrary (not necessarily Gaussian) probability distributions.

Illustrative Example

To illustrate the Bayesian procedure used, and in particular the construction of the likelihood function we will consider a simple case where all quantities are one-dimensional ($m=n=1$, with m the number of experimental observations and n the number of material properties). We consider the three bar truss where we have a single property to be identified, the Young modulus E , and a single measurement, the strain in bar C.

Of course there is little interest in applying the Bayesian procedure to such a one-dimensional case but we use it here only for illustrative purposes, the basic principle remaining the same when extending it to multi-dimensional cases (several properties to be identified and several measurement points).

Applied to the present one-dimensional case Equation 3-12 of the Bayesian formulation can be written as shown in Equation 3-22.

$$\pi_{E/\varepsilon_C=\varepsilon_C^{measure}}(E) = \frac{1}{K} \pi_{\varepsilon_C/E}(\varepsilon_C^{measure}) \cdot \pi_E^{prior}(E) \quad (3-22)$$

That is, the distribution of E given that in bar C we measured $\varepsilon_C^{measure}$ is equal to a normalization constant times the likelihood function of E given that we measured $\varepsilon_C^{measure}$ times the prior distribution of E . The prior distribution used here is the same wide distribution described in the previous subsection.

Next we describe in more detail the likelihood function and its construction. This function measures the probability of getting the test result $\varepsilon_C^{measure}$ for a given value of the modulus, and consequently, it provides an estimate of the likelihood of different modulus values given the test

results. Seen as a function of E we can construct it point by point. That is we fix an E successively from $-\infty$ to ∞ and calculate $\pi_{\varepsilon_C/E=E^{fixed}}(\varepsilon_C^{measure})$. As mentioned earlier, infinity is truncated to reasonable bounds for the properties to be identified. For example let us fix E to 5 GPa ($E^{fixed}=5$ GPa). We substitute this E back into Equation 3-18 and we propagate the uncertainties in the loads p and r in the same formula. For doing this we use 100,000 samples by Monte Carlo simulation. Thus we obtain the distribution function of ε_C if E was 5 GPa and given the uncertainties in p and r : $\pi_{\varepsilon_C/E=5GPa}(\varepsilon_C)$. In the general case we obtain this distribution from the Monte Carlo simulations through the empirical histogram. In this particular case we even know that the strain distribution will be normal so we just calculated the mean and standard deviation and used the corresponding normal distribution.

We can note that if E were 5 GPa, the strain in bar C would be much higher (in absolute value) than if E was 10 GPa, that is $\pi_{\varepsilon_C/E=5GPa}(\varepsilon_C)$ is centered around $-5.27 m\varepsilon$ compared to the value of $-2.87 m\varepsilon$, which is the actual (measured) strain in the bar with the true E of 10 GPa and the true values of loads. This is reflected in Figure 3-2.

Looking back at the construction of the likelihood function, we need to take the distribution $\pi_{\varepsilon_C/E=5GPa}(\varepsilon_C)$ at the point $\varepsilon_C = \varepsilon_C^{measure}$, that is we need to compute $\pi_{\varepsilon_C/E=5GPa}(\varepsilon_C^{measure})$. From Figure 3-2 we can see that this point is located in the tail of the distribution of $\pi_{\varepsilon_C/E=5GPa}(\varepsilon_C)$, so the corresponding value of $\pi_{\varepsilon_C/E=5GPa}(\varepsilon_C^{measure})$ will be relatively low. That means the likelihood that we measure $\varepsilon_C^{measure} = -2.87 m\varepsilon$ if E was 5 GPa is relatively low.

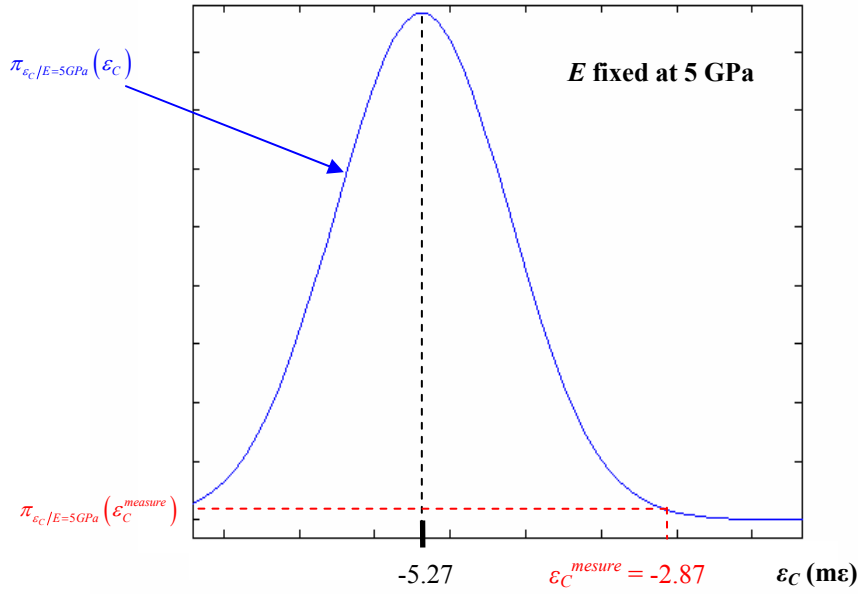


Figure 3-2. Likelihood value using the distribution of ε_C if E were 5 GPa.

Now let us assume that we fix $E = 9.18$ GPa and repeat the same procedure. In this case we will obtain a distribution similar to that in Figure 3-2 except that it will be centered in -2.87 mε. This means that the point $\pi_{\varepsilon_C|E=9.18GPa}(\varepsilon_C^{measure})$ is the highest point on the distribution, so the likelihood that we measure $\varepsilon_C^{measure} = -2.87$ mε is the highest if E was 9.18 GPa.

Note that if we assume that there is also a uniformly distributed measurement error (noise) which clouds the true value of the truss response $\varepsilon_C^{true} \in [\varepsilon_C^{measure} - \Delta\varepsilon_C, \varepsilon_C^{measure} + \Delta\varepsilon_C]$ then the calculation of the likelihood point would involve the integral over the uncertainty range. For example instead of calculating a likelihood point by using $\pi_{\varepsilon_C|E=9.18GPa}(\varepsilon_C^{measure})$ one would use

$\int_{\varepsilon_C^{measure} - \Delta\varepsilon_C}^{\varepsilon_C^{measure} + \Delta\varepsilon_C} \pi_{\varepsilon_C|E=9.18GPa}(\varepsilon_C) d\varepsilon_C$ instead. Calculating this integral is equivalent to saying that the likelihood of measuring $\varepsilon_C^{measure}$ is equal to the probability that the simulated strain ε_C fall inside the measurement uncertainty bounds. Measurement errors other than uniformly distributed

would be taken into account directly during the Monte Carlo simulation leading to the strain distribution.

After seeing how to compute 2 points of the likelihood function, one for 5 GPa and one for 9.18 GPa, we can in the same way compute $\pi_{\varepsilon_C/E=E^{fixed}}(\varepsilon_C^{measure})$ where E^{fixed} describes successively points between $-\infty$ and ∞ with a given infinitesimally small step. In practice we varied E between 8 and 11 GPa (with a step of 5 MPa) based on the prior distribution truncation bounds. If we do this we obtain $l(E) = \pi_{\varepsilon_C/E}(\varepsilon_C^{measure})$, the likelihood function of E given $\varepsilon_C^{measure}$, which is a function of E and is plotted in Figure 3-3 in our case. Note that the point obtained when we fixed $E=5$ GPa had such a low value that it does not even figure on this plot. This makes sense since measuring $\varepsilon_C^{measure} = -2.87m\varepsilon$ if E were 5 GPa is extremely unlikely. As previously mentioned the most likely value of E given only the measurement in bar C is $E=9.18$ GPa.

Had we used a deterministic analysis using the nominal values of the loads and $\varepsilon_C^{measure} = -2.87m\varepsilon$, we would substitute these values back into Equation 3-18 and solve for E , obtaining $E=9.18$ GPa. It is logical then that we find that 9.18 GPa is the most likely value for the Young modulus since we assumed that the nominal values for the loads are the most likely ones. However, we considered here an unlucky case where the actual values of the loads fell relatively far away from the most likely values (we considered the true loads to be two standard deviations (2σ) away from their mean values), which explains why 9.18 GPa is far from 10 GPa, the actual Young modulus of the bars.

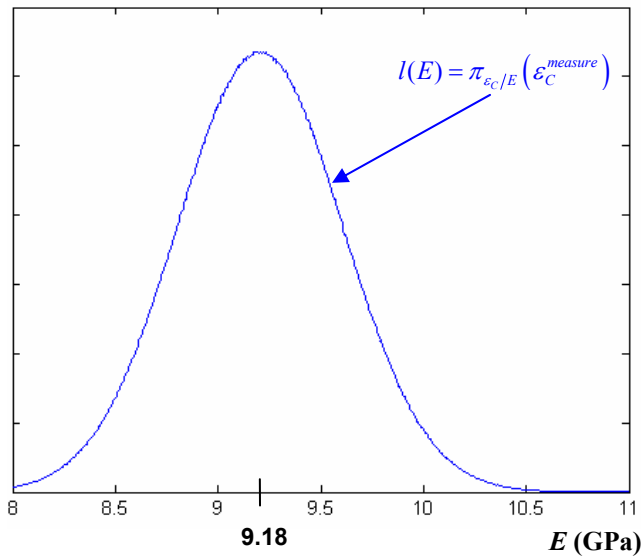


Figure 3-3. Likelihood function of E given $\epsilon_C^{measure}$.

Note that even though the likelihood function is centered in 9.18 GPa there is a small but non negligible probability that the Young modulus is around 10 GPa (cf. Figure 3-3). The true value of 10 GPa is actually about 2σ away from the mean value of 9.18 GPa, which seems to make sense as well since the true values of the loads were 2σ away from their mean.

At this point we can finalize the Bayesian procedure. We have the wide prior distribution of E we defined in the previous subsection, we have just calculated the likelihood function of E given $\epsilon_C^{measure}$ (Figure 3-3), all that remains is to apply the Bayesian formulation of Equation 3-22 that is multiply the two functions and normalize the resulting distribution. This is the probability distribution of the identified Young's modulus given that we measured $\epsilon_C^{measure}$.

On a final note recall that this one-dimensional example was used only for illustration purposes. In our main problems discussed in the following sections we have multiple strains, respectively frequencies for the vibration problem. The basic procedure though remains the same.

If we have more than one parameter to identify we have to define a joint probability distribution for the prior. This is illustrated on the vibration problem. The construction of the likelihood function would also be more time consuming since instead of describing an interval point by point we would have to describe a surface.

If we have multiple measurement points (for example strains in each of the bars) we would have to consider the joint probability distribution of the measurements when constructing the likelihood function. On our problem if we have the strains in the three bars for example, Figure 3-2 would have to be replaced by the three-dimensional joint strain distribution which would have to be evaluated at the measurement point $\{\varepsilon_A^{measure}, \varepsilon_B^{measure}, \varepsilon_C^{measure}\}$.

Least Squares and Bayesian Comparison for the Three Bar Truss Problem

The Comparison Method

The results of both the least squares and Bayesian approaches depend on the actual, but unknown, values of the loads p and r in an actual experiment. We compare the two methods in two different ways. In the next six subsections we use extreme cases where the actual values of p and r are two standard deviations away from their mean values: $p_{true}=p_m+2\sigma_p$ and $r_{true}=r_m-2\sigma_m$. Then in the following subsection we consider 1000 repetitions of the identification processes where the true values of p and r are obtained by Monte Carlo simulations from their distributions. This second case provides the average performance of each method measured by the dispersion (e.g., standard deviation) in the modulus estimate as the loads are varied.

For all the cases we compare the modulus obtained from the least squares approach to the most likely value from the Bayesian probability distribution. The differences between the two methods are likely to be influenced by three factors (i) differences in the sensitivity of strains to Young modulus; (ii) differences in the uncertainty of the measured strains; and (iii) correlation

between measured strains. For investigating points (i) and (ii) we use the three bars truss example with strain measurements on two of the bars while for point (iii) we use strain measurements on all three bars.

Note that the prior distribution of which the Bayesian identification can benefit, can potentially bias the comparison in favor of the Bayesian approach. This is why we chose a wide prior distribution, which, as will be illustrated at the end of the extreme cases comparison, has a negligible effect on the current identification results.

Results for Different-Sensitivity Strains

In this investigation case we create a situation where the strain in bar A is more sensitive to Young's modulus variations than the strain in bar B. Since all strains are inversely proportional to Young's modulus the sensitivity of the strain is proportional to the strain's magnitude. A high strain (in absolute value) in one of the bars means that the strain in that bar has a high sensitivity to E and vice versa. This equivalence is used in the next sections where we provide the magnitude of the strains as a measure of their sensitivity to E . Note, however, that when a measured quantity has a more complex dependence on the parameter to be estimated, the sensitivity may no longer be simply proportional to the magnitude.

To create a high strain in bar A which is about three times higher than that in bar B (hence three times more sensitive) we use the values in Table 3-1. The same relative uncertainty in the loads is applied (2.5%), which propagates to about the same relative uncertainty in ϵ_A and ϵ_B .

Table 3-1. Numerical values for different-sensitivity strains.

Parameter	Input parameters				Strains	
	A_A (m ²)	A_B (m ²)	p (N)	r (N)	ϵ_A (mm/m)	ϵ_B (mm/m)
(Mean) value	$2 \cdot 10^{-4}$	$1 \cdot 10^{-2}$	10^4	10^5	3.13	0.995
Standard deviation	-	-	250	2500	0.0725	0.0248
Measured strains*					3.26	0.945

* obtained from Eq. (3-17) and (3-19) with $E=10$ GPa, $p=p_{mean}+2\sigma_p$ and $r=r_{mean}-2\sigma_r$

Table 3-2. Extreme case identification results for different-sensitivity strain (true value of modulus is 10GPa).

	From $\varepsilon_A^{measure}$ alone	From $\varepsilon_B^{measure}$ alone	Least squares	Bayesian
E (GPa)	9.59	10.52	9.67	9.97 (most likely value) 0.174 (standard deviation)

The results of the two identification procedures are presented in Table 3-2. We also provide the Young modulus that would be obtained with each of the measurements alone by inverting Equations 3-17 and 3-19. The relatively poor results of the least squares method are because it implicitly assigns more weight to $\varepsilon_A^{measure}$. As we will prove in the next subsection the basic least squares formulation implicitly assigns more weight to quantities that have high sensitivity with respect to the parameter to be identified.

Normalizing the strain residue with respect to the measured strains would seem to be an obvious solution to this problem. However, while it solves indeed the variable sensitivity issue it can create another problem. Both measurement and calculation errors in small strains are often of similar absolute magnitude as the errors in the large strains. So small strains may have very large relative errors. Without normalization, these small and erroneous strains will have only a small effect on the identified property, while normalization will increase their influence. Let's assume, for example, that uncertainties in loads propagate to an uncertainty in strains of 0.1 mε in each of the bars. If one of the strains is 10 mε then the uncertainty represents only 1%, however if the other strain is 0.5 mε then the uncertainty represents 20%. If we normalize these two strains we take the risk of assigning the same weight to a measurement that can be 20% off as to a measurement that can be only 1% off.

This means that it is risky to perform normalization without taking into account the uncertainties in the measurements. This brings us to the advantage of taking into account the

uncertainty in the measured (and calculated) results, which is discussed hereafter. Note that if someone does not want to use the Bayesian approach for taking into account uncertainties, the simplest method which appropriately handles both normalization and uncertainty is generalized least squares (see the subsection above entitled least squares formulations).

Least Squares Implicit Weighting According to Response Sensitivity

We provide here the proof of the statement made in the previous subsection: the basic least squares formulation implicitly assigns more weight to quantities which have high sensitivity with respect to the parameter to be identified.

For simplicity we consider only linear models of the quantity to be identified: $\mathbf{y} = A\mathbf{x} + \mathbf{b}$ using the notations introduced at the beginning of the chapter. Note that on the three bar truss example we have a linear model after the change of variable $x=1/E$.

The least squares formulation can be written in this case as shown in Equation 3-23:

$$x^* = \arg \min_x J(x) \text{ where } J(x) = \frac{1}{2} (A\mathbf{x} + \mathbf{b} - \mathbf{y}^0)^T (A\mathbf{x} + \mathbf{b} - \mathbf{y}^0) \quad (3-23)$$

To eliminate the constant \mathbf{b} , we perform the change of variables: $\mathbf{z} = \mathbf{y} - \mathbf{b}$, so that $\mathbf{z}(x) = A\mathbf{x}$ and $\mathbf{z}^0 = \mathbf{y}^0 - \mathbf{b}$. Equation 3-23 can then be rewritten as follows.

$$x^* = \arg \min_x J(x) \text{ where } J(x) = \frac{1}{2} (A\mathbf{x} - \mathbf{z}^0)^T (A\mathbf{x} - \mathbf{z}^0) \quad (3-24)$$

Since J is convex in x the solution satisfies $\nabla J(x^*) = 0$, which gives the normal equations:

$$A^T A\mathbf{x}^* = A^T \mathbf{z}^0 \quad (3-25)$$

and $A^T A$ is usually invertible when $m > n$ (with m the number of experimental observations and n the number of material properties). Solving this equation leads to x^* . The normal equations can also be written as:

$$A^T (A\mathbf{x}^* - \mathbf{z}^0) = 0 \quad (3-26)$$

which shows that in the space of the measurements \mathbf{z} , the residual vector $A\mathbf{x}^* - \mathbf{z}^0$ is perpendicular to the model surface whose directing vectors are A^i . This also means that the solution \mathbf{x}^* to the basic least squares formulation of Equation 3-23 is obtained by projecting the experimental measurement point \mathbf{z}^0 onto the model surface $\mathbf{z}=A\mathbf{x}$. This is illustrated in Figure 3-4 when $m=2, n=1$.

In order to find how different measurements are weighted, we obtain solutions based on a single measurement as well (this is possible since $n=1$). The solution for measurement i is

$$x^{*i} = \arg \min_x \frac{1}{2} (A_i x - z_i^0)^2 \quad \text{for } i = 1, \dots, m \quad (3-27)$$

where subscript i represents the i^{th} line of the respective matrix/vector. Accordingly x^{*i} is the parameter found when only the measurement z_i^0 was used and \mathbf{z}^{*i} is the corresponding value on the surface of the response: $\mathbf{z}^{*i} = A \mathbf{x}^{*i}$. We call x^{*i} partial solutions and \mathbf{z}^{*i} the corresponding virtual measurements which are represented in Figure 3-4.

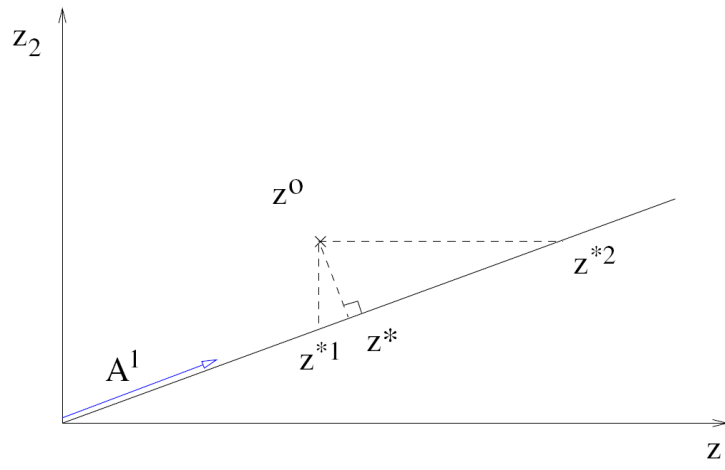


Figure 3-4. Illustration of least squares solution $\mathbf{z}^* = A\mathbf{x}^*$ and partial solutions \mathbf{z}^{*i} for $m=2, n=1$.

We can now investigate how the least squares solution \mathbf{z}^* depends on the virtual measurements \mathbf{z}^{*i} and thus, on the partial solutions x^{*i} . If \mathbf{z}^* is closer to \mathbf{z}^{*i} this can be seen as the

least squares procedure implicitly assigning more weight to z^{*i} . Figure 3-5 illustrates two cases with different slopes. In the case where z_1 is more sensitive to E variations than z_2 (low slope in the (z_1, z_2) plane) then the basic least squares formulation assigns more weight to z^{*1} and inversely. We can deduce that which partial solution is assigned more weight depends on the sensitivity of the response to the parameter to be identified. Mathematically this can be

quantified by: $\frac{\partial x^*}{\partial y_i^0}$ which is also equal to $\frac{\partial x^*}{\partial z_i^0}$. Deriving the normal equation 3-25 we obtain:

$$A^T A \frac{\partial x^*}{\partial z_i^0} = A^T \begin{Bmatrix} 0 \\ \vdots \\ 1 \\ \vdots \\ 0 \end{Bmatrix} = A_i^T \quad (3-28)$$

From Equation 3-20 we can deduce that the sensitivity of the identified parameters to the i^{th} experiment depends on the i^{th} line of A.

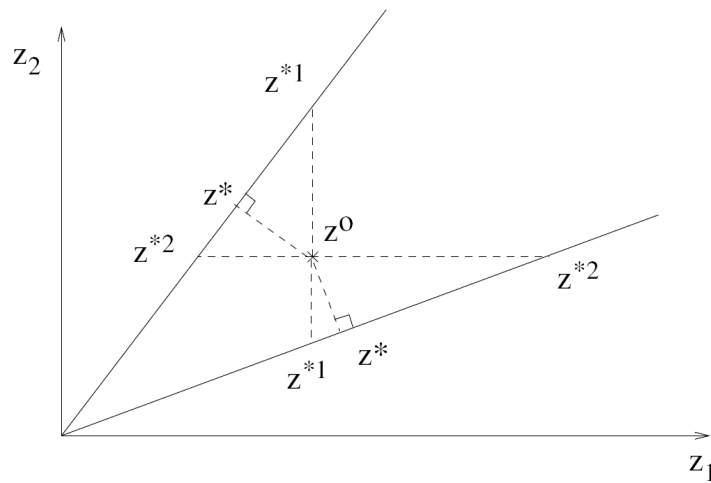


Figure 3-5. Illustration of least squares solution $z^* = Ax^*$ and virtual measurements z^{*i} for two different slopes A. In one case the basic least squares formulation assigns more weight to z^{*1} in the other to in the other to z^{*2} .

After this demonstration, it is interesting to analyze how the least squares and the Bayesian approaches are represented graphically for the three bar truss example. We illustrate in Figure 3-6 the case of different strain sensitivity to E , which translates into different strain magnitudes (studied in the previous subsection). The blue line is the model surface $\mathbf{y} = A\mathbf{x} + \mathbf{b}$. In our case $\mathbf{x} = 1/E$ and $\mathbf{b} = \mathbf{0}$ so that $\mathbf{z} = \mathbf{y} = \{\varepsilon_A, \varepsilon_B\}^T$. The red circle is the experimental measurement and its orthogonal projection on the model surface (red cross) is the least squares identified modulus, $E = 9.67$ GPa. The center of the ellipses, $E_{Bayes}^* = 9.97$ GPa, is the Bayesian identified modulus (most likely point). The ellipses represent the joint strain distribution function

$\pi_{\{\varepsilon_A, \varepsilon_B\} | E = 9.97 \text{ GPa}}(\{\varepsilon_A, \varepsilon_B\})$. If we vary E this is the distribution leading to the highest likelihood of the experimental measurement, meaning that if we translate the distribution along the model surface, this is the distribution for which the outer ellipse gets the closest to the experimental point. Note that this explanation does not take into account the impact of the prior which we have shown to be negligible in our case, because we have chosen a wide prior.

Figure 3-6 also helps understanding why the basic least squares formulation leads to poor results in the case of different sensitivity to E (i.e. different strain magnitude). Due to the different sensitivity to E the model surface (blue line) has a low slope. The uncertainties in the loads propagate to the same relative uncertainties in the two strains, but different absolute uncertainties due to the different strain sensitivities, meaning that the joint strain distribution will be elliptical instead of circular. The low slope in combination with the elliptical distribution leads the orthogonal projection of the measurement to be relatively far away from the maximum likelihood point as illustrated in Figure 3-6.

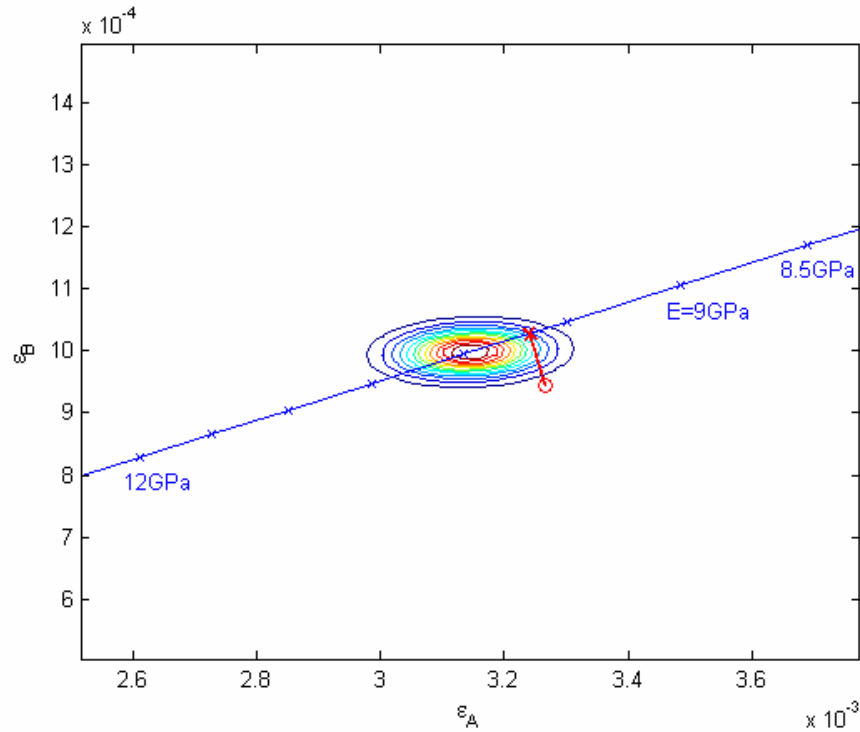


Figure 3-6. Graphical representation of the least squares and Bayesian results for the three bar truss example for the different sensitivity case (i.e. different strain magnitude). The red circle is the experimental measurement, its orthogonal projection (red cross) the least squares identified modulus while the center of the ellipses is the Bayesian identified modulus. The ellipses represent the contour plot of the strain distribution

$$\pi_{\{\varepsilon_A, \varepsilon_B\} / E = E_{Bayes}^*}(\{\varepsilon_A, \varepsilon_B\}).$$

Results for Different Uncertainty in the Strains

To create different uncertainty in the two strains we used the values given in Table 3-3. To isolate this effect from the previous one, the calculated strains have about the same magnitude, thus the same sensitivity to E . We chose 5% uncertainty in p and 0.5% in r , which result in ε_A having about 7 times higher uncertainty than ε_B . The results of the two identification procedures are presented in Table 3-4 for the extreme case where the actual values of p and r are two standard deviations away from the mean values. Again the Bayesian approach is much more accurate than the least squares approach.

Table 3-3. Numerical values for variable response uncertainty.

Parameter	Input parameters				Strains	
	A_A (m ²)	A_B (m ²)	p (N)	r (N)	ε_A (mm/m)	ε_B (mm/m)
(Mean) value	$7.85 \cdot 10^{-4}$	$1 \cdot 10^{-2}$	10^4	10^5	0.980	0.980
Standard deviation	-	-	500	500	0.0368	0.0049
Measured strains*					1.05	0.970

* obtained from Eq. (3-17) and (3-19) with $E=10$ GPa, $p=p_{mean}+2\sigma_p$ and $r=r_{mean}-2\sigma_r$

Table 3-4. Extreme case identification results for different response uncertainty (true value of E is 10 GPa).

	From $\varepsilon_A^{measure}$ alone	From $\varepsilon_B^{measure}$ alone	Least squares	Bayesian
E (GPa)	9.32	10.10	9.69	10.08 (most likely value) 0.058 (standard deviation)

Since the two strains have about the same sensitivity to E (due to same magnitude), least squares assigns about the same weight to each, so the identified E is at about the average between the E found with each measurement alone. The uncertainty information is taken into account by the Bayesian method through the likelihood function, which may be viewed as assigning more weight to the measurement having low uncertainty. This explains why the Bayesian identified modulus is much closer to the one found using $\varepsilon_B^{measure}$ alone.

Similar to the graphical representation provided in the previous subsection for different response sensitivity, we provide here an interpretation of the three bar truss results in the case of different response uncertainty. Figure 3-7 illustrates the present case of different uncertainty in the loads which propagates to different uncertainty in the strains. We can note that here we have same sensitivity of the strains to the Young modulus, which can be seen by the 45° slope of the model surface. Note also that the elliptical shape of the joint strain distributions is due this time not to different strain sensitivity as is in the previous subsection but to different uncertainties in the loads, which propagates to a higher uncertainty in ε_A than in ε_B .

In addition to the joint strain distribution centered in the Bayesian identified modulus (ellipses in full line) we also provide what would be this joint strain distribution if the modulus was the one found by least squares. This shows that the experimental measurement has the maximum likelihood on the strain distribution with the Bayesian modulus. Indeed the measurement point is the closest possible to the outer most ellipse of all possible distributions translated along the model surface line. In particular the strain distribution centered in the least squares modulus has a significantly lower likelihood.

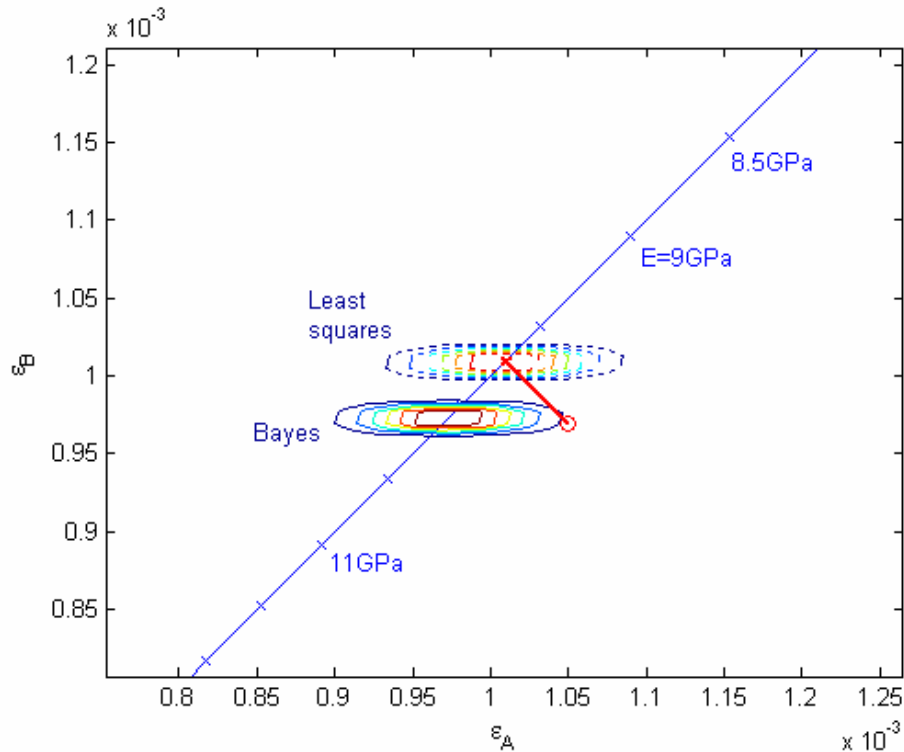


Figure 3-7. Graphical representation of the least squares and Bayesian results for the three bar truss example for the different uncertainty case. The red circle is the experimental measurement and its orthogonal projection (red cross) the least squares identified modulus. The ellipses are the contour plot of the strain distribution $\pi_{\{\varepsilon_A, \varepsilon_B\} / E = E_i^*}(\{\varepsilon_A, \varepsilon_B\})$ where E_i^* is the least squares identified modulus E_{LS}^* (dashed line) or the Bayesian identified modulus E_{Bayes}^* (full line).

Results for Correlation among the Responses

To show the effect of correlation we need three strain measurements with two strongly correlated but not correlated to the third. For this purpose we used the parameter values in Table 3-5.

Note that, in order to isolate this effect from the previous one, we have the same relative uncertainty in p and in r which propagates to about the same relative uncertainty in all three strains. We could not, however, find values that lead to the same amplitude for all three strain measurements. Therefore, the least squares approach will pay less attention to the small $\varepsilon_B^{measure}$. The correlation between ε_A and ε_C is -0.985 while the correlation between the other two couples is 0.086, meaning that only ε_A and ε_C are highly correlated.

Table 3-5. Numerical values for response correlation.

Parameter	Input parameters				Strains		
	A_A (m ²)	A_B (m ²)	p_m (N)	r_m (N)	ε_A (mm/m)	ε_B (mm/m)	ε_C (mm/m)
(Mean) value	$2 \cdot 10^{-4}$	$1 \cdot 10^{-2}$	10^4	10^5	3.13	0.995	-2.64
Standard deviation	-	-	250	2500	0.0725	0.0248	0.0725
Measured strains*					3.27	0.945	-2.79

* obtained from Eq. (3-17) to (3-19) with $E=10$ GPa, $p=p_{mean}+2\sigma_p$ and $r=r_{mean}-2\sigma_r$

Table 3-6. Extreme case identification results for response correlation (true value of $E=10$ GPa).

	From $\varepsilon_A^{measure}$	From $\varepsilon_B^{measure}$	From $\varepsilon_C^{measure}$	Least squares	Bayesian
E (GPa)	9.59	10.52	9.43	9.58	9.96 (most likely value) 0.196 (standard deviation)

Comparison between Table 3-2 and Table 3-6 shows that the least squares method is more affected by adding a correlated measurement (+ 0.9% difference) than the Bayesian approach (+ 0.1% difference). The explanation is that least squares treats all three measurements as independent and due to the small magnitude of $\varepsilon_B^{measure}$ it mainly averages $\varepsilon_A^{measure}$ and $\varepsilon_C^{measure}$.

The Bayesian approach may be viewed as averaging the highly correlated $\varepsilon_A^{measure}$ and $\varepsilon_C^{measure}$ first, then considering the average value as a single experiment it combines it with the uncorrelated one.

Results for All Three Effects Together

In this last case we combine all three effects, which is what may sometimes happen in a real situation. For this purpose we used the numerical values given in Table 3-7. We have different magnitude of the strains, different uncertainty in the loads and correlation among the strains: the correlation between ε_A and ε_C is -0.999, between ε_A and ε_B 0.014 and between ε_B and ε_C 0.002.

Table 3-7. Numerical values for the three combined effects.

Parameter	Input parameters				Strains		
	A_A (m ²)	A_B (m ²)	p_m (N)	r_m (N)	ε_A (mm/m)	ε_B (mm/m)	ε_C (mm/m)
(Mean) value	$2 \cdot 10^{-4}$	$1 \cdot 10^{-2}$	10^4	10^5	3.13	0.995	-2.64
Standard deviation	-	-	500	500	0.144	0.005	0.144
Measured strains*					3.42	0.985	-2.93

* obtained from Eq. (3-17) to (3-19) with $E=10$ GPa, $p=p_{mean}+2\sigma_p$ and $r=r_{mean}-2\sigma_r$

Table 3-8. Extreme case identification results for the three combined effects (true value of the E is 10 GPa).

	From $\varepsilon_A^{measure}$	From $\varepsilon_B^{measure}$	From $\varepsilon_C^{measure}$	Least squares	Bayesian
E (GPa)	9.16	10.10	9.00	9.14	10.08 (most likely value) 0.058 (standard deviation)

We can see in Table 3-8 that in this case the error in the least squares approach is exacerbated. All effects act together and against the least squares method. On the other hand the Bayesian method considers almost only ε_B , which has by far the lowest uncertainty, leading the Bayesian method to be much closer to the true Young modulus.

Additional details on how the Bayesian approach handles correctly normalization, uncertainty and correlation of the measurements are provided next.

The loads having normal distributions and the problem being linear in the loads this leads to the strain distribution given E to be Gaussian as well. Using again the general notation introduced at the beginning of this chapter we can write:

$$\pi_{Y/X=x}(\mathbf{y}) = \frac{1}{(2\pi)^{m/2} |C_y(x)|^{1/2}} \exp\left(-\frac{1}{2}(\mathbf{y} - \mathbf{m}_y(x))^T C_y^{-1}(x)(\mathbf{y} - \mathbf{m}_y(x))\right) \quad (3-29)$$

where $\mathbf{m}_y(x)$ and $C_y(x)$ are the mean of the response and the variance-covariance matrix of the response for the given x .

The term $(\mathbf{y} - \mathbf{m}_y(x))^T C_y^{-1}(x)(\mathbf{y} - \mathbf{m}_y(x))$ in the previous expression is the one which scales and de-correlates the measurements according to the magnitude, uncertainty and correlation provided by C_y . This can be further understood after a change of coordinates. First note that since C_y is a variance-covariance matrix it is symmetric and positive definite so it can

be decomposed into $C_y = BD^2B^T$ where $D = \begin{bmatrix} d_1^2 & \dots & 0 \\ 0 & \ddots & 0 \\ 0 & \dots & d_m^2 \end{bmatrix}$ and $B = [\mathbf{b}_1 \dots \mathbf{b}_m]$; B is the

eigenvectors matrix of C_y (i.e. $C_y \mathbf{b}_i = d_i^2 \mathbf{b}_i$).

Then we can write $C_y^{-1} = (BD^2B^T)^{-1} = BD^{-1}D^{-1}B^T$ which leads to Equation 3-30.

$$(\mathbf{y} - \mathbf{m}_y)^T C_y^{-1} (\mathbf{y} - \mathbf{m}_y) = (D^{-1}B^T (\mathbf{y} - \mathbf{m}_y))^T (D^{-1}B^T (\mathbf{y} - \mathbf{m}_y)) \quad (3-30)$$

Substituting this expression back into Equation 3-29 of the Gaussian distribution of the response \mathbf{y} for a given x this illustrates how for any given measurements \mathbf{y}^0 , the measurements are de-correlated (by the multiplication by B^T , which implements a change of reference into the

basis of the eigenvectors) and scaled (by the multiplication by D^{-1} , containing the variance terms in the eigenvector directions and which account for both response sensitivity and uncertainty).

This means that each time that in the Bayesian procedure $\pi_{Y|X=x}(\mathbf{y})$ is evaluated at the experimental measurements point $\mathbf{y}=\mathbf{y}^0$, the measurements are subsequently scaled and de-correlated, which provides an alternative explanation of why the Bayesian approach correctly handles different response magnitudes, response uncertainties and correlation.

At this point we briefly discuss the influence of the prior distribution on the Bayesian identification results. All the previous results were obtained for a truncated, normally distributed wide prior with mean value 9.5 GPa and a large standard deviation of 1.5 GPa. If we change the standard deviation of the prior to 0.75 GPa keeping the same mean and same truncation bounds we obtain for this extreme case a most likely value of 10.07 GPa (10.08 previously, see Table 3-8), which is a small improvement due to a narrower prior. If we change the mean of the prior distribution to 10.5 GPa keeping the standard deviation and the truncation bounds the same, we obtain a most likely value of 10.09 GPa (compared to 10.08). So even though we changed the prior significantly it had very small effects on the Bayesian identification results. Of course a much narrower, more accurate prior distribution would have improved the accuracy a lot. So it is worth noting that one of the advantages of the Bayesian approach is the facility with which it can incorporate prior knowledge, even though investigating the influence of the prior was not among our primary objectives in this work.

As a final note we need to mention again that the advanced least squares approach involving the variance-covariance matrix would also handle this three bar truss problem appropriately by de-correlating and scaling the measurements similarly to Equation 3-30. In fact if we neglect the influence of the prior, the Bayesian and the advanced least squares approach

would lead to the same results on this problem. This might not be the case however on more complex problems, such as the vibration problem that we will treat in the next sections, where the uncertainties no longer propagate to Gaussian uncertainties on the measurements. In such types of problems the Bayesian approach based on Monte Carlo simulation would appropriately handle non-Gaussian uncertainties as well.

Average Performance of the Least Squares and Bayesian Approach

To complement the results obtained for the extreme case we repeat the previous procedure 1000 times, for random values of the loads obtained by Monte Carlo simulation instead of the extreme values. The numerical values for the cross sections, the loads and their uncertainty are those given earlier for each case. The quality of the methods will be measured mainly by the standard deviation of E as the loads are varied (see Table 3-9). For the individual cases the standard deviations of the Bayesian approach are lower by a fraction (different sensitivity case) to a factor of 3.5 (different uncertainty) The difference is even more striking for the three effects combined, since, on average, the E found by the Bayesian approach will be almost 10 times closer to the true value.

Table 3-9. Average performance of the methods in the different cases (note that the differences in the mean value mainly reflect the limited sample size of 1000 cases). The numerical values for the cross sections, the loads and their uncertainties are those given in the previous sections.

		Mean of E (GPa)	Standard deviation of E (GPa)
Different sensitivity	Least squares	10.01	0.200
	Bayesian	9.99	0.167
Different uncertainty	Least squares	10.00	0.178
	Bayesian	9.99	0.051
Correlation	Least squares	10.01	0.221
	Bayesian	9.99	0.167
All three together	Least squares	10.04	0.447
	Bayesian	9.99	0.050

Vibration Identification Problem

Description of the Problem

In this section we explore how the two methods compare for a more realistic identification problem of identifying the elastic properties from the natural frequencies of a composite plate. This problem also illustrates the results on a case where uncertainties on the response are no longer Gaussian. Since we are only interested here in comparing the two identification methods, we simulate experiments from analytical expressions available for simply supported plates and error models explained hereafter. This also eases computational cost which would be a major issue if more realistic boundary conditions requiring more complex numerical models were used (finite elements for example).

We consider a $[0, 90]_s$ simply supported graphite/epoxy composite laminate of dimensions $a = 200$ mm, $b = 250$ mm and of total thickness $h = 3$ mm. We assume that the true elastic constants of the laminate are those given in Table 3-10. Note that our aim here is to identify these properties of the laminate and not those of an individual ply. For the sake of simplicity and easy graphical representation, we identify only two properties, assuming that ν_{xy} is known as well as $E_x = E_y$. This leaves E_x and G_{xy} to be identified. Note however that the procedure described remains the same if all four properties would be identified.

Table 3-10. Assumed true values of the laminate elastic constants.

Parameter	E_x (GPa)	E_y (GPa)	G_{xy} (GPa)	ν_{xy}
True value	57.6	57.6	4.26	0.05

The simulated experiment consists of measuring the first nine natural frequencies of the plate. The measured frequencies are generated using thin plate theory as well as simulating various sources of uncertainty such as measurement errors, which will be detailed in the next section. We use the thin plate theory for obtaining the frequencies in terms of density ρ and

rigidities D_{ij} , which leads to Equation 3-31. The bending rigidities D_{ij} are a function of the individual in plane properties of a ply (longitudinal and transverse Young's moduli E_1 and E_2 , Poisson ratio ν_{12} and shear modulus G_{12}), the thickness and the composite layup orientation. For a detailed procedure for calculating the rigidities of a composite laminate from the ply properties the reader can refer to Gurdal et al. (1998).

$$f_{kl} = \frac{\pi}{2\sqrt{\rho h}} \sqrt{D_{11} \left(\frac{k}{a}\right)^4 + 2(D_{12} + 2D_{66}) \left(\frac{k}{a}\right)^2 \left(\frac{l}{b}\right)^2 + D_{22} \left(\frac{l}{b}\right)^4} \quad (3-31)$$

Sources of uncertainty

For this problem we considered that there is uncertainty on input parameters to the model, measurement uncertainty, which was assumed uniformly distributed, and finally modeling error.

In terms of the model input parameters, denoted \mathbf{p} , we assumed that there are uncertainties in the plate dimensions and density. These uncertainties, which were assumed normally distributed and uncorrelated, are given in Table 3-11. Note that we can expect that the resulting uncertainty on the response (frequencies here) will be normal only if the response is linear in the dimensions, which it is clearly not (see Equation 3-31).

Table 3-11. Assumed uncertainties in the plate length, width, thickness and density (a , b , h and ρ). Normal distributions are considered.

Parameter	a (mm)	b (mm)	h (mm)	ρ (kg/m ³)
Mean value	200	250	3	1536
Standard deviation	0.5	0.5	0.01	7.67

We assume uniformly distributed measurement error in an interval which gets higher for the higher natural frequencies, mainly because the higher vibration modes have smaller amplitudes than the lower modes. To this we add a systematic modeling error, which is zero for the fundamental frequency and increases linearly. This error may account for the difference

between thin and thick plate theory, since higher modes have shorter wavelength. The measured frequencies can then be simulated using the following equation:

$$f_{kl}^{measure} = f_{kl}^{resp} \left(\{E_x, G_{xy}\}^{true}, p^{true} \right) + u_{kl} \quad (3-32)$$

where f^{resp} is obtained from Equation 3-31, which is a function of $\{E_x, G_{xy}\}^{true}$, which are the true values of the material properties and p^{true} , which are the true values of the other input parameters a, b, h and ρ . Variable u_{kl} is a random variable uniformly distributed in the interval $[a_{kl}, b_{kl}]$ where

$$a_{kl} = f_{11}^{resp} \left(a_{lb} + a_{ub} \frac{k+l-2}{k_{max} + l_{max} - 2} \right) \quad b_{kl} = f_{11}^{resp} \left(b_{lb} + b_{ub} \frac{k+l-2}{k_{max} + l_{max} - 2} \right) \quad (3-33)$$

For nine frequencies $k_{max}=l_{max}=3$. We chose $a_{lb} = -2.5 \cdot 10^{-3}$, $a_{ub} = -4 \cdot 10^{-2}$, $b_{lb} = 2.5 \cdot 10^{-3}$ and $b_{ub} = -2 \cdot 10^{-2}$. With these numerical values the error for the lowest natural frequency f_{11} would be uniformly distributed within the bounds $[-0.0025 f_{11}, 0.0025 f_{11}]$. The error for the highest (ninth) natural frequency measured would be uniformly distributed within the bounds $[-0.04 f_{11}, -0.02 f_{11}]$. In between these frequencies the bounds of the error vary linearly with respect to k and l , which is assumed to model the increase in the measurement error for the higher frequencies. The fact that the center of the interval is not zero for all frequencies, but decreases with the frequencies, is assumed to model the error between thin and thick plate theory. The random variable u_{kl} thus aggregates the modeling and measurement uncertainties Σ^{model} and Σ^{meas} of Eq. 3-10 into a single quantity.

The Identification Methods

The least squares method minimizes the objective function shown in Equation 3-34, where $f_{kl}^{resp}(E_x, G_{xy})$ is the response calculated using Equation 3-31 using the mean values of a, b, h and ρ .

$$J(E_x, G_{xy}) = \sum_{k,l=1..3} \left(f_{kl}^{resp}(E_x, G_{xy}) - f_{kl}^{measure} \right)^2 \quad (3-34)$$

For the experimental measurements we assume we know the average of the systematic error $(a_{kl} + b_{kl})/2$ for which we correct each experimental frequency $f_{kl}^{measure}$. Note that this is a significant assumption in favor of least squares. In reality, the systematic error might be less well known which would then create a bias in the identified properties. On the other hand the Bayesian approach can handle even vague information on the systematic error as we will show in the next paragraphs.

The Bayesian approach can be written as shown in Equation 3-35.

$$\pi_{\{E_x, G_{xy}\} / \{f_{11}=f_{11}^{measure}, \dots, f_{33}=f_{33}^{measure}\}}(\{E_x, G_{xy}\}) = \frac{1}{K} \pi_{\{f_{11}, \dots, f_{33}\} / \{E_x, G_{xy}\}}(\{f_{11}^{measure}, \dots, f_{33}^{measure}\}) \cdot \pi_{\{E_x, G_{xy}\}}^{prior}(\{E_x, G_{xy}\}) \quad (3-35)$$

A major difference compared to the three bar truss is that we now also have measurement error which we can take into account in the Bayesian approach. We assume that we know there is some numerical noise and that thin plate theory over-predicts the natural frequency but we assume we do not know the exact amount. For the Bayesian identification we use an error model accounting for the various sources of uncertainty described in the previous subsection:

$$f_{kl} = f_{kl}^{resp}(\{E_x, G_{xy}\}, \mathbf{p}) + \tilde{u}_{kl} \quad (3-36)$$

where f^{resp} is the model response using Equation 3-31, $\{E_x, G_{xy}\}$ are the values of the material properties considered at each identification step, and \mathbf{p} are simulated values of the other input parameters a, b, h and ρ . Variable \tilde{u} is a random variable uniformly distributed in the interval

$[\tilde{a}_{kl}, \tilde{b}_{kl}]$ where \tilde{a}_{kl} and \tilde{b}_{kl} are obtained using Equation 3-33 with $a_{lb} = -5 \cdot 10^{-3}$, $a_{ub} = 5 \cdot 10^{-2}$, $b_{lb} = 5 \cdot 10^{-3}$ and $b_{ub} = 5 \cdot 10^{-2}$. Note that these error bounds are significantly wider than the ones used for

simulating the actual experiment (see previous subsection), reflecting the fact that we only have vague knowledge of the error model, and we tend to be conservative.

Another major difference with the three bar truss formulation is that we work with the joint probability distribution of E_x and G_{xy} instead of the one dimensional distribution of E and the nine-dimensional joint frequencies distribution function for the measurements instead of the two- or three-dimensional strains distribution. The higher dimensions significantly increase computational cost of the Bayesian identification. Furthermore, the model here is no longer linear in the material properties x (see notations introduced at the beginning of the chapter).

Note also that the joint frequencies distribution is of unknown shape because the frequency response is non-linear in the uncertain input parameters of Table 3-11. This means that we cannot use the empirical mean and variance-covariance matrix to fit the frequencies distribution with a joint normal pdf. Instead, given that we assumed a uniformly distributed error we can directly calculate the likelihood function by integrating the simulated frequencies pdf between the uncertainty bounds as shown in Equation 3-37.

$$\pi_{f/\{E_x, G_{xy}\}}(\mathbf{f}^{measure}) = \frac{1}{K} \int_{\mathbf{f}^{measure} - \tilde{\mathbf{a}}}^{\mathbf{f}^{measure} + \tilde{\mathbf{b}}} \pi_{f^{MC}/\{E_x, G_{xy}\}}(\mathbf{f}^{input_MC}) d\mathbf{f}^{input_MC} \quad (3-37)$$

where K is a normalizing constant, \mathbf{f} is the nine-dimensional random variable of the frequencies measurement prediction, $\mathbf{f}^{measure}$ is the nine-dimensional vector of the measured frequencies, \mathbf{a} and \mathbf{b} are the nine-dimensional vectors of the measurement uncertainty bounds \tilde{a}_{kl} and \tilde{b}_{kl} .

Finally $\mathbf{f}^{input_MC} = f_{kl}^{resp}(\{E_x, G_{xy}\}, \mathbf{p})$ is the nine-dimensional random variable of the frequencies due only to uncertainty on input parameters \mathbf{p} , and obtained by Monte Carlo simulation on the frequency expression of Equation 3-31 with the input uncertainties of Table 3-11. Equation 3-37 is equivalent to saying that the likelihood of measuring the frequencies $\mathbf{f}^{measure}$ is equal to the

probability that the simulated frequencies f^{input_MC} fall inside the measurement uncertainty bounds. The integral in Equation 3-37 is evaluated by counting the number of frequencies within the bounds $[f^{measure} - \tilde{a}, f^{measure} + \tilde{b}]$ out of the total number of simulated frequencies f^{input_MC} . We used 50,000 Monte Carlo simulations. The present calculation approach can also be seen as implicitly using the independence of the measurement uncertainty and of the uncertainty due to input parameters, which allows to reduce cost by avoiding the calculation of the full histogram.

The prior distribution for the Bayesian identification was assumed to be a truncated uncorrelated bi-normal distribution with mean 57 GPa and standard deviation 10 GPa for E_x and 4.2 GPa and 1.5 GPa, respectively for G_{xy} . This is again a wide distribution to avoid that the prior gives the Bayesian method a significant advantage. The distribution was truncated for E_x at 55.6 GPa and 58.4GPa and for G_{xy} at 37.8 GPa and 46.2 GPa. The truncation bounds were chosen around the mean value of the prior and iteratively reduced so that they eventually cover about five standard deviations of the posterior pdf.

Results

To illustrate the benefits of the Bayesian method we present first the results for a particular simulation where we randomly simulated a single experiment (simulated according to the procedure explained previously and including uncertainty in model input parameters, model error as well as measurement uncertainty). The simulated frequencies which we assume we measure are given in Table 3-12. When repeating the simulation of measured frequencies a few times we found that the frequencies of Table 3-12 lead to rather high differences between the Bayesian and the least squares approach. This case can then be considered to be a rather extreme case, which is fine however, since we also provide below the average performance over 100 repetitions of the simulated experimental frequencies.

Table 3-12. Simulated experimental frequencies.

Frequency	f_{11}	f_{12}	f_{13}	f_{21}	f_{22}	f_{23}	f_{31}	f_{32}	f_{33}
Value (Hz)	267.9	612.9	1266.3	863.6	1070.5	1594.4	1892.0	2032.5	2409.1

The identification results for this case are presented in Table 3-13. The Bayesian approach obtained the probability distribution shown in Figure 3-8. The maximum of the distribution is in $E_x = 57.9$ GPa , $G_{xy} = 4.30$ GPa .

Table 3-13. Least squares and Bayesian results for a randomly simulated particular case.

	E_x (GPa)	G_{xy} (GPa)
True values	57.6	4.26
Least squares values	56.9	4.66
Bayesian most likely values	57.9	4.30

Both approaches found an E_x which is very close to the true value (about 1%). However the G_{xy} found by the least squares is more than 8% off the true value while the one found by the Bayesian method is only 0.9% off.

Furthermore the Bayesian approach provides additional information in form of the distribution shown in Figure 3-8 (in particular information on the standard deviation of the properties identified). Note that the distribution along G_{xy} is much wider than the one along E_x (note different scales in Figure 3-8). This means that the confidence in the most likely value of G_{xy} is much poorer than in the one of E_x . This reflects the well known fact that G_{xy} is harder to identify accurately than E_x from a vibration test.

The average performance over 100 repetitions of the identification with randomly simulated experiments is given in Table 3-14. The two methods are comparable for E_x but the Bayesian approach is about 1.9 times more accurate for G_{xy} .

Table 3-14. Average performance for the plate vibration problem with 100 repetitions.

	Mean value (GPa)	Standard deviation (GPa)
Least squares	$E_x = 57.5$; $G_{xy} = 4.26$	For E_x : 0.65 (1.13%) ; for G_{xy} : 0.15 (3.63%)
Bayesian	$E_x = 57.5$; $G_{xy} = 4.26$	For E_x : 0.50 (0.88%) ; for G_{xy} : 0.083 (1.96%)

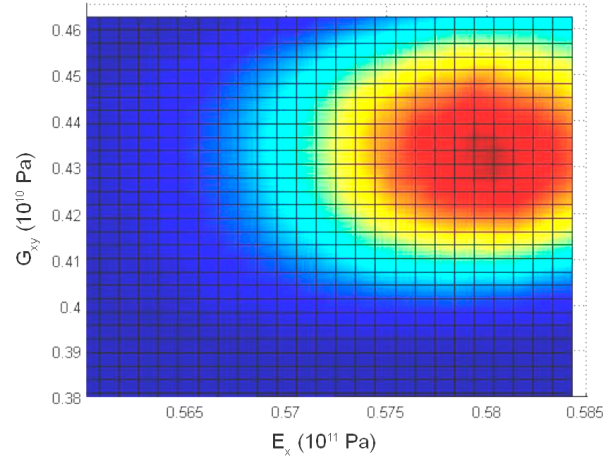


Figure 3-8. Posterior distribution of $\{ E_x, G_{xy} \}$ found with the Bayesian approach

Importance of Handling Multiple Uncertainty Sources

Previous studies on Bayesian identification of elastic constants from natural frequencies (Sol 1986, Marwala and Sibisi 2005, Daghia et al. 2007) considered that the only uncertainty in the problem is measurement error, which was assumed to be normally distributed. In our present work we seek to build a procedure that can also handle uncertainty on other input parameters of the model, such as plate dimensions or plate density in the current example and also, if necessary, handle non-Gaussian measurement error. Accounting only for Gaussian measurement error allows a computationally cheap analytical treatment while accounting for the other uncertainty makes the problem substantially more costly. A question that arises in this case is the following: is the more complex procedure for accounting for other uncertainties worth it? In other words, will accounting for the other uncertainties in the problem make a substantial difference for the identified probability density function?

To answer this question we treat the present identification problem for three cases:

i. Only Gaussian measurement noise on the natural frequencies. We assumed that the noise has a normal distribution with zero mean and a standard deviation of 0.5% of the measured natural frequencies.

ii. Only uncertainty on the input parameters to the vibration model: plate length a , width b , thickness h and density ρ . The uncertainties assumed are those provided in Table 3-11.

iii. Both Gaussian measurement noise and uncertainty on the model input parameters. The uncertainty models are those of the previous two cases respectively.

Case i., with Gaussian measurement noise only, is the most common in Bayesian identification studies. The identified posterior pdf using the Bayesian approach are provided in Figure 3-9 for the three cases.

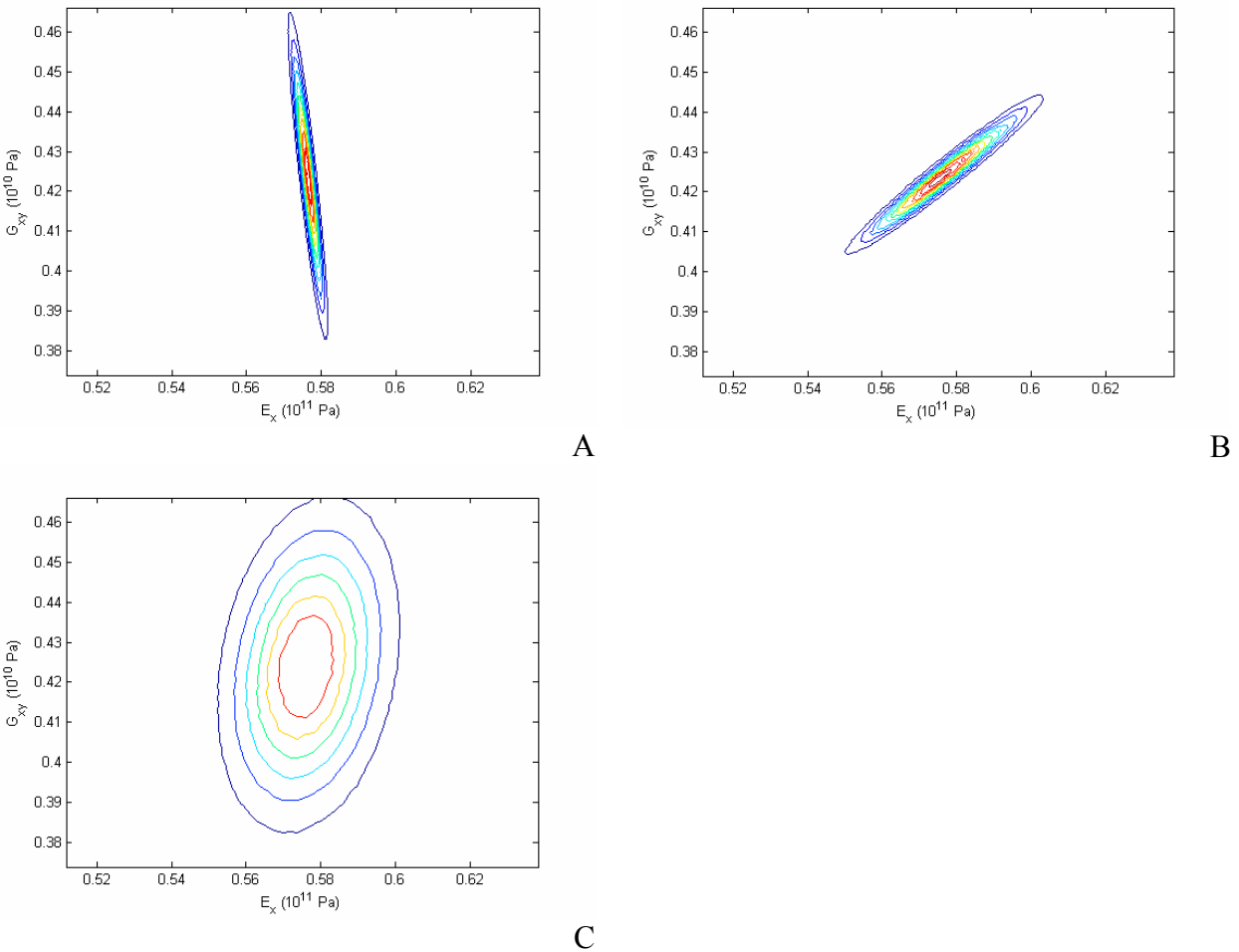


Figure 3-9. Identified posterior pdf for: A) Only Gaussian measurement noise (case i.) B) Only model input parameters uncertainty (case ii.) C) Both Gaussian measurement noise and model input parameters uncertainty (case iii.).

Figure 3-9 shows that the identified pdf differ substantially when only measurement noise is assumed and when only uncertainty on model input parameters is assumed. The third case, where both uncertainties are assumed, is as expected a mix of the two previous ones. It is important to note that the pdf obtained with the combination of the two uncertainties differs substantially from the one with only Gaussian measurement noise thus answering the previous question and illustrating the interest in considering uncertainty in model input parameters as well. Considering only measurement noise would have led on this problem to substantially underestimating the uncertainty in the identified properties.

To confirm the findings of this section we sought a basic physical interpretation based on a simplified model. This interpretation is provided in Appendix C.

As a final note it is worth recalling that the identified probability distribution depends essentially on the physics of the problem on one hand and on the uncertainties considered in the problem on the other. The results of the present section hint towards the identified probability distribution being quite sensitive to the input uncertainties assumed. This means that if the method is to be applied to actual identifications, accurate input uncertainty quantification would be required in order to obtain results which can also provided quantitative rather than mainly qualitative information. Accurate input uncertainty quantification would without a doubt require a significant time and resources investment on actual experiments. If such resources are not available, the identification approach should be applied with conservative uncertainty estimates.

Summary

The present chapter first introduced with a relatively simple, didactic three bar truss identification example the Bayesian approach to identification. The chapter is however more than just an introduction to Bayesian identification.

We compared for two examples two approaches to parameter identification: a basic least squares approach and a statistical approach, the Bayesian method with the aim of identifying situations where the two approaches lead to significantly different results. Using the three bar truss example we identified the following conditions under which the basic least squares method, which is non-statistical, is systematically outperformed by the Bayesian statistical approach: (i) different sensitivity of the response components to the parameters to be identified; (ii) different uncertainty in the measurements; and (iii) high correlation among the measurements. The ratio of the accuracy of the two approaches depends on the specific problem but for the truss problem we illustrated that it can reach a factor of ten when all the effects add up.

We then considered the identification of elastic constants from natural frequencies of a simply supported plate. Using simulated experiments affected by uncertainty in input parameters, measurement noise and model error, we compared the two identification approaches. We found that the Bayesian approach was more accurate, especially for identifying the shear modulus, which is typically a harder to identify property of composite materials. Finally we showed the advantage of a Bayesian procedure that can handle not only measurement error but also uncertainty on other input parameters.

In the next two chapters we continue to analyze the identification problem of orthotropic elastic constants from the natural frequencies of vibrating plates. We move now to an actual identification using real measured natural frequencies. The actual measurements of plate's natural frequencies are usually done on freely hanging plates, since these boundary conditions can be best approached with a numerical model. For these boundary conditions there are no exact analytical solutions so numerical models such as finite elements need to be used. The major issue then in applying a Bayesian approach is computational cost. The vibration problem in the present

chapter already involved about 340 Million function evaluations for the Bayesian approach. It is thus impossible to use finite element solutions directly. In the next chapter we investigate two options for reducing the cost: approximate analytical solutions to the vibration problem and response surface methodology. Then in the following chapter we apply the Bayesian approach to the identification problem using the reduced cost solution retained. Note that while we have seen in the last part of the chapter that the identified distribution can be quite sensitive to the assumed uncertainties, we choose in accordance with the objective of this work to concentrate in the next chapters on making the Bayesian approach computationally tractable for the more complex problems that are considered. The results we would obtain would still provide novel, plausible information, but a more accurate input uncertainty quantification study would be required in order to fully confirm some of the findings.

CHAPTER 4 CHOOSING AN APPROPRIATE FIDELITY FOR THE APPROXIMATION OF NATURAL FREQUENCIES FOR ELASTIC CONSTANTS IDENTIFICATION

Introduction

Plate vibration has been frequently used for identifying elastic constants of a plate (Leissa 1987, Mottershead and Friswell 1993), especially composite laminates. The identification is usually done with free-hanging plates (attached through strings only) in order to avoid difficult-to-model boundary conditions. Bayesian statistical identification approaches have the advantage of handling different sources of uncertainty in the identification procedure as has been shown in the previous chapter. They can also provide confidence intervals and correlation information on the identified properties. However, the Bayesian method can require Monte Carlo simulation which implies large number of vibration calculations for many combinations of the uncertain parameters such as geometry, material parameters, and measurement errors. Numerical solutions for free plate vibration natural frequencies are too slow to be used in such a context. Accordingly there is a need for simple approximate analytical formulas that can be evaluated very quickly.

A simple, closed-form approximate analytical solution for the vibration problem of orthotropic plates with free boundary conditions was proposed by Dickinson (1978). This solution is applicable to wide ranges of geometries and materials, but its accuracy might not be sufficient for identification purpose. The aim of the present chapter is twofold. First we seek to develop a procedure for a high fidelity, analytical, approximate formula for the natural frequencies of free orthotropic plates based on response surface (RS) methodology. To achieve the desired fidelity the response surface method is combined with dimensional analysis. Our second goal is to compare the effect of the approximation fidelity on the identification results. For this purpose we compare the results of a least squares and a Bayesian identification approach

using the high fidelity RS approximation and the low fidelity closed-form frequency approximations. This will allow us to choose between these two approximations the most appropriate one for the present identification. The identification analyses are done using experimental data obtained by Pedersen and Fredriksen (1992). Note that while we use Bayesian identification in this section we will not calculate or analyze the variance co-variance matrix of the identified properties. This will be done with a more complex model in Chapter 5. We also do not compare the least squares and the Bayesian identification in the present chapter, but use them together to determine the effect of the approximation fidelity on the identification results. This helps us in finding what is an appropriate fidelity frequency approximation for use in Chapter 5 in a detailed Bayesian identification.

In the first section we give a quick overview of the approximate analytical solution developed by Dickinson. In the second section we apply dimensional analysis to determine the variables of the response surface approximations (RSA) that lead to the best accuracy. Then we construct the design of experiment for the RSAs and compare their fidelity to finite element analyses and to that of the analytical solution by Dickinson. We then introduce the least squares and Bayesian identification schemes for this problem. We present the identification results using the high and the low fidelity approximations. Finally we provide concluding remarks.

Dickinson's Analytical Approximation

The only simple approximate analytical formula for free vibration of orthotropic plates the authors could find was by Dickinson (1978). He applied characteristic beam functions in Rayleigh's method to obtain an approximate formula for the flexural vibration of specially orthotropic plates. The formula for free boundary conditions on all four edges is provided in Equation 4-1.

$$f_{mn} = \frac{\pi}{2\sqrt{\rho h}} \sqrt{D_{11} \left(\frac{G_m}{a}\right)^4 + 2H_m H_n D_{12} \left(\frac{1}{a}\right)^2 \left(\frac{1}{b}\right)^2 + 4J_m J_n D_{66} \left(\frac{1}{a}\right)^2 \left(\frac{1}{b}\right)^2 + D_{22} \left(\frac{G_n}{b}\right)^4} \quad (4-1)$$

where f_{mn} is the natural frequency of the mode with wave numbers m and n ; ρ is the density of the plate; a , b , h its length, width respectively thickness and D_{ij} the plate flexural rigidities (for detailed expressions of the D_{ij} refer to Grdal et al. (1998)). G_i , H_i , J_i are constants, depending only on the mode numbers m and n , whose expressions are given in Table 4-1.

Note that determining the wave number of an experimentally or numerically obtained mode is not always straightforward. In general the mode number m respectively n can be obtained by adding one to the number of nodal lines perpendicular to the edge x respectively y (i.e. it is the number of half wave length in each direction). There are however exceptions, notably for low mode numbers. For a detailed study of the modes and associated mode numbers of free plates refer to Waller (1939 and 1949).

Table 4-1. Expression of the coefficients in Dickinson's approximate formula (Eq. 4-1) for natural frequencies of free plate

Mode index i	G_i	H_i	J_i
1	0	0	0
2	0	0	1.216
3	1.506	1.248	5.017
$i (i > 3)$	$i - \frac{3}{2}$	$\left(i - \frac{3}{2}\right)^2 \left(1 - \frac{2}{(i-3/2)\pi}\right)$	$\left(i - \frac{3}{2}\right)^2 \left(1 + \frac{6}{(i-3/2)\pi}\right)$

Dickinson's simple analytical expression is computationally inexpensive, thus a priori suitable for use in statistical methods which require its repeated use a large number of times. However the fidelity of the approximation must also be acceptable for use with the considered identification problem. Typically Dickinson's approximation was reported to be within 5% of the exact numerical solution (Blevins 1979). It is not clear whether this accuracy is sufficient when used for identifying accurate elastic constants from vibration experiments. Therefore, in the next

sections we will also develop more accurate response surface approximations of the natural frequencies.

Frequency Response Surface Approximation (RSA)

Determining Nondimensional Variables for the Frequency RSA

For the present problem of elastic constants identification, we propose to construct, based on finite element simulations, polynomial response surface (PRS) approximations of the natural frequencies of the plate in terms of parameters that may have some uncertainty in their values : ρ , a , b , h as well as the four D_{ij} that involve the elastic constants that we seek to identify. We could directly construct a polynomial response surface as a function of these individual model parameters. However, as already mentioned in the second chapter, the accuracy of the RSA is generally improved and the number of required simulations is reduced if the number of variables is reduced by using the nondimensional parameters characterizing the problem (cf. also Kaufman et al. (1996), Vignaux and Scott (1999), Lacey and Steele (2006), Gogu et al. (2007b)). To find these parameters we nondimensionalize the equations describing the vibration of a symmetric, specially orthotropic laminate.

$$\text{Governing equation: } D_{11} \frac{\partial^4 w}{\partial x^4} + 2(D_{12} + 2D_{66}) \frac{\partial^4 w}{\partial x^2 \partial y^2} + D_{22} \frac{\partial^4 w}{\partial y^4} + \rho h \frac{\partial^2 w}{\partial t^2} = 0$$

where w is the out of plane displacement.

Boundary conditions:

On edge $x = 0$ and $x = a$ (denoted $x = 0;a$):

$$M_x = 0 \quad \Leftrightarrow \quad -D_{11} \frac{\partial^2 w}{\partial x^2} \Big|_{x=0;a} - D_{12} \frac{\partial^2 w}{\partial y^2} \Big|_{x=0;a} = 0$$

$$Q_x + \frac{\partial M_{xy}}{\partial y} = 0 \quad \Leftrightarrow \quad -D_{11} \frac{\partial^3 w}{\partial x^3} \Big|_{x=0;a} - (D_{12} + 4D_{66}) \frac{\partial^3 w}{\partial x \partial y^2} \Big|_{x=0;a} = 0$$

On edge $y = 0$ and $y = b$ (denoted $y = 0;b$):

$$M_y = 0 \quad \Leftrightarrow \quad -D_{12} \frac{\partial^2 w}{\partial x^2} \Big|_{y=0;b} - D_{22} \frac{\partial^2 w}{\partial y^2} \Big|_{y=0;b} = 0$$

$$Q_y + \frac{\partial M_{xy}}{\partial x} = 0 \quad \Leftrightarrow \quad -D_{22} \frac{\partial^3 w}{\partial y^3} \Big|_{y=0;b} - (D_{12} + 4D_{66}) \frac{\partial^3 w}{\partial x^2 \partial y} \Big|_{y=0;b} = 0$$

This vibration problem involves 11 variables to which we add the variable of the natural frequencies f_{mn} that we seek, so a total of 12 variables for the problem of determining the plate's natural frequency (see Table 4-2).

Table 4-2. Variables involved in the vibration problem and their units

Variable	f_{mn}	w	x	y	a	b	t	ρh	D_{11}	D_{12}	D_{22}	D_{66}
Unit	$\frac{1}{s}$	m	m	m	m	m	s	$\frac{kg}{m^2}$	$\frac{kg \cdot m^2}{s^2}$	$\frac{kg \cdot m^2}{s^2}$	$\frac{kg \cdot m^2}{s^2}$	$\frac{kg \cdot m^2}{s^2}$

These 12 variables involve 3 dimension groups (m, kg, s). According to the Vaschy-Buckingham theorem (Vaschy 1892, Buckingham 1914) we know that we can have a minimum of $12 - 3 = 9$ nondimensional groups.

Defining $\tau = \sqrt{\frac{\rho h a^4}{D_{11}}}$, which is a characteristic time constant, the 9 nondimensional groups

can be expressed as in Table 4-3.

Table 4-3. Nondimensional parameters characterizing the vibration problem

$\Omega = \frac{w}{h}$	$\theta = \frac{t}{\tau}$	$\xi = \frac{x}{a}$	$\eta = \frac{y}{b}$	$\gamma = \frac{a}{b}$
$\Psi_{mn} = \tau f_{mn}$	$\Delta_{12} = \frac{D_{12}}{D_{11}}$	$\Delta_{22} = \frac{D_{22}}{D_{11}}$	$\Delta_{66} = \frac{D_{66}}{D_{11}}$	

As function of these nondimensional variables the vibration problem can be written as follows:

Governing equation:
$$\frac{\partial^4 \Omega}{\partial \xi^4} + 2(\Delta_{12} + 2\Delta_{66})\gamma^2 \frac{\partial^4 \Omega}{\partial \xi^2 \partial \eta^2} + \Delta_{22}\gamma^4 \frac{\partial^4 \Omega}{\partial \eta^4} + \frac{\partial^2 \Omega}{\partial \theta^2} = 0$$

Boundary conditions:

On edge $\xi = 0$ and $\xi = 1$ (denoted $\xi = 0;1$):

$$-\frac{\partial^2 \Omega}{\partial \xi^2} \Big|_{\xi=0;1} - \Delta_{12}\gamma^2 \frac{\partial^2 \Omega}{\partial \eta^2} \Big|_{\xi=0;1} = 0$$

$$-\frac{\partial^3 \Omega}{\partial \xi^3} \Big|_{\xi=0;1} - (\Delta_{12} + 4\Delta_{66})\gamma^2 \frac{\partial^3 \Omega}{\partial \xi \partial \eta^2} \Big|_{\xi=0;1} = 0$$

On edge $\eta = 0$ and $\eta = 1$ (denoted $\eta = 0;1$):

$$-\Delta_{12} \frac{\partial^2 \Omega}{\partial \xi^2} \Big|_{\eta=0;1} - \Delta_{22}\gamma^2 \frac{\partial^2 \Omega}{\partial \eta^2} \Big|_{\eta=0;1} = 0$$

$$-\Delta_{22}\gamma^3 \frac{\partial^3 \Omega}{\partial \eta^3} \Big|_{\eta=0;1} - (\Delta_{12} + 4\Delta_{66})\gamma \frac{\partial^3 \Omega}{\partial \xi^2 \partial \eta} \Big|_{\eta=0;1} = 0$$

For finding an RSA of the nondimensional natural frequency Ψ_{mn} , we are not interested in the vibration mode shapes and we do not need the nondimensional out-of-plane displacement Ω , nor the nondimensional time θ , nor the nondimensional coordinates ξ and η . This means that the nondimensional natural frequency Ψ_{mn} can be expressed as a function of only four nondimensional parameters $\Psi_{mn} = \Psi_{mn}(\Delta_{12}, \Delta_{22}, \Delta_{66}, \gamma)$.

Note that rewriting the analytical approximation of Equation 4-1 in its nondimensional form leads to a polynomial function of the nondimensional parameters:

$$(\psi_{mn})^2 = \frac{\pi^2}{4} (G_m^4 + 2H_m H_n \Delta_{12} \gamma^2 + 4J_m J_n \Delta_{66} \gamma^2 + \Delta_{22} \gamma^4 G_n^4) \quad (4-2)$$

Equation 4-2 is a cubic polynomial in Δ_{12} , Δ_{22} , Δ_{66} and γ^2 . We therefore expressed the squared nondimensional frequency as a cubic polynomial response surface (PRS) in terms of

these four variables. Such a PRS has 31 additional polynomial terms beyond those in those in Equation 4-2, that can potentially increase the fidelity of the response surface approximation.

RSA Construction Procedure

To fit the RSA we need to sample points in the four-dimensional space of the nondimensional parameters. For details on the methodology for polynomial response surface construction the reader can refer to Appendix A. The ranges of the sampling space depend on the application, and we selected experiments carried out by Pedersen and Fredriksen (1992) for comparing the analytical and RS approximations.

If we sample in the nondimensional variables directly, it would be difficult however to deduce values for the dimensional variables needed for the FE model (E_1 , E_2 , ν_{12} , G_{12} , a , b , h and ρ). Accordingly we chose the following procedure to obtain the points in the nondimensional space and their corresponding dimensional parameters:

i. Sample N_i points (5000 points here) in the eight dimensional-variables space $\{E_1, E_2, \nu_{12}, G_{12}, a, b, h, \rho\}$ with uniform Latin Hypercube sampling within the bounds considered for the problem.

ii. Out of the N_i points extract N_s (typically 250 points here) in the nondimensional space by maximizing the minimum (max-min) distance between any two points. The Matlab routines from the Surrogates ToolBox (Viana and Goel 2008) were used. These steps ensure that the points are well distributed (space-filling) in the nondimensional space.

Figure 4-1 illustrates this procedure in a two-dimensional case with Δ_{12} and γ only. The blue crosses are representative of the N_i points sampled in step i. The red circles are representative of the N_s points selected in step two. Because we stopped the max-min search after 100,000 iterations (to keep computational cost reasonable) we might not have gotten the absolute maximum, but this is not required for good accuracy of the RSA.

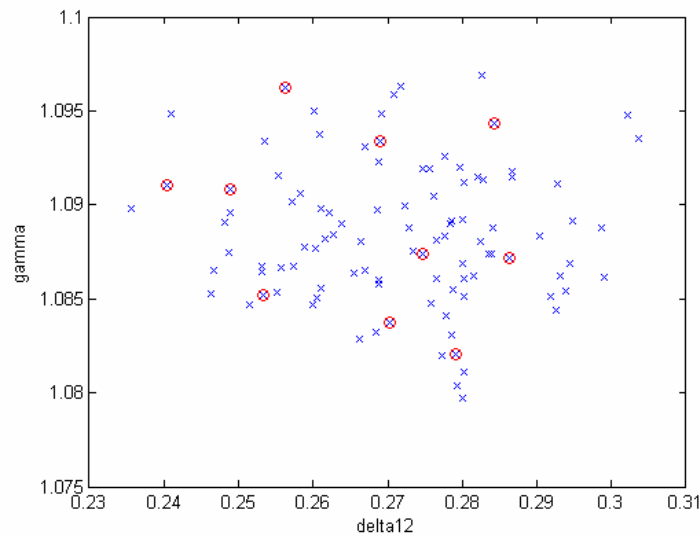


Figure 4-1. Illustration of the procedure for sampling points in the nondimensional space.

Frequency RSA Results

The frequency RSA is fitted to finite element (FE) simulations of the plate using Abaqus[®] commercial FE software. We used 400 thin plate elements (S8R5) to model the composite plate.

The bounds on the variables given in Table 4-4 were chosen with the elastic constants identification problem in mind, based on experiments from Pedersen and Frederiksen (1992). The plate considered was a glass-epoxy composite panel with stacking sequence $[0,-40,40,90,40,0,90,-40]_s$. In our case the RSA would be used to carry out least squares and Bayesian identification approaches for the material properties. The bounds ranges on the elastic constants encompass a fairly wide region in which we'd expect to find the identified properties. The ranges on the other input parameters (geometry and plate density), which are somewhat narrower, were chosen such as to allow accounting for uncertainties in the Bayesian approach and to allow future applicability of the RSA to slightly different plates.

We decided to construct two sets of RSAs with two different bounds. This is because we found that we can use somewhat narrower bound for the Bayesian identification RSAs without this

compromising the results. This behaviour is most likely due, as will be shown later, to the fact that the least squares identification problem is more ill-conditioned than the Bayesian problem. Table 4-4 presents the wide bounds (denoted WB) used for constructing the first RSA, that will be used for least squares based identification.

Table 4-4. Wide Bounds on the model input parameters (denoted WB)

	E_1 (GPa)	E_2 (GPa)	ν_{12}	G_{12} (GPa)	a (mm)	b (mm)	h (mm)	ρ (kg/m ³)
Low bound	43	15	0.2	7	188	172	2.2	1800
High bound	80	28	0.36	13	230	211	3.0	2450

We constructed a cubic polynomial response surface (PRS) approximation for each of the first ten squared nondimensional natural frequencies as a function of the nondimensional parameters determined previously. We used the procedure described in the previous section with $N_s = 250$ sampling points within the bounds WB. The response surface approximations fitted through these 250 points are denoted RSA_{WB}.

To test the accuracy of the RSAs we tested them at an additional 250 finite element points (denoted P250), sampled using the same procedure as described in the previous section, using the bounds given in Table 4-4. The results are given in Table 4-5, f_i being the dimensional frequencies in order of increasing frequency values. The reader can also refer to Table 4-9 to get an idea of the order of magnitude of the different frequencies.

Table 4-5. Mean and maximum relative absolute error of the frequency RSA predictions (denoted RSA_{WB}) compared at 250 test points

Abs. Error (%)	f_1	f_2	f_3	f_4	f_5	f_6	f_7	f_8	f_9	f_{10}
mean	0.033	0.548	0.290	0.032	0.038	0.680	0.667	0.583	1.110	0.590
max	0.175	4.197	1.695	0.140	0.195	5.219	5.610	3.680	7.834	7.498

For comparison purpose we also provide in Table 4-6 the error of the analytical frequency approximation of Equation 4-1 compared at these same 250 test points.

Table 4-6. Mean and maximum relative absolute error of the analytical formula frequency predictions compared at 250 test points

Abs. Error (%)	f_1	f_2	f_3	f_4	f_5	f_6	f_7	f_8	f_9	f_{10}
mean	5.98	8.50	3.47	4.28	7.22	4.68	2.77	5.72	5.75	1.22
max	6.54	16.28	8.06	9.43	23.32	21.11	18.30	10.28	12.05	10.01

The average error in the analytical approximation over the first ten frequencies was found to be 4.9%. This is consistent with previous studies (Blevins 1979) which reported the error of using the analytical formula to be about 5%. On the other hand the errors in the RSAs are about an order of magnitude lower.

The second RSA set we construct is for the narrower bounds given in Table 4-7. These are sufficient for the Bayesian identification given the range of uncertainties that we will consider (see next section).

Table 4-7. Narrow bounds on the model input parameters (denoted NB)

	E_1 (GPa)	E_2 (GPa)	ν_{12}	G_{12} (GPa)	a (mm)	b (mm)	h (mm)	ρ (kg/m ³)
Low bound	52	18	0.23	8.3	202	185	2.55	2000
High bound	70	25	0.32	11	216	200	2.65	2240

Cubic PRS were again fitted for each of the first ten nondimensional natural frequencies using the procedure described in the previous section with $N_s = 200$ finite element simulations. We used slightly less sampling points here because of the narrower bounds (denoted NB). The RSA fidelity was tested at 250 additional points sampled within the bounds of Table 4-7. The results are presented in Table 4-8.

Table 4-8. Mean and maximum relative absolute error of the frequency RSA predictions (denoted RSA_{NB}) compared at 250 test points

Abs. Error (%)	f_1	f_2	f_3	f_4	f_5	f_6	f_7	f_8	f_9	f_{10}
mean	0.004	0.004	0.003	0.005	0.004	0.003	0.003	0.005	0.006	0.005
max	0.021	0.033	0.030	0.016	0.020	0.016	0.010	0.017	0.061	0.041

For these narrower bounds the RSA fidelity achieved was excellent, the mean of the error among the 250 test points being smaller than 0.01% for all the frequencies. The maximum error among the 250 test points was found to be only about 0.06% for the 9th frequency.

We need to mention at this point that in order to obtain the good quality of the fit for all ten frequency RSAs astute modeling was required. Indeed, initially the RSAs for the frequencies number four to seven were very poor both for the wide and the narrow bounds. Typical values for these frequencies are as in Table 4-9. We can see that frequencies four and five are relatively close as are six and seven. This is because the corresponding modes are symmetric relatively to the x and y axis and the aspect ratio of the plate is close to one. For each of the 200 sampling points the dimension parameters vary slightly and for some of these points the two symmetric modes switch, meaning that the x-symmetric mode becomes lower in frequency than the y-symmetric mode for some points and not for others. This issue of switching modes was resolved by modeling only half of the plate and using symmetry boundary conditions for constructing the RSA for frequencies four to seven. Using X- or Y-symmetry boundary conditions allowed to follow the same mode for varying plate parameters.

Identification Schemes

We use the low fidelity analytical approximate solution and high fidelity frequency RSAs in two different material properties identification schemes in order to compare the effect of the approximation error on the identified results.

The identification procedure seeks the four orthotropic ply elastic constants (E_1 , E_2 , ν_{12} , and G_{12}) of a glass/epoxy composite based on the first ten natural frequencies of a [0,-40,40,90,40,0,90,-40]_s laminate vibrating under free boundary conditions. We use the values measured by Pedersen and Frederiksen (1992) as experimental frequencies in the identification

procedure. For convenience these measured frequencies are also given in Table 4-9 and the plate properties and dimensions in Table 4-10.

Table 4-9. Experimental frequencies from Pedersen and Frederiksen (1992)

Frequency	f_1	f_2	f_3	f_4	f_5	f_6	f_7	f_8	f_9	f_{10}
Value (Hz)	172.5	250.2	300.6	437.9	443.6	760.3	766.2	797.4	872.6	963.4
Mode (n,m)	(2,2)	(3,1)	(1,3)	(2,3)	(3,2)	(1,4)	(4,1)	(3,3)	(2,4)	(4,2)

Table 4-10. Plate properties: length (a), width (b), thickness(h) and density (ρ)

Parameter	a (mm)	b (mm)	h (mm)	ρ (kg/m ³)
Value	209	192	2.59	2120

The first identification scheme is a basic least squares approach. The identified parameters correspond to the minimum of the following objective function:

$$J(\mathbf{E}) = \sum_{i=1}^m \left(\frac{f_i^{num}(\mathbf{E}) - f_i^{measure}}{f_i^{measure}} \right)^2 \quad (4-3)$$

where $\mathbf{E} = \{E_1, E_2, \nu_{12}, G_{12}\}$, $f_i^{measure}$ is the i^{th} experimental frequency from Table 4-9 and f_i^{num} is a numerical frequency prediction.

The second identification scheme is a Bayesian approach. It seeks the probability density function of the material properties given the test results. This distribution can be written as:

$$\pi_{\mathbf{E}|f=f^{measure}}(\mathbf{E}) = \frac{1}{K} \pi_{f|E}(\mathbf{f}^{measure}) \cdot \pi_{\mathbf{E}}^{prior}(\mathbf{E}) \quad (4-4)$$

where π denotes a probability density function (pdf), $\mathbf{E} = \{E_1, E_2, \nu_{12}, G_{12}\}$ is the four dimensional random variable of the elastic constants, $\mathbf{f} = \{f_1 \dots f_{10}\}$ the ten dimensional random variable of the frequencies measurement prediction and $\mathbf{f}^{measure} = \{f_1^{measure} \dots f_{10}^{measure}\}$ the vector of the ten measured natural frequencies. $\pi_{\mathbf{E}}^{prior}(\mathbf{E})$ is the pdf of \mathbf{E} prior to the measurements and $\pi_{f|E}(\mathbf{f}^{measure})$ is also called the likelihood function of \mathbf{E} given the measurements $\mathbf{f}^{measure}$.

As prior distribution for the properties we assumed a truncated, uncorrelated normal distribution characterized by the parameters in Table 4-11. This is a wide prior distribution corresponding to the fact that we have only vague prior information about the properties. The distribution was truncated at the bounds given in Table 4-12.

Table 4-11. Normal uncorrelated prior distribution of the material properties

Parameter	E_1 (GPa)	E_2 (GPa)	ν_{12}	G_{12} (GPa)
Mean value	60	21	0.28	10
Standard deviation	10	5	0.05	1.5

Table 4-12. Truncation bounds on the prior distribution of the material properties

Parameter	E_1 (GPa)	E_2 (GPa)	ν_{12}	G_{12} (GPa)
Low truncation bound	42	11	0.2	7
High truncation bound	78	31	0.36	13

The mean or most likely values of the posterior distribution given in Equation 4-4 are usually taken as the identified property. We have shown in Chapter 3 that for a similar vibration problem the Bayesian identification is generally more accurate than the basic least squares method. The difference between the two approaches depends, however, on the problem and can range from negligible to significant.

Sources of uncertainty affecting the identification

As illustrated in the Chapter 3 the Bayesian identification can account for different sources of uncertainty. We considered here that three sources of uncertainty are present.

First we assumed normally distributed measurement uncertainty for the natural frequencies. Then we assumed epistemic uncertainty due to modeling error. Since this uncertainty depends on the numerical model considered its implementation will be described in later sections.

Finally we considered uncertainties on the input parameters to the vibration model. Apart from the four material properties, the thin plate model also involves four other parameters: the plate length, width and thickness (a , b and h) and the plate density ρ . These parameters are measured beforehand and are known only with a certain confidence. We assumed these uncertainties to be normally distributed as shown in Table 4-13.

Table 4-13. Assumed uncertainties in the plate length, width, thickness and density (a , b , h and ρ). Normal distributions are considered.

Parameter	a (mm)	b (mm)	h (mm)	ρ (kg/m ³)
Mean value	209	192	2.59	2120
Standard deviation	0.25	0.25	0.01	10.6

Identification Using the Response Surface Approximation

As mentioned earlier the least squares identification will use the RSAs with wide bounds (denoted RSA_{WB}) while the Bayesian identification will use the RSAs with narrow bounds (denoted RSA_{NB}).

Least Squares Identification

The least squares (LS) optimization was carried out using Matlab's *lsqnonlin* routine without imposing any bounds on the variables and led to the optimum shown in Table 4-14. Note that Pedersen and Frederiksen (1992) applied a least squares approach coupled directly to a Rayleigh-Ritz numerical code to identify the elastic constants. The properties that they found are denoted as "literature" values in Table 4-14.

Table 4-14. LS identified properties using the frequency RSA_{WB}

Parameter	E_1 (GPa)	E_2 (GPa)	ν_{12}	G_{12} (GPa)
Identified values	60.9	22.7	0.217	9.6
Literature values (from Pedersen and Frederiksen 1992)	61.3	21.4	0.279	9.8

For our identification results the residuals between the RSA frequencies at the optimal points and the experimental frequencies are given in Table 4-15. They are relatively small and the identified values are also reasonably close to the literature values. This means that the accuracy of the RSA_{WB} is good enough to lead to reasonable results.

Table 4-15. Residuals for LS identification using the frequency RSAs. $J(\mathbf{E}) = 1.7807 \cdot 10^{-4}$.

Frequency	f_1	f_2	f_3	f_4	f_5	f_6	f_7	f_8	f_9	f_{10}
Residual (%)	0.11	-0.60	0.09	0.88	-0.25	0.30	-0.18	0.38	-0.46	-0.30

Bayesian Identification

The Bayesian model using the frequency RSAs considered the following uncertainty on the natural frequencies. Additive normal uncertainty was assumed to stem from the inaccuracies in the experimental frequency measurement. We considered a zero mean and a standard deviation varying linearly between 0.5% for the lowest frequency and 0.75% for the highest. This leads to the error model shown in Equation 4-5.

$$f_m = f_m^{RSA} (1 + u_m) \text{ where } u_m \square N \left[0, \left(0.0075 \frac{(m-1)}{10-1} - 0.005 \frac{(m-10)}{10-1} \right)^2 \right] \quad (4-5)$$

The likelihood function and the posterior probability density function (pdf) of the material properties were calculated using Equation 4-4. This calculation required about 130 million frequency calculations thus motivating the need for fast to evaluate analytical frequency approximations (in contrast least squares based identification usually requires between 100 and 100,000 evaluations, depending on the conditioning of the problem). The most likely point of the posterior pdf is given in Table 4-16. The “literature values” by Pedersen and Frederiksen (1992) are also provided in Table 4-16.

Table 4-16. Most likely point of the posterior pdf using the frequency RSA_{NB}

Parameter	E_1 (GPa)	E_2 (GPa)	ν_{12}	G_{12} (GPa)
Identified values	61.6	20.3	0.280	10.0
Literature values (from Pedersen and Frederiksen 1992)	61.3	21.4	0.279	9.8

The Bayesian identified values are fairly close to the literature values and also relatively close to the values identified with the RSA based least squares approach in Table 4-14. Note that the literature values by Pedersen and Frederiksen (1992) are a good comparison point, but this does not mean these are the true values. The true values are probably close but the reference article did not calculate any uncertainty measure (such as confidence intervals). The Bayesian method can on the other hand provide an estimated confidence interval based on the posterior pdf. We have shown on the vibration example problem in Chapter 3 that the Bayesian most likely point is on average closer to the true values than the least squares estimate.

All in all, using the response surface approximations in the identification schemes leads to reasonable results which are in agreement with the literature values, whether using the least squares or the Bayesian identification method. This is not surprising since the RSAs have good accuracy allowing both methods to unfold properly.

In the next section we investigate the identification results obtained with the lower fidelity analytical approximate solution (Dickinson 1978). This could lead to more significant differences between the two identification methods.

Identification Using Dickinson's Analytical Approximate Solution

Least Squares Identification with Bounds

Using Dickinson's analytical approximate solution, the least squares (LS) optimization was carried out first while imposing bounds on the variables. We imposed on E_1 , E_2 , ν_{12} , and G_{12} the bounds given in Table 4-7, which seem reasonable for the properties that we are seeking. The

results of the optimization are given in Tables 4-17 and 4-18. The norm of the residuals (i.e. the value of the objective function) is $J(\mathbf{E}) = 0.019812$.

Table 4-17. LS identified properties using the analytical approximate solution (bounded variables)

Parameter	E_1 (GPa)	E_2 (GPa)	ν_{12}	G_{12} (GPa)
Identified values	52.0	25.0	0.298	8.3
Literature values (from Pedersen and Frederiksen 1992)	61.3	21.4	0.279	9.8

Table 4-18. Residuals for LS identification using the analytical approximate solution. Residuals' norm $J(\mathbf{E}) = 0.019812$.

Frequency	f_1	f_2	f_3	f_4	f_5	f_6	f_7	f_8	f_9	f_{10}
Residual (%)	-1.27	7.06	-6.84	1.64	-1.37	-2.91	0.72	1.77	6.19	-6.70

We can note that several variables hit the bounds. We could keep these results since the bounds we imposed are quite wide and from a physical point of view it is quite unlikely that the true parameters lie outside the bounds. We wanted however to also know what happens when imposing no bounds at all and the corresponding results are provided in the next subsection.

Least Squares Identification without Bounds

The least squares optimization is carried out again without imposing any bounds. The optimum found is given in Table 4-19. The residuals between the frequencies at the optimal points and the experimental frequencies are given in Table 4-20. The norm of the residuals (i.e. the value of the objective function) is $J(\mathbf{E}) = 0.019709$.

Table 4-19. LS identified properties using the analytical approximate solution (unbounded variables)

Parameter	E_1 (GPa)	E_2 (GPa)	ν_{12}	G_{12} (GPa)
Identified values	71.1	46.2	-0.402	-17.1
Literature values (from Pedersen and Frederiksen 1992)	61.3	21.4	0.279	9.8

Table 4-20. Residuals for LS identification using the analytical approximate solution. Residuals' norm $J(\mathbf{E}) = 0.019709$.

Frequency	f_1	f_2	f_3	f_4	f_5	f_6	f_7	f_8	f_9	f_{10}
Residual (%)	-1.24	6.96	-6.77	1.69	-1.38	-3.00	0.79	1.48	6.25	-6.75

It is obvious from the identified results that the optimum found is not plausible. Not only are the parameters quite far away from the literature values but the Poisson's ratio and shear modulus have negative values. While a negative Poisson's ratio could be physically possible, negative shear modulus has no physical meaning.

What is more surprising however is that in spite of the implausible optimum the residuals are not very large. All are of the order of a few percent, which for recall is also the order of the accuracy of the analytical approximate solution compared to finite element analyses (see Table 4-6). It is also worth noting that the residuals and their norm remain practically unchanged compared to the bounded optimization (Table 4-18). This is a sign of the ill-conditioning of the least squares problem due to a very flat objective function around the optimum. It hints that the accuracy of the frequency approximation has a large effect on the identified results and while a few percent error might seem very reasonable for some application, it can lead to extremely poor results when applied to the present identification problem.

Summing up, the least squares identification with the low fidelity analytical approximation leads to significantly worse results (independently whether bounded or unbounded) than the same identification using the high fidelity response surface approximations.

Bayesian Identification

The Bayesian model using the analytical approximate solution considered the following uncertainty on the natural frequencies. The uncertainty was assumed to have two sources. The first is due to the inaccuracy in the analytical approximation. The error in the formula was shown

in Table 4-6 to be typically of the order of 5% so a normally distributed uncertainty with standard deviation of 5% was assumed. A second additive uncertainty was assumed to stem from the inaccuracies in the experimental measurement of the natural frequencies. As before this uncertainty was assumed normal, with the standard deviation varying linearly between 0.5% for the lowest frequency and 0.75% for the highest. This leads to the error model shown in Equation 4-6.

$$f_m = f_m^{RSA} (1 + u_m) \text{ where } u_m \sim N \left[0, 0.05^2 + \left(0.0075 \frac{(m-1)}{10-1} - 0.005 \frac{(m-10)}{10-1} \right)^2 \right] \quad (4-6)$$

The likelihood function and the posterior probability density function (pdf) of the material properties were calculated using Equation 4-4. The most likely point of the posterior pdf is given in Table 4-21.

Table 4-21. Most likely point of the posterior pdf using the analytical approximate solution.

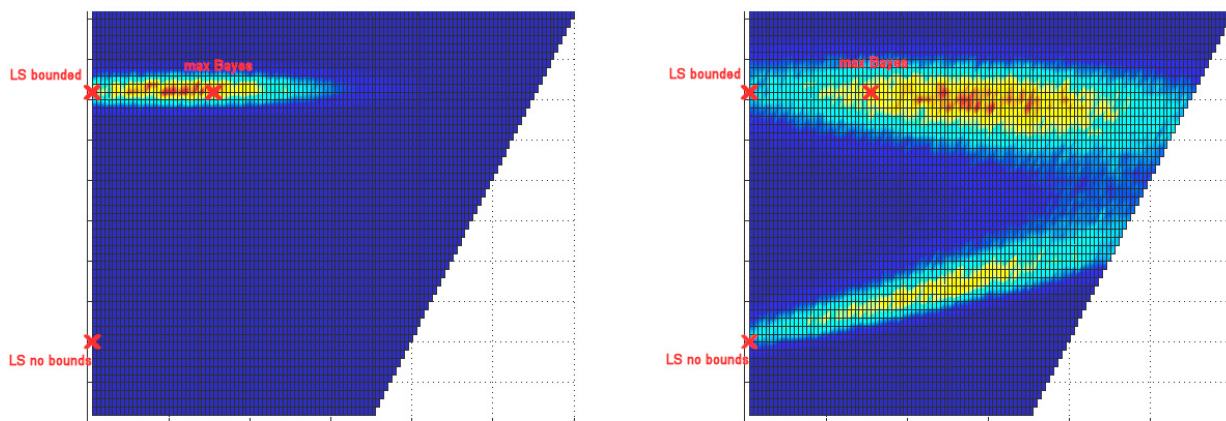
Parameter	E ₁ (GPa)	E ₂ (GPa)	ν ₁₂	G ₁₂ (GPa)
Identified values	47.2	27.6	0.29	9.4
Literature values (from Pedersen and Frederiksen 1992)	61.3	21.4	0.279	9.8

The results of the Bayesian identification obtained with low fidelity analytical approximations are again significantly worse than the results obtained using the Bayesian identification with the high fidelity response surface approximations (see Table 4-16). This illustrates again the importance of having high fidelity frequency approximations in order to obtain accurate identification results for this vibration based problem.

On a side note we see that in spite of using the approximate analytical frequency solution, which led to very poor results with the least squares formulation, the Bayesian approach identified properties that are physically plausible, though still very far from the literature values.

Graphical Comparison of the Identification Approaches with the Low Fidelity Approximation

To provide a better understanding of what is happening in the two identification approaches when using the low fidelity approximate analytical solution we plot the posterior pdf and the least squares (LS) objective function in a representative plane. Note that both functions are four dimensional thus problematic to represent graphically. To obtain a meaningful representation of these functions we decided to plot them in the two dimensional plane defined by the following three characteristic points of the problem: the LS bounded optimum, the LS unbounded optimum and the most likely point of the posterior pdf (see Tables 4-16, 4-18 and 4-20 respectively for the coordinates of these points). The posterior pdf as well as the likelihood function of the material properties are represented in Figure 4-2. For comparison purposes the least squares objective function is also represented in this same plane in Figure 4-3. Note that for representing the posterior pdf in this section we removed the truncation bounds on the prior distribution (i.e. we considered a purely Gaussian prior). The truncation would have further narrowed the posterior pdf.



A

B

Figure 4-2. Two dimensional representation in a three point plane of: A) The posterior pdf. B) The likelihood function.

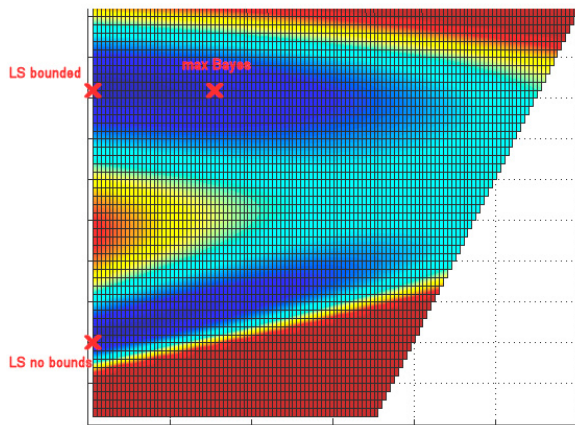


Figure 4-3. Two dimensional representation in a three point plane of the least squares objective function

Figure 4-2-B shows that the likelihood function might be multimodal since the distribution function has a local peak in the bottom half of the image. Note that we cannot claim with certainty that the function is multimodal because we do not know what is happening in the other two dimensions not represented in the plot. The small local peak is relatively far away from the area of physically reasonable properties around the points *max Bayes* and *LS bounded*. The global most likely point of the likelihood function is however much closer to this area, which is reassuring.

Figure 4-2-A shows the posterior pdf, that is, the distribution obtained by multiplying the likelihood function by the prior distribution. The prior distribution had the effect of killing the local peak and significantly narrowing down the distribution. This is somewhat unusual because we assumed a relatively wide prior distribution which in a typical identification problem is expected to have little impact on the results. It is due however to the ill-posedness of the problem which manifested itself in the least square results as well.

Note that on Figure 4-2-A the point denoted *max Bayes* does not perfectly correspond with the center of the distribution. This is due to the fact that only 1000 Monte Carlo simulations were

used in the Bayesian approach in order to keep a reduced computational cost. The effect is a relatively noisy likelihood function and posterior pdf, which slightly offset the estimate of the posterior pdf maximum but don't affect the qualitative conclusions. If the aim would be to accurately identify the posterior distribution more simulations would have to be used.

Figure 4-3 shows the objective function of the least squares identification plotted in the same three points plane. As calculated in Tables 4-17 and 4-19 the two points *LS bounded* and *LS no bounds* have a very close value of the objective function. *LS no bounds* has however a slightly lower objective function value, thus making it the minimum among the two. Of course in reality the point is physically implausible, which is because the problem is ill-posed. By ill-conditioned we mean that the two points *LS bounded* and *LS no bounds*, while being very far away from each other in the moduli space, lead to a very close value of the objective function. It is not a local minimum though because the LS algorithm moves continuously from the optimum *LS bounded* to the optimum *LS no bounds*. The continuous path is likely to be in the other two dimensions that are not represented graphically in the Figure 4-3.

We can note that there are similarities in shape between the least squares objective function of Figure 4-3 and the likelihood function of Figure 4-2-B. This would be expected since the two are based on the same analytical approximate solution for the frequency calculations, so errors in this approximation would affect the two approaches. However apart from being somewhat shifted, the major difference between the two is that while the LS objective function has the overall minimum in the lower lobe, the likelihood function has the most likely point in the upper lobe, which from a physical point of view is much more plausible. This shows that while the two approaches are affected by the poor accuracy of the analytical frequency approximation, the Bayesian method handles this significantly better than the basic least squares method.

Summary

In the first part of this chapter a procedure was detailed for obtaining polynomial response surface approximations (RSA) for the natural frequencies of a vibrating orthotropic plate. The RSA achieved high accuracy, allowing them to be used in most applications that require fast function evaluations together with high fidelity, such as Monte Carlo simulation for Bayesian identification analysis. The RSAs constructed were between one and two orders of magnitudes more accurate than an existing approximate analytical formula due to Dickinson for vibration of free orthotropic plates. To achieve such high fidelity the RSAs were fitted to the nondimensional parameters characterising the vibration problem.

Note that the overall procedure is applicable not only to free but any boundary conditions as long as the RSAs are refitted to the corresponding design of experiments in terms of the nondimensional parameters characterizing the vibration problem with the specific boundary conditions.

In the second part we showed that for the material properties identification problem we consider the fidelity of the frequency approximation had significant impact on the identified material properties. The high fidelity nondimensional frequency RSAs led to reasonable results with both least squares and Bayesian identification schemes.

The lower fidelity frequency approximations due to Dickinson (1978) led to unreasonable identification results. Using a least squares approach led in our case to physically implausible results. The Bayesian approach, while obtaining physically reasonable results, also performed significantly worse than the identification with high fidelity approximations.

In the next chapter we will investigate in more details the Bayesian approach applied to the problem of orthotropic elastic constants identification from vibrating plates using the experimental data from Pedersen and Frederiksen (1992). We already used these experiments in

the present chapter for a basic Bayesian identification where all the uncertainties in the problem (on measurement and input parameters) were normally distributed. The main goal here was to investigate the difference between low and fidelity approximations in identification. In the next chapter the focus will be on the additional capabilities that the Bayesian identification allows. We will thus construct a more complex uncertainty model which handles systematic modelling errors as well as non-Gaussian uncertainties. We will also analyse in details the identified probability density function characterizing it by variance and correlation coefficients. In the entire next chapter we will use for the Bayesian identification the high fidelity response surface approximation that we constructed here.

CHAPTER 5
BAYESIAN IDENTIFICATION OF ORTHOTROPIC ELASTIC CONSTANTS
ACCOUNTING FOR MEASUREMENT ERROR, MODELLING ERROR AND
PARAMETER UNCERTAINTY

Introduction

Accurate determination of the orthotropic mechanical properties of a composite material has always been a challenge to the composites community. This challenge is threefold: designing the most appropriate experiment for determining the properties sought, handling inherent uncertainties in the experiment and modeling of the experiment and finally estimating and controlling the uncertainty with which the properties are determined.

The design of an experiment for identifying the four in-plane elastic constants of an orthotropic material as accurately as possible has been a rich area of investigation (e.g. Kernevez et al. 1978, Rouger et al. (1990), Grediac and Vautrin 1990, Arafeh et al. 1995, Vautrin 2000, Le Magorou et al. 2000, 2002). Vibration testing is considered as an effective experimental method for this purpose. This technique was introduced by De Wilde et al. (1984, 1986) and Deobald and Gibson (1986) in the context of determining the elastic constants of a composite. These studies involved measuring the natural frequencies of a freely hanging composite plate, frequencies which were used for identifying the four elastic constants of the laminate using model updating. Some of the advantages of vibration testing are outlined in De Wilde et al. (1984, 1986), Deobald and Gibson (1986), Grediac and Paris (1996), Grediac et al. (1998a), Gibson (2000). These advantages include single test of nondestructive nature and determination of homogenized properties as opposed to local properties using strain gauges. Note however that identification from vibration usually leads to more accurate results with laminate properties rather than ply properties. In the present study we limit the discussion to vibration testing and focus on the two remaining points relative to handling uncertainty.

In identifications using a single test to determine all four elastic constants it is often observed that the different material properties are not obtained with the same confidence. Typically the shear modulus and the Poisson's ratio are known with significantly less accuracy from a vibration test for example. Accordingly, estimating the uncertainty with which a property is determined can be of great interest. A possible natural representation of this uncertainty is through the joint probability density function of the properties which provides not only estimates of uncertainty in the properties (variances) but also estimates of the correlation between them (covariances).

Determining the uncertainty in the output values (identified properties) requires however some knowledge of the uncertainty in the input (measurement errors, model errors). Indeed multiple sources of uncertainties are present which have an effect on the identification. First there is the uncertainty in the measured frequencies. Furthermore there are uncertainties on the input parameters of the model (e.g. dimensions and density of the plate). Finally there is uncertainty in the ability of the model to predict the actual experiment. These uncertainties should be taken into account when identifying the material properties.

The aim of the present chapter is then to identify the probability distribution of the four orthotropic ply elastic constants of a thin composite laminate from natural frequency measurements using a Bayesian approach which can handle all three previously discussed uncertainties: measurement uncertainties on the natural frequencies, uncertainty on the other input parameters involved and modeling uncertainty.

In a first section we describe the vibration problem that serves for material properties identification. We then provide a detailed description of the Bayesian identification procedure.

Finally we give the Bayesian identification results. We close the chapter with concluding remarks.

Vibration Problem

The vibration problem is the one presented in the previous Chapter using data from Pedersen and Frederiksen (1992). The problem is briefly summarized again in this section for convenience. We seek the four in-plane ply-elastic constants of a thin composite laminate: E_1 , E_2 , G_{12} and ν_{12} . As in the previous chapter we use again the experimental measurements obtained by Pedersen and Frederiksen (1992), who measured the first ten natural frequencies of a thin glass/epoxy composite laminate with a stacking sequence of $[0,-40,40,90,40,0,90,-40]_s$, which for convenience are provided again in Table 5-1. The rectangular plate dimensions (length a , width b and thickness h) are given again in Table 5-2. The plate was attached by two strings which were assumed to be modeled appropriately by free boundary conditions.

Table 5-1. Experimental frequencies from Pedersen and Frederiksen (1992).

Frequency	f_1	f_2	f_3	f_4	f_5	f_6	f_7	f_8	f_9	f_{10}
Value (Hz)	172.5	250.2	300.6	437.9	443.6	760.3	766.2	797.4	872.6	963.4

Table 5-2. Plate properties: length (a), width (b), thickness(h) and density (ρ).

Parameter	a (mm)	b (mm)	h (mm)	ρ (kg/m ³)
Value	209	192	2.59	2120

Pedersen and Frederiksen (1992) had applied a basic least squares approach for identifying the four ply-elastic constants: E_1 , E_2 , G_{12} and ν_{12} . This involved minimizing the following objective function:

$$J(\mathbf{E}) = \sum_{i=1}^m \left(\frac{f_i^{resp}(\mathbf{E}) - f_i^{measure}}{f_i^{measure}} \right)^2 \quad (5-1)$$

where $\mathbf{E} = \{ E_1, E_2, \nu_{12}, G_{12} \}$, $f_i^{measure}$ is the i^{th} experimental frequency from Table 5-1 and f_i^{resp} is the response prediction of a numerical model (a Rayleigh-Ritz method was used by Pedersen and Frederiksen (1992)).

Bayesian Identification

Bayesian Formulation

The Bayesian formulation for identifying the probability distribution of the four ply-elastic constants is similar to the ones introduced in the previous chapters. The main difference is that we assume a more complex error model which is detailed in the next section. For convenience we provide again the Bayesian formulation in the current section. Readers who are familiar with the previous chapter can skip this section.

The Bayesian formulation can be written as follows for the present vibration problem:

$$\pi_{\mathbf{E}|\mathbf{f}=\mathbf{f}^{measure}}(\mathbf{E}) = \frac{1}{K} \pi_{\mathbf{f}|\mathbf{E}}(\mathbf{f}^{measure}) \cdot \pi_{\mathbf{E}}^{prior}(\mathbf{E}) \quad (5-2)$$

where $\mathbf{E} = \{ E_1, E_2, \nu_{12}, G_{12} \}$ is the four dimensional random variable of the elastic constants, $\mathbf{f} = \{ f_1 \dots f_{10} \}$ the ten dimensional random variable of the frequencies measurements prediction and $\mathbf{f}^{measure} = \{ f_1^{measure} \dots f_{10}^{measure} \}$ the vector of the ten measured natural frequencies.

Equation 5-2 provides the joint probability density function (pdf) of the four elastic constants given the measurements $\mathbf{f}^{measure}$. This pdf is equal to a normalizing constant times the likelihood function of the elastic constants \mathbf{E} given the measurements $\mathbf{f}^{measure}$ times the prior distribution of the elastic constants \mathbf{E} . The prior distribution of \mathbf{E} reflects the prior knowledge we have on the elastic constants. This knowledge can come from manufacturer specifications for example. It has a regularization purpose by reducing the likelihood of values of \mathbf{E} which are too far off from reasonable values defined by the prior knowledge on the composite studied. In our case we assumed that we only have relatively vague prior knowledge by defining a truncated

joint normal prior distribution with relatively wide standard deviations as defined in Table 5-3.

The distribution was truncated at the bounds given in Table 5-4, which were chosen in an iterative way such that eventually the posterior pdf is approximately in the center of the bounds and their range covers approximately four standard deviations of the posterior pdf.

Table 5-3. Normal uncorrelated prior distribution for the glass/epoxy composite material.

Parameter	E_1 (GPa)	E_2 (GPa)	ν_{12}	G_{12} (GPa)
Mean value	60	21	0.28	10
Standard deviation	10	5	0.05	1.5

Table 5-4. Truncation bounds on the prior distribution of the material properties

Parameter	E_1 (GPa)	E_2 (GPa)	ν_{12}	G_{12} (GPa)
Low truncation bound	53.5	18.5	0.22	9
High truncation bound	64.5	25.2	0.34	11.5

The other term on the right hand side of Equation 5-2 is the likelihood function of the elastic constants given the measurements $f^{measure}$. This function measures the probability of getting the test results for a given value of the elastic constants E , and consequently, it provides an estimate of the likelihood of different E values given the test results. Note that there is uncertainty in f , since for a given value of E we need to calculate the probability of obtaining the measurements. This uncertainty can have several causes which are detailed next.

Sources of Uncertainty

A typical cause of uncertainty in the identification process is measurement error on the natural frequencies. Previous studies by Sol (1986), Papazoglou et al. (1996), Lai and Ip (1996), Hua et al. (2000), Daghia et al. (2007) assumed this to be the only uncertainty and also made the assumption that it is normally distributed. These assumptions allow a purely analytical treatment of the likelihood function, which has the advantage of reduced computational cost. This might not always be the most realistic assumption though. For example Gaussian distributions have

infinite tails, that for elastic constants are devoid of any physical meaning. To prove the ability of our approach to handle any type of distribution we assume here a uniformly distributed measurement error. Treating uniform distributions is possible because we do not use the previous analytical approach but use instead Monte Carlo simulation for the calculation of the likelihood function.

Note that presently we do not have enough information to determine the exact error structure of the measurement uncertainty. A detailed uncertainty propagation study and test campaign would be necessary to determine it. Whatever the uncertainty structure though, our procedure can incorporate it in the Bayesian approach unlike the analytical approaches that can consider only Gaussian measurement noise.

This numerical treatment based on Monte Carlo simulation also allows us to consider errors that do not stem from the measurements, such as the errors presented next.

Another uncertainty in the identification process is modeling error. One potential modeling error is due to the use of thin plate theory, which is more severe for higher modes due to the lower wave length of the higher modes. Other modeling errors, such as discretization errors also increase for higher modes because of the more complex mode shapes.

Finally, yet another uncertainty in the identification process is due to uncertainty in the other input parameters of the vibration model: dimensions of the plate and its density.

The next section develops the implementation of the error model corresponding to these uncertainties. Monte Carlo simulation is then used to propagate the uncertainty effect to the natural frequencies and finally to the likelihood function.

Error and Uncertainty Models

We chose to model the different sources of uncertainty described in the previous subsection as shown in Eq. 5-3.

$$f_m = f_m^{thin\ plate}(\mathbf{E}, \mathbf{p}) + \Delta f_m^{thick-thin} + u_m \quad (5-3)$$

where f_m is the random variable of the frequency measurement prediction for the m^{th} natural frequency of the plate, $f_m^{thin\ plate}$ is the frequency response obtained from a thin plate theory model and which depends on the material properties \mathbf{E} and the other model input parameters \mathbf{p} , which might be known with some uncertainty, $\Delta f_m^{thick-thin}$ is the modelling error due to the difference between thin and thick plate theory and u_m is a uniformly distributed random variable modelling measurement error. Note that other types of modelling errors could also be considered in a similar way, such as discretization errors, errors in the numerical solving of the problem or errors due to an imperfect model representation of the actual experiment. In our case discretization error was found to be small compared to the other sources of error and uncertainty we considered in the problem. Also note that $\Delta f_m^{thick-thin}$ is not considered here to be a random variable but is precisely defined as described in the next paragraphs. Other types of modelling errors which might be less well known, could be defined as random variables though.

We chose to consider a modeling error between thin and thick plate theory because, even though we used a thin plate (see dimensions in Table 5-2), transverse shear effects can become non-negligible for higher modes. The difference between the two model predictions remains small however and will change little as the elastic constants change during the updating procedure. Accordingly we evaluated this difference, which was assumed not to vary during the updating, using the mean values of the prior distribution of the four in-plane properties (see Table 5-3). For the transverse shear values we considered $G_{13} = G_{12}$ and $G_{23} = 0.9 G_{12}$, which is typical for such a glass/epoxy composite. Using an Abaqus[®] model with thick plate elements we found the absolute differences given in Table 5-5.

Table 5-5. Absolute difference between the frequencies obtained with thin plate theory and thick plate theory for the mean values of the a priori material properties (see Table 5-3) and $G_{13} = G_{12}$ and $G_{23} = 0.9 G_{12}$.

Frequency	f_1	f_2	f_3	f_4	f_5	f_6	f_7	f_8	f_9	f_{10}
Difference (%)	0.31	0.03	0.04	0.29	0.29	0.10	0.07	0.42	0.32	0.23

Note that thick plate theory could have been used directly in the numerical model.

However we chose thin plate theory for the numerical model because we needed to construct response surface approximations of the frequencies in order to reduce computational cost. As has been shown in the previous chapter, the thin plate theory natural frequencies can be expressed with great accuracy in a relatively simple polynomial form. The more complex governing equations of the thick plate theory would have required more complex response surface approximations. So we chose to use thin plate theory during the Bayesian updating procedure and model the difference to thick plate theory by the correction term $\Delta f_m^{thick-thin}$ defined through Table 5-5.

To define all the terms of Eq. 5-3 we need to define the bounds of the uniformly distributed random variable u_m , modelling the measurement error. We consider that the bounds of the distribution increase with the mode number, which can be explained as follows:

- due to noise it is harder to numerically extract the higher frequencies
- the higher modes, due to their higher frequencies and more complex mode shapes may start involving effects which were considered negligible for the fundamental frequency (surrounding air effects, damping, more complex material behavior)

Accordingly we considered that the upper/lower bound is +/- 0.5% of the measured experimental frequency for the fundamental mode ($m=1$) and +/- 2% for the highest mode measured ($m=10$). The bounds vary linearly with m in-between. In summary, the error model is given in Equation 5-4.

$$u_m \square U[-\Delta_m, \Delta_m] \text{ where } \Delta_m = f_m \left(0.02 \frac{(m-1)}{10-1} - 0.005 \frac{(m-10)}{10-1} \right) \quad (5-4)$$

Note that there is also a modeling error due to the use of response surface approximations instead of the finite element analyses. We have shown however in the previous chapter that this error is very small (maximum of 0.06%, see Table 4-8). Compared to the measurement errors of the order 0.5 to 2% this has a negligible impact in terms of total variance. We thus did all the calculation with the error model of Equation 5-4.

The final source of uncertainty in the identification process is related to the uncertainties on the other input parameters \mathbf{p} to the thin plate numerical model (see Eq. 5-3). As in the previous chapter we assumed these uncertainties to be normally distributed, characterized as shown in Table 5-6. The standard deviations considered are reasonable uncertainties for measuring these parameters for the present experiment.

Table 5-6. Assumed uncertainties in the plate length, width, thickness and density (a , b , h and ρ). Normal distributions are used.

Parameter	a (mm)	b (mm)	h (mm)	ρ (kg/m ³)
Mean value	209	192	2.59	2120
Standard deviation	0.25	0.25	0.01	10.6

Bayesian Numerical Procedure

The Bayesian identification involves evaluating the posterior distribution defined by Equation 5-2. The prior distribution in the right hand side is an analytical expression (normal distribution characterized in Table 5-3) so the major challenge is in constructing the likelihood function. We chose to construct this function point by point: we evaluate it at a grid in the four-dimensional space of the material properties $\mathbf{E} = \{ E_1, E_2, \nu_{12}, G_{12} \}$. We chose here a 16^4 grid, which is determined by computational cost considerations. The grid is bounded by the truncation bounds on the prior distribution. A convergence study is given at the end of this chapter.

At each of the grid points E is fixed and we need to evaluate the probability density function (pdf) of the frequencies measurement prediction, $\pi_{f|E=E^{fixed}}(\mathbf{f})$, at the point $\mathbf{f} = \mathbf{f}^{measure}$.

The pdf of the frequencies measurement prediction for a fixed E is determined by propagating through Monte Carlo simulation the uncertainties in the input parameters and the error model defined in the previous subsection. This is done in two steps for each E point on the grid:

- Propagate the normal uncertainties on the input parameters (see Table 5-6) to the natural frequencies using Monte Carlo simulation. We denote \mathbf{f}^{input_MC} the random variable of the frequencies due only to the uncertainty in input parameters and the thick-thin plate correction term but not to the measurement uncertainty.
- Calculate the point of the likelihood function using Equation 5-5 which accounts for the measurement uncertainty u (see Equation 5-4).

$$\pi_{f|E=E^{fixed}}(\mathbf{f}^{measure}) = \frac{1}{K} \int_{\mathbf{f}^{measure} - \mathbf{u}^{lb}}^{\mathbf{f}^{measure} + \mathbf{u}^{ub}} \pi_{\mathbf{f}^{input_MC}|E=E^{fixed}}(\mathbf{f}^{input_MC}) d\mathbf{f}^{input_MC} \quad (5-5)$$

where K is a normalizing constant.

The use of Equation 5-5 is possible because the measurement error is uniformly distributed within the bounds $[u^{lb}, u^{ub}] = [-\Delta_m, \Delta_m]$ (see Equation 5-4). Equation 5-5 is equivalent to saying that the likelihood of measuring the frequencies $\mathbf{f}^{measure}$ is equal to the probability that the simulated frequencies \mathbf{f}^{input_MC} fall inside the measurement uncertainty bounds $[\mathbf{f}^{measure} - \mathbf{u}^{lb}, \mathbf{f}^{measure} + \mathbf{u}^{ub}]$. The integral in Equation 5-5 is evaluated by counting the number of frequencies within the bounds $[\mathbf{f}^{measure} - \mathbf{u}^{lb}, \mathbf{f}^{measure} + \mathbf{u}^{ub}]$ out of the total number of simulated frequencies \mathbf{f}^{input_MC} . We used 50,000 Monte Carlo simulations.

In all the cases, since the Bayesian updating procedure used involves Monte Carlo simulation we are confronted with significant computational cost. For each of the 16^4 grid points 50,000 Monte Carlo simulations of the first 10 natural frequencies are carried out. This means that in total we have about 2 billion frequency evaluations. In such a context it is obvious that a

numerical model (such as finite elements) is by far too expensive for calculating the natural frequencies.

To reduce the cost we chose to construct response surface approximations of the frequencies. The response surface method allows to reduce the cost of a frequency evaluation from about 4s using the finite element model to about 0.3ms with the surrogate model (on an Intel Core2 Duo 2GHz machine). This brings the computational cost of the Bayesian procedure down to tractable levels.

Applicability and Benefits of Separable Monte Carlo Simulation to Bayesian Identification

At this point we would like to note that in spite of the significant reduction in computational cost, the approach remains at the edge of what is usually considered reasonable, an identification taking up to a week. This could become problematic if the Bayesian procedure that we developed cannot be directly applied due to a different nature of the uncertainty structure for example. Indeed in our procedure we used to our advantage the fact that the measurement noise was considered uniformly distributed in order to further reduce computational cost.

In a more general case where the measurement uncertainty is not uniformly distributed such as to allow the use of Equation 5-5 and the total uncertainty can also not be approximated by a joint normal distribution, then following procedure can potentially be applied instead. For each fixed \mathbf{E} point on the grid sample values for the uncertain input parameters a , b , h and ρ , propagate these by Monte Carlo simulation to the natural frequencies and add a sampled value for the modeling and measuring uncertainty \mathbf{u} . This will lead to a sample of simulated frequencies. A distribution needs to be fitted to these frequencies and be evaluated at $\mathbf{f} = \mathbf{f}^{measure}$, which would lead to the likelihood value we seek $\pi_{\mathbf{f}/\mathbf{E}=\mathbf{E}^{fixed}}(\mathbf{f}^{measure})$. To fit the sampled frequencies we can construct the empirical histogram and fit it using a kernel method for

example. The major issue with this approach however would be greatly increased computational cost leading to no longer reasonable computation times.

A possible way to address this issue is by using separable Monte Carlo sampling (Smarlsok 2009), which can decrease by several orders of magnitude the number of simulations required. Separable Monte Carlo simulation uses to its advantage the independence of the random variables involved.

To show its applicability we use the Bayesian identification formulation of Eqs. 3-8 and 3-9. The two random variables that appear in \mathbf{D} are on one hand the true value of the response based on the measurement \mathbf{Y}_{true}^{meas} and on the other side the true value based on the model $\mathbf{Y}_{true}^{model}$. The independence of these random variables means that the two can be sampled separately. The conditional expectation method (Ayyub and Chia 1992) allows then to calculate the likelihood function as shown in Equation 5-6, by using N samples of $\mathbf{Y}_{true}^{model}$ into the pdf of \mathbf{Y}_{true}^{meas} .

$$l(\mathbf{x}) \approx \frac{1}{N} \sum_{i=1}^N \int_{\|\mathbf{y}_{true}^{model} - \mathbf{y}_{true}^{meas}\| < \varepsilon} \pi_{\mathbf{y}_{true}^{meas}}(\mathbf{y}_{true}^{model}) d\mathbf{y}_{true}^{meas} \quad (5-6)$$

Since for a same estimation accuracy ε , the method requires much fewer samples of the independent variables than what is required when sampling \mathbf{D} directly, a significant cost reduction is thus possible. While we will not explore this approach in the present work, we still wanted to mention its potential applicability and benefits.

Bayesian Identification Results

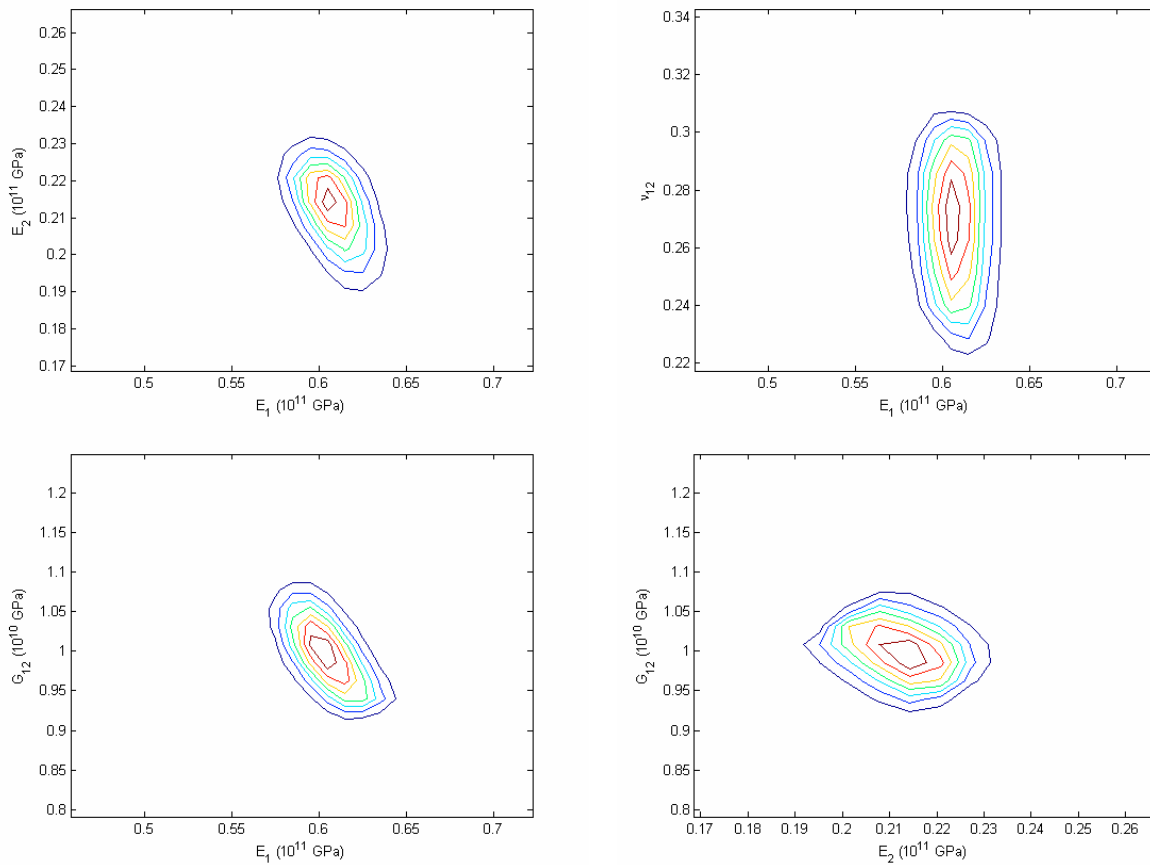
All the results that are presented in this chapter were obtained using the high fidelity frequency RSA constructed in Chapter 4 with the bounds given in Table 4-7. This RSA was tested in Chapter 4 and was shown to have very good accuracy (see Table 4-8) over the domain for which we will use it here for Bayesian identification.

To serve as a comparison point for the Bayesian results we provide first the least squares identified values. The least squares results are given in Table 5-7 and were obtained using the least square formulation described at the beginning of the chapter and the high fidelity frequency RSA obtained in Chapter 4.

Table 5-7. Least squares identified properties.

Parameter	E_1 (GPa)	E_2 (GPa)	ν_{12}	G_{12} (GPa)
Value	60.9	22.7	0.217	9.6

The identified posterior distribution by the Bayesian approach is represented graphically in Figure 5-1, by fixing two of the material properties at the mean values of the posterior distribution and plotting the distribution as a function of the remaining two properties.



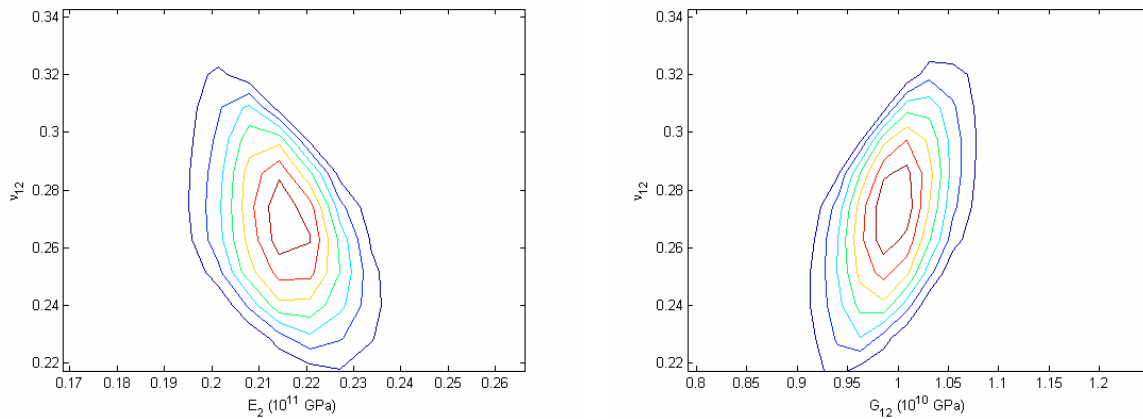


Figure 5-1. Identified posterior joint distribution plots. Since the joint probability distribution is four-dimensional it is plotted in 2D by fixing the two variables not plotted at their mean values. The plots are then six cuts through the distribution mean value point.

We can characterize the identified posterior distribution by the mean values and the variance-covariance matrix as shown in Tables 5-8 and 5-9. Note that before we had used the most likely value to characterize the identified properties. We use the mean value here because our grid is relatively sparse, thus the highest point of the grid might not be a good estimate of the true maximum. Considering the shape of the distributions we considered that the mean value is a better estimate of the most likely point as well.

Interpreting the variance-covariance matrix is not very easy so we also provided the coefficient of variation in Table 5-8 and the correlation matrix in the Table and 5-10, which facilitate the interpretation of the results.

Table 5-8. Mean values and coefficient of variation of the identified posterior distribution.

Parameter	E_1 (GPa)	E_2 (GPa)	ν_{12}	G_{12} (GPa)
Mean value	60.8	21.3	0.27	9.87
COV (%)	3.05	5.46	12.2	5.96

Table 5-9. Variance-covariance matrix (symmetric) of the identified posterior distribution.

	E_1 (Pa)	E_2 (Pa)	ν_{12} (Pa)	G_{12} (Pa)
E_1 (Pa)	3.45E+18	-3.05E+17	-2.31E+07	-6.85E+17
E_2 (Pa)	-	1.36E+18	-2.28E+07	-2.46E+17
ν_{12}	-	-	1.10E-03	1.49E+07
G_{12} (Pa)	-	-	-	3.47E+17

Table 5-10. Correlation matrix (symmetric) of the identified posterior distribution.

	E_1	E_2	ν_{12}	G_{12}
E_1	1	-0.141	-0.378	-0.626
E_2	-	1	-0.593	-0.358
ν_{12}	-	-	1	0.768
G_{12}	-	-	-	1

It is worth noting that while for the three bar truss problem the prior distribution had a negligible effect on the identification, the prior would have more significant effect here in the identification of ν_{12} notably. The ply's Poisson's ratio is identified with relatively high uncertainty (about 12% COV), which is no longer small enough compared to the prior distribution's COV of about 18%. So while the prior will affect the identification in this case, this is reasonable since the prior has a relatively high COV in absolute terms, which is generally available to the experimentalist (based on fiber/matrix properties homogenization for example). The prior allows in this case to avoid implausible results.

A convergence study was carried out in order to estimate the error in the parameters characterizing the identified probability density function. Mean values and variance-covariance matrix are indeed dependent on the pdf domain used to calculate them. In our case this domain is defined by the truncation bounds on the prior distribution. Since tight truncation bounds reduce the computational cost we initially started with an 8^4 grid. This grid was then increased by two points at each step of the convergence study. Note that the step size remained the same, that is we did not refine the domain but enlarge it during the convergence study. The final domain used a 16^4 grid with the domain bounds being those given in Table 5-4.

The convergence results are illustrated in Figure 5-2. As far as mean values convergence (Figure 5-2A) we can say that the results are relatively stable and the estimates are very close to

convergence. The highest error seems to be in the shear modulus, which has an estimated truncation error of less than 0.4%.

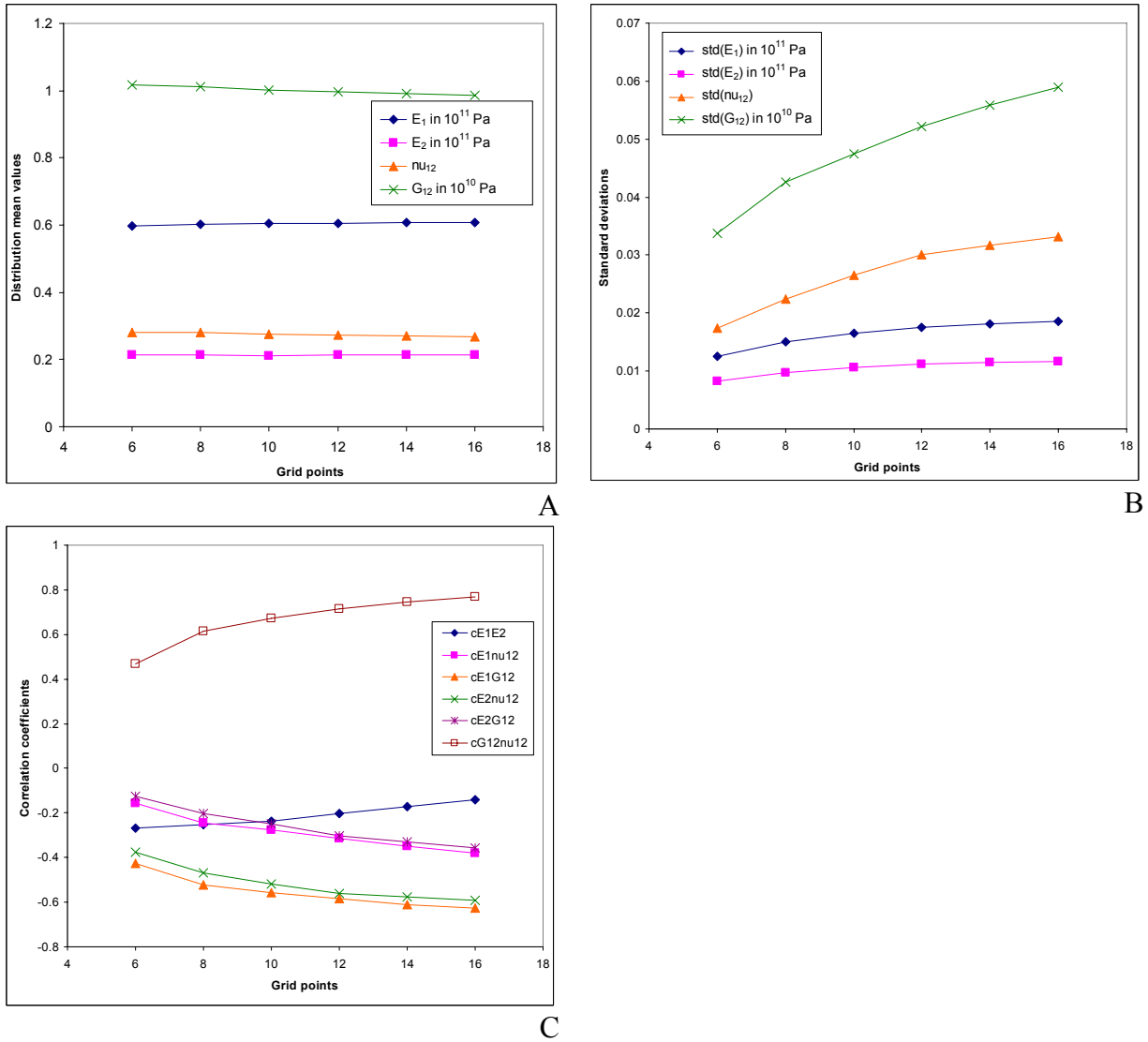


Figure 5-2. Convergence of the: A) mean value. B) standard deviation. C) correlation coefficient of the identified distribution.

The variance-covariance matrix on the other hand seems less converged. Regarding standard deviations the highest error seems to be again relative to G_{12} which has an estimated truncation error in the standard deviation of less than 8%. The truncation error in the correlation coefficients is estimated to be less than 5% except for the correlation coefficient between E_1 and

E_2 which seems poorly converged. Note however that these two parameters have the lowest correlation among all so the accuracy on this coefficient is less critical.

The truncation errors could have been further reduced by continuing to enlarge the calculation domain. Since we are in a four dimensional space however, adding points quickly becomes computationally prohibitive. In our case moving from a 16 to an 18 points grid would have required an additional week of calculations on an Intel Core2 Duo 2GHz machine in spite of the use of response surface approximations. Accordingly we decided to stop at a 16^4 grid. It is however important to note that only the variance co-variance matrix is estimated with somewhat larger errors. The mean values are estimated very accurately. Considering that the variance-covariance matrix is rarely provided at all in identification studies we consider important to estimate it even if only with about 10% accuracy.

Comparing Tables 5-6 and 5-7 we can note that the least square identified values and the mean values of the posterior distribution are relatively far apart for some properties. However, considering the uncertainties characterizing the posterior distribution and since the least squares values also have an uncertainty at least as high as the Bayesian values, typically higher (see Chapter 3), the results of the two methods seem plausible.

The results of Table 5-8 show that the four material properties are identified with different confidence from the vibration test we used. The longitudinal Young's modulus is identified most accurately while the Poisson's ratio is identified with a high uncertainty. This trend has been often observed in the composites community, since repeated tests on a same specimen typically lead to much higher dispersion on some properties than on others (Poisson's ratio and shear modulus are typically known more poorly). However it is rarer that the difference in uncertainty is quantified and the Bayesian identification approach provides a natural tool for this purpose.

Note that the uncertainties depend on the experiment and a different lay-up or another experimental technique would lead to different uncertainties. Note also that the identified pdf is not a representation of the variability of the material properties, it just provides the uncertainty with which they are identified from this particular experiment.

Table 5-10 shows that there is also non-negligible correlation between the different properties. This is an important result and we could not find any previous study giving the correlation matrix of the orthotropic constants identified. Ignoring the correlation would lead to significantly overestimating the uncertainty in the identified properties. On a final note, the results of Table 5-8 and 5-9 can provide a realistic model of experimental uncertainty which can be used in probabilistic studies instead of simple uncorrelated uncertainty models.

Uncertainty propagation through least squares identification

At this point it is worth looking into the question if the uncertainty model identified for the material properties using the Bayesian method could have been obtained using other identification methods, least squares identification in particular. Indeed even though the least squares identification provides a single value for the identified properties it is possible to account for the uncertain input parameters by simulating them with Monte Carlo simulation and repeating the least squares identification for each set of simulated parameters.

The uncertain parameters to be propagated through the least squares identification are in our case the four model input parameters length, width, thickness and density (see Table 5-6) as well as the measurement errors on the 10 natural frequencies, which were assumed distributed as described in Eq. 5-3. To carry out this least squares uncertainty propagation we simulated by Monte Carlo 1000 values for the 14 uncertain parameters: four input parameters and a measurement error for each of natural frequency, which was added to the experimentally measured frequencies of Table 5-1. For each of these 1000 simulations a least squares

identification was carried out using the formulation of Eq. 5-1. Based on the 1000 sets of identified properties we calculated their statistics, which are given in Table 5-11.

Table 5-11. Mean values and coefficient of variation obtained by uncertainty propagation through the least squares identification.

Parameter	E_1 (GPa)	E_2 (GPa)	ν_{12}	G_{12} (GPa)
Mean value	60.7	22.7	0.22	9.59
COV (%)	2.93	8.27	21.2	8.92

Since we used the same uncertainty model as for the Bayesian identification these results can be compared to those obtained through the Bayesian method in Table 5-8. First we note that the mean values obtained through least squares are different from those obtained using Bayesian identification. We have discussed in Chapter 3 several effects that can cause this difference, in particular different sensitivity, uncertainty or correlation among the responses. Second we note that while the coefficient of variation (COV) of E_1 is slightly underestimated using least squares, the COV of the other three properties is well overestimated. These differences can be explained both by the effect of the prior and by the different effects we investigated in Chapter 3 and notably the effect of different sensitivity of the response to the properties. E_1 is indeed the most sensitive of the four properties, thus it is identified most accurately, while the other properties are identified with higher error due to their lower sensitivity. We have seen that this effect is unwanted since it increases the error with which the properties are identified and we have also seen in Chapter 3 that it affects the basic least squares identification substantially more than Bayesian identification. This leads us to affirming that the Bayesian identified uncertainty model is more realistic than the one obtained through least squares uncertainty propagation.

We need to point out again at this point that we used the basic least squares formulation here. As seen in Chapter 3 there is also a generalized least squares formulations that considers the variance-covariance matrix of the response. We expect that, in the case where we can

approximate the frequencies uncertainty as a joint normal distribution, performing the uncertainty propagation using the generalized least squares formulation would lead to about the same results as the Bayesian identification (minus the effect of the prior). However the generalized least squares formulation requires calculating the variance covariance matrix of the frequencies as a function of the material properties, which is computationally expensive, and would thus also require cost reduction techniques to make the approach tractable. The same dimensionality reduction, response surface and Monte Carlo simulation approach that we developed for the Bayesian identification could then be applied as well to obtain at reasonable cost the variance-covariance matrix for generalized least squares.

Identification of the plate's homogenized parameters

Up to this point we identified the elastic constants of the ply of the composite laminate. This is a more challenging problem than identifying the plate's homogenized orthotropic constants because the ply's properties affect the vibration indirectly through the homogenized properties which can potentially reduce the sensitivity of some parameters to the natural frequencies. The advantage of identifying ply properties is however that they can provide both extensional and bending homogenized properties.

In order to have a better understanding of the effect of uncertainties we did also the identification of the homogenized bending elastic constants $\{E_x, E_y, \nu_{xy}, G_{xy}\}$ and of the bending rigidities $\{D_{11}, D_{22}, D_{12}, D_{66}\}$ of the plate. Note that for the bending rigidities we kept the standard notations with the numerical subscripts, but the rigidities are those in the directions x and y of the plate.

Since this serves only as a comparative study we reduced the computational cost of the identification to about 12 hours by considering normally distributed measurement uncertainty on the frequencies instead of a uniform distribution. We kept the same standard deviations for the

normal distribution as for the uniform one. 10,000 Monte Carlo simulations were used and the grid size was 6^4 . The results of the identifications are presented in Table 5-11 to 5-12.

Table 5-11. Least squares and Bayesian results for ply elastic constants identification with normally distributed measurement error.

	Parameter	E_1 (GPa)	E_2 (GPa)	ν_{12}	G_{12} (GPa)
Least squares	Value	60.9	22.7	0.217	9.6
Bayesian	Mean value	60.8	20.5	0.27	9.86
	COV (%)	2.58	4.74	10.7	5.07

Table 5-12. Least squares and Bayesian results for homogenized bending elastic constants identification with normally distributed measurement error.

	Parameter	E_x (GPa)	E_y (GPa)	ν_{xy}	G_{xy} (GPa)
Least squares	Value	43.7	30.3	0.21	13.8
Bayesian	Mean value	43.6	30.3	0.22	13.9
	COV (%)	1.61	1.39	3.59	1.23

Table 5-13. Least squares and Bayesian results for bending rigidities identification with normally distributed measurement error.

	Parameter	D_{11} (N.m)	D_{22} (N.m)	D_{66} (N.m)	D_{12} (N.m)
Least squares	Value	64.0	45.3	20.8	14.6
Bayesian	Mean value	65.2	45.3	20.2	14.0
	COV (%)	1.49	1.49	1.20	3.85

These results show that the homogenized properties are indeed identified with a lower uncertainty than the ply properties. This is mainly due to the fact that the homogenized properties are more insensitive to variations of some ply properties (the Poisson's ratio of the ply for example).

Summary

An implementation of the Bayesian approach for identifying the probability distribution of the orthotropic constants of a composite from natural frequency measurements of a plate was presented. The proposed approach can handle measurement as well as modeling uncertainty through the use of Monte Carlo simulation. Due to the high computational cost of the simulation,

response surface approximations of the frequencies were required. Polynomial response surfaces of the natural frequencies as a function of nondimensional parameters were used, which brought down the computational cost by a factor of about 1,000 making the procedure computationally tractable. However, in spite of the substantial cost reduction, the procedure remains at the limit of reasonable computation time.

The identified Bayesian posterior distribution was found to have different uncertainties in the different orthotropic constants as well as non-negligible correlation between them. These uncertainties and correlations were quantified and allow the construction of an experimental uncertainty model for the particular experiment used.

CHAPTER 6 REDUCING THE DIMENSIONALITY OF FULL FIELDS BY THE PROPER ORTHOGONAL DECOMPOSITION METHOD

Introduction

Optical full field measurement methods for displacements or strains typically provide large quantities of information since each pixel of the image represents a measurement point. This has the great advantage of allowing to measure field heterogeneities. The sheer size of the data can however also pose problems in some situations.

Such a situation can arise if Bayesian identification needs to be applied to full field measurements. Due to its statistical nature it handles probability density functions. In the case of full field methods we can have between thousands and millions of measurement points. Thousands-dimensional joint probability density functions for the measurements are however out of the realm of what can be numerically handled. A reduced dimensional representation of the measurements would thus be useful.

A possible method for achieving such a dimensionality reduction is the principal components analysis (PCA). This method has its origin in statistical analysis and depending on the field of application it is also known as proper orthogonal decomposition (POD) or the Karhunen-Loeve expansion.

The proper orthogonal decomposition method was initially used in computational fluid dynamics to represent complex, turbulent flows (Berkooz et al. 1993). For a review of different uses of POD in computational fluid dynamics the reader can refer to Lucia et al. 2004. Other uses of POD include representing the structural response of non linear finite element under stochastic loading (Schenk et al. 2005) or real-time nonlinear mechanical modeling for interactive design and manufacturing (Dulong et al. 2007). POD was also applied to a multidisciplinary optimization problem of an aircraft wing (Coelho et al. 2009). Usually cited as

Karhunen Loeve, the POD method is also used in stochastic finite elements (Ghanem and Spanos 2003) or more generally to represent arbitrary random fields (Sakamoto and Ghanem 2002, Schenk and Schueller 2003).

The POD method seeks a reduced dimensional basis for the representation of the response (full fields in our case). This basis is constructed from a set of fields, called snapshots, obtained with input parameters within a certain domain. The decomposition ensures that any field within the corresponding domain can be written as a linear combination of fixed POD fields (usually called POD modes). This is similar to other types of modal decompositions (Fourier decomposition, vibration modes), the major specificity of POD being that it is sampled based leading to error minimization properties as we will see in the next section. The accuracy of the field representation increases as expected with the number of POD modes used. Typically we seek to represent the fields as a linear combination of less than a dozen POD modes while keeping reasonable accuracy in the reduced dimensional representation. It is important to note that for a full field with thousand measurement points this represents a dimensionality reduction in the field representation of one thousand to only a few dozen. The POD method can potentially allow to achieve this goal without losing any significant amount of information.

The rest of the chapter is organized as follows. In a first section, we present the theoretical basis of proper orthogonal decomposition. Next, we present the simulated experiment for obtaining full fields. We then describe the dimensionality reduction problem applied to our specific case. Finally we present the proper orthogonal decomposition results.

Proper Orthogonal Decomposition

Let us consider a set of N vectors $\{\mathbf{U}^i\}_{i=1..N}$. A vector $\mathbf{U}^i \in \mathbb{R}^n$, also called snapshot, can be the vector representation of a displacement field for example. The aim of the proper orthogonal

decomposition (POD) method is to construct an optimal, reduced dimensional basis for the representation of the snapshots. For the POD method to work, it is necessary that the snapshot vectors have zero mean. If this is not the case the mean value needs to be subtracted from each vector.

We denote $\{\Phi_i\}_{i=1..K}$ the vectors of the orthogonal basis of the reduced dimensional representation of the snapshots. The POD method seeks to find the Φ_i that minimize the representation error:

$$\min \frac{1}{2} \sum_{i=1}^N \left\| U^i - \sum_{k=1}^K \alpha_{i,k} \Phi_k \right\|_{L2}^2 \quad (6-1)$$

Because $\{\Phi_i\}_{i=1..K}$ is an orthogonal basis the coefficients $\alpha_{i,k}$ is given by the orthogonal projection of the snapshots onto the basis vectors:

$$\alpha_{i,k} = \langle U^i, \Phi_k \rangle \quad (6-2)$$

As a result we have the following reduced dimensional representation \bar{U}^i of the vectors of the snapshot set:

$$\bar{U}^i = \sum_{k=1}^K \alpha_{i,k} \Phi_k = \sum_{k=1}^K \langle U^i, \Phi_k \rangle \Phi_k \quad (6-3)$$

The reduction in dimension is from N to K . The truncation order K needs to be selected such as to maintain a reasonably small error in the representations \bar{U}^i of U^i . Selecting such a K is always problem specific.

The POD approach provides however a construction method for obtaining the optimal basis vectors that minimize the error defined in Equation 6-1. This means that for a given truncation order we cannot find any other basis that better represents the snapshots subspace.

The basis $\{\Phi_i\}_{i=1..K}$ is constructed using the following matrix:

$$X = \begin{pmatrix} U_1^1 & \dots & U_1^N \\ \vdots & \ddots & \vdots \\ U_n^1 & \dots & U_n^N \end{pmatrix} \quad (6-4)$$

The vectors $\{\Phi_i\}_{i=1..K}$ are then obtained by the singular values decomposition of X , or equivalently by calculating the eigenvectors of the matrix XX^T . The singular values decomposition allows writing that:

$$X = \Phi \Sigma \Lambda^T \quad (6-5)$$

where Φ is the matrix of the column vectors Φ_i . Standard singular value decomposition routines (such as LAPACK (Anderson et al. 1999)) typically provide the matrix Φ . The *svd()* function in Matlab also implements this routine, which was used here.

In the rest of the chapter we will apply the POD decomposition to full field displacement measurements.

A truncation error criterion can be obtained by the following procedure. This criterion ε is defined for the sum of the error norms as shown in Equation 6-6.

$$\sum_{i=1}^N \left\| U^i - \sum_{k=1}^K \alpha_{i,k} \Phi_k \right\|_{L2}^2 \leq \varepsilon \sum_{i=1}^N \|U^i\|_{L2}^2 \quad (6-6)$$

With $\varepsilon = 1 - \frac{\sum_{i=1}^K \sigma_i^2}{\sum_{i=1}^N \sigma_i^2}$, where σ_i are the diagonal terms of the diagonal matrix Σ . For a

derivation of this criterion the reader can refer to Filomeno Coelho and Breikopf (2009).

Simulated Experiment

Experiment Description

The experiment we model is a tensile test on a composite plate with a hole. The laminate is made of graphite/epoxy with a stacking sequence of $[45,-45,0]_s$. The plate has the dimensions given in Figure 6-1. The applied tensile force is 1200 N.

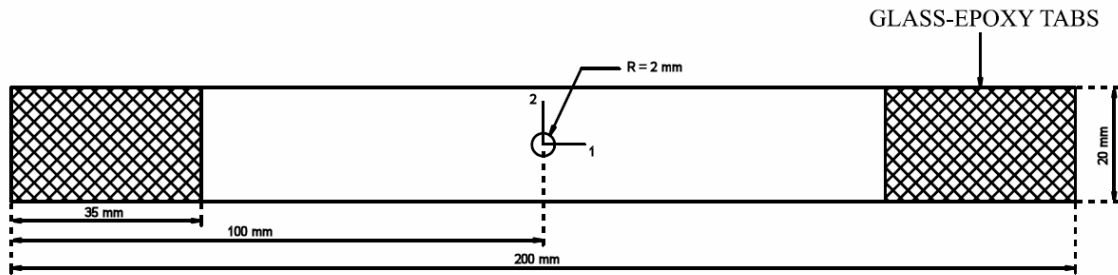


Figure 6-1. Specimen geometry. The specimen material is graphite/epoxy and the stacking sequence $[45,-45,0]_s$. The tensile force is 1200 N.

Numerical Model

The plate is modeled using Abaqus[®] finite element software. A total of 8020 S4R elements (general purpose, four nodes per element, reduced integration) were used. The simulated measurement is assumed to take place on a reference area of 20 mm x 20 mm at the center of the plate. This would be a typical area of an optical full field measurement (Moiré interferometry for example). The finite element mesh in the area of interest is represented in Figure 6-2 and the simulated measurement area highlighted in red. Note that Figure 6-2 does not represent the entire mesh. Since the hole plate is modeled in Abaqus there is a transition using triangular elements towards a larger mesh at the grip edges of the plate where the stress are relatively uniform compared to the area around the hole.

A finite element mesh convergence study was carried out and it was found that with the present mesh the discretization error in the area of interest was of the order of $6 \cdot 10^{-4}\%$ of the average absolute value of the field, which was considered acceptable.

To illustrate the applicability of the dimensionality reduction method we used here finite element generated fields instead of actually measured fields, thus the term simulated measurement. Note however that this does not mean that only finite element fields could be represented in the reduced dimensional space. Once the POD modes are determined, measured fields can very well be projected onto these modes and expressed in the corresponding basis. This can even have some advantages, such as noise filtering as will be shown in the last section of the chapter.

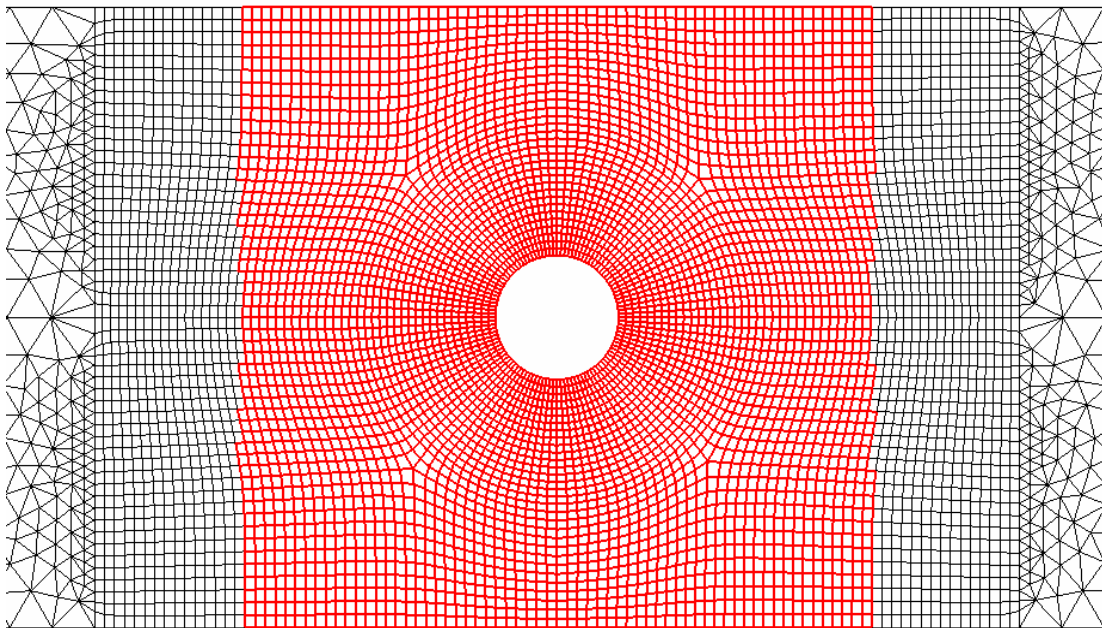


Figure 6-2. Finite element mesh. The area of the simulated measurements (20 mm x 20 mm) is highlighted.

Dimensionality Reduction Problem

Problem Statement

The general framework of the problem is in our case the following. We vary a certain number of model parameters such as elastic constants or plate dimensions and obtain each time by finite element simulation the corresponding full field. The field is described here by the displacement values at the 4569 nodes within the reference area (see highlighted area in Figure 6-2).

If such a field calculation needs to be repeated a large number of times (for statistical sampling for example) or needs to be used within statistical frameworks it is not practical to describe the fields by their value at each point (at the 4569 nodes here). A major reason is because if statistical methods (such as Bayesian identification) need to be used on the fields, thousands dimensional probability density functions required to describe the correlation between the different measurement points are far outside the realm of what the statistical methods can handle with reasonable computational resources.

The problem statement can then be formulated as follows. Can we find a reduced dimensional representation of the full fields for whatever combination of input parameters (elastic constants, plate dimensions in our case) within a certain domain?

To address this problem we propose to use the proper orthogonal decomposition method described in the first section, which will provide us the optimal basis to represent field samples within a certain domain of input parameters.

POD Implementation

For the open hole plate identification problem we will consider we are interested in accounting for variations of the following parameters: ply elastic constants E_1 , E_2 , ν_{12} , G_{12} and ply thickness t (we are looking at variations of the homogenized properties here and not at spatial

variations within the plate). Accounting for variations in the elastic constants is typically of interest in material properties identification problems. We added here the ply thickness to illustrate a typical case for Bayesian identification. Bayesian identification allows to identify the elastic constants while accounting for other sources of uncertainty. The ply thickness was considered here to be one of such sources of uncertainty that potentially affects the identification. The Bayesian identification itself will be carried out in the next chapter.

We are interested in variations of the parameters E_1 , E_2 , ν_{12} , G_{12} and t within the bounds given in Table 6-1. Again these could be typical values for an identification problem.

Table 6-1. Bounds on the input parameters of interest (for a graphite/epoxy composite material).

Parameter	E_1 (GPa)	E_2 (GPa)	ν_{12}	G_{12} (GPa)	t (mm)
Lower bound	126	7	0.189	3.5	0.12
Upper bound	234	13	0.351	6.5	0.18

We obtain the snapshots required for the POD approach by sampling 200 points within the bounds of Table 6-1. The points are obtained by Latin hypercube sampling, which consists in obtaining the 200 sample points by dividing the range of each parameter into 200 sections of equal marginal probability $1/200$ and sampling once from each section. Latin hypercube sampling typically ensures that the points are reasonably well distributed in the entire space.

At each of the 200 sampled points we run the finite element analysis, which gives the corresponding horizontal and vertical displacement fields U and V respectively. Each of the 200 fields of U (and 200 of V) represents a snapshot and is stored as a column vector that will be used for the POD decomposition. The simulated measurement area (see highlighted area in Figure 6-2) covers 4569 finite element nodes so we obtain snapshots vectors of size 4569×1 . The snapshots matrix X has then a size of 4569×200 . Note that as mentioned in the POD theory section the snapshots need to have zero mean. In our case this was true for the U field but not for

the V field, so we needed to subtract the mean value of each snapshot as shown in Equation 6-7, where the bar notation denotes the mean value of the field.

$$X = \begin{pmatrix} V_1^I - \bar{V}_1 & \dots & V_1^N - \bar{V}_N \\ \vdots & \ddots & \vdots \\ V_n^I - \bar{V}_1 & \dots & V_n^N - \bar{V}_N \end{pmatrix} \quad (6-7)$$

The POD modes of the 200 fields are then calculated using the singular value decomposition as shown in Equation 6-5. Note that there are two potential ways to do the POD decomposition: on U and V independently or on U and V together (i.e. a single vector of size 9138 x 1). With U and V together we have for a given truncation order half as many degrees of freedom as with U and V independently. While for a given truncation order the error using U and V together is smaller, we found that it is more difficult in this case to construct response surface approximations (RSA) of the POD coefficients due to higher errors in the RSA. Since for the identification we will need to construct RSA we chose to do the POD decomposition on U and V independently.

Two snapshots (snapshot 1 and 199) that led to substantially different fields are illustrated next. The input parameters of the two snapshots are provided in Table 6-2.

Table 6-2. Input parameters for snapshots 1 and 199.

Parameter	E_1 (GPa)	E_2 (GPa)	ν_{12}	G_{12} (GPa)	t (mm)
Snapshot 1	191.2	12.67	0.231	5.160	0.1446
Snapshot 199	129.1	11.67	0.294	6.039	0.1343

The fields of snapshot 1 are represented in Figure 6-3, which allows to get an idea of the spatial variations of the fields and have an order of magnitude of the different fields for the parameters of interest. Snapshot 199 has displacement and strain fields that are similar to those

of snapshot 1. Among the notable differences are $\text{Max}(U) = 0.0148$ mm and $\text{Max}(V) = 0.0105$ mm for snapshot 199.

POD Results

POD Modes

In total we obtained 200 POD modes. The first six are represented graphically in Figures 6-4 and 6-5. We can note that the first modes are relatively close (but not identical even though the differences cannot be seen by naked eye) to the typical U and V displacement fields (see Figure 6-3). Furthermore we can see that the modes have a more complicated shape with increasing mode number, as expected for a modal decomposition basis. Note also that the POD decomposition is applied twice, once for the U fields and once for the V fields, thus the different modes for the two displacement components.

In Figure 6-6 we also provide the strain equivalents of the POD modes. Note that these are not calculated using the POD decomposition of the strain fields. Instead the displacement POD modes are differentiated to obtain the strain equivalents of the POD modes. In this study we are interested in the displacements POD decomposition so the strain equivalent POD modes are provided here mainly to facilitate understanding and qualitative comparison. If one would work with strain fields rather than displacement fields than he should carry out the POD decomposition directly on the finite element strains which would lead to more accurate results.

In order to differentiate the displacement POD modes two additional steps were required. The displacements were interpolated on a 256×256 grid using cubic polynomials (Matlab `griddata` command). They were then differentiated using the `BibImages` toolbox (Molimard 2007) that fits a polynomial locally around each point and computes the derivative based on the polynomial. These two steps can introduce numerical derivation artifacts (as we will see later) so they are not advised if accurate strain POD modes are sought.

Note that we stop graphical representation at 5 strain equivalent POD modes (Figure 6-6) precisely because of numerical artifacts. For mode 5 some artifacts can already be noticed.

POD Truncation

For recall, the POD decomposition allows to represent a displacement field obtained with any combination of input parameters within the bounds of Table 6-1 as a linear combination of the POD modes.

Even though we obtained 200 POD modes, typically substantially fewer modes are required to represent the fields with reasonable accuracy. In the present section we seek the truncation order that still allows keeping reasonable accuracy. Table 6-3 provides the truncation error criterion defined in Equation 6-6.

Table 6-3. Error norm truncation criterion (ϵ is defined in Eq. 6-6).

K	2	3	4	5
ϵ for U fields	$2.439 \cdot 10^{-7}$	$4.701 \cdot 10^{-9}$	$7.280 \cdot 10^{-11}$	$1.211 \cdot 10^{-11}$
ϵ for V fields	$1.054 \cdot 10^{-6}$	$2.900 \cdot 10^{-9}$	$4.136 \cdot 10^{-10}$	$3.517 \cdot 10^{-11}$

Since ϵ is an overall error criterion, it is not easy to interpret in terms of errors at different points of the field. Accordingly we will also seek to visualize what happens with the errors for individual snapshots. Figure 6-7 provides the truncation error maps in the reconstruction of snapshot 1 when using only the first 3, 4 and 5 POD modes. Similarly for snapshot 199 in Figure 6-8. We can note that already with 3 modes the maximum displacement error in the field is about 1000 times less than the maximum value of the field. The error further decreases by one to two orders of magnitudes when reaching 5 modes. We can also note that the truncation error using K modes looks close to the mode K+1, which is also what would be expected. Furthermore we can note that with 5 POD modes we start seeing artifacts in the error maps that are not likely to have a physical meaning. Since for the displacement maps we don't use any numerical differentiation

these artifacts are likely to be due to the finite element discretization. We also note a slight asymmetry in the V displacement errors. This asymmetry is due to a slight asymmetry of the mesh. Indeed the finite element V displacements have their origin at the edge of the plate. In order to carry out the POD decomposition we had to subtract the mean values from the snapshots. In case of slight mesh dissymmetry the numerical estimate of the mean is slightly off the true value which causes a dissymmetry in the POD modes and thus subsequent error maps. Note that the dissymmetry of the mesh is quite small (see Figure 6-2). The effects of the dissymmetry are noticeable only from mode 5 on, meaning that their corresponding error is of the same order of as the discretization error.

Finally in Figures 6-9 and 6-10 we provide the strain equivalent truncation error. This is to check that the POD modes have not missed any important features that have small characteristics on the displacement fields but larger characteristics on the strain maps. As for the displacement truncation errors we can see that the strain equivalent truncation error field using K modes has shape similarities with the strain equivalent mode $K+1$ field. Note that the equivalent strain error maps were again obtained using numerical differentiation thus exhibit more numerical artifacts. We note however the same trend as for the displacements as far as the truncation error behavior, the error for $K=5$ being of the order of 0.1 microstrains or less.

Cross Validation for Truncation Error

The error norm truncation criterion (cf. Table 6-3), while being a global error criterion, is relatively hard to interpret physically. Furthermore the criterion is based only on the convergence of the snapshots that served for the POD basis construction. However in most cases we will want to decompose a field that is not among the snapshots, so we also want to know the convergence of the truncation error in such cases.

Accordingly we chose to construct a different error measure based on cross validation. The basic idea of cross validation is the following: if we have N snapshots, instead of using them all for the POD basis construction we can use only $N-1$ snapshots and compute the error between the actual fields of the snapshot that was left out and its truncated POD decomposition. By successively changing the snapshot that is left out we can thus obtain N errors. The root mean square of these N errors, which we denote by CV_{RMS} , is then a global error criterion that can be used to assess the truncation inaccuracy.

In order to use the cross validation technique we need to define how to measure the error between two strain fields (the actual strain field and its truncated POD decomposition). We chose the maximum error between two fields, that is the maximum among all the points of the field of the absolute value of the difference between the two fields. This maximum error is computed at each of the N ($N=200$ here) cross validation steps and the root mean square leads to the global error criterion CV_{RMS} . Table 6-4 provides these values for different truncation orders and is illustrated in Figure 6-11. The relative CV_{RMS} error with respect to the value of the field where the maximum error occurs is also given in Table 6-4.

Table 6-4. Cross validation CV_{RMS} truncation error criterion.

	K	2	3	4	5
U field	CV_{RMS} (mm)	$9.35 \cdot 10^{-6}$	$1.05 \cdot 10^{-6}$	$1.65 \cdot 10^{-7}$	$7.83 \cdot 10^{-8}$
	CV_{RMS} (%)	$9.96 \cdot 10^{-2}$	$1.13 \cdot 10^{-2}$	$2.37 \cdot 10^{-3}$	$9.49 \cdot 10^{-4}$
V field	CV_{RMS} (mm)	$1.00 \cdot 10^{-5}$	$6.30 \cdot 10^{-7}$	$3.05 \cdot 10^{-7}$	$7.32 \cdot 10^{-8}$
	CV_{RMS} (%)	$1.10 \cdot 10^{-1}$	$4.71 \cdot 10^{-2}$	$3.71 \cdot 10^{-3}$	$1.84 \cdot 10^{-3}$

At this point we want to make the following remark. Truncating at $K=5$ means that the POD decomposition achieved a dimensionality reduction from 4569 to 5. The error maps for snapshots 1 and 199, as well as the global error criterions show that this is achieved without losing any significant displacement information. It is important to note as well that the obtained

reduction does not depend on the number of measured points (4569 here). As with other modal decompositions the reduction relies on expressing the fields as a linear combination of the determined POD modes. As long as the discretization error is reasonably converged, whether describing each field and POD mode using 4569 or 1 Million points is irrelevant to the fact the field's variations can be expressed with good accuracy as a linear combination of only five modes.

Material Properties Sensitivities Truncation Error

Our final goal is to use the POD decomposition for the identification of the orthotropic elastic constants. Based on the convergence behavior from Tables 6-3 and 6-4 it is somewhat hard to determine what the most appropriate truncation order is for identification purposes. The most relevant quantities for identification are the sensitivity fields of U and V with respect to the four different elastic constants. The sensitivity of the generic field X to the generic elastic constant Y is given by Equation 6-8.

$$Sensitivity(Y) = \left. \frac{\partial X}{\partial Y} \right|_{Y=Y_0} \quad (6-8)$$

The sensitivity is calculated at the point Y_0 which is the one defined in Table 6-5. Note that since X is a field the sensitivity will also be a field.

Table 6-5. Input parameters to the finite element simulation for the sensitivity study and the simulated experiment.

Parameter	E_1 (GPa)	E_2 (GPa)	ν_{12}	G_{12} (GPa)	t (mm)
Value	155	11	0.3	5	0.16

Keeping in mind the identification goal, we are looking for the truncation order that allows to represent with enough accuracy the sensitivities to the four elastic constants. For this purpose we calculated the errors between the actual sensitivities based on finite element simulations and

the sensitivities obtained based on the truncated POD decompositions of the FE simulations. The sensitivities were calculated in both cases by finite difference. The results are presented in Table 6-6 in terms of average error. Note that since the error is also a field we defined the average relative error in percent as being the average of the errors in the sensitivity field divided by the average value of the sensitivity field.

We can see that while from Table 6-4 the U and V fields are calculated already with a relatively small error for $K=2$, this truncation order is not sufficient for describing the sensitivities to all four properties with enough accuracy. To determine a truncation order for the identification we set ourselves a threshold of 0.5% or less average error on the four sensitivities. We can see from Table 6-6 that $K=4$ for both fields allows to be significantly below this threshold.

Table 6-6. Truncation errors for the sensitivities to the elastic constants.

K		2	3	4	5
U field	Average error (%) in Sensitivity(E_1)	0.28	$1.4 \cdot 10^{-2}$	$2.5 \cdot 10^{-3}$	$1.4 \cdot 10^{-3}$
	Average error (%) in Sensitivity(E_2)	11	0.14	$4.7 \cdot 10^{-2}$	$4.1 \cdot 10^{-2}$
	Average error (%) in Sensitivity(ν_{12})	5.2	4.6	$5.4 \cdot 10^{-2}$	$2.9 \cdot 10^{-2}$
	Average error (%) in Sensitivity(G_{12})	$7.3 \cdot 10^{-2}$	$3.0 \cdot 10^{-2}$	$1.6 \cdot 10^{-2}$	$3.4 \cdot 10^{-3}$
V field	Average error (%) in Sensitivity(E_1)	0.81	$1.8 \cdot 10^{-2}$	$1.3 \cdot 10^{-2}$	$7.5 \cdot 10^{-3}$
	Average error (%) in Sensitivity(E_2)	10	0.15	0.12	$8.8 \cdot 10^{-2}$
	Average error (%) in Sensitivity(ν_{12})	5.3	0.74	$9.0 \cdot 10^{-2}$	$8.3 \cdot 10^{-2}$
	Average error (%) in Sensitivity(G_{12})	0.71	$3.2 \cdot 10^{-2}$	$2.0 \cdot 10^{-2}$	$1.3 \cdot 10^{-2}$

POD Noise Filtering

Before concluding we also want to draw the reader's attention on the fact that the POD reduction acts also as a filter. This can have beneficial effects in some situations. The filter effect is obvious when analyzing the truncation error maps. When truncating at $K=4$ for example, the corresponding field reconstruction will obviously not include any of the higher modes. If the higher modes start representing mainly finite element discretization errors, then truncating at $K=4$ will filter out these errors.

A different filtering can arise when constructing the POD modes using finite element results, then projecting noisy fields (such as actual measurements) on the POD basis. The projected representation will then filter out the noise. To illustrate this behavior we simulated a noisy experimental field. This was done by adding white noise to a finite element field, obtained for a composite plate with the properties given in Table 6-5.

A normally distributed noise value with zero mean and a standard deviation of 2.5% of the maximum value of the field was added to each of the 4569 points of the field. The obtained displacement maps are represented graphically in Figure 6-12.

Projecting the simulated experiment U and V fields onto the first five POD basis vectors filters out a significant part of the noise. This is shown in Table 6-7, which gives the maximum difference in the fields between the simulated experiment and the finite element fields with parameters of Table 6-5 (i.e. the fields before the noise was added). While the first column gives the difference in mm, the second gives the difference relative to the value of the field at which the maximum difference occurs. The projection on the POD basis achieved here a reduction in the noise level by a factor of more than 6 for the V field and a factor of more than 12 for the U field, illustrating the noise filtering capabilities of the approach.

Table 6-7. Difference (in absolute value) between the finite element field and the projection of the noisy field onto the first 5 POD basis vectors.

	Max. difference	Relative max. difference
U field	$2.03 \cdot 10^{-5}$ mm	0.203 %
V field	$2.54 \cdot 10^{-5}$ mm	0.426 %

Summary

In the present chapter we sought a reduced dimensional representation of full field displacement maps from a plate with a hole. For our problem we were interested in the variations of five parameters (four elastic constants and one plate dimension) within +/-30% bounds. We wanted to represent any field stemming from within this domain in a reduced dimensional basis of only a few vectors (less than a dozen). This was achieved by using the proper orthogonal decomposition (POD) method. We used finite element based displacement fields to calculate the POD modes required for the reduced dimensional representation. We then showed that using only the first five POD modes allows a representation of two of the field snapshots with an error of less than 0.1%. We thus achieved in our case a dimensionality reduction of 4569 to 5 without losing any significant information in the field's representation. Since the POD decomposition is not directly affected by the discretization used, reductions from several tens or hundreds of thousands of points to only a few POD mode coefficients are potentially possible. Finally we illustrated the filtering capabilities of the POD projection, which is of great interest for actual experimental fields that are usually noisy.

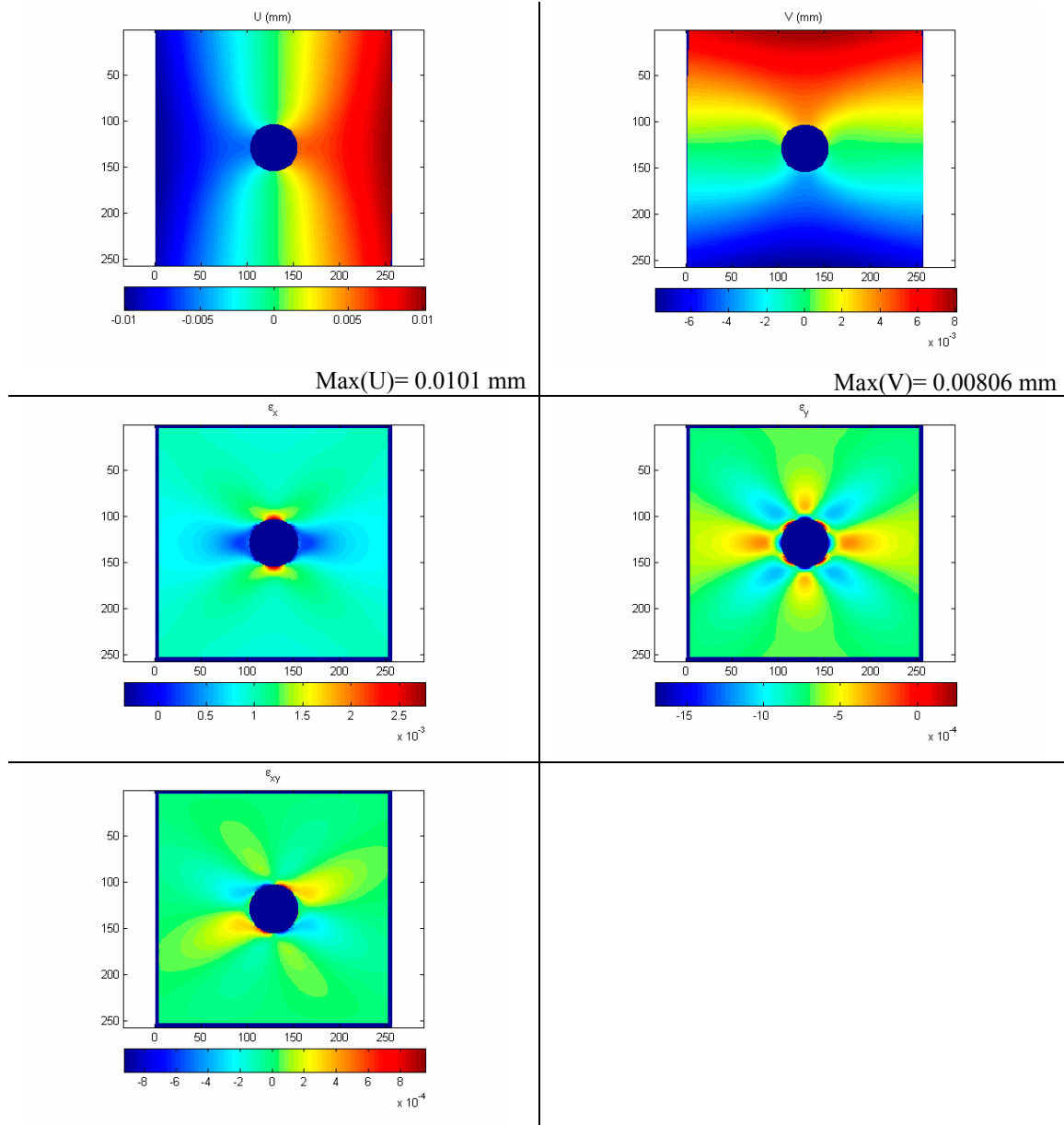
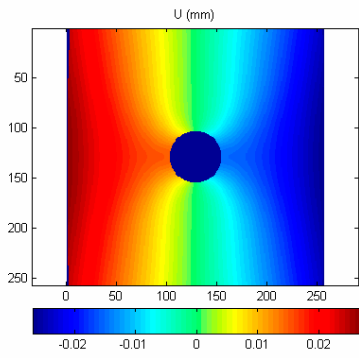
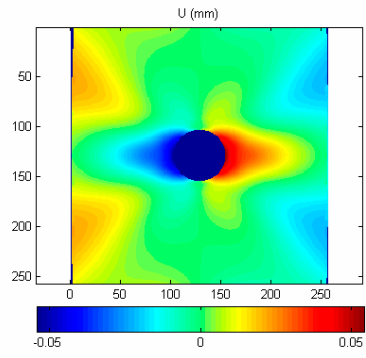


Figure 6-3. Displacement and strain maps for snapshot 1

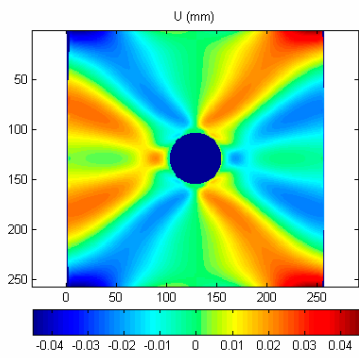
i=1



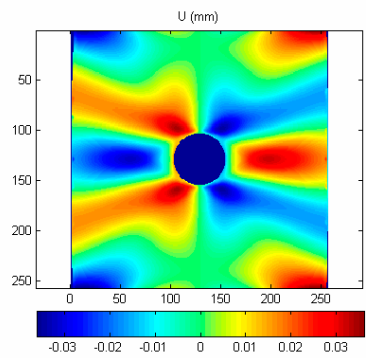
i=2



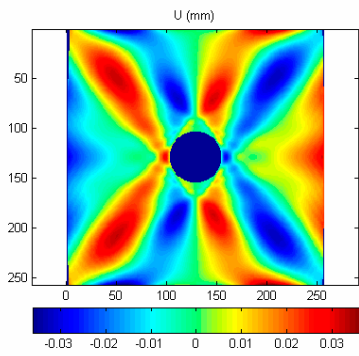
i=3



i=4



i=5



i=6

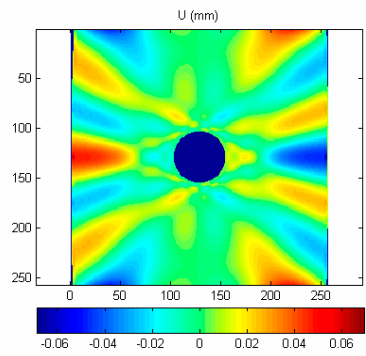
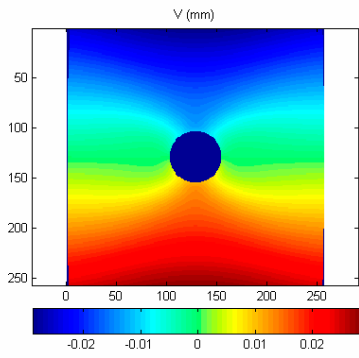
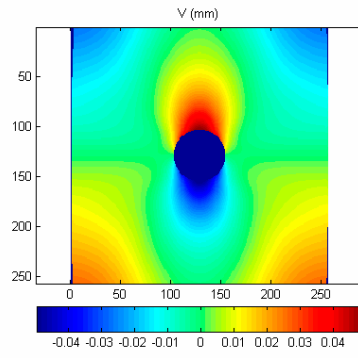


Figure 6-4. First six POD modes for U displacement fields

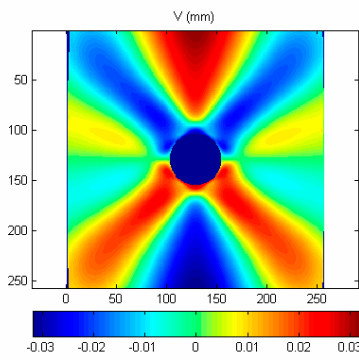
i=1



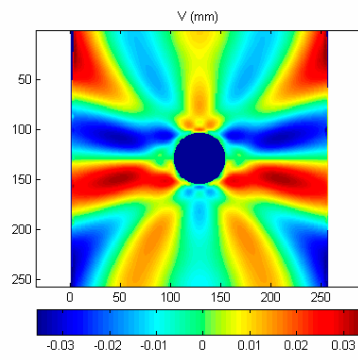
i=2



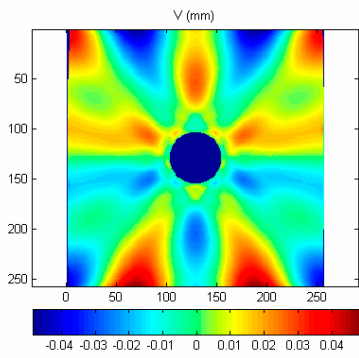
i=3



i=4



i=5



i=6

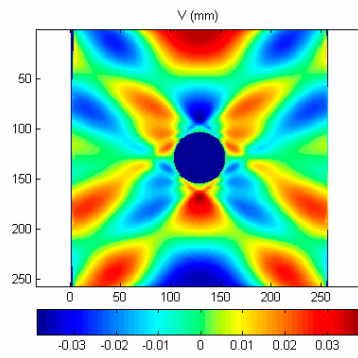
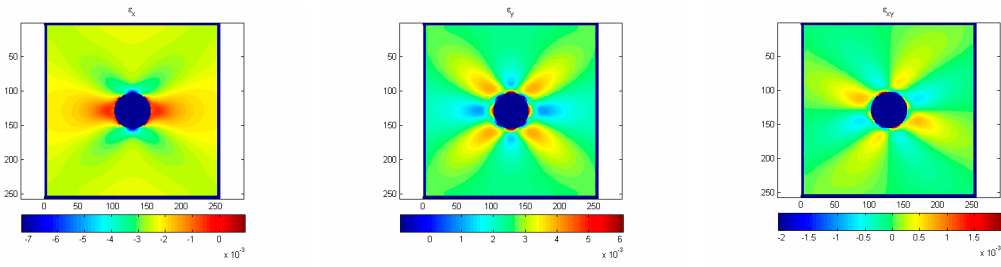
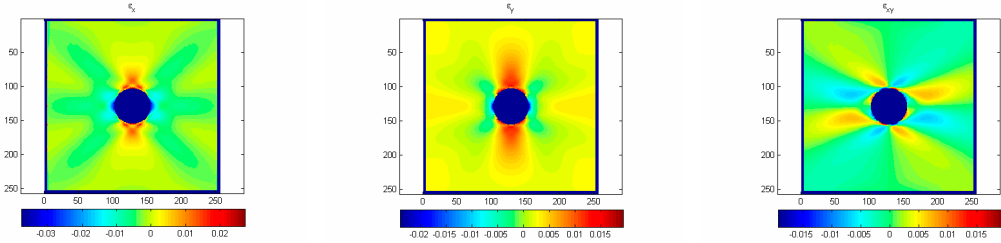


Figure 6-5. First six POD modes for V displacement fields

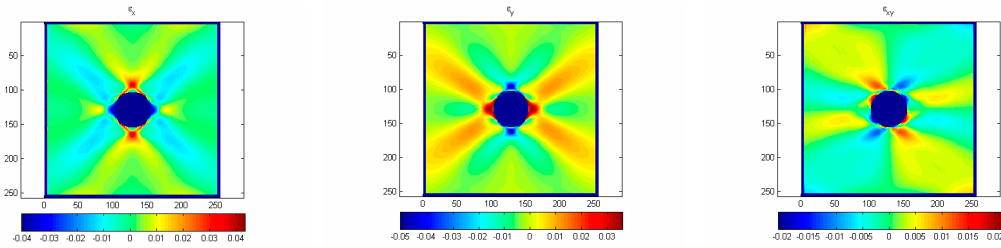
i=1



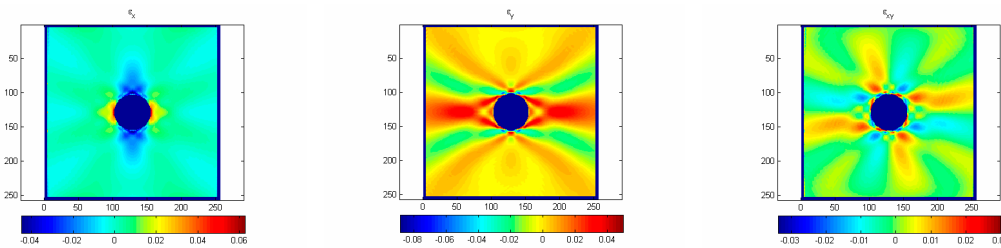
i=2



i=3



i=4



i=5

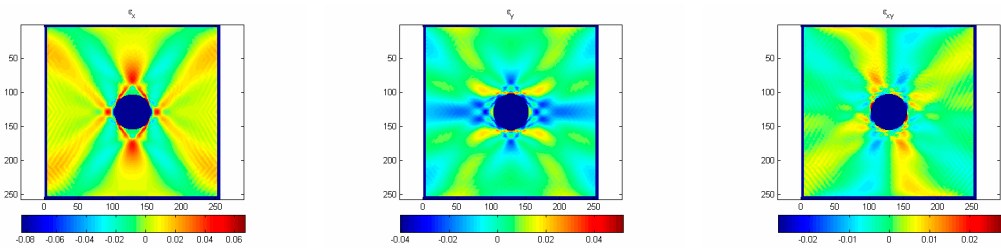
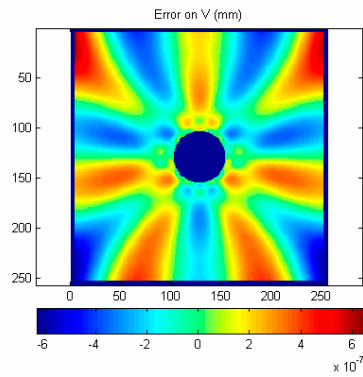
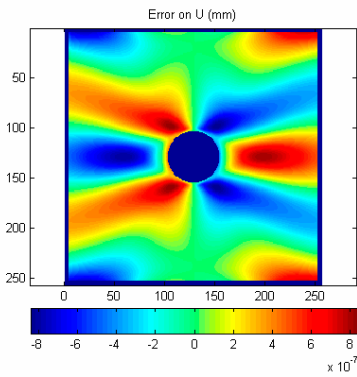


Figure 6-6. First five strain equivalent POD modes for ε_x (first column), ε_y (second column) and ε_{xy} (third column)

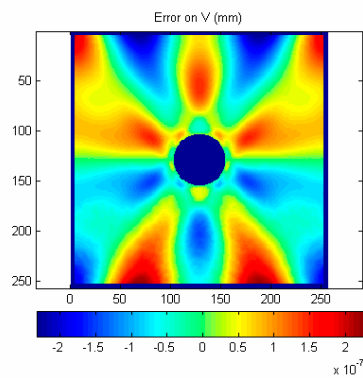
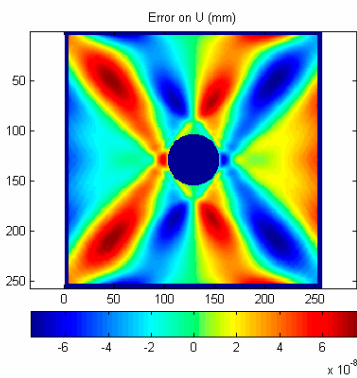
K=3



Max error: 8.991e-007 mm

Max error: 6.329e-007 mm

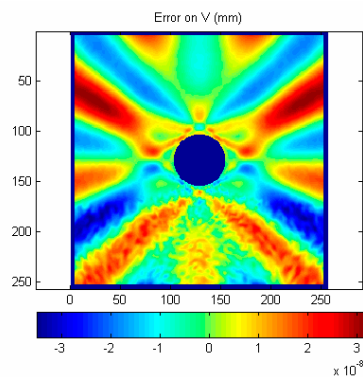
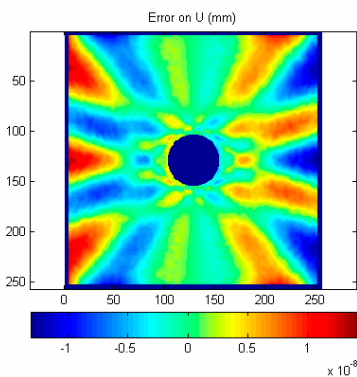
K=4



Max error: 9.479e-008 mm

Max error: 2.526e-007 mm

K=5

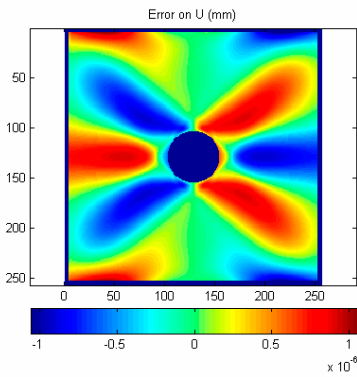


Max error: 1.698e-008 mm

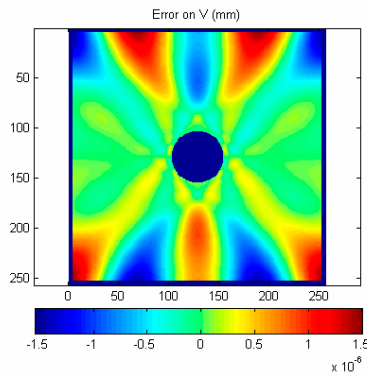
Max error: 3.132e-008 mm

Figure 6-7. Displacements truncation error in snapshot 1 using 3, 4 and 5 modes. The maximum error can be compared to the maximum of the U and V fields, $\text{Max}(U) = 0.0101$ mm, $\text{Max}(V) = 0.00806$ mm.

K=3

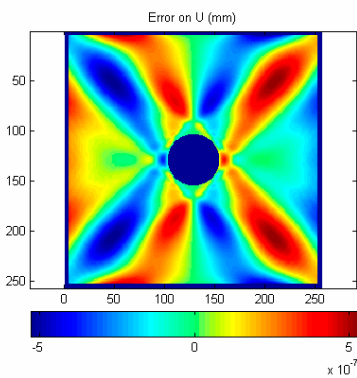


Max error: 1.353e-006 mm

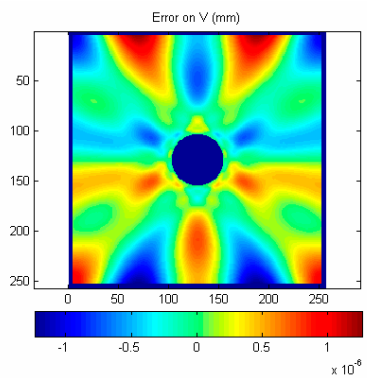


Max error: 1.552e-006 mm

K=4

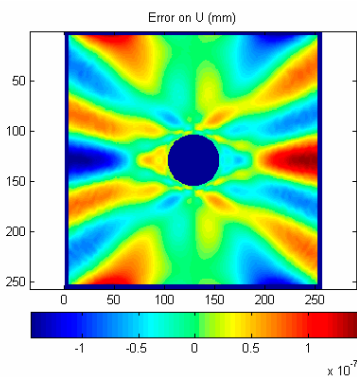


Max error: 6.929e-007 mm

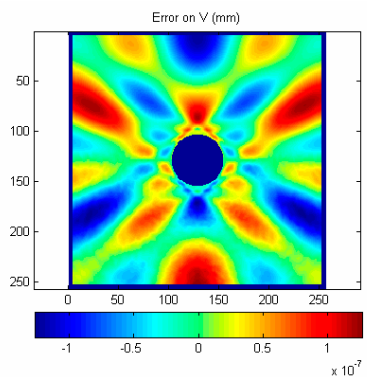


Max error: 1.355e-006 mm

K=5



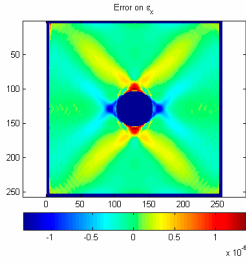
Max error: 1.623e-007 mm



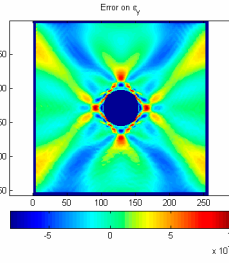
Max error: 1.257e-007 mm

Figure 6-8. Displacements truncation error in snapshot 199 using 3, 4 and 5 modes. The maximum error can be compared to the maximum of the U and V fields, $\text{Max}(U)=0.0148$ mm, $\text{Max}(V)=0.0105$ mm.

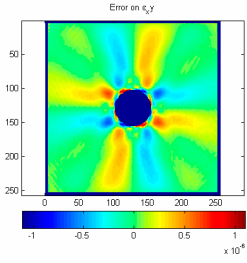
K=3



Max error: 1.397e-006

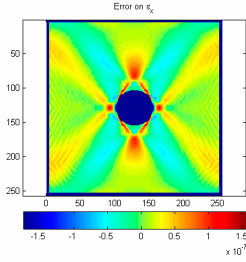


Max error: 6.728e-007

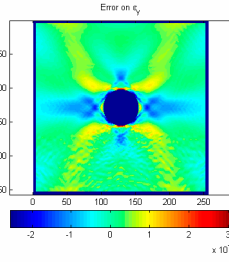


Max error: 8.579e-007

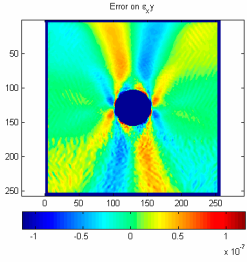
K=4



Max error: 1.567e-007

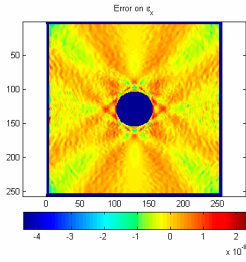


Max error: 3.119e-007

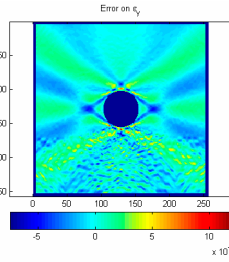


Max error: 1.201e-007

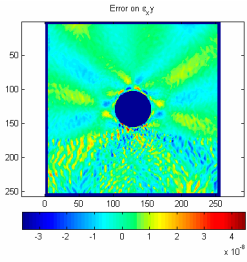
K=5



Max error: 2.328e-008



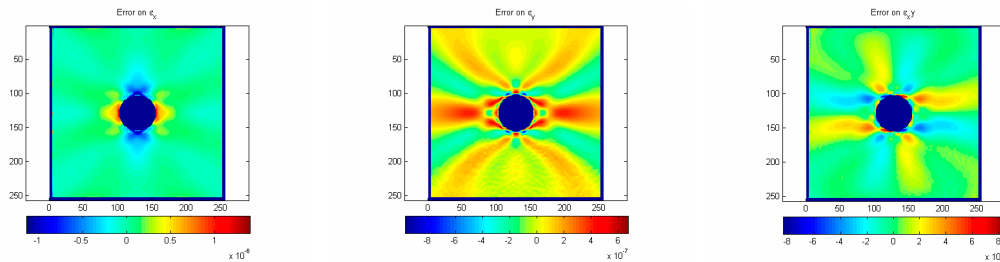
Max error: 1.206e-007



Max error: 4.482e-008

Figure 6-9. Strain equivalent truncation error in snapshot 1 using 3, 4 and 5 modes for ϵ_x (first column), ϵ_y (second column) and ϵ_{xy} (third column)

K=3

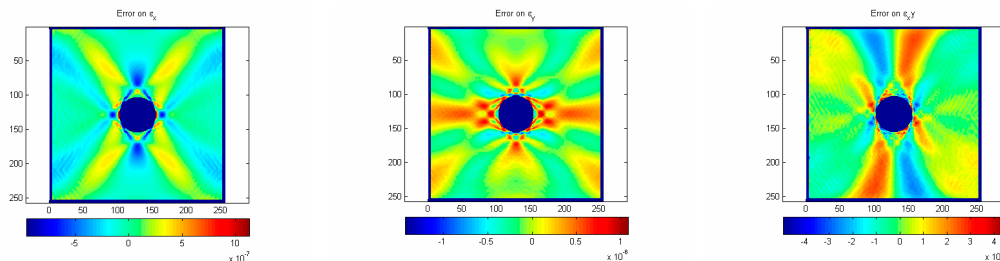


Max error: 1.377e-006

Max error: 1.007e-006

Max error: 1.097e-006

K=4

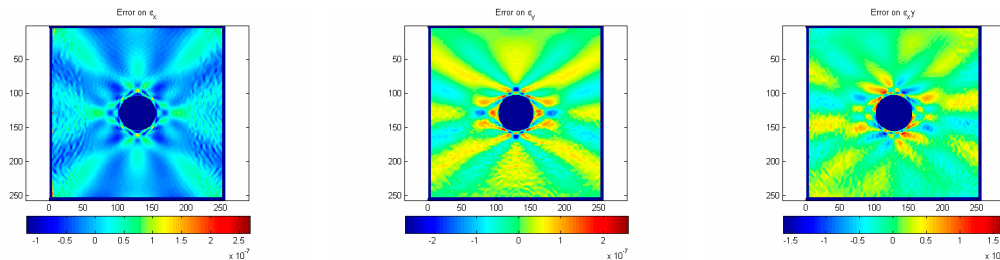


Max error: 1.138e-006

Max error: 1.082e-006

Max error: 4.508e-007

K=5



Max error: 2.683e-007

Max error: 2.589e-007

Max error: 1.689e-007

Figure 6-10. Strain equivalent truncation error in snapshot 199 using 3, 4 and 5 modes for ϵ_x (first column), ϵ_y (second column) and ϵ_{xy} (third column)

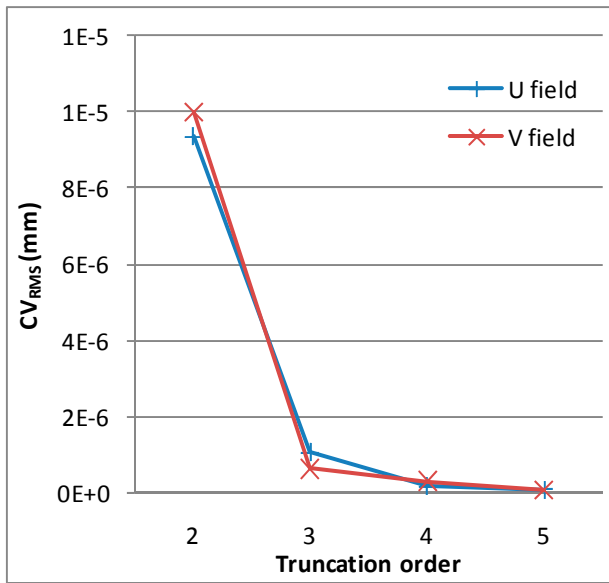


Figure 6-11. Cross validation error (CV_{RMS}) as a function of truncation order.

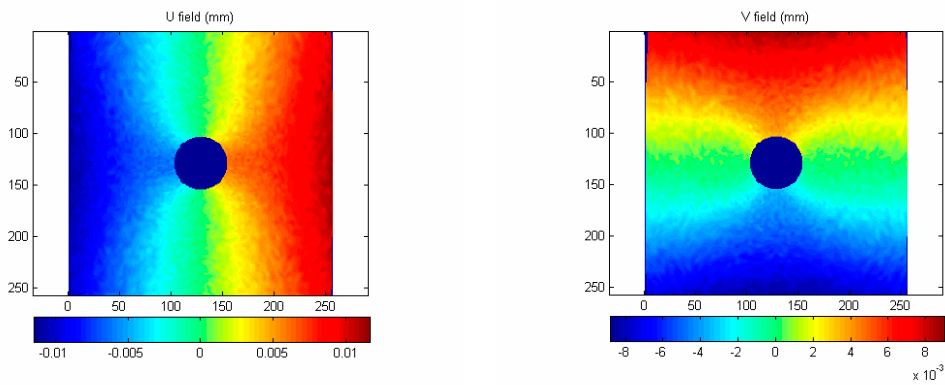


Figure 6-12. Noisy U and V fields of the simulated experiment.

CHAPTER 7

BAYESIAN IDENTIFICATION OF ORTHOTROPIC ELASTIC CONSTANTS FROM FULL FIELD MEASUREMENTS ON A PLATE WITH A HOLE

Introduction

Identification of the four orthotropic elastic constants of a composite from a tensile test on a plate with a hole was carried out by several authors in the past (Lecompte et al. 2005, Silva et al. 2007, Silva 2009) using finite element model updating based on a least squares framework. Some of the advantages of doing the identification from measurements on a plate with a hole are the ability to identify all four properties at the same time from a single experiment. This is possible because of the heterogeneous strain field exhibited during this test which involves all four elastic constants, unlike tension tests on simple rectangular specimen which exhibit uniform strain fields and usually involve only two of the elastic constants. A further advantage is that the heterogeneous fields can provide information on spatial variations of the material properties as well.

In order to capture the strain and displacement non-uniformity on the specimen used for identification, the measurements need to be obtained with high spatial resolution over a large part of the specimen. Techniques that allow to achieve this are called full field measurement techniques. A large variety of optical full field measurement techniques exist and we can divide them into two main categories: white light techniques and interferometric techniques. The most common white light techniques are the grid method (Surrel 2005) and digital image correlation (Sutton et al. 2000). Interferometric full field techniques for displacement measurements are Moiré interferometry (Post et al. 1997) and speckle interferometry (Cloud et al. 1998). An excellent review of identification of material properties based on different full field techniques is provided by Avril et al. (2008).

The objective of the present chapter is to apply the previously developed approach to Bayesian identification to the case of identifying the four ply-elastic constants from Moiré interferometry full field displacement measurements on a plate with a hole. Note that as in the previous chapters we seek here to identify the properties of the ply of the composite laminate. This is more challenging than identifying the homogenized orthotropic elastic constants of the plate because the ply properties affect the displacements in a more indirect way than the homogenized properties, which usually implies that the sensitivity of the displacements to the ply properties is smaller than to the homogenized properties as has been shown in Chapter 5. The interest of identifying ply properties is that it allows to obtain both the extensional and the bending stiffnesses of the laminate. Due however to the varying sensitivity of the strain and displacement fields to the different ply properties, it is of primary importance to estimate the uncertainty with which these properties are identified. The Bayesian approach that we developed in the previous chapters will allow us to do this by taking into account the physics of the problem (i.e. the different sensitivities of the fields to the different properties), measurement uncertainty as well as uncertainty on other input parameters to the model such as the specimen geometry.

The rest of the chapter is organized as follows. First we give a quick overview of the open hole tension test and the way it was modeled. Second we give the Bayesian formulation for the present problem. We then provide details on the response surface construction. This is followed by the Bayesian identification results using a simulated experiment. In the final parts of this chapter we carry out Bayesian identification using actual experimental results on a plate with a hole. We present the Moiré interferometry measurement setup we used, followed by the results of the identification. Finally we provide concluding remarks.

Open Hole Plate Tension Test

The experiment and numerical model used for identification are the same as the ones described in the previous chapter for the POD decomposition. A reader familiar with the previous chapter can thus skip this section.

The experiment considered for the identification is a tensile test on a composite plate with a hole. The laminate is made of graphite/epoxy with a stacking sequence of $[45,-45,0]_s$. The plate has the dimensions given in Figure 7-1, with a ply thickness of 0.16 mm. The applied tensile force is 1200 N. The full field measurement takes place on a square area $20 \times 20 \text{ mm}^2$ around center of the hole.

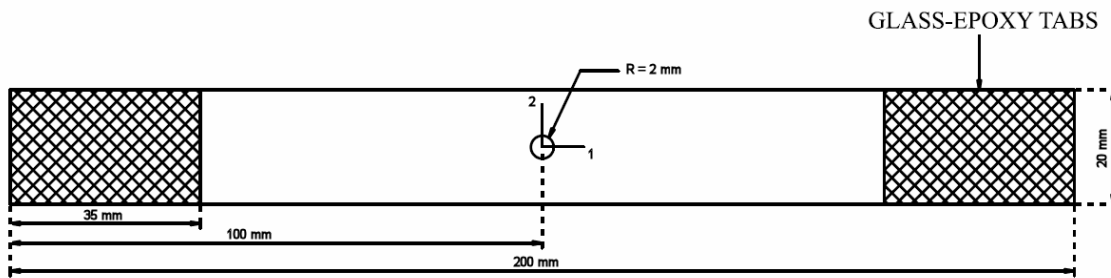


Figure 7-1. Specimen geometry. The specimen material is graphite/epoxy and the stacking sequence $[45,-45,0]_s$. The tensile force is 1200 N.

The plate is modeled using Abaqus[®] finite element software using a total of 8020 S4R (general purpose, four nodes, reduced integration) elements. The center part of the mesh used is represented in Figure 6-2.

The U and V displacements fields from the finite element simulations are described by their POD coefficients α_k . These coefficients are obtained by projecting the fields on the POD basis obtained in the previous chapter. Accordingly a given field U is described approximately by the truncated representation \bar{U} as shown in Eq. 7-1, where Φ_k are the POD modes (i.e. basis vectors) calculated in the previous chapter.

$$\bar{U} = \sum_{k=1}^K \alpha_k \Phi_k = \sum_{k=1}^K \langle U, \Phi_k \rangle \Phi_k \quad (7-1)$$

The truncation order used in this chapter is $K=4$, which we have shown in the previous chapter to lead to a small enough truncation error on the sensitivity fields of the displacements with respect to the material properties to allow potential use in the present identification problem.

Bayesian Identification Problem

Formulation

The Bayesian formulation can be written as follows for the present plate with a hole problem:

$$\pi_{E|\alpha=\alpha^{measure}}(\mathbf{E}) = \frac{1}{K} \pi_{\alpha|E}(\alpha^{measure}) \cdot \pi_E^{prior}(\mathbf{E}) \quad (7-2)$$

where $\mathbf{E} = \{E_1, E_2, \nu_{12}, G_{12}\}$ is the four dimensional random variable of the ply-elastic constants.

$\alpha = \{\alpha_1^U, \dots, \alpha_4^U, \alpha_1^V, \dots, \alpha_4^V\}$ is the eight dimensional random variable of the POD coefficients of the

U and V field. $\alpha^{measure} = \{\alpha_1^{U,measure}, \dots, \alpha_4^{U,measure}, \alpha_1^{V,measure}, \dots, \alpha_4^{V,measure}\}$ is the vector of the eight

“measured” POD coefficients, obtained by projecting the measured full field onto the POD basis.

Equation 7-2 provides the joint probability density function (pdf) of the four elastic constants given the coefficients $\alpha^{measure}$. This pdf is equal to a normalizing constant times the likelihood function of the elastic constants \mathbf{E} given the coefficients $\alpha^{measure}$ times the prior distribution of the elastic constants \mathbf{E} . The prior distribution of \mathbf{E} reflects the prior knowledge we have on the elastic constants based on manufacturer’s specifications. In our case we assumed that we have relatively vague prior knowledge by defining a joint normal prior distribution with relatively wide standard deviations (10%) as defined in Table 7-1. The prior distribution was truncated at the bounds given in Table 5-4, which were chosen in an iterative way such that

eventually the posterior pdf is approximately in the center of the bounds and their range covers approximately four standard deviations of the posterior pdf.

Table 7-1. Normal uncorrelated prior distribution of the material properties for a graphite/epoxy composite material.

Parameter	E ₁ (GPa)	E ₂ (GPa)	ν_{12}	G ₁₂ (GPa)
Mean value	155	11.5	0.3	5
Standard deviation	15.5	1.15	0.03	0.5

Table 7-2. Truncation bounds on the prior distribution of the material properties

Parameter	E ₁ (GPa)	E ₂ (GPa)	ν_{12}	G ₁₂ (GPa)
Lower truncation bound	148	9	0.25	4.7
Upper truncation bound	162	12	0.35	5.3

The other term on the right hand side of Equation 7-2 is the likelihood function of the elastic constants given the POD coefficients $\alpha^{measure}$. This function measures the probability of getting the test results for a given value of the elastic constants \mathbf{E} , and consequently, it provides an estimate of the likelihood of different \mathbf{E} values given the test results. The uncertainty in the POD coefficients can have several causes which are detailed next.

Sources of Uncertainty

A typical cause of uncertainty in the problem is measurement error. In the case of full field measurements we usually obtain a noisy field, that can possibly be decomposed into a signal component and a white noise component.

Another uncertainty in the identification process is due to uncertainty in the other input parameters of the plate model such as uncertainty in the thickness of the plate. Other sources of uncertainty, such as misalignment of the center of the hole or misalignment of the loading direction can also be present. These could also be accounted for in the Bayesian identification by a more complex parameterization of the numerical finite element model. For simplicity we

parameterized in the present chapter only uncertainty in the thickness of the plate h , which was assumed to be distributed normally with a mean value of 0.96 mm (the prescribed specimen thickness) and a standard deviation of 0.005 mm (the typical accuracy of a microcaliper). Alignment uncertainty as well as other types of uncertainty can however still be considered with somewhat decreased fidelity through a generic uncertainty term on the POD coefficients.

The next section develops the implementation of the error model corresponding to these uncertainties. Monte Carlo simulation is then used to propagate the uncertainty effect to the POD coefficients and finally to the likelihood function.

Error Model

In the present section we describe the procedure we developed for moving from the measurement noise on the full field displacement fields to corresponding measurement uncertainties on the POD coefficients $\alpha^{measure}$. This involves understanding the way the noise is projected onto the POD basis.

We make here the assumption that the measurement noise is a white Gaussian noise. In this case a measured field can be decomposed into the signal component and the white noise component as shown in Equation 7-3.

$$\mathbf{U}^{measure} = \mathbf{U}^{ms} + \boldsymbol{\varepsilon} \quad \text{where} \quad \boldsymbol{\varepsilon} \sim \square(0, \sigma^2) \quad (7-3)$$

$\mathbf{U}^{measure}$ is the vector of the measured displacements and has a size of $N \times 1$, with N being the number of points (pixels) where a measurement is available. \mathbf{U}^{ms} is the vector of the signal part in the measured field, while $\boldsymbol{\varepsilon}$ is the vector of the noise with each of the N components being normally distributed with a mean value of 0 and a standard deviation of σ .

We look now at what happens if we project the measured field onto the POD basis.

Denoting by Φ the matrix of the Φ_k basis vectors, $\Phi = [\Phi_1, \dots, \Phi_K]$, which has a size of $N \times K$, the projection can be written as shown in Equation 7-4.

$$\Phi^T \mathbf{U}^{measure} = \Phi^T \mathbf{U}^{ms} + \Phi^T \boldsymbol{\varepsilon} \Leftrightarrow \boldsymbol{\alpha}^{measure} = \boldsymbol{\alpha}^{ms} + \boldsymbol{\eta} \quad (7-4)$$

At this point we seek to characterize the noise on the POD coefficients $\boldsymbol{\eta} = \Phi^T \boldsymbol{\varepsilon}$, which results from the noise on the displacement field. Since $\boldsymbol{\eta}$ is a linear combination of Gaussian random variables it is also Gaussian. Accordingly we only need to calculate its mean and variance-covariance matrix, provided in Eq. 7-5 and 7-6 respectively.

$$E(\boldsymbol{\eta}) = E(\Phi^T \boldsymbol{\varepsilon}) = \Phi^T E(\boldsymbol{\varepsilon}) = 0 \quad (7-5)$$

$$VCov(\boldsymbol{\eta}) = E\left[(\boldsymbol{\eta} - E(\boldsymbol{\eta}))(\boldsymbol{\eta} - E(\boldsymbol{\eta}))^T\right] = E(\boldsymbol{\eta}\boldsymbol{\eta}^T) = E(\Phi^T \boldsymbol{\varepsilon}\boldsymbol{\varepsilon}^T \Phi) = \Phi^T E(\boldsymbol{\varepsilon}\boldsymbol{\varepsilon}^T) \Phi = \sigma^2 \Phi^T \Phi \quad (7-6)$$

Because the POD vectors form an orthonormal basis we have $\Phi^T \Phi = I_K$, where I_K represents the identity matrix of size $K \times K$. This means that the variance covariance matrix can be written simply as:

$$VCov(\boldsymbol{\eta}) = \sigma^2 I_K \quad (7-7)$$

Equations 7-5 and 7-7 imply that the uncertainty on the POD coefficients resulting from the white noise on the displacement fields is also normally distributed and has a zero mean, zero correlation and the same standard deviation as the white gaussian noise on the displacement field.

Note that since we use a truncated POD projection of the fields there is also truncation error involved in the modeling. Since we have shown in the previous chapter that the truncation error was smaller than 0.01% using four POD modes, it would have a negligible effect compared to the other sources of uncertainty in the problem.

Bayesian Numerical Procedure

As in the previous chapters the major challenge is in constructing the likelihood function, which we construct point by point again. We evaluate it at a grid in the four-dimensional space of the material properties $\mathbf{E} = \{ E_1, E_2, \nu_{12}, G_{12} \}$. We chose here an 17^4 grid, which is determined by convergence and computational cost considerations.

At each of the grid points, \mathbf{E} is fixed and we need to evaluate the probability density function (pdf) of the POD coefficients, $\pi_{\alpha/E=E^{fixed}}(\boldsymbol{\alpha})$, at the point $\boldsymbol{\alpha} = \boldsymbol{\alpha}^{measure}$. The pdf of the POD coefficients is determined by propagating through Monte Carlo with 4000 simulations the uncertainties in the plate thickness and adding a sampled value of the normally distributed uncertainty on the POD coefficients resulting from the measurement noise, as described in the previous section.

The resulting samples were found to be close to Gaussian, they were thus fitted by such a distribution, by calculating mean and variance-covariance matrix. This Gaussian nature is due to the fact that the uncertainty resulting from the measurement noise is Gaussian and the uncertainty due to thickness is proportional to $1/h$ which can in this case be well approximated by a normal distribution. The distribution $\pi_{\alpha/E=E^{fixed}}(\boldsymbol{\alpha})$ was then evaluated at the point $\boldsymbol{\alpha} = \boldsymbol{\alpha}^{measure}$, leading to $\pi_{\alpha/E=E^{fixed}}(\boldsymbol{\alpha}^{measure})$. \mathbf{E}^{fixed} is then changed to the next point on the grid and the procedure repeated.

Response Surface Approximations of the POD coefficients

Even though we reduced the dimensionality of the full field using the POD decomposition, the calculation of the POD coefficients is up to now still based on finite element results. Since about 700 million evaluations need to be used for the Bayesian identification procedure, finite element simulations remain prohibitive so we will seek to construct response surface

approximations (RSA) of the POD coefficients, α_k , as functions of the four elastic constants to be identified and the thickness of the plate, which has some uncertainty that we want to account for.

We seek polynomial response surface (PRS) approximations under the form $\alpha_k = \text{PRS}(E_1, E_2, \nu_{12}, G_{12}, h)$. Note that we will not construct nondimensional RSA in the present chapter because the time that had to be spent on going through the process did not seem to be justified by the advantages of doing so. The two main advantages of nondimensionalization are either a significantly reduced number of variables or increased accuracy due to the response having a more easily expressible form in terms of the nondimensional variables. For the plate with hole problem the maximum reduction in the number of variables could have been only from 5 to 4. As far as accuracy goes we found that the dimensional response surface already have very good accuracy as will be shown a few paragraphs later. Accordingly, we chose to keep dimensional response surface approximations in this chapter.

Third degree polynomial response surface approximations were constructed from the same 200 samples that were used in the previous chapter to construct the POD basis. These 200 points were sampled using Latin hypercube within the bounds given in Table 6-1.

The error measures used to assess the quality of the RSA fits are given in Table 7-3 for the first four POD coefficients of the U fields and in Table 7-4 for those of the V fields. The second row gives the mean value of the POD coefficient across the design of experiments (DoE). The third row provides the standard deviation of the coefficients across the DoE, which gives an idea of magnitude of variation in the coefficients. Row four provides R^2 , the correlation coefficient obtained for the fit, while row five gives the root mean square error among the DoE points. The final column gives the cross validation PRESS error (Allen 1971, see also Appendix A) which was also used in the previous chapters.

Table 7-3. Error measures for RSA of the U-field POD.

POD coefficient RSA	α_1	α_2	α_3	α_4
Mean value of α_i	$-4.04 \cdot 10^{-1}$	$-3.40 \cdot 10^{-5}$	$-2.20 \cdot 10^{-5}$	$-8.35 \cdot 10^{-7}$
Standard deviation of α_i	$8.19 \cdot 10^{-2}$	$6.92 \cdot 10^{-4}$	$2.01 \cdot 10^{-4}$	$2.80 \cdot 10^{-5}$
R^2	0.99999	0.99993	0.99992	0.99951
RMS error	$2.77 \cdot 10^{-4}$	$6.32 \cdot 10^{-6}$	$2.01 \cdot 10^{-6}$	$6.75 \cdot 10^{-7}$
PRESS error	$3.61 \cdot 10^{-4}$	$7.92 \cdot 10^{-6}$	$2.67 \cdot 10^{-6}$	$9.33 \cdot 10^{-7}$

Table 7-4. Error measures for RSA of the V-field POD.

POD coefficient RSA	α_1	α_2	α_3	α_4
Mean value of α_i	$-2.97 \cdot 10^{-1}$	$-9.51 \cdot 10^{-5}$	$-2.14 \cdot 10^{-5}$	$9.76 \cdot 10^{-7}$
Standard deviation of α_i	$5.40 \cdot 10^{-2}$	$2.26 \cdot 10^{-3}$	$3.10 \cdot 10^{-4}$	$1.50 \cdot 10^{-5}$
R^2	0.99999	0.99992	0.99987	0.99830
RMS error	$1.69 \cdot 10^{-4}$	$2.26 \cdot 10^{-5}$	$3.88 \cdot 10^{-6}$	$6.89 \cdot 10^{-7}$
PRESS error	$2.45 \cdot 10^{-4}$	$3.05 \cdot 10^{-6}$	$5.27 \cdot 10^{-6}$	$1.04 \cdot 10^{-6}$

Comparing the error measures to the standard deviations of the coefficients we considered that the RSA have good enough quality to be used in the identification process, with the approximation error being small enough to be considered negligible compared to the other sources of uncertainty.

As a summary, a flow chart of the cost and dimensionality reduction procedure used for the likelihood function construction is provided in Figure 7-2. The cost reduction achieved by the RSA is shown in green while the dimensionality reduction achieved by the POD in red. The construction of the POD basis from finite element samples was described in the previous chapter. The same finite element simulations also served for the construction of the response surface approximations in terms of the POD coefficients as described in the present section. Finally the experimental displacement fields are also projected onto the POD basis to obtain the terms $\alpha^{measure}$.

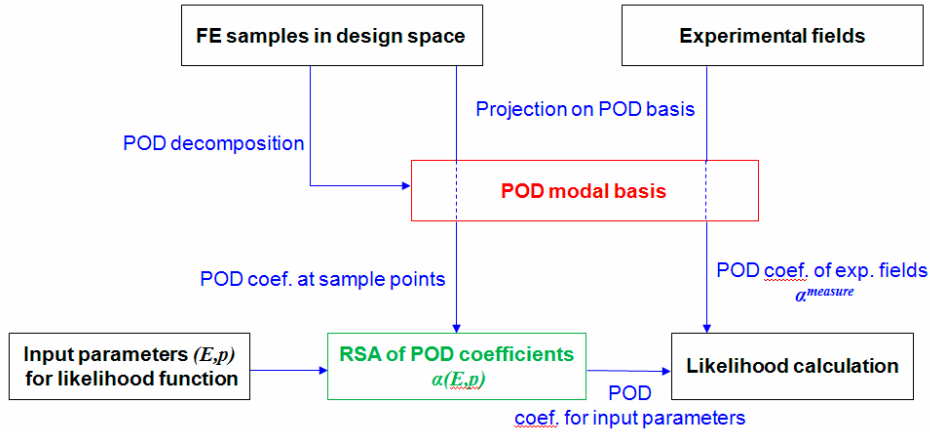


Figure 7-2. Flow chart of the cost (in green) and dimensionality reduction (in red) procedure used for the likelihood function calculation.

Bayesian Identification on a Simulated Experiment

In order to test our procedure we carried out the Bayesian identification on a simulated experiment first. The U and V fields of the first simulated experiment were obtained by running the Abaqus finite element model of the plate with the parameters given in Table 7-5.

Coming from a finite element simulation the fields are relatively smooth, thus not representative of true experimental fields that are usually noisier. Thus we added white noise on top of the finite element fields with a standard deviation of 2.5% of the mean value of the field. For a graphical representation of the noisy fields of the simulated experiment see Figure 6-12. The results of the identification are provided in Tables 7-6 and 7-7.

Table 7-5. Material properties used for the simulated experiments.

Parameter	E_1 (GPa)	E_2 (GPa)	ν_{12}	G_{12} (GPa)
Value	155	11	0.3	5

Table 7-6. Mean values and coefficient of variation of the identified posterior distribution for the simulated experiment.

Parameter	E_1 (GPa)	E_2 (GPa)	ν_{12}	G_{12} (GPa)
Mean value	155	10.7	0.29	5.01
COV (%)	2.23	5.67	9.33	3.02

Table 7-7. Correlation matrix (symmetric) of the identified posterior distribution for the simulated experiment.

	E_1	E_2	ν_{12}	G_{12}
E_1	1	0.43	-0.18	0.60
E_2	-	1	-0.22	-0.07
ν_{12}	-	-	1	0.62
G_{12}	-	-	-	1

The mean value of the identified distribution was found to be very close to the true values used in the Abaqus simulation, which is reassuring. As far as the coefficients of variation, there are, as for the vibration based identification, significant differences between the parameters. While the longitudinal Young's modulus E_1 of the ply is identified most accurately, the Poisson's ratio ν_{12} of the ply is again identified with the highest uncertainty. Unlike for the vibration problem, E_2 is identified here with a higher uncertainty than G_{12} . This is due to the stacking sequence $[45,-45,0]_s$ which does not have a 90° ply, thus making it more difficult to identify E_2 from this traction test in the 1-direction.

As for the vibration based identification, the uncertainty with which ν_{12} is identified is relatively high, much higher than what would be obtained from a tensile test on a unidirectional laminate. The high uncertainty in this case, results from the fact that we identify the ply properties of a laminate that is not unidirectional, which, as mentioned on previous occasions, is a more challenging problem than identifying the properties of a unidirectional laminate or the homogenized properties of a more complex laminate. As we have shown in the last section of Chapter 5 for the vibration problem, identifying the homogenized properties of the laminate results in a significantly reduced uncertainty in the Poisson's ratio of the plate ν_{xy} .

Bayesian Identification on a Moiré Full Field Experiment

To apply the Bayesian identification to actual experimental data we carried out full field measurements on an open hole tension test using the Moiré interferometry technique. This measurement technique was chosen because of its good resolution, its insensitivity to out-of-plane displacements, its ability to directly compensate for rigid body rotations and its very high spatial resolution. Furthermore significant firsthand experience was available at the University of Florida through the Experimental Stress Analysis Laboratory of Dr. Peter Ifju, which facilitated the setup of the experiment. For details on the Moiré interferometry technique and associated theory refer to Appendix D.

Full Field Experiment

Initially, specimens according to the specifications provided at the beginning of this chapter were thought to be fabricated. Due to various manufacturing constraints and tolerances however, the final specimen used for the measurements had slight differences for some of the dimensions: the width of the specimen was 24.3 mm, the hole radius was 2.05 mm and the total laminate thickness was 0.78mm. The plate was made out of a Toray[®] T800/3631 graphite/epoxy prepreg. The manufacturer's specifications for this material are given in Table 7-8 together with the properties obtained by Noh (2004). Noh obtained the material properties based on a four points bending test at the University of Florida on a composite made from the exact same prepreg roll that we used.

Table 7-8. Manufacturer's specifications and properties found by Noh (2004) based on a four points bending test.

Parameter	E_1 (GPa)	E_2 (GPa)	ν_{12}	G_{12} (GPa)
Manufacturer's specifications	162	7.58	0.34	4.41
Noh (2004) values	144	7.99	0.34	7.78

A picture of our specimen with the diffraction grating (1200 lines/mm) is shown in Figure 7-3. The specimen was loaded at 700 N for the measurements. The experiment was carried out together with Weiqi Yin from the Experimental Stress Analysis Laboratory. An ESM Technologies PEMI II 2020-X Moiré interferometer using a Pulnix TM-1040 digital camera were utilized. The traction machine was an MTI-30K. Rotations of the grips holding the specimen were allowed by using a lubricated ball bearing for the bottom grip and two lubricated shafts for the top grip. This allowed to reduce parasitic bending during the tension test. A picture of the experimental setup is given in Figure 7-4.

The fringe patterns observed for a force of 700 N are shown in Figures 7-5. The two smaller holes and other parasitic lines are due to imperfections in the diffraction grating.

The phase shifting method (see Appendix D) was used to extract the displacement fields from the fringe patterns. A Matlab automated phase extraction tool developed by Yin (2008) was utilized and the corresponding displacement maps are provided in Figures 7-6. The two displacement maps will be used in the Bayesian identification procedure.

At this point it is worth noting that the identification procedure will use the POD projection of these maps, which will filter out some information present in the initial fields. This can have both positive and negative effects. Obvious negative effects are that the identification procedure will not be able to account for any information that was filtered out and that might have been useful to the identification or the propagation of uncertainties.

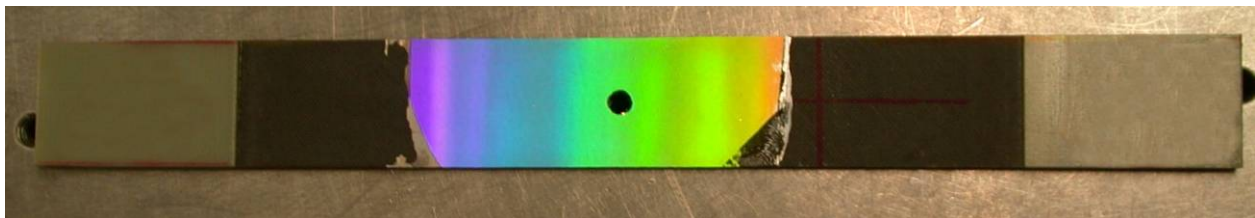


Figure 7-3. Specimen with the Moiré diffraction grating (1200 lines/mm).

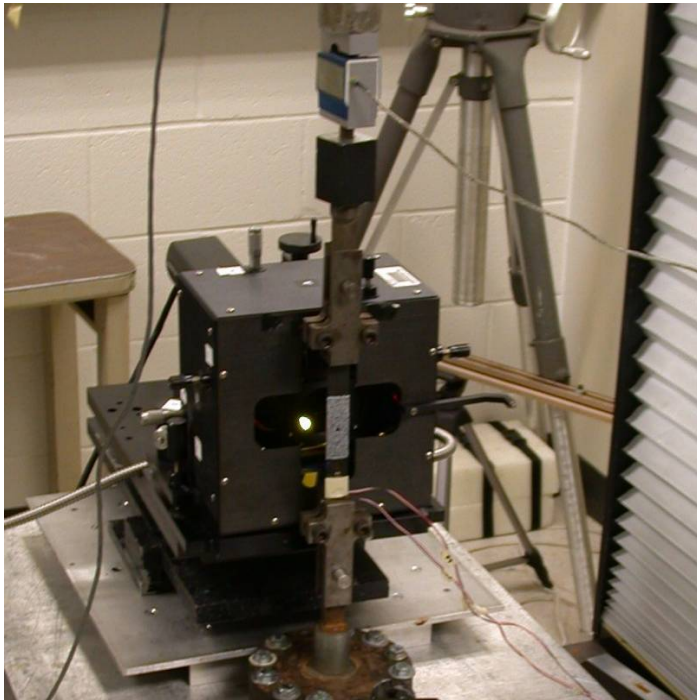


Figure 7-4. Experimental setup for the open hole tension test.

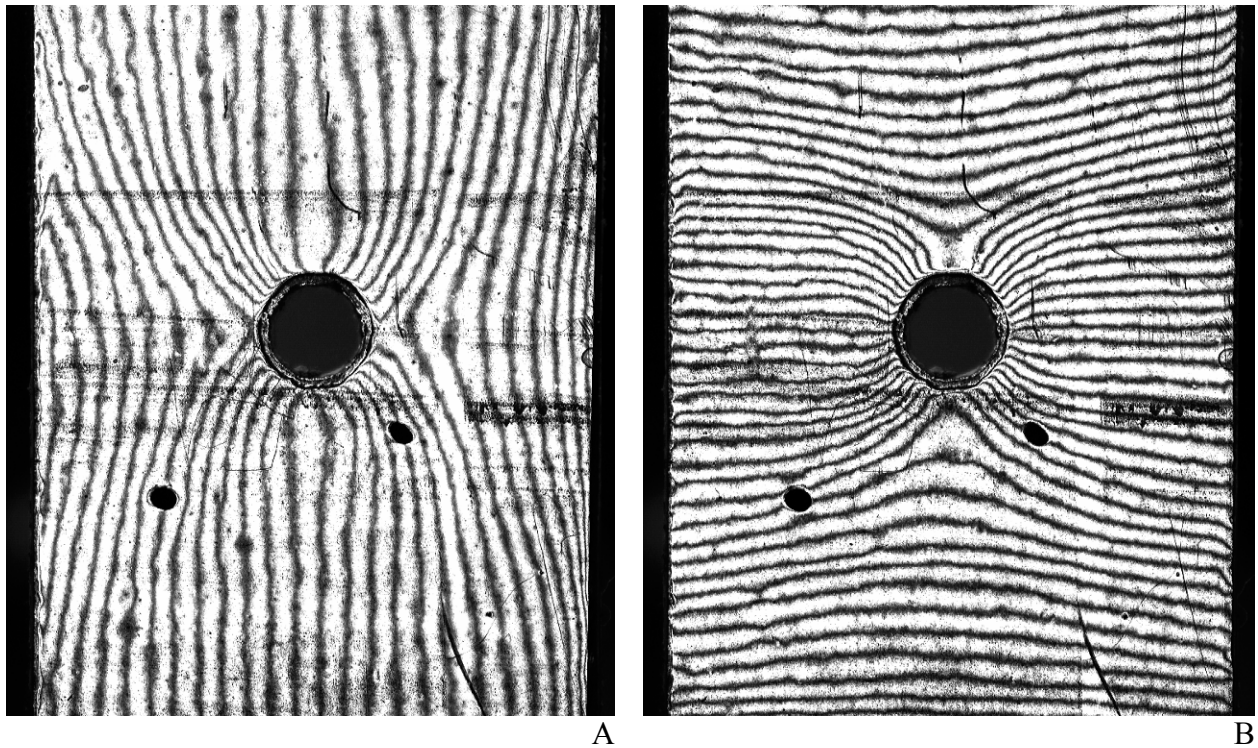


Figure 7-5. Fringe patterns in the: A) U direction. B) V direction for a force of 700N.

On the other hand if the information filtered out is mainly related to the analysis tools used (e.g. phase extraction algorithm) it can be useful to leave out these artifacts since they do not have physical meaning in relation to the material properties. An investigation of the errors left out is presented in Appendix E, where we found that while the difference between the experimental fields and their POD projection is not necessarily negligible, a significant part of it seems to be related to phase the extraction algorithm, thus not having a physical meaning directly related to the experiment.

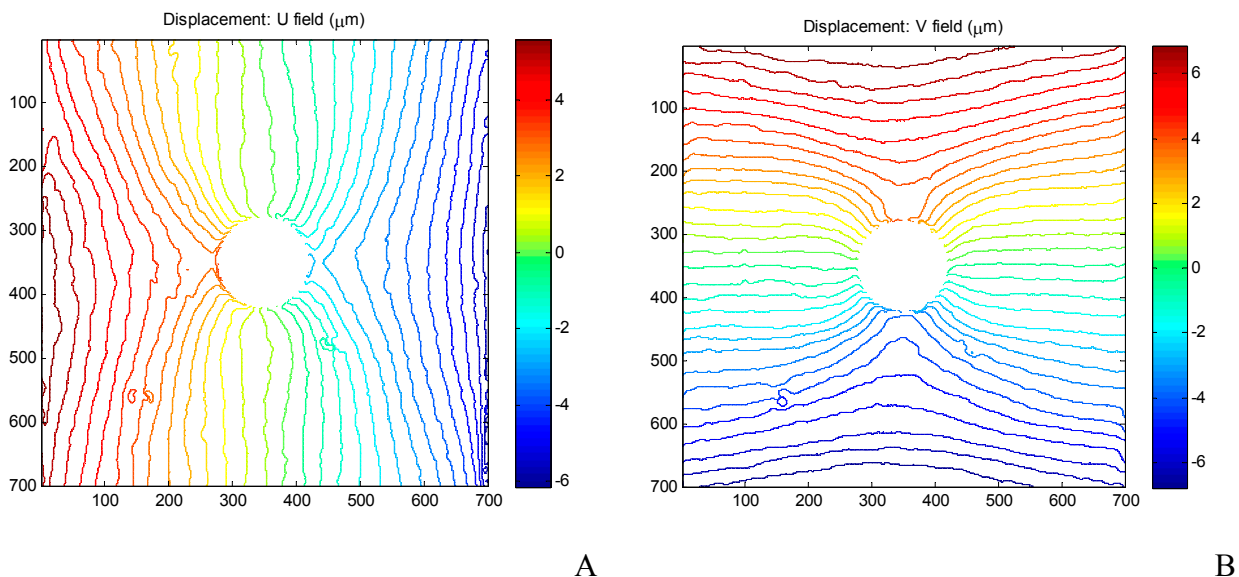


Figure 7-6. Displacement fields obtained from the fringe patterns (no filtering was used at all) in: A) The U direction. B) The V direction.

Bayesian Identification on Moiré Full Field Displacements

The dimensions of the specimen for the Moiré experiment were slightly different than those used to construct the response surface approximations (RSA) in the previous sections. Accordingly new RSA of the POD coefficients were constructed for the dimensions of the Moiré specimen. A similar quality of the fit was obtained which was again considered good enough to use the RSA in the Bayesian procedure.

The experimental fields obtained in the previous section were projected onto the POD basis providing the coefficients $\alpha_i^{measure}$. Same Bayesian procedure was used as for the simulated experiment. However, an additional source of uncertainty had to be accounted for, representing various sources of modeling errors. This is because our Abaqus[®] model does not perfectly model the actual experiment and additional possible error sources are misalignment of the grips or of the traction force or variation in the position of the hole. These potential errors are modeled as an additional normally distributed uncertainty on the POD coefficients. Zero mean is assumed and the magnitude of the uncertainty (standard deviation) is determined iteratively in an empirical way. A quick Bayesian identification is carried out using a high standard deviation, which is then reduced to the value of the difference between the experimental POD coefficients and the mean value of the identified POD coefficients (the noise uncertainty component on the POD coefficients is also subtracted). The difference was found to be of the order of 0.4% of the POD coefficients.

The prior distribution is assumed to have the parameters given in Table 7-9 based on the Toray[®] prepreg specification (see Table 7-8). The prior distribution was truncated at the bounds given in Table 7-10, which were chosen in an iterative way such that eventually the posterior pdf is approximately in the center of the bounds and their range covers approximately four standard deviations of the posterior pdf.

The results of the identification are provided in Tables 7-11 and 7-12. We will also provide later the results using a prior based on Noh's values. Note that we assumed a relatively wide prior with a 10% COV due to the relatively large differences between the manufacturer's specifications and Noh's values.

Table 7-9. Normal uncorrelated prior distribution of the material properties. Mean values are based on Toray[®] material specifications.

Parameter	E_1 (GPa)	E_2 (GPa)	ν_{12}	G_{12} (GPa)
Mean value	162	7.58	0.34	4.41
Standard deviation	16	0.75	0.03	0.5

Table 7-10. Truncation bounds on the prior distribution of the material properties

Parameter	E_1 (GPa)	E_2 (GPa)	ν_{12}	G_{12} (GPa)
Lower truncation bound	126	6	0.26	4.25
Upper truncation bound	151	9.5	0.36	5.75

Table 7-11. Mean values and coefficient of variation of the identified posterior distribution from the Moiré interferometry experiment.

Parameter	E_1 (GPa)	E_2 (GPa)	ν_{12}	G_{12} (GPa)
Mean value	138	7.48	0.33	5.02
COV (%)	3.12	9.46	10.3	4.29

Table 7-12. Correlation matrix (symmetric) of the identified posterior distribution from the Moiré interferometry experiment.

	E_1	E_2	ν_{12}	G_{12}
E_1	1	0.020	-0.045	0.52
E_2	-	1	-0.005	-0.17
ν_{12}	-	-	1	0.24
G_{12}	-	-	-	1

Overall the mean values of the identified distribution are in agreement with the manufacturer's specifications. The largest difference is in longitudinal Young's modulus, which could seem somewhat surprising. However Noh (2004) found a similar value on the exact same prepreg roll that we used. The mean values of E_2 , ν_{12} and G_{12} are close to the specification values. G_{12} is far however from Noh's values but it should be noted that the four point bending test is relatively poor for identifying G_{12} .

In terms of uncertainty we find the same trend as with the simulated experiment, namely E_2 and ν_{12} being identified with the largest uncertainties. It seems however that the added

uncertainty accounting for misalignment does not affect the uncertainties of the four properties in the same way, E_2 being the most affected.

In terms of correlation between the material properties we find that the same general trend is observed as for the simulated experiment. However the current correlations are somewhat lower in absolute value, which is due to the added normal uncorrelated uncertainty on the POD coefficients compared to the simulated experiment.

In Table 7-12 we also provide the mean values and COV of the posterior distribution that was identified using a prior centered in the properties found by Noh (2004), see Table 7-8, with a 10% standard deviation again and the same truncation bounds (see Table 7-10). We can see that the identified parameters change very little. This is because the properties where there is a big difference in the prior mean values can be determined quite accurately from this experiment, meaning that the prior will have relatively little effect on them.

Table 7-12. Mean values and coefficient of variation of the identified posterior distribution from the Moiré interferometry experiment using a prior based on Noh's (2004) values.

Parameter	E_1 (GPa)	E_2 (GPa)	ν_{12}	G_{12} (GPa)
Mean value	139	7.69	0.33	5.22
COV (%)	3.05	9.31	10.3	4.10

It is worth noting however that the prior distribution had a significant effect on the uncertainty with which E_2 and ν_{12} were identified. If for example we only had a uniform prior (with bounds of +/-20% around the mean value of the likelihood function) instead of the Gaussian one, then ν_{12} would have been identified with a 14.5% COV instead of 10.3%. This is again due to the relative insensitivity of the fields to ν_{12} . So while the prior had a large effect on the uncertainty of some of the properties, we did not assume a particularly narrow prior. Based on tests on unidirectional laminates, prior estimates of E_2 and ν_{12} with a standard deviation of about 5% or less can probably be obtained. The applicability of priors obtained from tests on

unidirectional laminates to the identification of ply properties from more complex laminates needs however to be investigated, since differences in the manufacturing of the two kinds of laminates might increase the uncertainty.

As a final remark, it might seem surprising that the property that is identified with the lowest uncertainty (E_I) is also the one which is the farthest away from the manufacturer's specifications. However it is worth recalling that the identification does not account for interspecimen variability of the material properties. The identified distribution of the properties is specific to the specimen and the experiment. Thus if the specimen deviates somewhat from the manufacturer's specification it is not contradictory that while identifying a property far away from the specifications this can still be the property identified with the lowest uncertainty. The interspecimen variability would then have to be estimated by repeating test on multiple specimens.

Summary

In the present chapter we implemented the Bayesian identification for full field displacements on a plate with a hole. This required the combined use of response surface methodology and dimensionality reduction based on proper orthogonal decomposition to make the approach computationally tractable.

A test case on a simulated experiment showed that the proposed approach can accurately identify the orthotropic elastic constants of the ply from noisy displacement fields. A real test case was then used based on Moiré interferometry measurements. This allowed, as for the vibration based identification, to quantify the uncertainties with which the material properties can be identified from the given experiment. At this point it is worth to remind that the uncertainty with which the properties are identified is specific to the specimen and the experiment and this can be easily verified by noting that the uncertainties identified from the

displacement fields is different than the one identified from the natural frequencies in the earlier chapters.

CHAPTER 8 SUMMARY AND FUTURE WORK

Summary

Estimating the uncertainties with which material properties are identified can be of great interest in the context of reliability analysis. Bayesian identification can estimate these by providing a probability density function for the identified properties. The approach can account for measurement and modeling uncertainty as well as the intrinsic equations of the problem when determining uncertainty (variance) and correlation (covariance) of the identified properties.

On simple analytical test problems we have identified situations where the statistical nature of the Bayesian approach allows it to systematically lead to more accurate results compared to a deterministic identification approach, the traditional least squares method. Such situations are when the responses have different sensitivity to the parameters to be identified or when the responses have different uncertainties or are correlated. The impact of these effects on the identified properties is problem dependent but can reach significant levels as we have shown on the three bar truss test problem.

A major issue in using the Bayesian identification to its full capabilities is however computational time. To be applicable in the general case, the Bayesian method requires Monte Carlo simulation, which substantially increases computational cost. While on the previous test problems the analytical nature of the response allowed reasonable computation times, this would no longer be the case if the Bayesian method was applied to more complex identifications that require numerical models for the response. To deal with the computational cost issue we chose to apply the response surface methodology to construct a surrogate model of the expensive numerical simulator. In order to obtain improved accuracy and reduced construction cost we developed a procedure that combines nondimensionalization and global sensitivity analysis for

the response surface approximation (RSA) construction. This procedure was first introduced and illustrated on a material selection problem for an integrated thermal protection system.

We then applied the procedure to construct nondimensional response surface approximations of the natural frequencies of free composite plates. These were to be used for the Bayesian identification of orthotropic elastic constants from plate vibration experimental results. We tested the accuracy of the approximations and showed that they had excellent fidelity. We also compared the use of these RSA and of analytical approximate vibration solutions in identification. We showed that only the high fidelity response surface approximations have a high enough accuracy to correctly identify the elastic constants for the vibration problem we considered.

To close the chapters on vibration based identification we applied the Bayesian method employing the developed frequency surrogates to the identification of orthotropic elastic constants using actual vibration measurements. We developed an error model accounting for measurement uncertainty, modeling error and uncertainty in other model input parameters. The identified probability density function for the elastic constants showed that the different properties are identified with different confidence and that some are strongly correlated.

In the last two chapters we considered the identification of elastic constants based on full field displacement measurements. This problem introduced an additional challenge due to the very high number of measurements (each pixel of the full field images representing a measurement point). We addressed this issue by reducing the dimensionality of the fields through modal reduction. Proper orthogonal decomposition was used to find the optimal modes based on a given number of samples and we have shown that only four modes for each of the two displacement components are sufficient to accurately represent the fields and carry out the

identification. It is worth noting that this approach allowed a dimensionality reduction from several thousands to only four parameters.

Finally, using the proper orthogonal decomposition in combination with response surface methodology, we applied the Bayesian identification approach to identifying orthotropic elastic constants from full field displacement measurements on a plate with a hole under tension. The approach was first validated on a simulated experiment. An actual Moiré interferometry experiment was then carried out, which provided the displacement full field measurements. The Bayesian identification was applied to these, providing the uncertainty structure with which the elastic constants are identified for this particular experiment.

Future Work

In this section we will provide a few directions that we think would be worth pursuing either in order to further enhance the Bayesian identification method or in order to make the best use of it.

In the present work we applied techniques such as response surface methodology or modal reduction in order to decrease the cost of Bayesian identification in cases that are more general than the usually considered Gaussian uncertainty structure. In spite of the drastic cost reduction achieved with these techniques the approach remains though on the verge of reasonable computational time. Since our technique is based on Monte Carlo simulation we think that using the independence of the different sources of uncertainty can allow to further decrease computational time by several orders of magnitudes. As mentioned in the Bayesian procedure section of Chapter 5 this involves using the expected improvement for multivariate distributions in order to sample the uncertainties separately.

A further interesting future work direction is in the possible combination of several experiments and experimental techniques for identifying the material properties. In the absence

of statistical information it is relatively difficult to combine identified properties coming from different experiments because there is no simple way to determine what confidence to affect to each experiment when combining them. Since the Bayesian approach identifies a probability density function it includes a measure of the confidence in the properties. This makes combining properties from multiple experiments or experimental techniques straightforward as long as the various sources of uncertainty in each can be accurately assessed. The potential of combining multiple experiments on the same specimen resides in narrowing the uncertainties for all four orthotropic elastic constants, since from one single experiment some properties can only be identified with relatively poor confidence. A first attempt in these directions is already planned by carrying out the Moiré experiment again at the laboratory in Saint Etienne. The use of digital image correlation of digital image correlation on the reverse side of the specimen is also being planned.

Another point worth further investigating would be determining the best way to use all available uncertainty information from tests in reliability based design. The uncertainty identified through Bayesian identification is specimen specific, thus represents only one part of the total uncertainty affecting design. The other part is inter-specimen variability and would have to be estimated from multiple tests. Since this variability is usually estimated from a usually low number of tests, the confidence in the statistical estimates will play a large role in the total uncertainty that would then be used in reliability based design. Initial work in combining the various uncertainties in a reliability based design framework has been started by Smarslok (2009).

APPENDIX A POLYNOMIAL RESPONSE SURFACE APPROXIMATIONS

Background

Response surface approximations also known as surrogate models are widely accepted as an extremely useful tool for approximating the response of computationally expensive problems. A polynomial response surface approximation is the simplest form of surrogate model. Yet in spite of its relative simplicity it has been successfully applied to engineering problems in numerous fields.

Kaufman et al. (1996), Balabanov et al. (1996, 1999), Papila and Haftka (1999, 2000), and Hosder et al. (2001) constructed polynomial response surface (PRS) approximations for multidisciplinary design optimization studies of high speed civil transport aircraft. Hill and Olson (2004) applied PRS to noise models for the conceptual design of transport aircrafts. Rikards et al. (2001, 2003, 2004) and Ragauskas and Skukis (2007) applied PRS to the identification of elastic constants from natural frequency measurements.

Polynomial response surface approximation is a type of surrogate modeling employing polynomial functions of the variables to approximate the desired response. The aim is to fit a polynomial function to a limited number of simulations of the response.

The basic idea is illustrated in Figure A-1 for a simple one-dimensional case. The circles are the available simulations y_i of the response y at a given number of design points $x^{(i)}$. A polynomial function in x (2nd degree polynomial here) is fitted through these points using classical regression techniques.

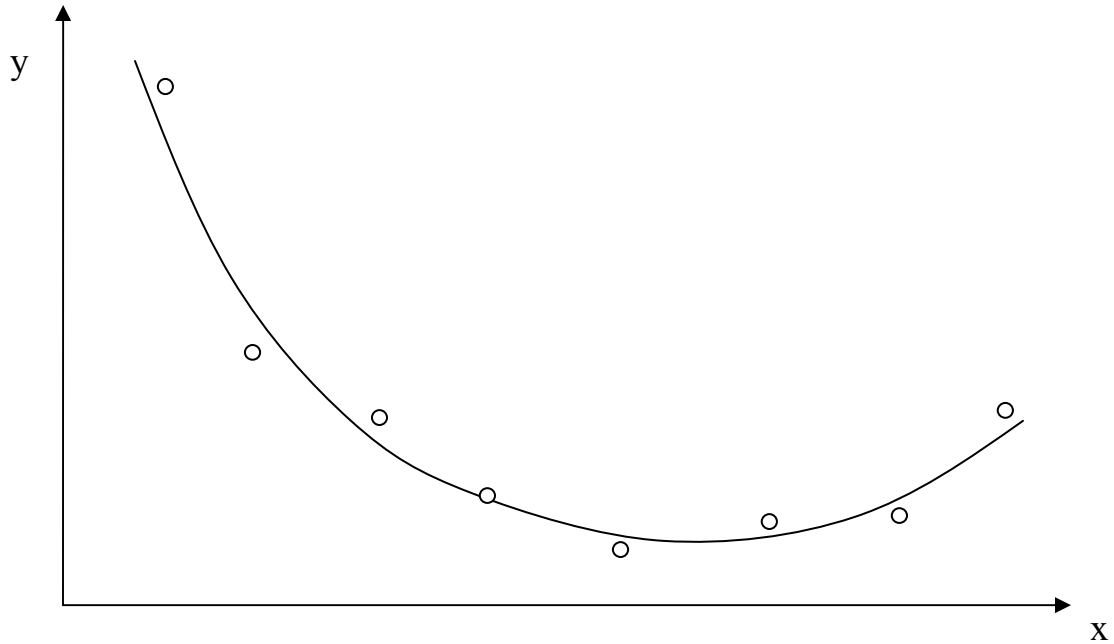


Figure A-1. One dimensional polynomial response surface approximation

Polynomial Response Surface Approximation Modeling

General Surrogate Modeling Framework

The general steps in the construction of a polynomial response surface, as for all surrogate models, are shown in the flowchart of Figure A-2.

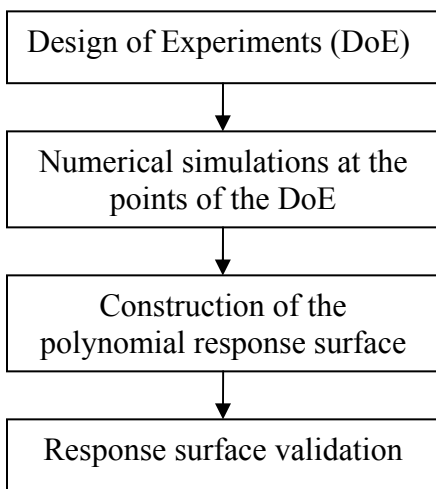


Figure A-2. Steps in surrogate modelling

Design of Experiments (DoE)

The first step is the design of experiments. This consists of sampling points in the original design space, points at which the numerical simulations will be carried out. Well known design of experiment strategies include factorial designs, central composite designs, Box-Behnken designs, variance optimal designs, orthogonal arrays, latin hypercube sampling. For a detailed overview of these techniques the reader can refer to Myers and Montgomery (2002). In the present work we will mostly use latin hypercube sampling. The basic idea consists in obtaining N_s sample points by dividing the range of each input variable into N_s sections of equal marginal probability $1/N_s$ and sampling once from each section.

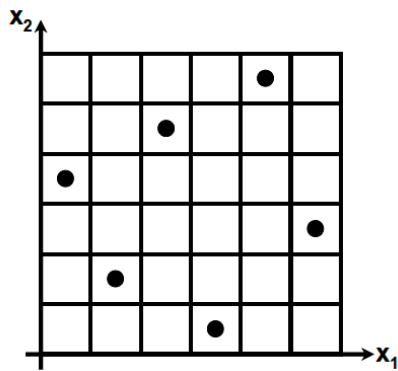


Figure A-3. Latin hypercube sampling with sampling size $N_s=6$.

Numerical Simulation

The next step in surrogate modeling consists in running the numerical simulations at the sampled points of the design of experiments. This step is straight forward and usually involves automatizing the running of the simulations.

Polynomial Response Surface Construction

The third step is the construction of the polynomial response surface approximation using regression techniques. Let us denote y the function of interest that we want to approximate based

on y_i samples of its response. We seek to express y as a function of N_{β_1} monomial basis functions f_j . In order to determine the coefficients of the approximation in this monomial basis (i.e. determine the coefficients of the polynomial) we can write for each observation i , a linear Equation A-1:

$$y_i(\mathbf{f}(\mathbf{x})) = \sum_{j=1}^{N_{\beta_1}} \beta_j f_j^{(i)} + \varepsilon_i; \quad E(\varepsilon_i) = 0, \quad V(\varepsilon_i) = \sigma^2, \quad (\text{A-1})$$

where the errors ε_i are considered independent with expected value equal to zero and variance σ^2 . Vector $\boldsymbol{\beta}$ represents the quantitative relation between basis functions and $\mathbf{f}(\mathbf{x})$ is the vector of the monomial basis functions. The set of equations specified in Equation A-1 can be expressed in matrix form as:

$$\mathbf{y} = X\boldsymbol{\beta} + \boldsymbol{\varepsilon}; \quad E(\boldsymbol{\varepsilon}) = 0, \quad V(\boldsymbol{\varepsilon}) = \sigma^2 I,$$

where X is an $N_s \times N_{\beta_1}$ matrix of the basis functions taken at the values of sampled design variables points from the DoE. This matrix is also known as Gramian design matrix. A Gramian design matrix for a full quadratic polynomial in two variables ($N_v = 2; N_{\beta_1} = 6$) is shown in Equation A-2.

$$X = \begin{bmatrix} 1 & x_1^{(1)} & x_2^{(1)} & x_1^{(1)2} & x_1^{(1)}x_2^{(1)} & x_2^{(1)2} \\ 1 & x_1^{(2)} & x_2^{(2)} & x_1^{(2)2} & x_1^{(2)}x_2^{(2)} & x_2^{(2)2} \\ \vdots & \vdots & \vdots & \vdots & \vdots & \vdots \\ 1 & x_1^{(i)} & x_2^{(i)} & x_1^{(i)2} & x_1^{(i)}x_2^{(i)} & x_2^{(i)2} \\ \vdots & \vdots & \vdots & \vdots & \vdots & \vdots \\ 1 & x_1^{(N_s)} & x_2^{(N_s)} & x_1^{(N_s)2} & x_1^{(N_s)}x_2^{(N_s)} & x_2^{(N_s)2} \end{bmatrix} \quad (\text{A-2})$$

The polynomial response surface approximation of the observed response $y(\mathbf{x})$ can then be expressed as

$$\hat{y}(\mathbf{x}) = \sum_{j=1}^{N_{\beta}} b_j f_j(\mathbf{x})$$

where b_j is the estimated value of the coefficient associated with the j^{th} basis function $f_j(\mathbf{x})$ (i.e. the j^{th} polynomial coefficient). The error in approximation at a design point \mathbf{x} is then given as $e(\mathbf{x}) = y(\mathbf{x}) - \hat{y}(\mathbf{x})$. The coefficients vector \mathbf{b} can be obtained by minimizing a loss function L , defined as

$$L = \sum_{i=1}^{N_s} |e_i|^p$$

where e_i is the error at i^{th} data point, p is the order of loss function, and N_s is the number of sampled design points. A quadratic loss function ($p = 2$) is usually thus leading to least squares minimization. Such a loss function, that minimizes the variance of the error in approximation, has the advantage that we can estimate coefficient vector \mathbf{b} using an analytical expression, as shown in Equation A-3.

$$\mathbf{b} = (X^T X)^{-1} X^T \mathbf{y} \quad (\text{A-3})$$

The estimated polynomial coefficients \mathbf{b} (Equation A-3) are unbiased estimates of $\boldsymbol{\beta}$ that minimize variance. For additional details on regression the reader can refer to Draper and Smith (1998, Section 5-1).

Response Surface Verification

Once the polynomial response surface approximation is constructed several tools exist for assessing its fidelity to the original response. The regression analysis directly provides a certain number of basic tools such as correlation coefficient R^2 and root means square (RMS) error to assess the quality of the fit. Another frequently used index of the quality of the fit have been proposed by Allen (1971): the predicted sum of squares (PRESS) error. The PRESS error is the

root mean square of the errors obtained by fitting a polynomial to each combination of N_s-1 samples and calculating the prediction error at the point that was left out.

APPENDIX B GLOBAL SENSITIVITY ANALYSIS

Global sensitivity analysis (GSA) was initially formalized by Sobol (1993). The method is a variance based technique used to estimate the effect of different variables on the total variability of the function. Global sensitivity analysis is usually used to:

- assess importance of the variables
- fix non-essential variables (which do not affect the variability of the function) thus reducing the problem dimensionality

Applications of GSA were presented by Homma and Saltelli (1996) (analytical functions and study of a chemical kinetics model), Saltelli et al. (1999) (analytical functions), Vaidyanathan et al. (2004b) (liquid rocket injector shape design), Jin et al. (2004) (piston shape design), Jacques et al. (2004) (flow parameters in a nuclear reactor), and Mack et al. (2005a) (bluff body shape optimization).

We provide next the theoretical formulation of GSA. Let us assume a square-integrable function $f(\mathbf{x})$ as a function of a vector of independent uniformly distributed random input variables \mathbf{x} in domain $[0, 1]$. The function can be decomposed as the sum of functions of increasing dimensionality as

$$f(\mathbf{x}) = f_0 + \sum_i f_i(x_i) + \sum_{i<j} f_{ij}(x_i, x_j) + \dots + f_{12\dots N_v}(x_1, x_2, \dots, x_{N_v}) \quad (\text{B-1})$$

where $f_0 = \int_{\mathbf{x}=0}^1 f d\mathbf{x}$. If the condition $\int_0^1 f_{i_1\dots i_s} dx_k = 0$ is imposed for $k = i_l, \dots, i_s$ then the

decomposition described in Equation B-1 is unique. In the context of global sensitivity analysis, the total variance denoted as $V(f)$ can be expressed as shown in Equation B-2.

$$V(f) = \sum_{i=1}^{N_v} V_i + \sum_{1 \leq i, j \leq N_v} V_{ij} + \dots + V_{1\dots N_v} \quad (\text{B-2})$$

where $V(f) = E((f - f_0)^2)$, and each of the terms in Equation B-2 represents the partial contribution or partial variance of the independent variables (V_i) or set of variables to the total variance, and provides an indication of their relative importance. The partial variances can be calculated using the following expressions:

$$\begin{aligned} V_i &= V(E[f | x_i]), \\ V_{ij} &= V(E[f | x_i, x_j]) - V_i - V_j, \\ V_{ijk} &= V(E[f | x_i, x_j, x_k]) - V_{ij} - V_{ik} - V_{jk} - V_i - V_j - V_k, \end{aligned}$$

and so on, where V and E denote variance and expected value respectively. Note that the expected values and variances with respect to x_i are computed by $E[f | x_i] = \int_0^1 f_i dx_i$ and

$$V(E[f | x_i]) = \int_0^1 f_i^2 dx_i.$$

This formulation facilitates the computation of the sensitivity indices corresponding to the independent variables and set of variables. For example, the first and second order sensitivity indices can be computed as

$$S_i = \frac{V_i}{V(f)} \quad S_{ij} = \frac{V_{ij}}{V(f)}$$

Under the independent model inputs assumption, the sum of all the sensitivity indices is equal to one. The first order sensitivity index for a given variable represents the main effect of the variable, but it does not take into account the effect of the interaction of the variables. The total contribution of a variable to the total variance is given as the sum of all the interactions and the main effect of the variable. The total sensitivity index of a variable is then defined as

$$S_i^{total} = \frac{V_i + \sum_{j, j \neq i} V_{ij} + \sum_{j, j \neq i} \sum_{k, k \neq i} V_{ijk} + \dots}{V(f)}$$

Note that the above referenced expressions can be easily evaluated using surrogate models of the objective functions. Sobol (1993) has proposed a variance-based non-parametric approach to estimate the global sensitivity for any combination of design variables using Monte Carlo methods. To calculate the total sensitivity of any design variable x_i , the design variable set is divided into two complementary subsets of x_i and Z ($Z = x_j, \forall j = 1, N_v; j \neq i$). The purpose of using these subsets is to isolate the influence of x_i from the influence of the remaining design variables included in Z . The total sensitivity index for x_i is then defined as

$$S_i^{total} = \frac{V_i^{total}}{V(f)}$$

$$V_i^{total} = V_i + V_{i,Z}$$

where V_i is the partial variance of the objective with respect to x_i , and $V_{i,Z}$ is the measure of the objective variance that is dependent on interactions between x_i and Z . Similarly, the partial variance for Z can be defined as V_Z . Therefore the total objective variability can be written as

$$V = V_i + V_Z + V_{i,Z}$$

While Sobol had used Monte Carlo simulations to conduct the global sensitivity analysis, the expressions given above can be easily computed analytically if $f(\mathbf{x})$ can be represented in a closed form (e.g., polynomial response surface approximation).

APPENDIX C
PHYSICAL INTERPRETATION OF THE BAYESIAN IDENTIFICATION RESULTS WITH
EITHER MEASUREMENT OR INPUT PARAMETERS UNCERTAINTIES

In the present Appendix we provide an interpretation of the results obtained in the last section of Chapter 3, which led to Figure 3-9. For convenience we provide this figure again, denoted Figure C-1.

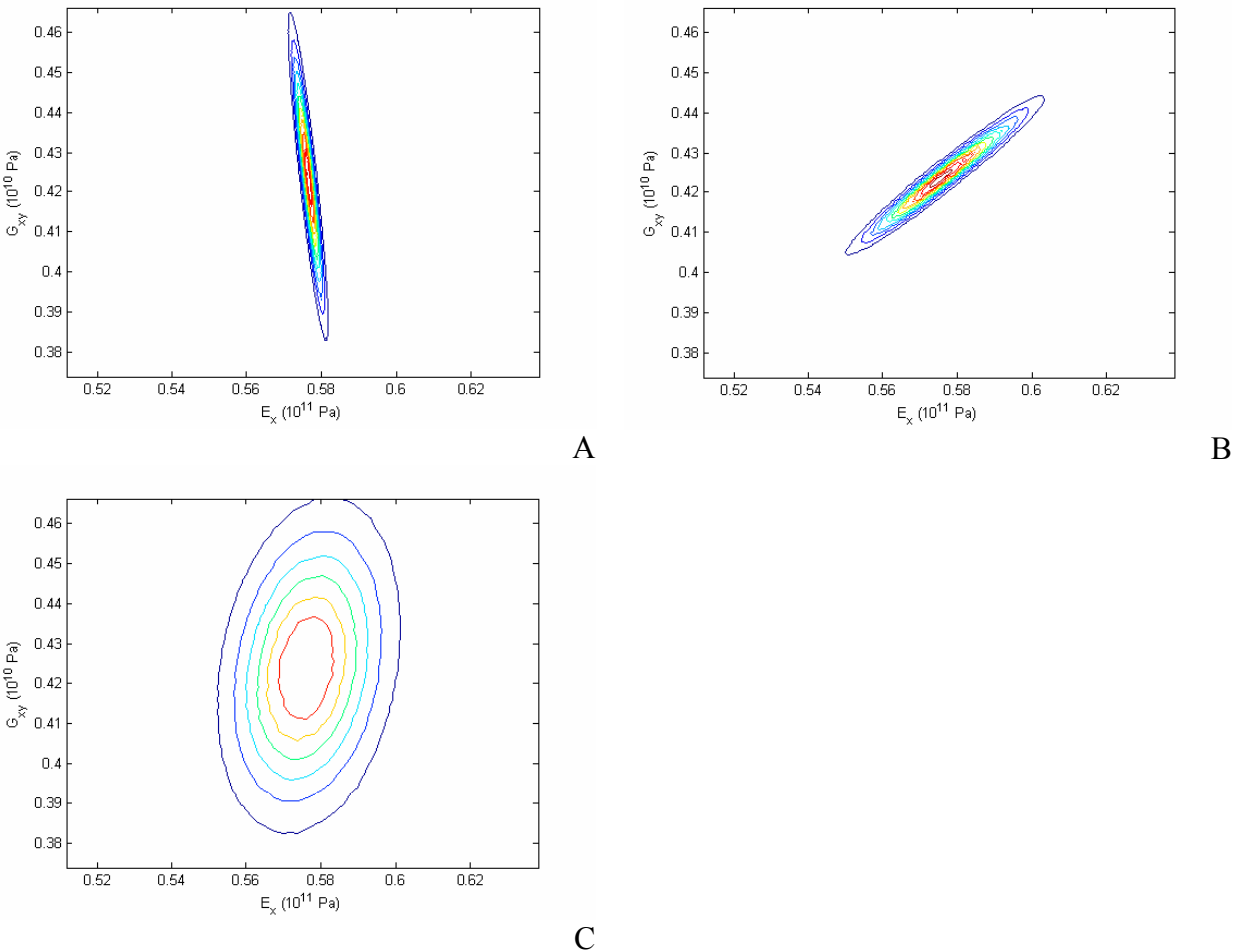


Figure C-1. Identified posterior pdf for: A) Only Gaussian measurement noise (case i.) B) Only model input parameters uncertainty (case ii.) C) Both Gaussian measurement noise and model input parameters uncertainty (case iii.).

Figure C-1 shows that the identified pdf differ substantially when only measurement noise is assumed and when only uncertainty on model input parameters is assumed. The third case,

where both uncertainties are assumed, is as expected a mix of the two previous ones. It is important to note that the pdf obtained with the combination of the two uncertainties differs substantially from the one with only Gaussian measurement noise thus illustrating the interest in considering uncertainty in model input parameters as well.

Since these are important results we provide next a basic physical interpretation based on a simplified model to confirm our findings. First we want to interpret the results of Figure C-1-B. For this purpose we rewrite the frequency formula of Equation 3-23 knowing that $E_x=E_y$ and assuming that $\nu_{xy} \approx 0$ (in reality $\nu_{xy} = 0.05$). Note that these assumptions are only done to facilitate the interpretation and not to obtain any results. Under these assumptions Equation 3-23 can be written as follows:

$$f_{kl}^2 = \frac{\pi^2 h^2}{48 \rho a^4} \left\{ E_x \left[k^4 + \left(\frac{a}{b} l \right)^4 \right] + 4G_{xy} k^2 l^2 \left(\frac{a}{b} \right)^2 \right\} \quad (C-1)$$

For the interpretation let's assume first that there is only uncertainty in ρ and h , which appear factorized in front of all the rest in Equation C-1. In this case uncertainty on ρ and h will have the exact same effect on all the frequencies meaning that it will lead to perfect positive correlation when E_x and G_{xy} are identified. Now we also have uncertainty in the aspect ratio a/b which leads to variable uncertainty depending on the frequency. It turns out that when propagating this uncertainty on aspect ratio, the 7th natural frequency ($k=3, l=1$) has an uncertainty almost an order of magnitude lower than that on the other frequencies. This means that when going back to E_x and G_{xy} , they will be identified with low uncertainty since the Bayesian approach mainly considers the measurement with the lowest uncertainty. When combining all the uncertainties on the input parameters it turns out that the uncertainties on the frequencies due to aspect ratio are smaller than that due to the other parameters, which means

that the major factor of uncertainty is that coming from the factor in front of the brackets in Equation C-1. As mentioned before, this leads to perfect positive correlation between the E_x and G_{xy} as well as same relative uncertainties on them. This is approximately what we see in Figure C-1-B (N.B. perfect correlation means that the axes of the ellipse are at 45° angle from the component axes).

We now move to the interpretation of Figure C-1-A, where we have only Gaussian measurement noise on the frequencies. Since we assume that the noise is decorrelated, it is not as easy to interpret the results by looking at all nine frequencies at a time (through Equation C-1). Instead, we isolated a small segment and considered that we have only two noisy frequency measurements (f_1 and f_3) from which we want to determine E_x and G_{xy} . Using again the simplified equation C-1 the problem boils down to solving a linear system of two equations (in f_1 and f_3) with two unknowns (E_x and G_{xy}). The uncertainty on f_1 and f_3 was thus easily propagated to E_x and G_{xy} and we found that E_x has about 9 times smaller uncertainty than G_{xy} and that they are negatively highly correlated. This is approximately what we see in Figure C-1-A.

Figure C-1-C is consistent with it being a combination of Figures C-1-A and C-1-B which what we would expect.

APPENDIX D
MOIRE INTERFEROMETRY FULL FIELD MEASUREMENTS TECHNIQUE

Moiré interferometry is measurement technique using the fringe patterns obtained by optical interference off a diffraction grating in order to obtain full field displacement or strain maps. A comprehensive description of the method and its applications is provided by Post et al. (1997). Among the main advantages of Moiré interferometry are its high signal to noise ratio, its excellent spatial resolution and its insensitivity to rigid body rotations (Walker 1994). Applications of Moiré interferometry include the mapping of displacements of a tooth (Wood et al. 2003) and characterization of advanced fabric composites (Lee et al. 2006). Additional applications are also provided by Post et al. (1997).

The schematic of a four beam Moiré interferometry setup, such as the one used for our experiment, is given in Figure D-1. It uses four collimated light beams thus provide both the horizontal and vertical displacement fields. The interference is obtained by choosing the angle α such that it corresponds to the first order refraction angle.

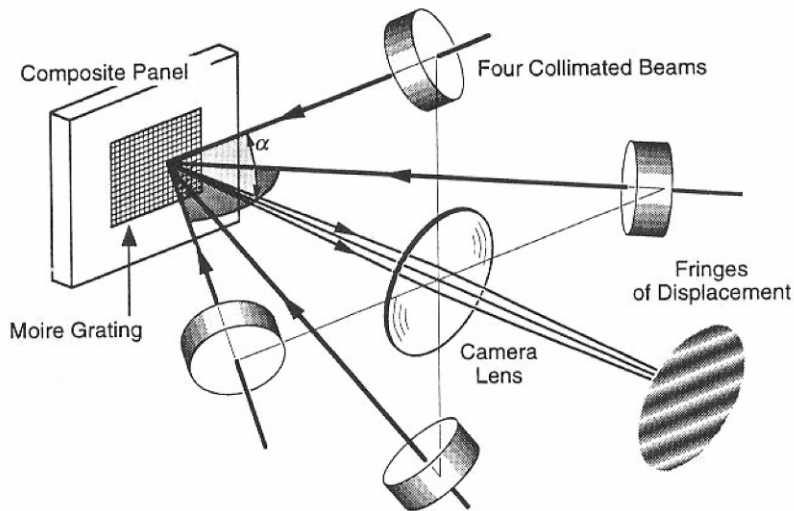


Figure D-1. Schematic of a Moiré interferometry setup.

The fringe patterns that result from the interference of two of the beams can be described by either intensity or phase information. While intensity methods have been developed first, a major issue limiting their accuracy resides in the determination of the exact maximum intensity locations. To address this issue, methods based on phase information were developed, such as phase shifting Moiré. All these methods use a carrier fringe pattern or a phase ramp in order to extract the phase φ , due to the fact that the cosine function is not bijective. Using a phase ramp λ , the intensity I can then be expressed as shown in Equation D-1.

$$I(x, y) = I_{backlight}(x, y) + I_{mod}(x, y) \cos[\varphi(x, y) + n\lambda] \quad n = 1 \dots N \quad (D-1)$$

Obtaining N fringe patterns (typically $N=4$) shifted by the imposed phase ramp allows to calculate the phase $\varphi(x, y)$. The displacement fields are then determined as follows:

$$U(x, y) = \frac{\Delta\varphi_x(x, y)}{2\pi f} \quad (D-2)$$

$$V(x, y) = \frac{\Delta\varphi_y(x, y)}{2\pi f} \quad (D-3)$$

where $\Delta\varphi$ is the phase difference between the initial and the final loading step and f is the frequency of the grating (1200 lines/mm in our case).

An automated phase extraction procedure was developed under Matlab by Yin (2008) at the Experimental Stress Analysis Laboratory at the University of Florida. This toolbox carries out the phase extraction and unwrapping from the four phase shifted Moiré fringe patterns. It then provides the corresponding displacement maps.

APPENDIX E COMPARISON OF THE MOIRÉ INTERFEROMETRY FIELDS AND THEIR PROPER ORTHOGONAL DECOMPOSITION PROJECTION

In this appendix we investigate the difference between the displacement fields obtained from the Moiré interferometry fringe patterns and their POD projection that is used for the Bayesian identification. Figure E-1 presents the maps of these differences for the U and V displacements.

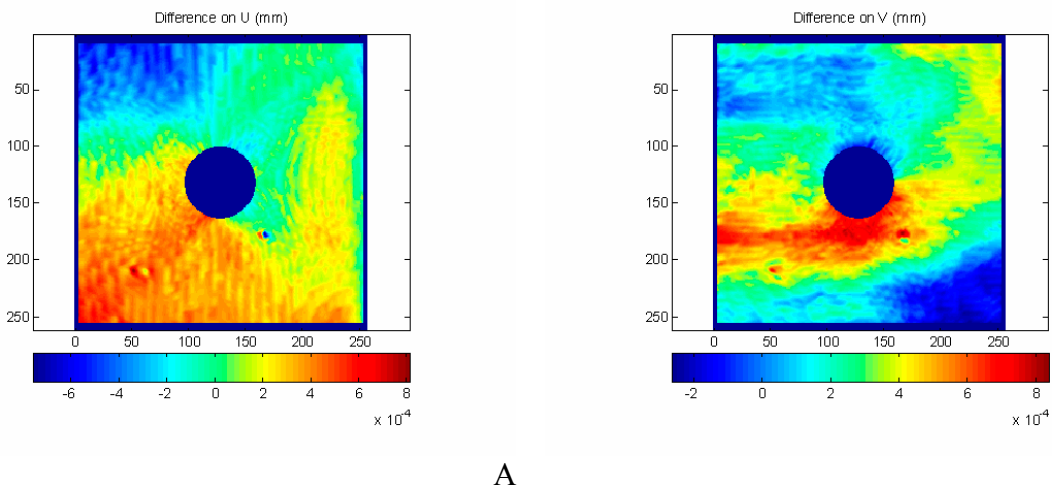


Figure E-1. Difference between the displacement fields obtained from the Moiré fringe patterns and their POD projection for the: A) U field. B) V field.

We can see that the POD projection filters out any dissymmetries in the field. The order of magnitude of the variations that are filtered out is about an order of magnitude smaller than the field values.

An important question at this point is to know if the variations that are filtered out by the POD projection would influence the identified parameters. To have a rough estimate of the resulting error on the material properties we move to the strain fields that correspond to the error maps shown in Figure E-1. By numerically differentiating the fields of Figure E-1 using the

BibImages toolbox (Molimard 2006) we obtain the strain equivalent maps representing the difference between the strains and their POD projection. These are shown in Figure E-2.

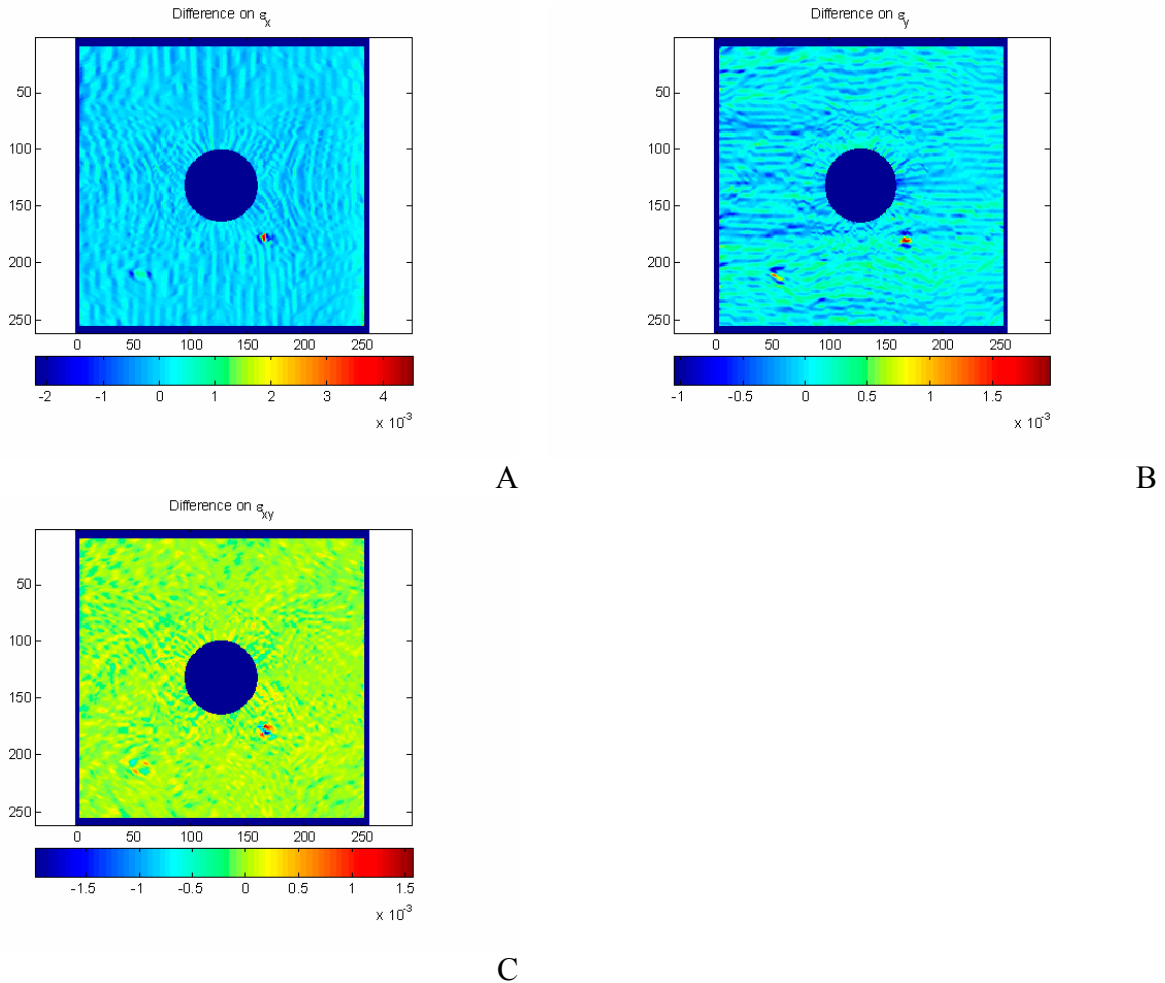


Figure E-2. Strain equivalent difference maps between the fields obtained from the Moiré fringe patterns and their POD projection for A) ϵ_x . B) ϵ_y . C) ϵ_{xy} .

We can note that while the displacement error fields in Figure E-1 had a non-negligible signal component, the major remaining component when calculating the strains is noise. We can also note that the noise is actually not random but seems to follow relatively well the Moiré fringe patterns on the initial images. This means that the noise is mainly induced by the fringe patterns themselves and the phase shifting algorithm that extracts the displacement fields from

these fringe patterns. In that case the filtered out components of the fields would in large parts independent of the material properties, thus almost not affecting the identification.

In order to have nevertheless an idea of the error committed on the estimation of the material properties by filtering out these variations we calculated the average value of ε_x and ε_y over the fields and used these averages to have a rough estimate of the errors on the properties E_x and ν_{xy} using the following formulas.

$$E_x \approx \frac{\sigma_x}{\varepsilon_x^{average}} \quad (E-1)$$

$$\nu_{xy} \approx \frac{\varepsilon_y^{average}}{\varepsilon_x^{average}} \quad (E-2)$$

Using the values given in Table E-1 we found that the error due filtering would be of the order of 1.6% on E_x and 0.5% on ν_{xy} . These errors are not negligible but it is important to keep in mind that due to the very high noise levels and the average errors on ε_x and ε_y that are close to zero, these average values are affected by the noise, which we have shown is related to the fringe patterns and displacement extraction algorithm rather than to the physics of the experiment itself. The error induced by filtering and which is not due to this type of noise would then be somewhat smaller.

Table E-1. Average values of the experimental fields and of the components of the fields that were filtered out by POD projection.

Average($\varepsilon_x^{experimental}$)	Average($\varepsilon_x^{filtered\ out}$)	Average($\varepsilon_y^{experimental}$)	Average($\varepsilon_y^{filtered\ out}$)
$6.29 \cdot 10^{-4}$	$1.02 \cdot 10^{-5}$	$-4.87 \cdot 10^{-4}$	$2.19 \cdot 10^{-6}$

LIST OF REFERENCES

- Acar, E., Kale, A., Haftka, R. T., and Stroud, W. J. (2006). "Structural Safety Measures for Airplanes." *J.Aircr.*, 43(1), 30-38.
- Allen, D. M. (1971). "Mean square error of prediction as a criterion for selecting variables." *Technometrics*, 13, 469-475.
- Alvin, K. F. (1997). "Finite element model update via Bayesian estimation and minimization of dynamic residuals." *AIAA J.*, 35(5), 879-886.
- Amiot, F., Hild, F., and Roger, J. P. (2007). "Identification of elastic property and loading fields from full-field measurements." *Int.J.Solids Structures*, 44(9), 2863-2887.
- Anderson, E., Bai, Z., Bischof, C., Blackford, S., Demmel, J., Dongarra, J., Du Croz, J., Greenbaum, A., Hammarling, S., McKenney, A., and Sorensen, D. (1999). *LAPACK User's Guide*. 3rd edition, SIAM, Philadelphia.
- Arafeh, M. H., Knopf-Lenoir Vayssade, C., and Rouger, F. (1995). "Conception optimale d'essais de flexion de plaques orthotropes et identification." *Comptes Rendus De l'Académie Des Sciences*, 321(II b), 351-354.
- Araújo, A. L., Mota Soares, C. M., Moreira de Freitas, M. J., Pedersen, P., and Herskovits, J. (2000). "Combined numerical–experimental model for the identification of mechanical properties of laminated structures." *Compos.Struct.*, 50(4), 363-372.
- ASTM D 3039. (2002). *Standard Test Method for Tensile Properties of Polymer Matrix Composite Materials*. ASTM International, West Conshohocken.
- Avril, S., Bonnet, M., Bretelle, A. S., Grédiac, M., Hild, F., Ienny, P., Latourte, F., Lemosse, D., Pagano, S., and Pagnacco, E. (2008). "Overview of Identification Methods of Mechanical Parameters Based on Full-field Measurements." *Exp.Mech.*, 48(4), 381-402.
- Ayorinde, E. O., and Yu, L. (1999). "On the Use of Diagonal Modes in the Elastic Identification of Thin Plates." *J. Vib. Acoust.*, 121, 33.
- Ayyub, B. M., and Chia, C. Y. (1992). "Generalized conditional expectation for structural reliability assessment." *Struct.Saf.*, 11(2), 131-146.
- Balabanov, V., Kaufman, M., Knill, D. L., Haim, D., Golovidov, O., Giunta, A. A., Haftka, R. T., Grossman, B., Mason, W. H., and Watson, L. T. (1996). "Dependence of optimal structural weight on aerodynamic shape for a high speed civil transport." *Proc., 6th AIAA/NASA/USAF Multidisciplinary Analysis & Optimization Symp.*, 96-4046.
- Balabanov, V. O., Giunta, A. A., Golovidov, O., Grossman, B., Mason, W. H., Watson, L. T., and Haftka, R. T. (1999). "Reasonable design space approach to response surface approximation." *J.Aircr.*, 36(1), 308-315.

- Bapanapalli, S. K., Martinez, O. M., Gogu, C., Sankar, B. V., Haftka, R. T., and Blosser, M. L. (2006). "Analysis and Design of Corrugated-Core Sandwich Panels for Thermal Protection Systems of Space Vehicles." *Proc., 47th AIAA/ASME/ASCE/AHS/ASC Structures, Structural Dynamics, and Materials Conf., Newport, RI*, AIAA Paper 2006-1942.
- Bayes, T. (1763). "An essay towards solving a problem in the doctrine of chances." *Philosophical Transactions of the Royal Society*, 53, 370-418.
- Beck, J. L., and Katafygiotis, L. S. (1998). "Updating Models and Their Uncertainties. I: Bayesian Statistical Framework." *J. Engrg. Mech.*, 124(4), 455-461.
- Berger, J. O. (1985). *Statistical Decision Theory and Bayesian Analysis*. Springer, New York.
- Berkooz, G., Holmes, P., and Lumley, J. L. (1993). "The proper orthogonal decomposition in the analysis of turbulent flows." *Annu.Rev.Fluid Mech.*, 25(1), 539-575.
- Björck, Å. (1996). *Numerical methods for least squares problems*. SIAM, Philadelphia.
- Blevins, R. D. (1979). *Formulas for natural frequency and mode shape*. Van Nostrand Reinhold, New York.
- Blosser, M. L., Chen, R. R., Schmidt, I. H., Dorsey, J. T., Poteet, C. C., Bird, R. K., and Wurster, K. E. (2004). "Development of advanced metallic thermal-protection-system prototype hardware." *J.Spacecraft Rockets*, 41(2), 183-194.
- Buckingham, E. (1914). "On Physically Similar Systems; Illustrations of the Use of Dimensional Equations." *Physical Review*, 4(4), 345-376.
- Cloud, G. L. (1998). *Optical methods of engineering analysis*. Cambridge University Press, Cambridge.
- Cugnoni, J. (2004). "Identification par recalage modal et fréquentiel des propriétés constitutives de coques en matériaux composites." *Ph.D. Thesis no. 3106, School of Engineering, Swiss Federal Institute of Technology, Lausanne*.
- Daghia, F., de Miranda, S., Ubertini, F., and Viola, E. (2007). "Estimation of elastic constants of thick laminated plates within a Bayesian framework." *Compos.Struct.*, 80(3), 461-473.
- Dascotte, E. (2004). "Identification of Random Material Properties using a Mixed Deterministic-Probabilistic Method." *International Seminar on Modal Analysis*, 20-22.
- De Wilde, W. P., Narmon, B., Sol, H., and Roovers, M. (1984). "Determination of the material constants of an anisotropic lamina by free vibration analysis." *Proc., 2nd International Modal Analysis Conf., Orlando, FL*, 44-49.
- De Wilde, W. P., Sol, H., and Van Overmeire, M. (1986). "Coupling of Lagrange interpolation, modal analysis and sensitivity analysis in the determination of anisotropic plate rigidities." *Proc., 4th International Modal Analysis Conf., Los Angeles, CA*, 1058-1063.

- Deobald, L. R., and Gibson, R. F. (1988). "Determination of elastic constants of orthotropic plates by a modal analysis/Rayleigh-Ritz technique." *J.Sound Vibrat.*, 124 269-283.
- Dickinson, S. M. (1978). "The buckling and frequency of flexural vibration of rectangular isotropic and orthotropic plates using Rayleigh's method." *J.Sound Vibrat.*, 61(1), 1-8.
- Draper, N. R., and Smith, H. (1998). *Applied regression analysis*. John Wiley & Sons, New York.
- Elishakoff, I. (1991). "Convex versus probabilistic modelling of uncertainty in structural dynamics." *Structural Dynamics: Recent Advances, London, Keynote Lecture*, 3–21.
- Elseifi, M. A., and Irvine, C. (2002). "Bayesian models for updated cured composite properties." *Proc., 43rd AIAA/ASME/ASCE/AHS/ASC Structures, Structural Dynamics, and Materials Conf., Denver, CO, AIAA Paper 2002-1273*.
- FAA. (2005). *Airworthiness Standards: Transport Category Airplanes*. Department of Transport, Washington.
- Filomeno Coelho, R., Breitkopf, P., and Knopf-Lenoir Vayssade, C. (2008). "Model reduction for multidisciplinary optimization-application to a 2D wing." *Struct. Multidisc. Optim.*, 37(1), 29-48.
- Filomeno Coelho, R. and Breitkopf, P. (2009). *Optimisation multidisciplinaire en mécanique: Réduction de modèles, robustesse, fiabilité, réalisations logicielles*. Hermes Science Publications, Paris.
- Fishman, G. S. (1996). *Monte Carlo: concepts, algorithms, and applications*. Springer, New York.
- Frederiksen, P. S. (1997). "Experimental Procedure and Results for the Identification of Elastic Constants of Thick Orthotropic Plates." *J.Composite Mater.*, 31(4), 360.
- Galilei, G. (1638). *Discorsi e dimostrazioni matematiche intorno a due nuove scienze*. Elsevirii, Leyden.
- Genovese, K., Lamberti, L., and Pappalettere, C. (2005). "Improved global–local simulated annealing formulation for solving non-smooth engineering optimization problems." *Int.J.Solids Structures*, 42(1), 203-237.
- Geymonat, G., Hild, F., and Pagano, S. (2002). "Identification of elastic parameters by displacement field measurement." *Comptes Rendus-Mécanique*, 330(6), 403-408.
- Geymonat, G., and Pagano, S. (2003). "Identification of mechanical properties by displacement field measurement: a variational approach." *Meccanica*, 38(5), 535-545.
- Ghanem, R. G., and Spanos, P. D. (2003). *Stochastic finite elements: a spectral approach*. Dover Publications, Dover.

- Gibson, R. F. (2000). "Modal vibration response measurements for characterization of composite materials and structures." *Composites Sci.Technol.*, 60(15), 2769-2780.
- Gogu, C., Bapanapalli, S. K., Haftka, R. T., and Sankar, B. V. (2007a). "Comparison of Materials for Integrated Thermal Protection Systems for Spacecraft Reentry." *Proc., 48th AIAA/ASME/ASCE/AHS/ASC Structures, Structural Dynamics, and Materials Conf., Honolulu, HI*, AIAA Paper 2007-1860.
- Gogu, C., Haftka, R. T., Bapanapalli, S. K., and Sankar, B. V. (2007b). "Reducing the number of variables in a response surface approximation - Application to thermal design." *Proc., ASME IDETC/CIE 2007 Conf., Las Vegas, NV*, Paper DETC2007-34674.
- Granta Design. (2005). *CES Selector Edupack 2005*.
- Grediac, M. (1989). "Principe des travaux virtuels et identification." *Comptes Rendus De l'Académie Des Sciences. Série 2, Mécanique, Physique, Chimie, Sciences De l'Univers, Sciences De La Terre*, 309(1), 1-5.
- Grédiac, M., and Vautrin, A. (1990). "A New Method for Determination of Bending Rigidities of Thin Anisotropic Plates." *J. Appl. Mech.*, 57(1), 964.
- Grédiac, M., and Paris, P. A. (1996). "Direct Identification of Elastic Constants of Anisotropic Plates by Modal Analysis: Theoretical and Numerical Aspects." *J.Sound Vibrat.*, 195(3), 401-415.
- Grédiac, M., Fournier, N., Paris, P. A., and Surrel, Y. (1998a). "Direct Identification of Elastic Constants of Anisotropic Plates by Modal Analysis: Experimental Results." *J.Sound Vibrat.*, 210(5), 643-659.
- Grediac, M., and Pierron, F. (1998b). "A T-shaped specimen for the direct characterization of orthotropic materials." *Int J Numer Methods Eng*, 41(2), 293-309.
- Gürdal, Z., Haftka, R. T., and Hajela, P. (1999). *Design and Optimization of Laminated Composite Materials*. Wiley-Interscience, New York.
- Hill, G. A., and Olson, E. D. (2004). "Applications of Response Surface-Based Methods to Noise Analysis in the Conceptual Design of Revolutionary Aircraft." *Proc., 10th AIAA/ISSMO Symposium on Multidisciplinary Analysis and Optimization Conf.*, AIAA Paper 2004-4437.
- Homma, T., and Saltelli, A. (1996). "Importance measures in global sensitivity analysis of nonlinear models." *Reliability Engineering & Systems Safety*, 52(1), 1-17.
- Hosder, S., Watson, L. T., Grossman, B., Mason, W. H., Kim, H., Haftka, R. T., and Cox, S. E. (2001). "Polynomial response surface approximations for the multidisciplinary design optimization of a high speed civil transport." *Optim. Eng.*, 2(4), 431-452.

- Hua, H., Sol, H., and De Wilde, W. P. (2000). "On a statistical optimization method used in finite element model updating." *J.Sound Vibrat.*, 231(4), 1071-1078.
- Isenberg, J. (1979). "Progressing from Least Squares to Bayesian Estimation." *Proc., ASME Winter Annual Meeting, New York, NY*, Paper 79-A/DSC-16.
- Jacques, J., Lavergne, C., and Devictor, N. (2006). "Sensitivity analysis in presence of model uncertainty and correlated inputs." *Reliab. Eng. Syst. Saf.*, 91(10-11), 1126-1134.
- Jin, R., Chen, W., and Sudjianto, A. (2004). "Analytical Metamodel Based Global Sensitivity Analysis and Uncertainty Propagation for Robust Design." *SAE Transactions*, 113(5), 835-846.
- Kaipio, J. P., and Somersalo, E. (2005). *Statistical and computational inverse problems*. Springer, New York.
- Kaufman, M., Balabanov, V., Grossman, B., Mason, W. H., Watson, L. T., and Haftka, R. T. (1996). "Multidisciplinary optimization via response surface techniques." *Proc., 36th Israel Annual Conf. on Aerospace Sciences, Tel Aviv and Haifa, Israel*, A-57-A-67.
- Kernevez, J. P., Knopf-Lenoir Vayssade, C., Touzot, G., and Verchery, G. (1978). "An identification method applied to an orthotropic plate bending experiment." *Int. J. Numer. Meth. Eng.*, 12(1), 129-139.
- Lacey, D., and Steele, C. (2006). "The use of dimensional analysis to augment design of experiments for optimization and robustification." *J.Eng.Des.*, 17(1), 55-73.
- Lai, T. C., and Ip, K. H. (1996). "Parameter estimation of orthotropic plates by Bayesian sensitivity analysis." *Compos.Struct.*, 34(1), 29-42.
- Lauwagie, T., Sol, H., Roebben, G., Heylen, W., Shi, Y., and Van der Biest, O. (2003). "Mixed numerical-experimental identification of elastic properties of orthotropic metal plates." *NDT and E International*, 36(7), 487-496.
- Lauwagie, T., Sol, H., Heylen, W., and Roebben, G. (2004). "Determination of the in-plane elastic properties of the different layers of laminated plates by means of vibration testing and model updating." *J.Sound Vibrat.*, 274(3-5), 529-546.
- Lawson, C. L., and Hanson, R. J. (1974). *Solving Least Squares Problems*. Prentice Hall, Englewood Cliffs.
- Le Magorou, L., Rouger, F., and Bos, F. (2000). "Identification of constitutive laws of wood based panels using inverse method." *Proc., 12eme Journées Nationales Sur Les Composites, Cachan, France*, 385-394.
- Le Magorou, L., Bos, F., and Rouger, F. (2002). "Identification of constitutive laws for wood-based panels by means of an inverse method." *Composites Sci.Technol.*, 62(4), 591-596.

- Lecompte, D., Sol, H., Vantomme, J., and Habraken, A. M. (2005). "Identification of elastic orthotropic material parameters based on ESPI measurements." *Proc., SEM Annual Conf. and Exposition on Experimental and Applied Mechanics*.
- Lecompte, D., Smits, A., Sol, H., Vantomme, J., and Van Hemelrijck, D. (2007). "Mixed numerical–experimental technique for orthotropic parameter identification using biaxial tensile tests on cruciform specimens." *Int.J.Solids Structures*, 44(5), 1643-1656.
- Lee, J., Haftka, R. T., Griffin, O. H., Watson, L. T., and Sensmeier, M. D. (1994). "Detecting delaminations in a composite beam using anti-optimization." *Struct. Multidisc. Optim.*, 8(2), 93-100.
- Lee, J. R., Molimard, J., Vautrin, A., and Surrel, Y. (2006). "Diffraction grating interferometers for mechanical characterisations of advanced fabric laminates." *Opt. Laser Technol.*, 38(1), 51-66.
- Leissa, A. W. (1987). "Recent studies in plate vibrations, 1981–1985, part II: complicating effects." *Shock Vib. Dig.*, 19(3), 10–24.
- Lucia, D. J., Beran, P. S., and Silva, W. A. (2004). "Reduced-order modeling: new approaches for computational physics." *Prog.Aerospace Sci.*, 40(1-2), 51-117.
- Mack, Y., Goel, T., Shyy, W., Haftka, R. T., and Queipo, N. V. (2005). "Multiple surrogates for the shape optimization of bluff body-facilitated mixing." *Proc., 43rd AIAA Aerospace Sciences Meeting and Exhibit, Reno, NV, AIAA Paper 2005-0333*.
- Maletta, C., and Pagnotta, L. (2004). "On the determination of mechanical properties of composite laminates using genetic algorithms." *Int. J. Mech. Mater. Des.*, 1(2), 199-211.
- Marwala, T., and Sibisi, S. (2005). "Finite Element Model Updating Using Bayesian Framework and Modal Properties." *J.Aircr.*, 42(1), 275-278.
- Matheron, G. (1963). "Principles of geostatistics." *Econ. Geol.*, 58, 1246-1266.
- Mauvoisin, G., Bremand, F., and Lagarde, A. (1994). "Three-dimensional shape reconstruction by phase-shifting shadow moiré." *Appl.Opt.*, 33 2163-2169.
- Molimard, J., Le Riche, R., Vautrin, A., and Lee, J. R. (2005). "Identification of the four orthotropic plate stiffnesses using a single open-hole tensile test." *Exp.Mech.*, 45(5), 404-411.
- Molimard, J. (2007). *BibImages Toolbox v0.2 User's Manual*.
- Mottershead, J. E., and Friswell, M. I. (1993). "Model Updating In Structural Dynamics: A Survey." *J.Sound Vibrat.*, 167(2), 347-375.

- Myers, D. E., Martin, C. J., and Blosser, M. L. (2000). "Parametric Weight Comparison of Advanced Metallic, Ceramic Tile, and Ceramic Blanket Thermal Protection Systems." *NASA/TM-2000-210289*, 1-44.
- Myers, R. H., and Montgomery, D. C. (2002). *Response Surface Methodology: Process and Product in Optimization Using Designed Experiments*. John Wiley & Sons, New York.
- Noh, W. J. (2004). "Mixed Mode Interfacial Fracture Toughness of Sandwich Composites at Cryogenic Temperatures." *Master's Thesis, University of Florida*.
- Norden, R. H. (1972). "A survey of maximum likelihood estimation." *International Statistical Review/Revue Internationale De Statistique*, 40(3), 329-354.
- Orr, M. J. L. (1996). "Introduction to radial basis function networks." *Center for Cognitive Science, Edinburg University, Scotland, UK*.
- Orr, M. J. L. (1999). "Recent advances in radial basis function networks." *Technical Report, Institute for Adaptive and Neural Computation Division for Informatics, Edinburg University, Scotland, UK*.
- Papazoglou, V. J., Tsouvalis, N. G., and Lazaridis, A. G. (1996). "A non-destructive evaluation of the material properties of a composite laminated plate." *Appl. Compos. Mater.*, 3(5), 321-334.
- Papila, M. H., and Haftka, R. T. (1999). "Uncertainty and Wing Structural Weight Approximations." *Proc., 40th AIAA/ASME/ASCE/AHS/ASC Structures, Structural Dynamics and Materials Conf. and Exhibit, St. Louis, MO*, 988-1002.
- Papila, M. H., and Haftka, R. T. (2000). "Response surface approximations: Noise, error repair, and modeling errors." *AIAA J.*, 38(12), 2336-2354.
- Pederson, P., and Frederiksen, P. S. (1992). "Identification of orthotropic material moduli by a combined experimental/numerical approach." *Measurement*, 10(3), 113-118.
- Post, D., Han, B., and Ifju, P. (1997). *High sensitivity moiré: experimental analysis for mechanics and materials*. Springer, New York.
- Poteet, C. C., Abu-Khajeel, H., and Hsu, S. Y. (2004). "Preliminary thermal-mechanical sizing of a metallic thermal protection system." *J.Spacecraft Rockets*, 41(2), 173-182.
- Qu, Z. Q. (2004). *Model Order Reduction Techniques: With Applications in Finite Element Analysis*. Springer, New York.
- Ragauskas, P., and Skukis, E. (2007). "Material properties identification. Comparison of two techniques." *Mechanika*, 6(68), 39-44.

- Rebba, R., and Mahadevan, S. (2006a). "Statistical Methods for Model Validation under Uncertainty." *Proc., 47th AIAA/ASME/ASCE/AHS/ASC Structures, Structural Dynamics, and Materials Conf., Newport, RI.*
- Rebba, R., Mahadevan, S., and Huang, S. (2006b). "Validation and error estimation of computational models." *Reliab. Eng. Syst. Saf.*, 91(10-11), 1390-1397.
- Rieutord, E. (1985). "Analyse dimensionnelle - Similitudes et essais sur modèle." *Mécanique Des Fluides*, INSA, Lyon.
- Rikards, R., Chate, A., and Gailis, G. (2001). "Identification of elastic properties of laminates based on experiment design." *Int.J.Solids Structures*, 38(30-31), 5097-5115.
- Rikards, R., Abramovich, H., Green, T., Auzins, J., and Chate, A. (2003). "Identification of Elastic Properties of Composite Laminates." *Mech. Adv. Mater. Struct.*, 10(4), 335-352.
- Rikards, R., and Auzins, J. (2004). "Response surface method for solution of structural identification problems." *Inv. Prob. Sci. Eng.*, 12(1), 59-70.
- Rouger, F., Khebibeche, M., and Govic, C. (1990). "Non-determined tests as a way to identify wood elastic parameters: the finite element approach." *Proc., Euromech Colloquium 269 Mechanical Identification of Composites*, 82-90.
- Rust, S. W., Todt, F. R., Harris, B., Neal, D., and Vangel, M. (1989). "Statistical methods for calculating material allowables for MIL-HDBK-17." *Test Methods and Design Allowables for Fibrous Composites*, C. C. Chamis, ed., ASTM International, 136-149.
- Sacks, J., Schiller, S. B., and Welch, W. J. (1989). "Designs for computer experiments." *Technometrics*, 31 41-47.
- Sakamoto, S., and Ghanem, R. (2002). "Simulation of multi-dimensional non-Gaussian non-stationary random fields." *Prob.Eng.Mech.*, 17(2), 167-176.
- Saltelli, A., Tarantola, S., and Chan, K. (1999). "A quantitative model-independent method for global sensitivity analysis of model output." *Technometrics*, 41(1), 39-56.
- Schenk, C. A., and Schueller, G. I. (2003). "Buckling analysis of cylindrical shells with random geometric imperfections." *Int.J.Non-Linear Mech.*, 38(7), 1119-1132.
- Schenk, C. A., Pradlwarter, H. J., Schueller, G.I. (2005). "Non-stationary response of large, non-linear finite element systems under stochastic loading." *Comp. & Struct.*, 83(14), 1086-1102.
- Shi, Y., Sol, H., and Hua, H. (2005). "Transverse shear modulus identification by an inverse method using measured flexural resonance frequencies from beams." *J.Sound Vibrat.*, 285(1-2), 425-442.

- Silva, G., Le Riche, R., Molimard, J., Vautrin, A., and Galerne, C. (2007). "Identification of Material Properties Using FEMU: Application to the Open Hole Tensile Test." *Adv. Exp. Mech.*, 7-8 73-78.
- Silva, G. H. C. (2009). "Identification of material properties using finite elements and full-field measurements with focus on the characterization of deterministic experimental errors." *Ph.D. Thesis, Ecole des Mines de Saint Etienne, France.*
- Smarslok, B. P. (2009). "Measuring, using and reducing experimental and computational uncertainty in reliability analysis of composite laminates." *Ph.D. Dissertation, University of Florida.*
- Sobol, I. M. (1993). "Sensitivity estimates for nonlinear mathematical models." *Math. Model. Comput. Exp.*, 1(4), 407-411.
- Sol, H. (1986). "Identification of anisotropic plate rigidities using free vibration data." *Ph.D. Thesis, Free University of Brussels, Belgium.*
- Sonin, A. A. (1997). *The physical basis of dimensional analysis*. Massachusetts Institute of Technology, Cambridge, MA.
- Surrel, Y. (2005). "Les techniques optiques de mesure de champ: essai de classification." *Instr. Mes. Metrol.*, 4(3-4), 11-42.
- Sutton, M. A., McNeill, S. R., Helm, J. D., and Chao, Y. J. (2000). "Advances in two-dimensional and three-dimensional computer vision." *Topics Appl. Phys.*, 77 323-372.
- Szirtes, T. (1997). *Applied dimensional analysis and modeling*. McGraw-Hill, New York.
- Tarantola, A. (2004). *Inverse Problem Theory and Methods for Model Parameter Estimation*. SIAM, Philadelphia.
- Vaidyanathan, R., Goel, T., Shyy, W., Haftka, R. T., Queipo, N. V., and Tucker, P. K. (2004). "Global sensitivity and trade-off analyses for multi-objective liquid rocket injector design." *Proc., 40th AIAA/ASME/SAE/ASEE Joint Propulsion Conference and Exhibit, Fort Lauderdale, FL, AIAA Paper 2004-4007.*
- Vapnik, V. (1998). *Statistical learning theory*. Wiley, New York.
- Vaschy, A. (1892). "Sur les lois de similitude en physique." *Annales Télégraphiques*, 19 25-28.
- Vautrin, A. (2000). "Mechanical identification of composite materials and structures." *Proc., 2nd Asian-Australasian Conf. on Composite Materials, Kyongju, Korea*, 1305-1323.
- Venter, G., Haftka, R. T., and Starnes Jr, J. H. (1998). "Construction of Response Surface Approximations for Design Optimization." *AIAA J.*, 36(12), 2242-2249.

- Viana, F. A. C., and Goel, T. (2008). "Surrogates Toolbox 1.1 User's Manual." [Http://fchegury.Googlepages.com/surrogatetoolbox](http://fchegury.Googlepages.com/surrogatetoolbox), [last consulted 8.17.2009].
- Vignaux, V. A., and Scott, J. L. (1999). "Simplifying Regression Models Using Dimensional Analysis." *Aust. N.Z. J. Stat.*, 41(1), 31-41.
- Waller, M. D. (1939). "Vibrations of free square plates: part I. Normal vibrating modes." *Proc. Phys. Soc.*, 51 831-844.
- Waller, M. D. (1949). "Vibrations of Free Rectangular Plates." *Proc. Phys. Soc., B*, 62(5), 277-285.
- Walker, C. A. (1994). "A historical review of moiré interferometry." *Exp. Mech.*, 34(4), 281-299.
- Wood, J. D., Wang, R., Weiner, S., and Pashley, D. H. (2003). "Mapping of tooth deformation caused by moisture change using moire interferometry." *Dent. Mater.*, 19(3), 159-166.
- Yin, W. (2008). "Automated strain analysis system: development and applications." *Ph.D. Proposal, University of Florida*.

BIOGRAPHICAL SKETCH

Christian Gogu obtained in 2006 the “Ingénieur Civil des Mines” degree as well as a master’s degree in Mechanical Engineering from the Ecole des Mines de Saint Etienne in France. The same year he started in a joint PhD program between the Ecole des Mines de Saint Etienne in France and the University of Florida. His research interests include response surface methodology, dimensionality reduction methods, multidisciplinary optimization, probabilistic approaches and composite materials.